Faculdade de Engenharia da Universidade do Porto

Design of a Flying Electrical Boat

Ana Rita da Silva Mata

Supervisor: Prof. Mário Vaz
Co-Supervisor: Prof.ª Carolina Silva
Co-Supervisor at 4DC Tech: Eng.º Ricardo Bencatel

Mechanical Engineering Masters
Departamento de Engenharia Mecânica (DEMec)
Faculdade de Engenharia (FEUP)
Universidade do Porto (UP)

Resumo

Hydrofoils são soluções promissoras para aumentar a eficiência de embarcações, reduzindo o arrasto e permitindo maior desempenho. Este trabalho apresenta o desenvolvimento de um *foil* e de uma *strut* para a aplicação de uma embarcação para testes, abrangendo design paramétrico, simulação numérica e comparação de processos de fabrico. Foram desenvolvidas macros em *SolidWorks* para a geração automática de geometrias, permitindo explorar alternativas rapidamente. As estruturas foram dimensionadas considerando requisitos hidrodinâmicos, resistência estrutural e integração de um sistema de atuação para o controlo das *flaps*.

A análise numérica foi realizada no *Abaqus*, através do Método dos Elementos Finitos, aplicando modelos isotrópicos e anisotrópicos. Foram estudados quatro casos de carga em diferentes materiais e processos de fabrico, nomeadamente, impressão 3D em ácido poliláctico, impressão 3D de um modelo redesenhado, alumínio produzido por deposição de metal ligado e laminado em fibra de carbono por moldagem por prensagem.

Os resultados evidenciaram que o ácido poliláctico apenas se revelou adequado estruturalmente para o modelo redesenhado, o qual demonstrou mais flexibilidade para rápidas alterações, tornando-se ideal para prototipagem. O alumínio garantiu ductilidade e segurança, mas com penalização em massa e tempo de fabrico elevado. O laminado em fibra de carbono apresentou a melhor relação resistência e peso, embora com maior custo e complexidade de fabrico.

Este estudo reforça a importância do equilíbrio entre design paramétrico, análise estrutural e escolha do processo de fabrico, fornecendo uma base sólida para futuras otimizações de hydrofoils.

Palavras-chave: Embarcação com *hydrofoils*; Design paramétrico; Impressão 3D; Materiais compósitos; Método dos Elementos Finitos.

Abstract

Hydrofoils are promising solutions to improve the efficiency of vessels by reducing drag and enabling higher performance. This work presents the development of a foil and a strut for their application on a test vessel, covering parametric design, numerical simulation and comparison of manufacturing processes. Macros were developed in *SolidWorks* for automatic geometry generation, allowing rapid exploration of alternatives. The components were designed considering hydrodynamic requirements, structural strength and the integration of an actuation system for flap control.

The numerical analysis was performed in *Abaqus* using the Finite Element Method, applying both isotropic and anisotropic models. Four load cases were studied across different materials and manufacturing processes, namely, 3D printing in polylactic acid, 3D printing of a redesigned model, aluminum produced via bound metal deposition and carbon fiber laminate manufactured through press molding.

The results showed that polylactic acid was only structurally suitable for the redesigned model, which demonstrated greater flexibility for rapid modifications, making it ideal for prototyping. Aluminum provided ductility and safety but at the cost of increased mass and longer manufacturing time. The carbon fiber laminate exhibited the best strength to weight ratio, although with higher cost and manufacturing complexity.

This study highlights the importance of balancing parametric design, structural analysis and manufacturing process selection, providing a solid foundation for future hydrofoil optimizations.

Keywords: Vessel with hydrofoils, Parametric design; 3D printing; Composite materials; Finite Element Method.

Contribution to the Sustainable Development Goals (SDGs)

The present work aligns with several of the United Nations Sustainable Development Goals (SDGs), as it integrates aspects of sustainable engineering , innovative design and responsible production. Although the primary focus was the structural design and analysis of a foil and hydrofoil strut for a test vessel, the methodologies and findings have broader implications for sustainable development. The sustainable development goals (SDGs) that this work aligns with are summarized in Table 1.

Table 1: Alignment of this work with the United Nations Sustainable Development Goals (SDGs).

SDG	**Action (Target)**	**Contribution**	**Metrics**
9	9.5: Enhance scientific research and encourage innovation	Development of SolidWorks macros for parametric hydrofoil modeling and FEM simulations in Abaqus, fostering technological innovation in marine engineering.	Faster design iterations, reduced reliance on physical prototypes
12	12.2: Achieve sustainable management and efficient use of natural resources	Comparative analysis of 3D printing, BMD, Forged Carbon and Press Molding, identifying trade-offs between material efficiency, complexity and performance.	Mass to strength ratio, material utilization and innovative manufacturing techniques.
13	13.3: Improve capacity for climate change mitigation and impact reduction	Hydrofoil design reduces drag and energy consumption, test vessel minimizes disturbance to marine life due to reduced wake.	Reduction in energy consumption, structural efficiency and energy demand
17	17.16: Enhance the global partnership for sustainable development	Methodology combining parametric design, FEM and manufacturing assessment can be shared with academia and industry to foster collaboration.	Replicability of workflow across manufacturing techniques and vessel designs

In summary, this work not only advances hydrofoil design from a technical perspective but also supports the broader sustainability agenda promoting innovation, resource efficiency and environmentally conscious marine transport solutions.

Agradecimentos

Ao Professor Mário Vaz e à Professora Carolina Silva, pelo privilégio da sua orientação, pela compreensão e generosidade na partilha de conhecimento ao longo da elaboração desta dissertação.

A todos os professores que foram parte integrante deste trajeto, pela disponibilidade e exemplo de dedicação.

À 4DC Tech, na pessoa do Eng.º Ricardo Bencatel, pelo acolhimento e pela oportunidade de integrar este projeto em ambiente empresarial, bem como pelo acompanhamento e apoio prestados ao longo do seu desenvolvimento.

Aos colegas e amigos que me acompanharam neste percurso, em especial à Rita, pelos muitos momentos de partilha e companheirismo.

Ao Simão, por ter despertado a minha melhor versão e ter estado sempre presente desde o início desta caminhada, fortalecendo-me nos dias mais difíceis.

Aos meus pais, irmão e restante família, pelo amor e apoio incondicional nos momentos mais importantes da minha vida.

Agradeço, por fim, a todos os que direta ou indiretamente tornaram possível a concretização desta etapa.

Aos meus Pais

"The struggle itself toward the heights is enough to fill a man's heart.
One must imagine Sisyphus happy."

Albert Camus

Contents

List of Figures

List of Tables

List of Acronyms

Acronym	Description
3D	Three Dimensional
2D	Two Dimensional
ABS	Acrylonitrile Butadiene Styrene
AC	Alternating Current
AM	Additive Manufacturing
AoA	Angle of Attack
AR	Aspect Ratio
BMD	Bound Metal Deposition
BLDC	Brushless DC Motor
CAD	Computer Aided Design
CFD	Computational Fluid Dynamics
CFRP	Carbon Fibre Reinforced Polymer
DC	Direct Current
DMA	Dynamic Mechanical Analysis
DoE	Design of Experiments
FCS	Flight Control System
FE	Finite Element
FEA	Finite Element Analysis
FEM	Finite Element Method
Fn_h	Submergence Froude Number
FDM	Fused Deposition Modeling
GFRP	Glass Fibre Reinforced Polymer
LIDAR	Light Detection and Ranging
MRS	Mesh Refinement Study
NATO	North Atlantic Treaty Organization
NL	Netherlands
PLA	Polylactic Acid
RPD	Rapid Prototyping and Development
RMF	Rotating Magnetic Field
RTM	Resin Transfer Molding
SAC	Single-Acting Cylinder
SMC	Sheet Molding Compound
US	United States
VBA	Visual Basic for Applications
VFD	Variable Frequency Drive

List of Nomenclature

Symbol	Description
α	Angle of attack (° or rad)
A_p	Projected planform area of the foil (m^2)
A	Flap planform area (m^2)
AR	Aspect ratio of the foil (–)
ABS	Acrylonitrile Butadiene Styrene (–)
b	Span of the foil (m)
$b_{\text{front, each}}$	Span of each front foil (m)
$b_{\text{rear, each}}$	Span of each rear foil (m)
C_D	Drag coefficient (–)
C_L	Lift coefficient (–)
C_l	Lift coefficient used in hydrodynamic pressure calculation (–)
ΔC_l	Incremental lift coefficient due to flap deflection (–)
c	Average chord length of the foil (m)
$c_{\text{front, mid each}}$	Chord at mid-span of each front foil (m)
$c_{\text{front, strut}}$	Chord of front strut (m)
$c_{\text{front, tip each}}$	Chord at tip of each front foil (m)
$c_{\text{rear, mid each}}$	Chord at mid-span of each rear foil (m)
$c_{\text{rear, strut}}$	Chord of rear strut (m)
$c_{\text{rear, tip each}}$	Chord at tip of each rear foil (m)
d	Draft of the vessel (m)
$d_{f,to}$	Required horn distance at takeoff (m)
e	Oswald efficiency factor (–)
E	Elastic modulus (isotropic) (Pa)
E_1	Elastic modulus along principal direction 1 (Pa)
E_2	Elastic modulus along principal direction 2 (Pa)
E_3	Elastic modulus along principal direction 3 (Pa)
F	Force generated by linear actuator (N)
$F_{\text{reaction,11}}$	Reaction force in the 11 direction (N)
$F_{\text{reaction,22}}$	Reaction force in the 22 direction (N)
$F_{\text{reaction,33}}$	Reaction force in the 33 direction (N)
$F_{\text{front flap}}$	Flap length of front foil (m)
$F_{\text{rear flap}}$	Flap length of rear foil (m)
Fn_h	Submergence Froude Number (–)
G_{12}	Shear modulus in plane 1–2 (Pa)
G_{13}	Shear modulus in plane 1–3 (Pa)
G_{23}	Shear modulus in plane 2–3 (Pa)
h_{front}	Height of front strut (m)
h_{rear}	Height of rear strut (m)
I	Electric current in DC motor (A)
k_t	Torque constant of motor (Nm/A)

Symbol	Definition
L	Lift force on the foil (N)
L_{hull}	Total length of the hull (m)
$L_{\text{front flap}}$	Flap length of front foil (m)
$L_{\text{rear flap}}$	Flap length of rear foil (m)
$L_{\text{front, each}}$	Planform area of each front foil (m^2)
$L_{\text{rear, each}}$	Planform area of each rear foil (m^2)
L_{takeoff}	Takeoff velocity of the vessel (m/s)
l	Lever arm from flap hinge to centre of pressure (m)
MRS	Mesh Refinement Study (–)
$M_{\text{hinge,to}}$	Hinge moment at takeoff (N·m)
n_r	Rotor speed of AC motor (rpm)
n_s	Synchronous speed of AC motor (rpm)
p	Pressure applied to the foil (Pa)
P	Engine power (hp)
P_h	Pressure of hydraulic fluid (Pa)
$P_{\max}$	Maximum applied pressure (Pa)
Q	Flow rate of hydraulic fluid (L/min or m^3/s)
q_{to}	Dynamic pressure at takeoff (Pa)
Re	Reynolds number (–)
r_s	Servo horn radius (m)
ρ	Fluid density (kg/m^3)
$\sigma_{\max}$	Maximum principal stress for a given load case (MPa)
σ_{11}	Principal stress in the 11 direction (MPa)
σ_{22}	Principal stress in the 22 direction (MPa)
σ_{33}	Principal stress in the 33 direction (MPa)
θ	Angular position of actuator / foil (° or rad)
$t_{\text{front, each}}$	Maximum thickness of each front foil (m)
$t_{\text{rear, each}}$	Maximum thickness of each rear foil (m)
$t_{\text{front, strut}}$	Thickness of front strut (m)
$t_{\text{rear, strut}}$	Thickness of rear strut (m)
τ_{servo}	Servo torque (N·m)
v	Vessel speed (km/h)
v_f	Linear velocity of actuator rod (m/s)
v_{takeoff}	Takeoff velocity of the vessel (m/s)
η	Mechanical efficiency of linkage (–)
λ	Taper ratio (tip chord / root chord) (–)
Λ	Sweep angle (°)
δ	Boundary layer thickness (m)
ν	Poisson's ratio (isotropic) (–)
ν_{12}	Poisson's ratio in plane 1–2 (–)
ν_{13}	Poisson's ratio in plane 1–3 (–)
ν_{23}	Poisson's ratio in plane 2–3 (–)

Symbol	Definition
S3R	3-node triangular reduced integration shell element (–)
S4	4-node quadrilateral general-purpose shell element (–)
SF	Safety Factor (ratio of allowable strength to max stress) (–)
x	Scaled coordinates of foil profile (m)
$x_{\text{default}}, y_{\text{default}}$	Non-dimensional foil coordinates (–)
y	Scaled coordinates of foil profile (m)

1

Introduction

The development of hydrofoil vessels has gained renewed attention in recent years, driven by the pursuit of greater efficiency, sustainability and innovation in marine transportation. This work is positioned within that context, focusing on the design, structural analysis and evaluation of a hydrofoil system tailored for a small scale test vessel. Beyond the hydrodynamic principles governing foil performance, the project required the integration of automated design tools, careful consideration of actuator mechanisms and the exploration of different manufacturing approaches. By combining parametric modeling in *SolidWorks* with numerical simulations in *Abaqus*, the study not only addresses the feasibility of multiple structural configurations but also lays the foundation for future experimental validation and refinement.

1.1 Contextualization

Hydrofoils are increasingly being studied and applied in modern naval engineering due to their ability to lift the hull of the vessel above the water surface. Thereby reducing drag and improving efficiency. This principle, first explored in the early 20th century, has seen renewed relevance in recent decades with advancements in materials, control systems and manufacturing techniques. The combination of reduced hydrodynamic resistance and enhanced performance makes hydrofoils attractive for applications ranging from recreational craft to high speed ferries and experimental platforms.

In parallel, the growth of additive manufacturing and advanced composites has expanded the possibilities for designing and producing complex hydrofoil structures. These technologies enable the creation of lightweight yet stiff components, customized geometries and rapid prototyping cycles, all of which are crucial for iterative design and testing. Furthermore, the integration of actuation systems allows for adjustable foils capable of adapting to varying operation conditions, an increasingly important requirement for experimental and high performance vessels.

Within this context, the present work focuses on the design and structural evaluation of a hydrofoil components, such as the foil and the strut, addressing not only its mechanical performance but also its manufacturability using different techniques. By situating the study within the broader landscape of hydrofoil research and modern production methods, the project contributes to the ongoing pursuit of efficient, adaptable and innovative marine vessel technologies.

1.2 Motivation

The motivation for this work stems from the growing need for efficient and adaptable experimental platforms that can support the development of hydrofoil technologies. While hydrofoils are well known for their ability to improve vessel performance by reducing drag

and increasing lift, their design and integration remain challenging due to the complex interplay between hydrodynamic, structural behavior and manufacturability. A test vessel equipped with an adjustable hydrofoil system provides an ideal environment for exploring these challenges, allowing design concepts to be evaluated in practice and refined based on experimental results.

From a structural perspective, the strut and the foil must simultaneously withstand significant hydrodynamic loads, accommodate actuation mechanisms and remain lightweight to avoid compromising overall efficiency. Balancing these requirements motivated the exploration of different design geometries and manufacturing methods. Additive manufacturing, advanced composites and hybrid solutions all present opportunities, but also trade-offs in terms of stiffness, strength, weight, cost and production complexity.

The overall motivation is therefore, first, create a functional and reliable test platform that enables experimental investigation of foil performance and second, to compare and evaluate manufacturing methods that may be applied to both prototypes and eventual operational vessels. By addressing these goals, the work contributes not only to the immediate objective of building a test vessel but also to the broader effort of advancing hydrofoil technology for practical marine applications.

1.3 Report Outline

This report is structured to follow the logical progression of the work, moving from background and methodology through analysis, discussion and conclusions.

After the introduction, which situates the study within broader context of hydrofoil development and defines its motivation, the second chapter reviews relevant literature on hydrofoil technologies, materials and manufacturing methods, providing the theoretical framework that supports the study.

The third chapter establishes the theoretical background necessary for the study, addressing key hydrodynamic principles such as foil theory, from foil geometry and aspect ratio to free surface effects and cavitation, as well as an introduction to finite element methods.

With this foundation in place, Chapter 4 describes the design process of the foils and strut, including the calculations that guided the selection of parameters, the development of *SolidWorks* macros to automate the generation of the geometry and the implementation of the actuator system.

The subsequent chapters present the numerical analysis carried out in *Abaqus*, beginning with the setup of materials, loads and boundary conditions and continuing with the evaluation of four case studies produced with different manufacturing methods.

The results are presented in detail in Chapter 6, while chapter 7 interprets these findings through a comparative discussion of stiffness, strength, weight and production complexity.

Finally, Chapter 8 concludes the report by consolidating the main outcomes of the work and identifying potential directions for future research and development.

2

State of Art and Literature Review

The present chapter will provide a comprehensive overview of the existing research work and advancements relevant to the design of hydrofoil boats. It is indispensable since, through the analysis of previous works, it is possible to identify key developments, methodologies and gaps that are present in the literature, which is essential in order to establish the foundation for this research. This chapter will give a contextualization of the study within the broader academic landscape, while highlighting the contributions of past research and identifying where there is room for improvement. It will ensure the right guidance for the research, allowing it to be developed upon prior work in a meaningful way.

In order to achieve this purpose and cover all the required concepts, this chapter will be divided into three main sections. First, the Hydrofoiling section will explore not only the historical evolution of the foils, but also their typical configurations and the respective advantages and disadvantages, as well as the most common materials and manufacturing techniques. The second section, Deployment Mechanisms, will review the different methods used for deploying hydrofoils, including patented designs and commercial solutions already in use. As for the final section, it will focus on the mechanisms responsible for the actual hydrofoil's movement and their differences, mainly between the fluid power and electric actuators.

2.1 Hydrofoiling

This section will provide an in-depth analysis of hydrofoils, beginning with a review of their historical evolution. It then explores the different types of hydrofoil configurations, along with their advantages and drawbacks. Finally, the most commonly used materials for hydrofoil manufacturing will be presented, as well as various manufacturing techniques. By analyzing these aspects, this section provides a comprehensive understanding of hydrofoils, their evolution in the boat industry, and the technological advancements that have shaped their development.

2.1.1 Historical Evolution

This section will highlight the key milestones that have contributed to advancements in the use of hydrofoils within the boat industry, along with the technological principles that have propelled their development.

The beginning of hydrofoils dates back to 1869 when the Parisian inventor Emmanuel Denis Farcot, was given a patent for an adaptation that incorporated a series of inclined planes along the sides of a boat. This innovation would aim to lift the vessel, reducing the draught effect. Farcot's idea sparked interest and further developments were made, leading to several subsequent patents that propelled the hydrofoil research forward, [1].

Since 1898, the Italian engineer Enrico Forlanini, began conducting research and experiments on hydrofoils, seeking to develop innovative designs. However, it was not until 1906 that he achieved successful results with a boat featuring a "ladder" foil system, as it can be seen in Figures 2.1 and 2.2. The vessel, weighting around 12000 N and powered by a 44.7 kW engine, reached a speed record of 68 km/h. This design was based on the insights obtained from his previous developments, which demonstrated that as speed increases, less foil area is required. This relationship follows the proportionality between lift and the square root of speed. This breakthrough paved the way for future advancements in hydrofoil technology, [1].

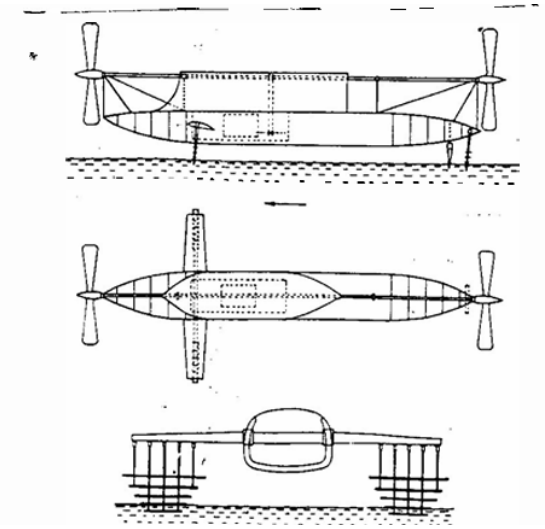

Figure 2.1: Forlanini's vessel design, [1].

Figure 2.2: Forlanini's vessel in Lake Maggiore in 1906, [1].

Also in Italy, engineer Guidoni, inspired by the work of Croco, another engineer who developed marine crafts supported by dihedral foils, merged these ideas with Forlanini's advancements. This collaboration led to the first successful take-off and landing of a hydrofoil seaplane in 1911, [1].

Even though significant advancements were made in Italy, one of the most remarkable developments took place in Canada, led by engineers Alexander Graham Bell and Frederick Casey Baldwin. Drawing inspiration from Forlanini's developments and incorporating some of his patents, they focused on constructing several hydrofoil vessels, which they referred to as hydrodomes. Among these, the HD-4 stood out, setting a speed record of 144 km/h in 1919. Both engineers also attempted to spark the interest of U.S Navy regarding the use of hydrofoil boats for military applications, however their efforts were ultimately unsuccessful, [1].

In 1927, Baron Hanns von Schertel began experimenting with hydrofoils. His studies covered all types of foils, submerged and surface piercing, transforming the previous unstable hydrofoil boat into a stable and weather resistant vessel, making it a viable commercial possibility as it can be seen in Figure 2.3. His designs, which featured two V-shaped foils, were later adopted by the German Navy for military purposes during the World War II, [1].

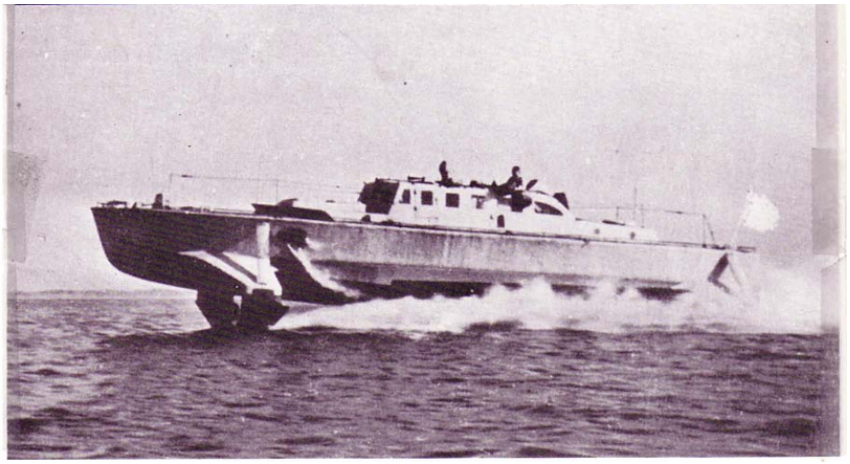

Figure 2.3: Schertel's VS-6 vessel, [1].

Further contributions to hydrofoil development came from the experiments of Russian engineer Wsevolode Grunberg. He designed the first vessel able to adjust multiple components, including the angle of attack of the main foil, submergence and roll stability, resulting in improved overall stability and control, [1].

The interest from the Canadian government in hydrofoils grew alongside the successful developments, leading to the funding of a new test craft in 1958 called *Bras D'Or*, later renamed *Baddeck*, which can be seen in Figure 2.4. Despite significant efforts, the vessel failed to achieve the desired performance as it could only maintain stability for a narrow scope of angles of attack, which was insufficient for operating in rough waters. Additionally, tests revealed that Bell and Baldwin's previous designs were incapable of supporting the vessel in rough waters. It was also concluded that the forward foil should be significantly smaller when compared to the main foil, allowing it to function similarly to a trimming device. These findings led to the development of the *canard* configuration. a key design for future advancements in surface piercing hydrofoil systems, [1].

Figure 2.4: Bras D'or, [1].

Around the same time, in 1951, engineer Gordon Baker directed two hydrofoil projects issued by the Office of Naval Research. One of the resulting vessels, *High Tail*, featured a three foil system along with three mechanical sensors capable of controlling the foil lift. The foils, sensors and propeller were able to retract hydraulically making them suitable for operations in shallow waters. Another key feature was the mechanical-hydraulic autopilot, which adjusted the foil incidence and angle. Despite its success, Baker concluded that future autopilots should be electro-hydraulic rather than mechanical-hydraulic. Along with *High Tail*, several other vessels featuring retractable components were developed, including *Halobates*, which incorporated an electronic automatic control system. This innovation paved the way for the integration of such systems in future vessels, [1].

Many other designs were developed, as hydrofoil technology evolved, allowing speed records to be continuously surpassed, [1].

These advancements sparked the interest of *Boeing*, which went on to develop several fully submerged hydrofoil vessels, for both research to passenger transportation purposes. One of these designs, *Pegasus*, ended up being used by NATO for military purposes. However, interest in hydrofoil vessels for both military and commercial passenger applications eventually declined, [1].

Nevertheless, in recent years, hydrofoils regained popularity, particularly in water sports. One of the most prestigious sailing competitions, the America's Cup, is a major stage for hydrofoil innovation when AC72 boats first incorporated them in 2012, a feature that has remained ever since and can be seen in Figure 2.5, [2]. Hydrofoils have also become a staple in other water sports such as windsurfing and kitesurfing, [3] [4]. Today, most of the latest advancements in hydrofoil technology are showcased in competition, offering new perspectives on their applications.

Figure 2.5: America's Cup Hydrofoil, [5].

Lastly, hydrofoils have gained attention for their potential in sustainable transportation. Projects such as *Rodriguez Hydrofoils*, [6], developed a hydrofoil vessel capable of carrying up to 200 passengers more comfortably and efficiently. However, these designs still relied on combustion engines and lacked automatic foil control. Limitations that companies such as *Seabubbles*, [7] and *Mobyfly* [8] are actively addressing. Their goal is to integrate renewable energy sources and implement fully automated foil control systems, making hydrofoil technology more sustainable and efficient.

2.1.2 Hydrofoils Typical Configurations

This section provides a concise overview of the various types of hydrofoils, focusing specifically on their arrangements and configurations.

Previous sections have establish that the main purpose of hydrofoils is to lift the hull of the vessel, thereby reducing the drag effect caused by the waves. In order to achieve this, hydrofoil configurations can be classified into two main systems, the surface piercing design, shown in Figure 2.6, and fully submerged system, which can be seen in Figure 2.7, [1].

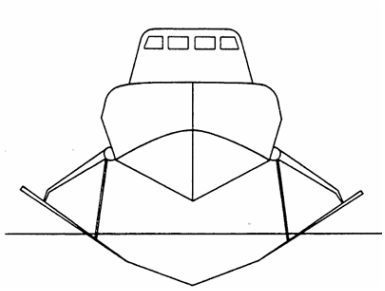

Figure 2.6: Surface-piercing foil system, [1].

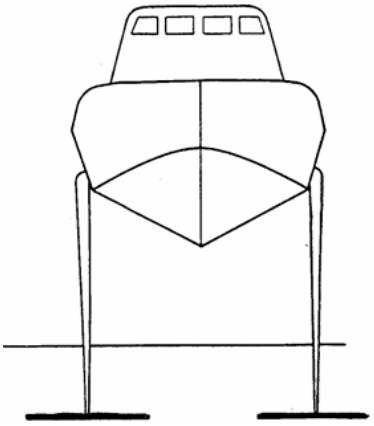

Figure 2.7: Fully-submerged foil system, [1].

The surface piercing system, as the name suggests, features foils that can remain partially above water while the hydrofoil is foilborne. As the vessel accelerates, lift is generated on the submerged portion of the foils and angled struts. Consequently, the foil area required to support the weight of the vessel decreases. The struts, which connect the hull to the hydrofoils, play a crucial role in maintaining sufficient height, allowing the vessel to remain above the water surface at its design flying speed. One defining characteristic of this system is its self-stabilizing response. When encountering a wave, the submerged portion of the foils varies. In order to maintain the total lift, which is equal to the weight of the vessel, the craft will either, pitch, roll, heave or a combination of the three. These adjustments occur automatically, making the system self-stabilizing, eliminating the need for active controls. However, this self-stabilization can also lead to the movement of the

hull, which can restrict the quality of the ride in rough waters. To mitigate this issue, modern surface piercing systems integrate electro-hydraulic control systems, enhancing stability and enabling smoother operation in more turbulent conditions while maintaining onboard comfort, [1].

On the other hand, fully submerged systems operate entirely beneath the water surface, ensuring continuous submersion during operation. In this configuration, the struts remain nearly vertical, meaning they do not contribute to any dynamic lift. This occurs because the vertical forces induced by buoyancy changes when encountering waves are relatively small. Unlike surface piercing systems, fully submerged designs lack self-stabilization and therefore require an automatic control system in order to maintain straight and level flight. However, a key advantage of this system configuration is its ability to decouple the vessel from direct sea and wave interactions, significantly reducing external disturbances and enabling an overall better stability, particularly in rough sea conditions, [1].

In addition to foil configurations, hydrofoils can also be categorized based on their geometric arrangements, as shown in Figure 2.8. Although various configurations exist, they can be classified into three primary types. The first one, referred as the conventional or the airplane arrangement, occurs when the majority of the foil area is positioned forward on the hull, identically to an airplane wing, with a smaller foil portion located toward the rear. In contrast, there is the canard configuration which is the opposite of the conventional, placing the majority of the foil area aft and the smaller section forward. Lastly, the tandem configuration represents an intermediate approach, where the foil areas are evenly distributed between the front and rear. This configuration can be beneficial when it comes to large hydrofoil vessels, since it prevents the foil spans from being excessively large and improves structural feasibility, [1].

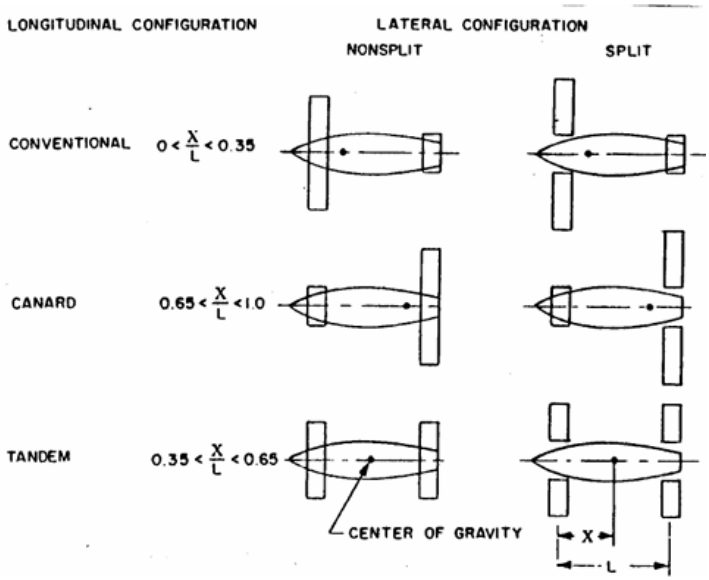

Figure 2.8: Foil geometric configurations, [1].

As previously mentioned, a fully submerged system is not inherently self-stabilizing, meaning that an automatic control system is required. This system is responsible for continuously adjusting the foil angle of attack or foil incidence throughout the operation of the craft. Such adjustments are done to all foils, both port and starboard and forward and aft, in order to maintain trim and ensure the hull remains at a consistent height above the water surface, in spite of external disturbances. The aim of these adjustments is to minimize the lift to drag ratio, in other words, reach the minimum drag for a given amount of lift, during cruise conditions. To maintain sufficient reserve capacity to generate control forces, the foils are designed to operate with relatively small mean incidence or flap angles. An illustration of the components involved and their respective movements is shown in Figure 2.9 and 2.10, [1].

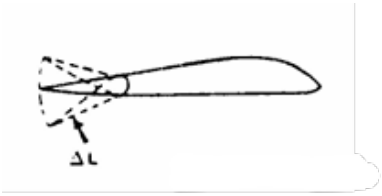

Figure 2.9: Varying edge flap control, [1].

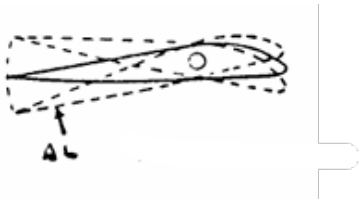

Figure 2.10: Varying incidence control, [1].

2.1.3 Hydrofoil Advantages and Disadvantages

As it is known all innovations have their benefits and limitations, being the hydrofoils not an exception to this. For that reason, this section aims to provide both points of view.

From the previous sections, it is evident that the principle motivation behind the development of hydrofoils was to mitigate drag and, consequently, enhance operational efficiency. A notable example of this technological advancement is *Nova*, an electric hydrofoil ferry recently implemented to Stockholm's public transport network. This vessel, capable of transporting up to 25 passengers at a maximum velocity of 56 km/h, achieves an 80% reduction in energy consumption compared to traditional ferries. One of its key advantages is its exemption from the 22 km/h speed limit, as it generates minimal wake. This not only allows for the increased operational speed but also significantly reduces environmental impact by minimizing shoreline erosion and disturbances to aquatic ecosystems. Beyond efficiency and environmentally benefits, hydrofoils also allow for an improved passenger comfort. By elevating the hull above the water surface, hydrofoils minimize wave induced motion, thereby reducing the incidence of seasickness and providing a smoother, more stable ride, [9] [10].

However, to achieve the high performance requirements, the construction of hydrofoil vessels necessitates the use of advanced materials, such as carbon fiber reinforced polymers, in order to meet the demanding mechanical requirements essential for their performance. While these materials offer superior mechanical properties, such as superior strength to weight ratios and durability, they also contribute to an increase in production costs due to their complexity in manufacturing and structural integration. Another critical factor influencing the efficiency of hydrofoil vessels is weight management. Given the

direct impact of weight on hydrodynamic performance, precise estimations and rigorous control are required throughout both the design and operational phases. Even minor deviations can significantly affect the stability, efficiency and overall performance, [10].

Nevertheless, despite the additional costs and complexity involved in implementing hydrofoil technology, companies such as *Mobyfly* consider it a worthwhile investment, as it contributes to the advancement of more environmentally sustainable alternatives in the marine industry, [8].

2.1.4 Common Materials in Hydrofoils

As revised previously, in order to achieve the high mechanical requirements that a hydrofoil vessel needs, the materials need to be carefully chosen, ensuring the vessel can perform efficiently and safely. The choice of materials for the foils and struts is influenced by several critical factors including strength, stiffness, weight, cost and production methods used. The relative importance of these factors varies depending on the specific application, particularly the size, speed capabilities and operational requirements, [11].

In general, the materials used in boat building can be categorized based on the weight of the craft. For smaller vessels, typically up to $1.0 \times 10^4\ kg$, wood is often the material of choice due to its availability and ease of use. For medium sized vessels, ranging up to $1.0 \times 10^5\ kg$, aluminum is commonly utilized, owing to its favorable balance of strength, stiffness and low weight. For larger vessels, high tensile steel is usually the preferred option due to its superior strength and durability under more demanding conditions, [11].

In recent years, reinforced polymers, such as glass fiber reinforced polymer, have emerged as viable materials for the construction of hydrofoils. However, carbon fiber reinforced polymer has gained the most popularity, especially in competition vessels and high performance sports equipment. This material offers superior stiffness to density and strength to density ratios when compared to metals and glass fiber reinforced polymers, making it a preferred choice for advanced hydrofoil systems, such as those used in the prestigious *America's Cup* competition, [12]. Carbon fiber reinforced polymer presents several advantages that contribute to its extensive use in hydrofoil technology. It allows for the optimization of fiber orientation, improving overall structural response and reducing the weight of the vessel. Moreover, it presents great mechanical properties, including high resistance to fatigue, creep and corrosion, which are essential for long term durability in challenging operational environments. Additionally, it enables the potential for controlled bend twist phenomena, which can be customized to improve the control of the angle of attack of the foil, enhancing the stability and performance of the vessel. Nonetheless, despite these benefits, carbon fiber reinforced polymers has some drawbacks. The material has a greater cost and its performance is heavily dependent on the production methods used and the skill of the operators. Furthermore, it is less impact resistance than other materials, which can limit its durability in certain high stress conditions, [13] [14].

Nowadays, there has been growing interest in the application of 3D printing for the production of prototype foils, particularly for small-scale testing, as is the case with the current project. This manufacturing method offers significant advantages in terms of rapid development and testing, thereby reducing the overall time required for a prototype

development. Besides, 3D printing does not require an highly skilled operator, making it a cost effective and efficient option for the production of test models. Even so, while 3D printing has been used for prototype development, testing it in a full scale still remains relatively limited. In the few instances where full scale 3D printed foils have been tested, they have often been relatively small in addition to being reinforced with supplementary materials, such as aluminum rods, in order to ensure sufficient structural integrity under operational conditions, [15] [16] [17] [18].

2.1.5 Production Methods

The manufacturing process plays a pivotal role in determining the performance, durability and cost effectiveness of hydrofoils. Traditional methods such as hand lay-up and vacuum infusion have been widely used. However, advancements in materials and technology have introduced innovative techniques. This section explores five distinct manufacturing approaches, traditional hydrofoil manufacturing methods, fused deposition modeling, bound metal deposition, forged carbon fiber composites and carbon fiber laminates. Each method offers unique advantages and drawbacks, influencing their suitability for specific applications. Understanding these processes is essential for optimizing hydrofoil design and performance.

2.1.6 Traditional Hydrofoil Manufacturing Methods

Several conventional composite manufacturing techniques have been widely used for hydrofoil components, each offering distinct advantages and limitations.

Prepreg

Prepreg refers to fibers that are pre-impregnated with resin to a controlled fiber volume fraction. These materials, available as unidirectional, multidirectional or woven fabrics, are laid onto a mold and typically consolidated using a vacuum bag to remove trapped air and improve fiber compaction. The part is then cured under controlled temperature and pressure, often in an oven or autoclave. Prepreg enables high fiber volume fractions and very low void content, producing components with excellent mechanical properties. However, it requires expensive equipment, careful storage at low temperatures and longer production times, which makes it less practical for marine applications where cost and time are critical, [14]. Figure 2.11 shows a schematic representation of this process.

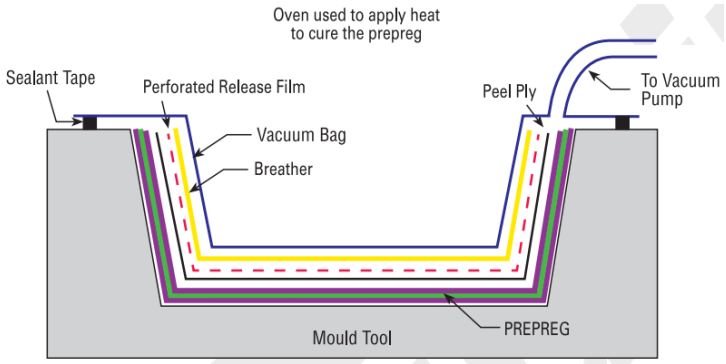

Figure 2.11: Prepreg process, [14].

Hand Lay-Up

Hand lay-up involves manually impregnating dry fibers with resin and placing them on a mold. This method is simple and low-cost and it can produce both monolithic and sandwich laminates. Applying vacuum can improve fiber consolidation and reduce void content. Nonetheless, the mechanical quality of the parts heavily depends on the operator skill, making it less suitable for high performance hydrofoil components, [14]. Figure 2.12 shows a schematic representation of this process.

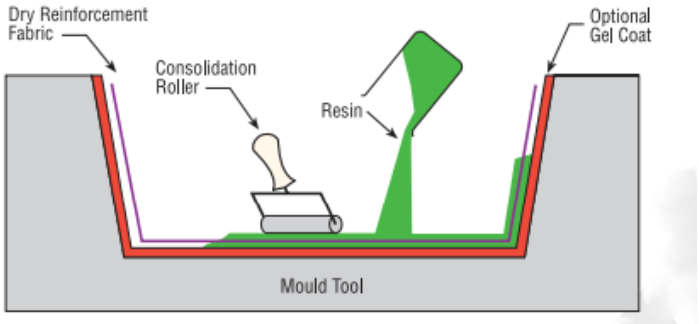

Figure 2.12: Hand lay-up process, [14].

Resin Transfer Molding

Resin transfer molding consists of placing dry fibers into a closed mold and injecting resin under pressure. This process allows high fibers volume fractions, low void content and a good surface finish on both sides of the part. Resin transfer molding tooling is more expensive, but the process is well-suited for producing complex hydrofoil components with consistent quality. For these reasons, this method is often preferred over prepreg or hand lay-up for structural hydrofoil elements where both performance and repeatability are essential, [14]. Figure 2.13 shows a schematic representation of this process.

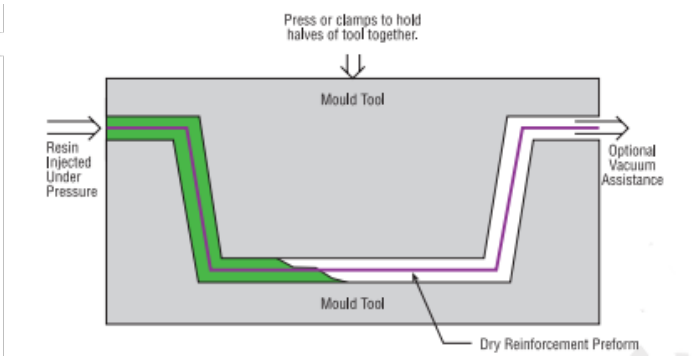

Figure 2.13: Resin transfer molding process, [14].

2.1.6.1 Fused Deposition Modeling

Additive Manufacturing (AM) is a set of processes in which material is deposited layer by layer to create a part directly from a digital Computer Aided Design (CAD) model. Unlike traditional subtractive methods, where material is removed from a solid block, polymer based AM builds components only where material is needed, minimizing waste and enabling highly complex geometries that would be challenging or impossible to achieve with conventional manufacturing, [19].

One of the most widespread polymer AM techniques is Fused Deposition Modeling (FDM), commonly known as 3D printing. In this process, a thermoplastic filament is heated until semi-liquid and extruded through a nozzle, depositing successive layers according to the CAD design. This approach allows precise control over geometry and internal structures, such as variable thickness walls, hollow sections or infill structures, which are particularly valuable for hydrofoil prototypes and small-scale testing, [20].

The main advantages of polymer FDM include rapid prototyping, low cost, minimal tooling requirements and high design flexibility. The automated deposition process reduces reliance on skilled operators, making it accessible for research, iterative design and early stage testing of hydrofoil components. Polymers can also be reinforced internally with short or continuous fibers during extrusion, which improves stiffness and strength and partially mitigates the inherent anisotropy of printed parts. This fiber reinforcement enables prototypes to better withstand hydrodynamic forces, extending their use beyond purely geometric or conceptual testing, [19] [21].

An alternative reinforcement strategy involves applying an external fiber layer, such as glass or carbon fiber, over the printed polymer part. In this hybrid approach, the base geometry is produced rapidly through FDM, while the fiber overplay provides additional stiffness, strength and resistance to hydrodynamic loads. This technique allows the production of functional hydrofoil prototypes that can be used in water based testing, combining the speed and flexibility of 3D printing with the mechanical benefits of traditional composite reinforcement. It also enables easy iteration of designs while maintaining improved mechanical performance compared to plain polymer prints, [22].

Despite these reinforced options, polymer FDM parts retain some limitations. The mechanical properties of printed parts are generally anisotropic, with reduced strength in the build direction due to imperfect inter layer adhesion. Porosity between layers, surface

roughness and dimensional inaccuracies may affect hydrodynamic performance. Careful control of printing parameters, such as nozzle temperature, layer height, print seed, raster orientation and cooling is essential to optimize part quality. Post-processing, including sanding or coating, may also be necessary to improve surface finish and reduce drag during water testing, [19] [20].

Overall, polymer FDM, wether reinforced internally with fibers or externally with hybrid fiber layer, provides a flexible, cost effective and rapid method for producing hydrofoil prototypes. These approaches allow engineers to evaluate geometry, test hydrodynamic performance and iterate designs efficiently before committing to full scale, high performance composite manufacturing methods, [22]. Figure 2.14 shows a schematic representation of this process.

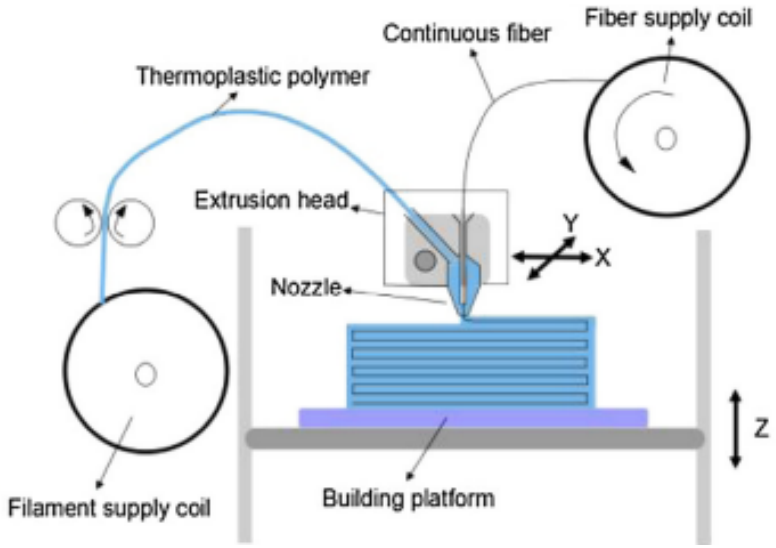

Figure 2.14: Fused deposition modeling, [23].

2.1.6.2 Bound Metal Deposition

Additive manufacturing can also be applied to metals, although the process differs substantially from polymer extrusion in terms of material handling, equipment and final properties. One common method for metal AM is Bound Metal Deposition (BMD) approach, where a filament or rod consisting of a mixture of fine metal powder and a polymer binder is extruded to create a *green part*, a component that retains overall geometry but lacks structural integrity. After printing, this part undergoes a debinding stage to remove the polymer matrix, followed by sintering at high temperatures to densify the structure and consolidate it into a fully metallic component, [24] [25].

This indirect process allows for the use of a wide variety of metals, including stainless steels, copper and aluminum alloys. The resulting parts can achieve mechanical properties approaching those of conventionally cast or machined metals, although the final density and strength are strongly dependent on the sintering process and parameters. Compared to polymer FDM, metallic parts exhibit significantly higher strength, stiffness and thermal stability and the anisotropy associated with layer by layer deposition is reduced, although

inter layer bonding still presents challenges, [26].

The main advantages of metal FDM include the ability to produce complex geometries that would be difficult or impossible to achieve through subtractive machining, as well as the production of functional prototypes and low volume components without the need for extensive tooling. This makes it attractive for applications in aerospace, automotive and high performance marine engineering, where metallic properties are essential. In the context of hydrofoils, such technology could be used for the production of small scale prototypes or specialized metallic fittings.

However, metal FDM also faces notable limitations. The equipment is specialized and expensive, requiring high temperature extrusion systems or laser assisted deposition variants. In addition, the mandatory post processing steps, such as debinding, sintering and often heat treatment or surface finishing, significantly increase production time and cost compared to polymer printing. Dimensional control and surface finish remain critical challenges, as shrinkage during sintering can lead to inaccuracies that require further machining or polishing, [24].

Overall, while metal FDM is less suited for rapid iteration than polymer printing, it offers a pathway to manufacturing complex metallic components with mechanical performance suitable for structural applications. For hydrofoil development, its potential lies primarily in the fabrication of functional prototypes, highly loaded components, complementing polymer based AM methods that are more appropriate for low cost, rapid prototyping. Figure 2.15 shows a schematic representation of this process.

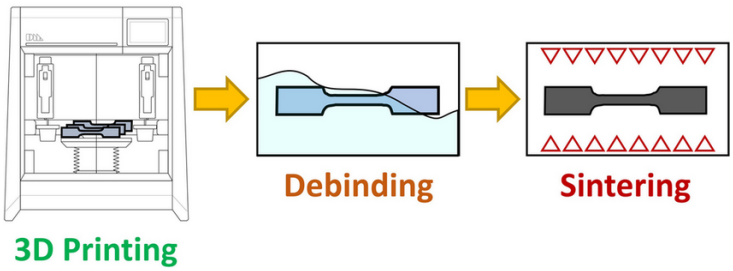

Figure 2.15: Bound deposition modeling, [27].

2.1.6.3 Forged Carbon Fiber Composites

Forged carbon fiber composites represent a relatively new branch of composite manufacturing, designed to address some of the limitations of traditional continuous fiber lay-ups. Instead of arranging woven or unidirectional plies in predetermined orientations, this method makes use of chopped carbon fibers combined with a thermoset or thermoplastic resin. The material is usually supplied as a sheet of chopped carbon fibers pre-impregnated with resin, similar to a sheet molding compound (SMC), which is then placed into a mold and compressed under high temperature and pressure. Because the material flow during molding resembles metal forging, the process has been referred to as a hybrid between conventional composite lamination and metal forming, [28] [29].

The biggest appeal of forged carbon lies in its manufacturing efficiency and design flexibility. Producing continuous fiber laminates typically requires careful alignment, hand

lay-up or automated placement systems, all of which are time consuming and labor intensive. In contrast, forged carbon can be pressed rapidly into complex three dimensional shapes, significantly reducing production times and lowering dependency on highly skilled labor. Furthermore, the use of randomly oriented chopped fibers results in quasi-isotropic behavior, giving the composite more uniform mechanical properties across different sections. This contrasts with traditional laminates, which are strong along fiber directions but can exhibit weakness in off-axis loading, [28] [30].

Applications of forged carbon have expanded across industries where lightweight structures with intricate geometries are in demand. In the automotive sector, Lamborghini famously pioneered its use in body and structural components, demonstrating the potential for combining strength, lightweight design and aesthetic appeal. The aerospace industry has also shown interest due to reduced cycle times and ability to fabricate geometries that would otherwise require multiple bonded sub components, [31] [29].

For the marine sector, particularly in hydrofoil applications, forged carbon presents an intriguing option. Its ability to create streamlined, load bearing parts with reduced lay-up complexity could lower production costs and increase accessibility compared to traditional lamination. However, there are important limitations. Because the fibers are short and discontinuous, the overall stiffness, tensile strength and fatigue resistance are generally inferior to continuous fiber laminates. This makes forged carbon less suitable for highly loaded primary structures but promising for secondary elements or prototypes. Additionally, the cost of raw chopped fiber material and the need for specialized compression molding equipment remain barriers to widespread adoption in marine composites, [30] [28] [32].

In summary, forged carbon fiber composites strike a balance between the efficiency of automated molding and the lightweight benefits of carbon fiber, but they trade off some of the superior mechanical performance of laminated structures. For hydrofoils, they could serve as an intermediate step between rapid prototyping and full scale laminated composite manufacturing, [29] [32]. Figure 2.16 shows a schematic representation of this process.

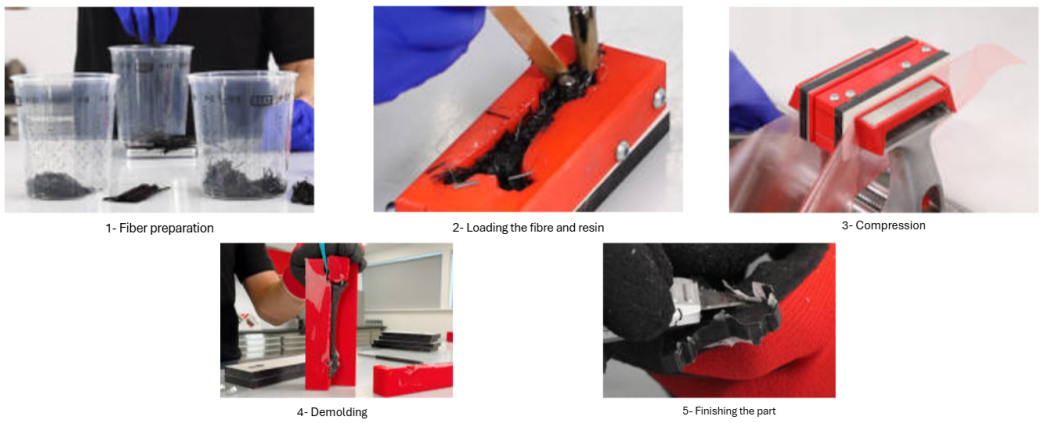

Figure 2.16: Forged carbon process, [33].

2.1.6.4 Press Molding

Press molding, also known as compression molding, is a composite manufacturing technique designed to produce solid, high precision parts by layering resin impregnated fibers in a shaped mold and curing them under heat and pressure. Unlike traditional fiber wrapping or hand lay-up methods, press molding allows the creation of parts with controlled thickness, consistent fiber volume and minimal void content, making it ideal for hydrofoils where structural performance and tight dimensional tolerances are critical, [34].

The process begins with a concave mold that defines the exact geometry of the component. Layers of prepreg sheets or sheet molding compound are cut and stacked inside the mold until the desired thickness. Each layer can be oriented to follow the principal load directions, allowing mechanical properties to be tailored for bending, torsion or localized stresses.

Once the stack is complete, the mold is closed and pressed while heat is applied. The pressure ensures intimate contact between layers, removes trapped air and facilitates resin flow, fully impregnating the fibers. The combination of heat and pressure initiates the curing reaction of the thermoset resin, producing a solid composite part with uniform mechanical properties and minimal defects, [35].

After curing the component is demolded and may undergo trimming or surface finishing to achieve final specifications. Press molding offers several advantages for hydrofoil manufacturing as it provides precise control over thickness, high dimensional accuracy and consistent fiber to resin ratios, ensuring optimal strength to weight performance. Moreover, this method is scalable from prototyping to small series production, enabling rapid iteration of hydrofoil designs without extensive manual labor.

Overall, press molding using prepreg or sheet molding compound layers in a concave provides a practical and reliable way to produce solid, high performance hydrofoil components. By carefully controlling layer orientation, thickness and curing conditions, a lightweight, structurally optimized component can be achieved, being suitable for high load marine applications. Figure 2.17 shows a schematic representation of this process.

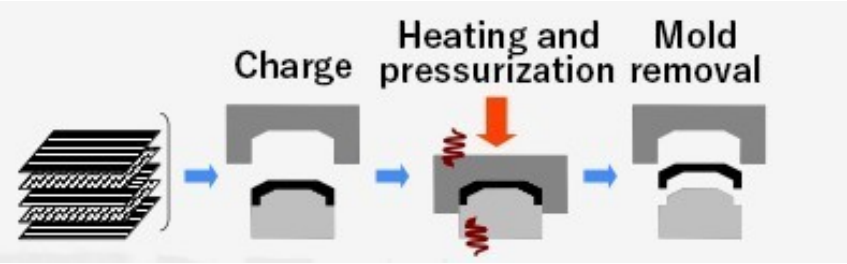

Figure 2.17: Press molding process, [36].

2.2 Control Systems

Vessels using hydrofoil technology rely on advanced control systems in order to optimize performance, stability and efficiency. These systems are utilized to regulate deployment, automate real time adjustments based on environmental conditions and provide the necessary actuation for controlled movement. The design of these types of systems is extremely important so that it can boost the hydrodynamic efficiency, minimize drag and ensure a smooth operation across diverse water conditions. For that reason, this section explores the key components of hydrofoil control, from deployment systems, to automated control systems and actuation technologies, highlighting the various solutions that exist and are being utilized.

2.2.1 Deployment Mechanisms

The aim of this section is to take a closer look at the deployment systems used in hydrofoil systems. In the previous section, Baker's *High Tail* hydrofoil was highlighted as a notable innovation due to its introduction of retractable foils, integrated sensors and propeller driven system, [1]. This configuration significantly influenced modern hydrofoil deployment systems, inspiring retractable and adaptive hydrofoil technologies. These mechanisms lead to the optimization of performance, stability and efficiency, by allowing hydrofoils to retract, adjust or dynamically adapt to different operational conditions, thereby minimizing drag and enhancing maneuverability. Some of the latest advancements in hydrofoil deployment systems include automated control systems, retractable designs for multi hull vessels and hybrid solutions integrating propulsion technologies.

Patents

This section explores key patents related to hydrofoil technologies, ranging from autonomous control systems to hydrofoils integrated into hull units. These patents illustrate the diversity and innovation in hydrofoil design while showcasing several deployment systems that enhance performance, efficiency and adaptability.

The patent US20230382496A1 is a great example for a hydrofoil control system which objective is to dynamically adjust hydrofoil positions in response to real time water conditions, its schematic representation is shown in Figure 2.18. By continuously optimizing lift and minimizing hydrodynamic resistance, this technology enhances the stability, performance and fuel efficiency of the vessel. Another characteristic this system presents is its ability to adapt according to various environmental factors, aligning with the remain advancements in automated hydrofoil control, while contributing to improved efficiency and sustainability, [37].

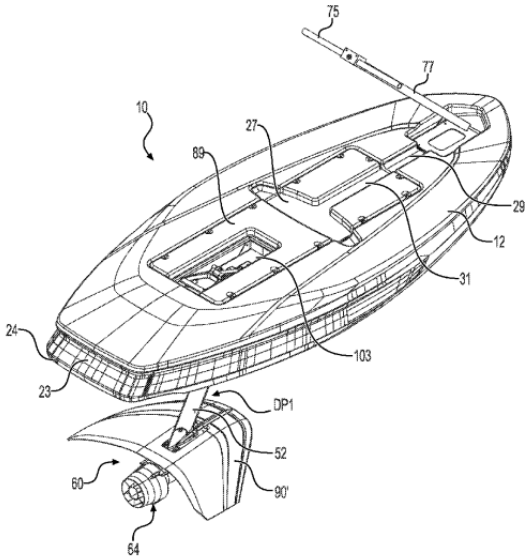

Figure 2.18: Patent US20230382496A1, [37].

The Chinese patent CN105905232B describes a rotational mechanism that incorporates a rack, gear, hydraulic and oil cylinder in order to facilitate controlled rotational movement, its schematic representation is shown in Figure 2.19. This configuration can be crucial for retractable or adjustable hydrofoil systems, as it influences the arrangement and structural integration of the hydrofoil strut with the vessel. Additionally, this patent includes a folding mechanism that allows the hydrofoil to be retracted or folded into a compact form, offering flexibility for vessels requiring variable operating modes, [38].

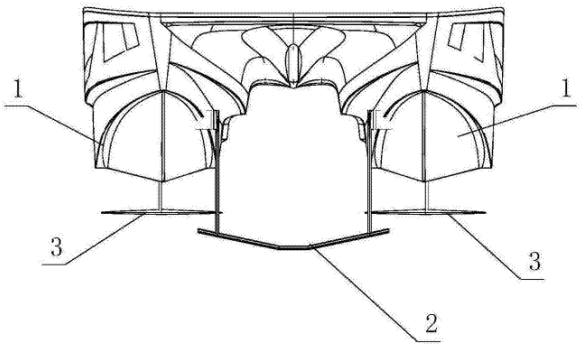

Figure 2.19: Patent CN105905232B, [38].

Two other important patents for significant advancements in the integration of deployment systems in hydrofoils are the US10179628B2 and NL2026134B1, each contributing to an upgraded vessel performance and efficiency. The US10179628B2 introduces a deployment system for hydrofoils on outboard boats, incorporating a leverage mechanism, as shown in Figure 2.20, where a linear actuator is employed to shift the hydrofoil between operational and retracted positions. This mechanism aims to improve the fuel efficiency by minimizing drag during retraction, thereby increasing adaptability to diverse operat-

ing conditions. In contrast, the NL2026134B1 patent describes a hydrofoil system that is integrated into the hull of the vessel, featuring a safety pin mechanism to secure the hydrofoil in place, preventing unintended movement and ensuring operational stability, which can be seen in Figure 2.21. Collectively, these patents highlight key innovations in hydrofoil technology that improve hydrodynamic performance, maneuverability, and safety across a range of maritime applications, [39] [40].

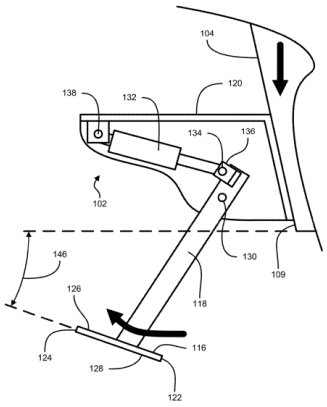

Figure 2.20: Patent US10179628B2, [39].

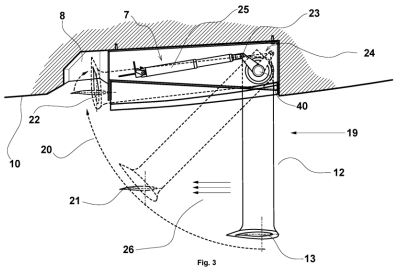

Figure 2.21: Patent NL2026134B1, [40].

Commercial Solutions

This section highlights some key commercial hydrofoil solutions currently in use, showcasing their impact on modern vessel design and operation.

The *Navier Electric Hydrofoiling Boats* company has developed a new fully electric hydrofoil vessel, the *N30 Pioneer Edition*, as shown in Figure 2.22. This boat features an advanced retractable deployment mechanism, with a draft ranging approximately from $0,45\,m$, when stowed to a maximum draft of $1,8\,m$ when in full foil. This feature allows for seamless adaptation to varying water depths, enabling efficient operation in shallow waters while ensuring a smooth ride in rough sea conditions. As a hydrofoil vessel, the *N30 Pioneer Edition*, benefits from reduced wake, improved ride comfort and boosted energy efficiency compared to traditional hull designs. Additionally, it features a sensor based control system which promotes stability and enables automated navigation assistance. Another advantage is its extended range in comparison to other electric boats, which enables it to cover longer distances up to $139\,km$ with a single charge, [41].

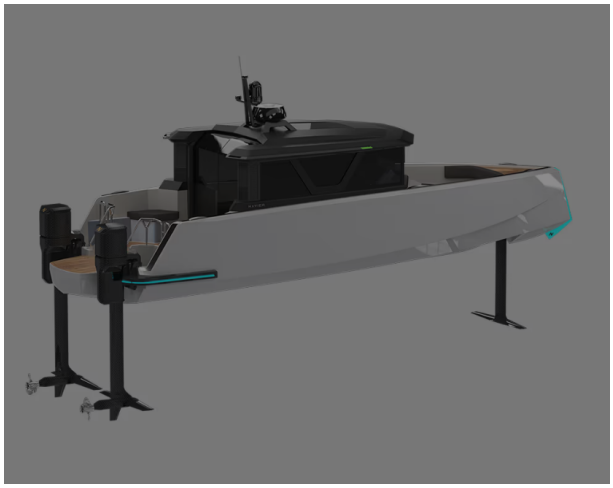

Figure 2.22: N30 hydrofoil vessel, [41].

The Swedish company *Candela* has also developed a hydrofoil vessel, *Candela P-12 Hydrofoil Ferry*, as shown in Figure 2.23, which incorporates a retraction deployment system, allowing it to operate in shallow waters, used for trailing and retracted when not in use. This leads to easier maintenance and adaptability in diverse water conditions. In addition, this vessel, by using hydrofoil lift and electric propulsion, is able to reduce energy consumption by 75% in comparison to conventional ferries, inevitably reducing emissions and operational costs. Similarly to the previous vessel, it takes advantage of the benefits of the hydrofoil system, minimizing the wake and contributing to a more environmentally friendly alternative for public transportation, [42].

Figure 2.23: Candela P-12 hydrofoil vessel, [42].

Another company that has incorporated these types of systems is *SeaBubbles*, by using retractable systems it not only enhances maneuverability but also protects the hydrofoils in use. Similarly to the previous deployment systems, it allows for the use of the vessel in shallow waters and retraction when docking. Its design, shown in Figure 2.24, is ideal for short range transportation, such as lakes and rivers, having a speed reach of $30\,km/h$. Besides, it reduces carbon emissions and noise pollution, making it an environmentally friendly alternative to traditional water vessels, [43].

Figure 2.24: SeaBubbles hydrofoil vessel, [43].

The *Foiler*, shown in Figure 2.25, is a hydrofoil vessel that integrates two turbo diesel V8 engines, delivering a combined 544.27 kW and reaching speeds up to 74 km/h. It also features a patented retracting system allowing it to transition from foiling mode to traditional Archimedean mode within seconds. This enables it to operate in shallow waters, reducing the draft to just 0.6 m. By taking the foils out of the water, it ensures they stay dry reducing the maintenance requirements. This is possible through the use of hydraulic actuators which provide a seamless and efficient operation. This vessel also benefits from the advantages of hydrofoils, improving fuel efficiency and enhanced stability when compared to traditional yachts.

Figure 2.25: Foiler hydrofoil vessel, [44].

Another alternative in the existing market is the hydrofoil vessel developed by *Mobyfly*, as shown in Figure 2.26. This design also integrates a retracting system which allows it to operate in waters as shallow as 50 cm, facilitating maintenance and trailering, as well as being stored away when not in use, protecting them from potential damage. The configuration adopted enables the deployment and retraction of the foils as needed, which guarantees the adaptability of the vessel to several water conditions and different operation requirements. Additionally, the *MobyFly* vessel incorporates an automated docking system that further improves its operational efficiency and safety. The vessel is equipped with electric or hydrogen powered engines, operating without producing greenhouse gas

engines, making it a viable eco-friendly alternative to traditional diesel ferries. Compared to conventional ferries, it can consume up to 95% less energy making it a cost effective and sustainable transportation. This zero-emission hydrofoil boat can comfortably transport up to 350 passengers while reaching speeds over 70 km/h. As in the previous options, this vessel is designed to operate quietly and without creating significant waves, ensuring minimal disruption to marine environments and urban waterways, [8] [45].

Figure 2.26: Mobyfly hydrofoil vessel, [8].

2.2.2 Automated Control and Stability Systems

Previously, it was mentioned that hydrofoil vessels with a fully-submerged configuration are not self-stabilizing and therefore require an automated control system to meet operational demands. This section explores essential control systems necessary for hydrofoil vessels. As highlighted earlier, automated control and stability systems are a critical component in hydrofoil vessels, ensuring smooth and efficient operation by adjusting the foils in real time. To accomplish this, these systems rely on advanced hydrodynamic sensors, gyroscopes and accelerometers to monitor the speed, pitch and roll of the vessel. One of the key technologies is active foil control, which continuously adjusts the angle and depth of the hydrofoils to maintain stability, even in rough waters. In addition, automated trim and ballast systems are used to help optimize weight distribution, improving lift and reducing drag. These technologies are fundamental in making hydrofoil vessels a viable and highly efficient alternative for modern maritime applications.

Sensor-based control systems, also known as flight control systems, are crucial for stabilizing and optimizing hydrofoil vessels. Borrowing the term from aviation, flight control refers to the automated system that continuously adjusts hydrofoil positions in real time to ensure stability. By integrating various sensors and advanced algorithms, hydrofoil vessels can optimize performance, enhance safety and improve ride quality even in rough weather and water conditions. Fully submerged hydrofoils are inherently unstable therefore require continuous control of pitch, roll and height. This is achieved through a combination of sensors and real time data processing, [46].

To measure the pitch, roll and yaw in hydrofoil vessels, precise motion sensing components such as gyroscopes and accelerometers are essential. As the vessel encounters waves or sudden changes in wind forces, gyroscopes detect rotational forces, while ac-

celerometers measure linear acceleration. This information is then processed in real time by a central control system that adjusts the hydrofoil angles accordingly to stabilize the boat and counteract external forces. By continuously fine-tuning the hydrofoil angles, the system prevents unwanted oscillations, ensuring a smoother and more energy efficient ride, [46].

Depth sensors play a crucial role in maintaining lift and minimizing drag by continuously measuring the distance between the vessel and the water surface in real time, a schematic representation is shown in Figure 2.27. Due to waves, currents or changing positions, the depth sensors detect fluctuations in water level. As the previous components, the obtained information is then processed in real time by a central control, allowing the foil angle and depth to be automatically adjusted, [46].

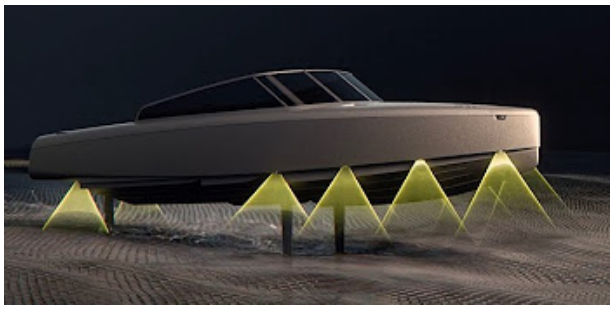

Figure 2.27: Candela depth sensor scheme, [42].

Other key components, such as high-resolution optical cameras and light detection and ranging sensors, are also used to detect obstacles and wave patterns ahead of the vessel. The light detection and ranging sensors, through the emission of laser pulses are able to map the water surface and detect objects that are in the vessel's path. Optical cameras enable the capture of real-time images of waves and surrounding conditions. Then, the acquired data is processed by the central control system, allowing the vessel to anticipate waves, adjust its hydrofoils preemptively and avoid obstacles, [47].

The *Candela C-8* vessel utilizes an advanced flight control system that continuously processes sensor data to maintain stability and optimize performance. The data gathered by sensors, such as gyroscopes, accelerometers and depth sensors, is transmitted to the flight control system at a frequency of 500 times per second, enabling real time adjustments to angles, velocities and accelerations across all three axes. By dynamically adjusting the angle of attack and fine-tuning the twist of the foil, the system maintains optimal stability, even in diverse water conditions. Additionally, the flight controller detects landing maneuvers and autonomously adjusts the hydrofoils to ensure a smooth descent onto the water, [42].

All fully submerged hydrofoils on the market rely on similar control systems, making them a critical component of modern hydrofoil technology. While these systems have significantly improved vessel stability and efficiency, there remains room for further improvement and innovation. Sensor-based control systems are revolutionizing hydrofoil vessels, making them more stable, efficient and sustainable.

2.2.3 Hydrofoil Actuation Systems

In order to control the lift, drag and stability, hydrofoil vessels rely on actuation systems. These actuation systems dynamically adjust the position and angle of attack of the foils according to the varying water and environmental conditions, ensuring optimal performance, stability and energy efficiency. There are two primary types of actuation systems used in hydrofoil vessels, fluid power actuators and electric actuators. Each has its advantages and drawbacks depending on their application. Some crucial factors when selecting the type of actuator to use depend on response time, power efficiency, and maintenance requirements.

Fluid Power Actuators

This section is meant to give a deeper knowledge about fluid power actuators. These components are responsible for generating motion using high-pressure fluids, operating via hydraulic forces, using oil or water, or pneumatically, using air. There are three main types of actuators, linear, rotary and semi-rotary actuators.

Linear actuators convert fluid power into linear mechanical movement and can be categorized in three types, single-acting cylinders, telescopic cylinders and rodless cylinders. Single-acting cylinders, as shown in Figure 2.28 consist of a cylinder and a piston-rod assembly, designed to produce force to extend or retract in only one direction. Due to this characteristic another element is needed in order to accomplish the other stroke, which can be either gravity or spring tension.

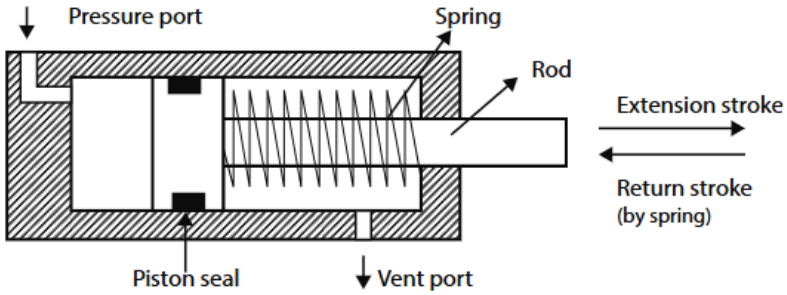

Figure 2.28: Single-acting cylinder, [48].

To achieve a longer stroke length within a compact design, multi-stage cylinders, also known as telescopic cylinders, can be used. These consist of multiple nested sections that slide into one another, allowing for an extended reach while maintaining a relatively short retracted length, as shown in Figure 2.29, [48].

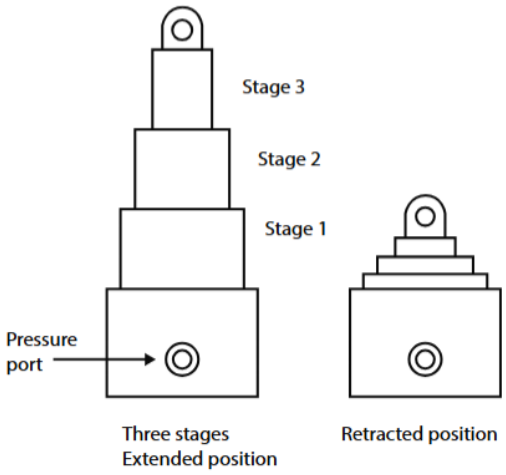

Figure 2.29: Telescopic cylinder, [48].

Lastly, the use of rodless cylinders is a popular alternative when conventional cylinders cannot be installed due to limited space. Their unique design eliminates the need for an extended rod, reducing bending moments and enabling longer stroke lengths while requiring minimal maintenance, making them a reliable and durable option for high-duty applications, [49].

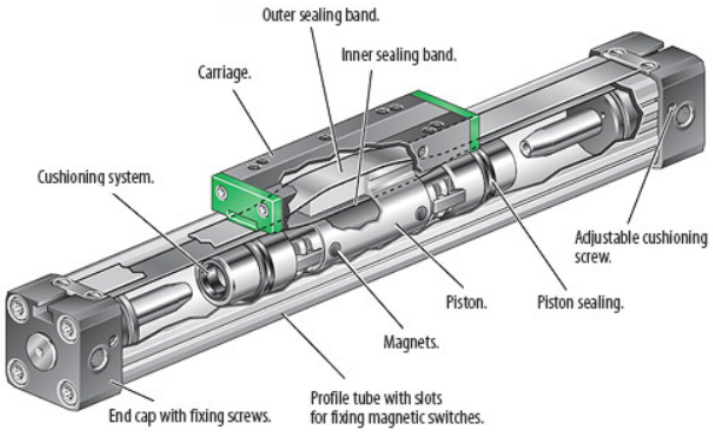

Figure 2.30: Rodless cylinder, [48].

On the other hand, rotary fluid power actuators convert fluid power into rotational movement. Similarly to linear actuators, they can operate hydraulically, using oil or water, or pneumatically, using air or gas. However, hydraulically operated rotary actuators provide a higher power to weight ratio and a greater torque output. By regulating fluid flow, they enable control over rotational velocity and output torque. These components can be divided into three primary categories, gear motors, piston motors and vane motors, [50].

Firstly, gear motors, as shown in Figure 2.31, utilize meshing gears to convert fluid pressure into rotary motion. One common type is the external gear motor, which consists

two identically shaped gears, one attached to an idler and another to an output shaft. Pressurized fluid forces the gears to rotate, generating an output motion. Another option is to use a gerotor motor, which is characterized by its high torque and low speed motor, incorporating an inner gear that rotates around the center while meshing with an outer gear to generate motion. A variation, the geroler motor, uses rollers instead of lobes, reducing friction, minimizing wear and improving low speed performance while decreasing energy consumption. Lastly, is the floating outer ring gerotor motor, in which the outer gear rotates alongside the inner gear, further reducing friction and enhancing efficiency, [50] [51].

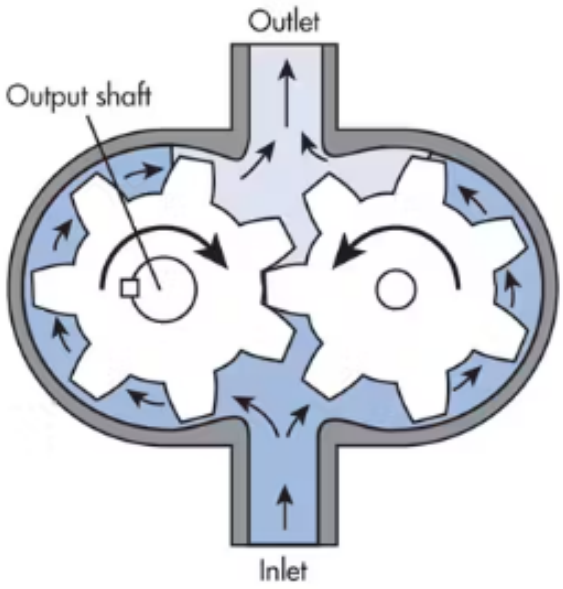

Figure 2.31: Gear motor, [50].

Moreover, piston motors, as shown in Figure 2.32, utilize multiple pistons to generate high torque for large applications and are categorized into two main types, radial and axial piston motors. Radial piston motors feature a driven shaft connected to a cylinder barrel containing multiple pistons. When pressurized fluid enters the motor, it forces the pistons outward against a thrust ring, generating rotary motion. These motors are highly efficient and deliver excellent torque output, however, their speed capabilities are limited due to their large displacement per revolution. Alternatively, axial piston motors, operate using either a swash plate or a bent-axis design. In the swash plate configuration, pressurized fluid forces the pistons against a tilted plate, causing the shaft to rotate. Instead, the bent-axis design features an angled cylinder block relative to the driveshaft. This design reduces internal friction, improving efficiency at higher pressures and speeds making it more reliable. Yet, bent-axis motors are generally more expensive to manufacture and maintain compared to swash plate motors, [50].

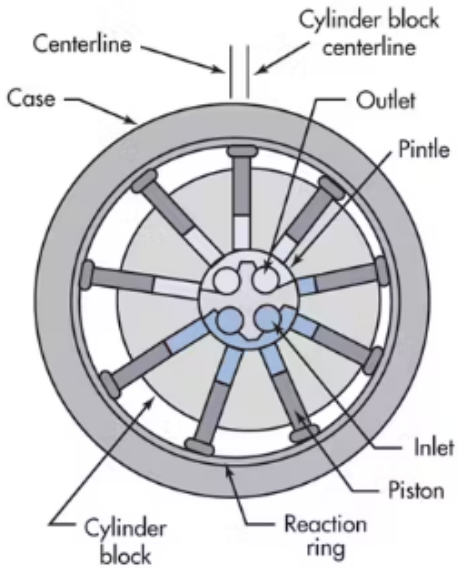

Figure 2.32: Piston motor, [50].

Lastly, vane motors, as shown in Figure 2.33, utilize a slotted rotor with vanes that extend and retract due to centrifugal force and fluid pressure. As pressurized fluid enters the motor, it creates a pressure differential that causes the rotor to spin, transferring torque to the output shaft. These motors can be configured with either two-port or four-port configuration. A four-port configuration increases torque output by maximizing pressure differentials across the vanes, although it results in lower rotational speed. Vane motors are compact, reliable and efficient under rated operating conditions. However, it has limited low speed performance and generally a shorter service life compared to piston motors, [50].

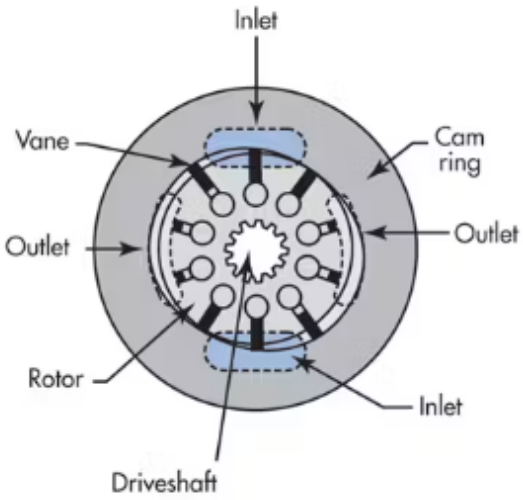

Figure 2.33: Vane motor, [50].

Electric Actuators

Another way to generate mechanical energy is through electric actuators. As the name suggests, these components convert electrical energy into mechanical motion using electric motors. Similarly to fluid power actuators, they can be divided into three primary categories, AC motors, DC motors and stepper motors. The next paragraphs will provide a more thorough analysis of each type, [52].

The key distinction between different types of electric actuators lies in the type of electrical current that each uses. AC motors convert alternating current (AC) electrical energy into mechanical motion, relying on the rotating magnetic field (RMF) as their core working principle. These motors are commonly used for applications that require continuous operation and precise speed control. AC motors are broadly classified into two types, induction motors and synchronous motors, examples of these components are shown in Figure 2.34, [52].

Induction motors, also known as asynchronous motors, operate based on electromagnetic induction. When an AC current flows through the stator, it generates a rotating magnetic field, which induces a current in the rotor creating torque. A key characteristic of induction motors is slip, the difference between the synchronous speed and the actual rotor speed. This property can be advantageous in applications where variable load conditions occur. To enhance efficiency and provide adjustable speed control, variable frequency drives have been integrated with induction motors. Variable frequency drives allow precise control over the motor speed by adjusting the frequency of the supplied power, improving performance in various industrial applications, [52] [53].

On the other hand, synchronous motors can be utilized in applications requiring constant speed operation. Unlike induction motors, synchronous motors operate at exactly synchronous speed, meaning their rotor speed is always in perfect sync with the rotating magnetic field of the stator, without any slip. Because of this characteristic, synchronous motors are ideal for applications that demand high precision in speed control, as they maintain a constant rotational speed regardless of load variations. This is due to the relationship between supply frequency and the number of pole pairs in the motor, which determines the rotational speed, [52] [53].

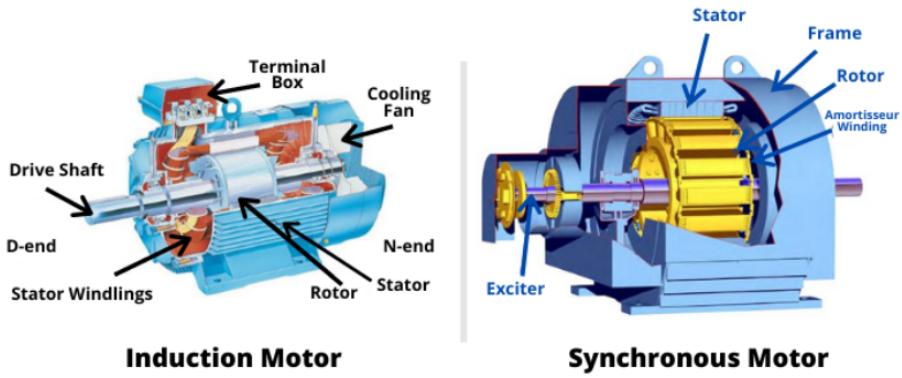

Figure 2.34: Induction vs. synchronous AC motor, [54].

Another widely used category of electric motors is DC motors, which operate using direct current electricity. These are characterized by their precise speed control, as their speed can be adjusted by varying the applied voltage, while the output torque is regulated by controlling the current flow. Due to these characteristics, DC motors are frequently used in applications requiring high precision, quick acceleration and efficient torque regulation. DC motors can be classified into three main types, brushed DC motor, brushless DC motor and coreless DC motor. However, this section will only focus on the first two, as they are the most commonly used in industrial and commercial applications, along with an example of these components which is shown in Figure 2.35, [55] [52].

Brushed DC motors, as the name implies, utilize brushes along with commutators to facilitate the connection between the stationary circuit and a rotating one. In this configuration, conductive brushes supply power to the rotor winding, allowing it to generate motion. While these motors are cost effective and mechanically simple, they come with the drawback of requiring regular maintenance due to the constant friction between the brushes and the commutator. This friction not only leads to wear and tear but also produces sparks, which can limit their efficiency and life span, [55] [52].

In contrast, brushless DC motors do not integrate brushes or commutators. Instead of supplying power to the rotor, the input current is delivered to the stator windings, while the rotor consists of permanent magnets. The windings of the stator are energized in sequence, creating a rotating magnetic field that drives the motion of the rotor. To ensure that the correct windings are activated at the right time, a hall effect sensor is used. The speed of this type of motor is determined by the frequency of the supplied power, making it function similarly to a synchronous motor. Brushless DC motors offer high efficiency, longer lifespan and minimal maintenance since they eliminate friction related wear and electromagnetic noise. Yet, they require a specialized controller, which increases the overall cost, often exceeding the price of the motor itself, [55] [52].

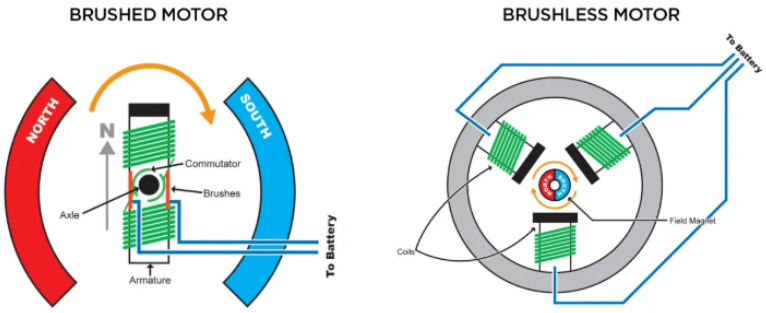

Figure 2.35: Brushed vs. brushless DC motor, [56].

3

Theoretical Background

Understanding the behavior of hydrofoils and their interaction with fluid dynamics requires a solid theoretical foundation. This section explores the key principles underlying hydrofoil performance, including the geometric characteristics of foils, the forces acting on them and the scaling laws that govern their behavior across different sizes and speeds. Additionally, it delves into methods for predicting hydrodynamic forces and moments and introduces the Finite Element Method (FEM) as a tool for analyzing structural performance.

3.1 Foil Theory

The previous section highlighted the advantages and applications of hydrofoils, yet it did not explore thoroughly the theoretical concepts that govern their operation. This section aims to fill that gap by providing an examination of the fundamental principles behind hydrofoil technology. Understanding these theoretical foundations is crucial for comprehending how hydrofoils generate lift, reduce drag and improve efficiency. By examining the key physical principles, such as fluid dynamics, Bernoulli's principle and the relationship between the angle of attack and lift generation. By delving into physical laws that govern hydrofoil behavior, this section will provide a comprehensive framework for understanding their design, operation and efficiency.

3.1.1 Foil Geometry

Similar to airfoils, hydrofoils are engineered to reduce hydrodynamic drag and enhance overall efficiency. This principle of drag reduction is not exclusive to mechanical engineering, it is also observed in nature. For instance, trees have flexible structures that enable them to reconfigure under high wind conditions, thereby decreasing aerodynamic drag. One practical example is the tulip tree, whose leafs curl into a conical, low-drag configuration as wind velocity increases. Inspired by such natural adaptations, engineers have developed numerous airfoil profiles over the years, aiming to optimize lift to drag ratios. These efforts have converged on a geometry resembling the cross sectional shape of a bird's wing, featuring a rounded leading edge, a sharp trailing edge and a relatively thin profile, as show in Figure 3.1, [57] [58] [59].

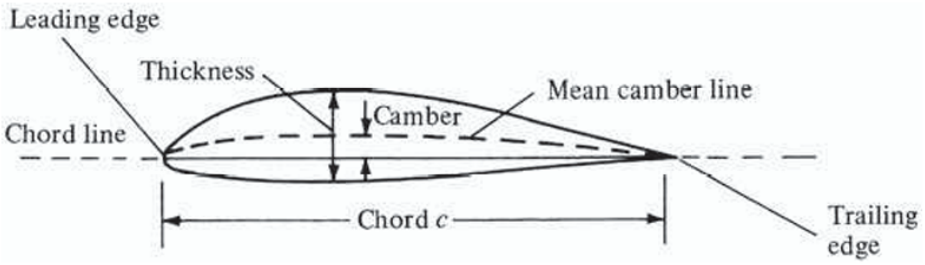

Figure 3.1: Foil scheme, [58].

There are two main types of foils, symmetric and asymmetric. The fundamental distinction between the two lies in their lift generation characteristics at varying angles of attack. Asymmetric foils are able to produce lift even at a zero degree angle of attack due to their cambered geometry. Consequently, they are commonly employed in applications where lift is required at neutral or small positive angles of attack and where negative angles are either minimal or nonexistent. On the other hand, symmetric foils, which exhibit identical upper and lower surface profiles, do not generate lift at a zero-degree angle of attack. However, they offer more balanced and extended range of angle of attack, making them particularly suitable for applications, such as hydrofoiling, where precise control of lift across a broad operating conditions is essential. Despite their advantages in control, symmetrical foils typically have a lower maximum lift coefficients compared to asymmetric foils, representing a trade-off that is often overlooked in favor of greater maneuverability and stability, [57] [58] [59].

3.1.2 Lift and Drag

The two principal properties associated with foils are lift and drag. As previously discussed, foil geometry is specifically designed to minimize drag. However, it is important to note that drag can never be entirely eliminated due to viscous and pressure induced effects inherent in fluid flow. By modifying the geometry of the foil, both lift and drag characteristics can be altered to meet specific performance requirements. These forces can be quantified using Equations 3.1 and 3.2, which define the lift and drag, respectively, [57] [58].

$$L = C_L \frac{1}{2} \rho V^2 A_p \tag{3.1}$$

$$D = C_D \frac{1}{2} \rho V^2 A_p \tag{3.2}$$

Where:

- C_L and C_D are the lift and drag coefficients respectively;
- ρ is the fluid density;
- V^2 is the flow velocity;

- A_p is the projected planform area of the foil.

A schematic representation of these forces is presented in Figure 3.2, illustrating how lift acts perpendicular to the flow direction, while drag acts parallel to it.

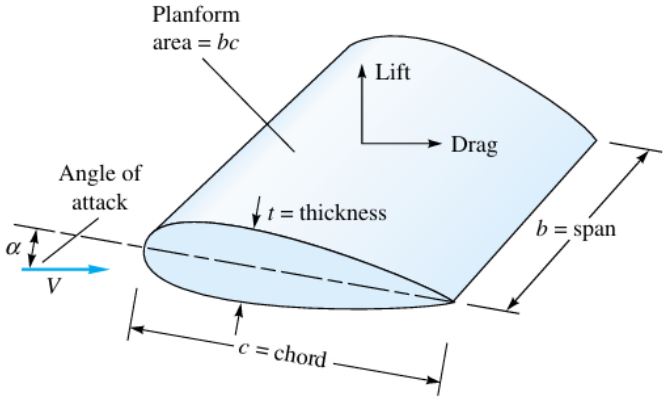

Figure 3.2: Lift and drag directions for general foil geometry, [57].

It is also essential to emphasize that both lift and drag are functions of the angle of attack. At low to moderate angles, the lift coefficient increases approximately linearly with the angle of attack, consistent with thin foil theory. Still, beyond a critical angle, typically around 15° to 20°, flow separation occurs on the upper surface of the foil. This phenomenon, known as stall, results in a sudden drop in lift and a corresponding rise in drag. An illustrative example of this behavior is shown in the graphic of Figure 3.3, [57] [58].

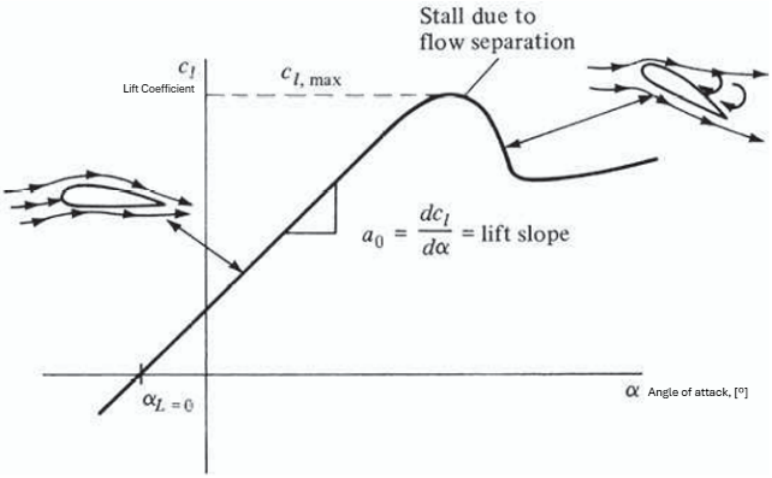

Figure 3.3: Foil behavior graphic, [58].

3.1.3 Aspect Ratio

Another fundamental geometric parameter in foil design is the aspect ratio (AR), a dimensionless quantity that significantly influences performance. It is typically defined in the range of 6 to 22 for hydrofoils and aircraft wings, depending on the structural constraints and intended application. The aspect ratio is given by Equation 3.3, [57] [58].

$$AR = \frac{b^2}{A_p} = \frac{b}{c} \tag{3.3}$$

Where b denotes the span of the foil, $A_p = b \cdot c$ is the projected planform area and c is the average chord length, [57] [58].

A higher aspect ratio implies a longer and slender foil, whereas a lower aspect ratio corresponds to a shorter and wider foil. One of the key interferences of aspect ratio is its influence on the induced drag. Specifically, the induced drag coefficient is inversely proportional to the aspect ratio, meaning that foils with higher aspect ratios experience lower induced drag. This, in turn, contributes to improved efficiency and higher lift-to-drag ratios. A visual representation of this relationship is given by the graphics in Figures 3.4 and 3.5, [57] [58].

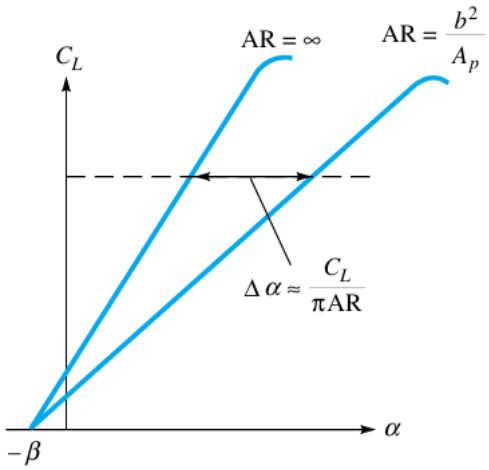

Figure 3.4: Effect of aspect ratio on lift coefficient, [57].

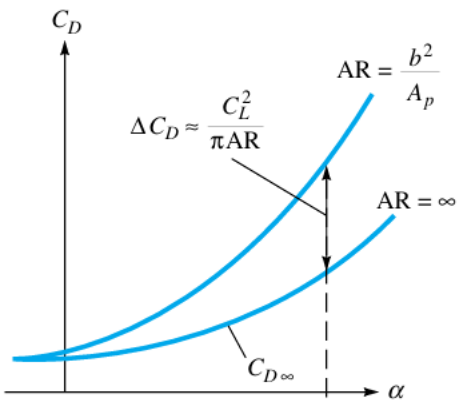

Figure 3.5: Effect of aspect ratio on drag coefficient, [57].

However, there are practical limitations to the increase of the aspect ratio. Slender foils are more susceptible to structural deformation and may require reinforcement to maintain stiffness under load, particularly in hydrodynamic environments where additional loads due to wave impact or cavitation may occur. On the other hand, foils with lower aspect ratios tend to experience higher loading, as a larger amount of lift must be generated over a smaller surface area, increasing the risk of structural failure or deflection, [57] [58].

In addition to drag considerations, aspect ratio also affects the stall behavior of foils. Foils with high aspect ratios tend to stall at lower angles of attack compared to those with lower aspect ratios, due to earlier flow separation. This trade-off between efficiency

and stall margin is crucial in the design of hydrofoils and aircraft wings. A qualitative representation of this relationship between the aspect ratio and stall angle is provided in the graphic shown in Figure 3.6, [57] [58].

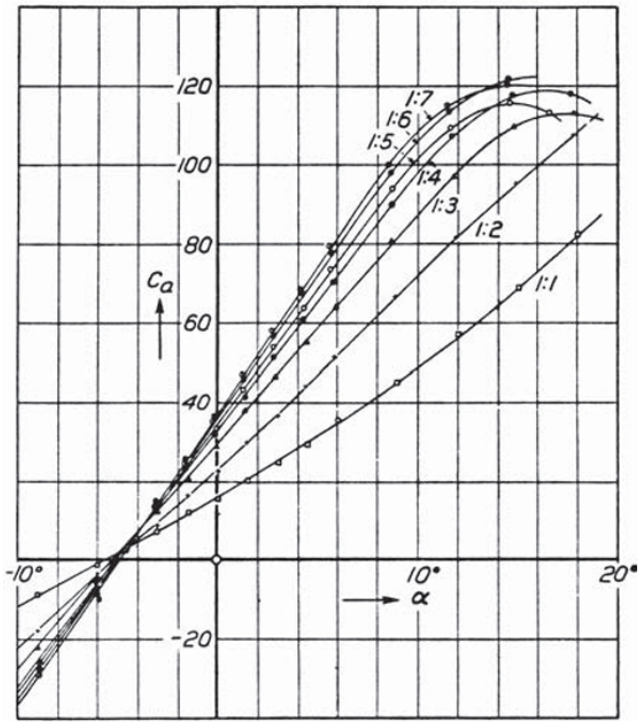

Figure 3.6: Effect of aspect ratio on stall angles graphic, [58].

3.1.4 Boundary Layer

The boundary layer is a fundamental concept in fluid dynamics that arises in the flow over immersed bodies. It refers to a thin region adjacent to the surface where viscous effects are significant, while in the outside region, the flow behaves as if it were inviscid due to the negligible influence of viscosity. Although the viscosity of the fluid remains constant throughout the domain, its relative impact becomes important only within the boundary layer, [57] [58] [59].

The formation of the boundary layer is a direct consequence of the no-slip boundary condition, which dictates that the fluid velocity relative to the solid surface must be zero. As a result, the flow velocity increases from zero at the wall to the free-stream velocity U over a short distance normal to the surface, [57] [58] [59]. In Figure 3.7 a schematic representation of the velocity profile within a boundary layer is shown.

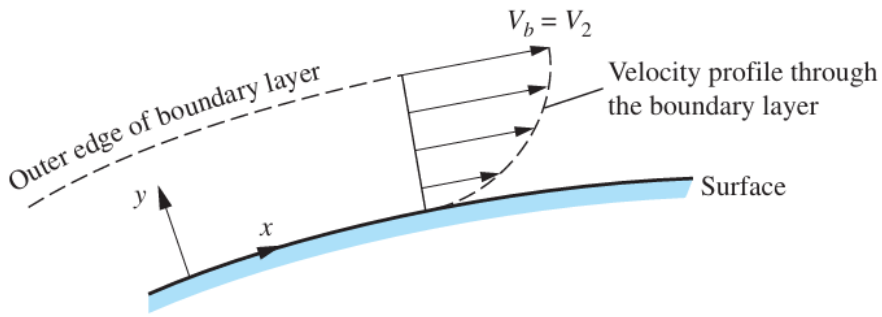

Figure 3.7: Velocity profile through a boundary layer, [58].

This phenomenon is particularly prominent at high Reynolds numbers, where the inertial forces dominate over viscous forces, leading to a thin boundary layer relative to the overall flow field. The boundary layer thickness, denoted as δ, is typically defined as the distance from the surface at which the velocity reaches 99% the upstream velocity, [57] [58] [59].

Within the boundary layer, energy exchanges occur between the kinematic energy of the fluid particles and the pressure energy of the flow. However, it is important to note that in an idealized, inviscid sense, there is no loss of mechanical energy, instead, the behavior of the viscous flow is influenced by the local pressure distribution, [57] [58] [59].

A favorable pressure gradient is characterized by a decrease in pressure in the flow direction, which results in acceleration of the fluid and a corresponding thinning of the boundary layer, which encourages it to remain attached to the surface. In contrast, an adverse pressure gradient, where pressure increases along the flow direction, can cause the fluid to decelerate. If the flow lacks sufficient kinetic energy to overcome the pressure rise, the velocity near the surface may reduce to zero and eventually reverse its direction. This leads to boundary layer separation, followed by the formation of a wake region behind the body, where the pressure is relatively low and nearly constant, [57] [58] [59]. A schematic representation of a general case of this phenomenon is shown in Figure 3.8.

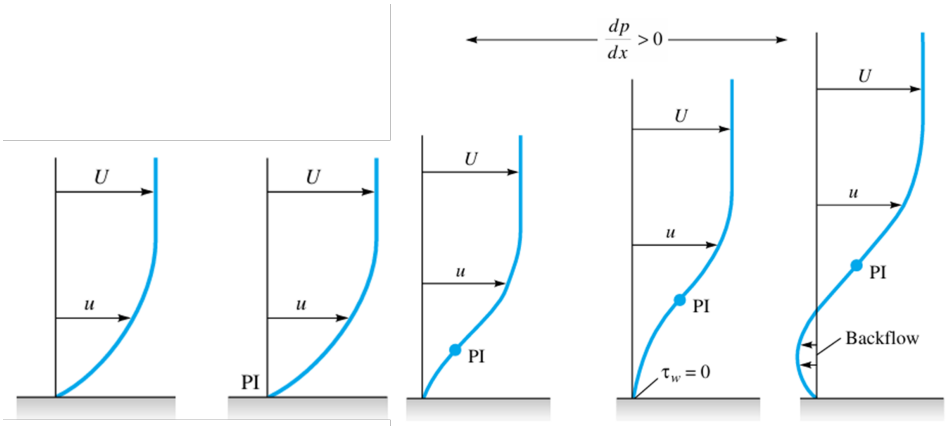

Figure 3.8: Effect of pressure gradient on boundary layer profiles where PI = point of inflection, [57].

The location of separation, width of the wake and the surface pressure distribution all depend on the characteristics of the boundary layer and the geometry of the body. Turbulent boundary layers, due to their higher momentum near the wall, are generally more resistant to separation than laminar ones, [57] [58] [59].

Another critical factor influencing boundary layer separation in hydrofoils is the angle of attack. As the angle increases, the adverse pressure gradient becomes more pronounced, making the separation more likely. When the angle of attack exceeds a certain limit, boundary layer separation occurs over a large portion of the foil surface, resulting in a sudden loss of lift, a phenomenon known as stall, as mentioned previously, [57] [58] [59].

It is important to highlight that hydrofoils are specifically designed to minimize drag and delay boundary layer separation, ensuring efficient performance across a range of operating conditions, [57] [58] [59].

3.1.5 Free Surface Related Effects

The flow over immersed bodies, such as hydrofoils, is significantly influenced by the proximity of the object to the free surface, leading to several physical phenomena that directly affect the performance of the hydrofoil. This section aims to examine these phenomena in greater detail and assess their impact on the performance and behavior of the hydrofoil.

The first phenomenon concerns the modification of the pressure field caused by the proximity of the hydrofoil to the free surface. This effect arises from the difference between density and resistance between air and water. As the hydrofoil operates closer to the free surface, the lighter air above provides significantly less resistance than the denser water below. This results in an asymmetric pressure distribution around the hydrofoil, leading to a reduction in the effective lift coefficient. This phenomenon can be characterized using the submergence Froude number, a dimensionless parameter defined as shown in Equation 3.4, [57] [58] [59].

$$Fn_h = \frac{U_\infty}{\sqrt{gh}} \tag{3.4}$$

Where,

- U_∞ is the free stream velocity;
- g is the gravitational acceleration;
- h is the immersion depth of the hydrofoil.

Lower values of h correspond to a higher Froude number, which are associated with a more significant free surface effects and greater reductions in lift. This relationship has been observed in both experimental and numerical studies, [57] [58] [59].

One of the consequences of pressure variation beneath water surface, in this case due to the presence of hydrofoils, is the deformation of the free surface, resulting in the formation of surface waves. These waves originate from disturbances in the pressure field

induced by the hydrofoils as they move through the fluid. As the velocity of the hydrofoils increases, the intensity and amplitude of these waves become more significant, leading to the development of a more pronounced wake. This, in turn, results in an increase in wave drag, which becomes particularly critical in shallow water conditions, where the depth limits wave energy dissipation, resulting in greater wave amplification and increased resistance. The interaction between the free surface and the hydrofoil induced pressure field not only affects hydrodynamic efficiency but also imposes design constraints on foil geometry and operating depth, [60].

Another physical phenomenon associated with wave formation is spray generation. Although not the primary consequence of hydrofoil induced surface disturbances, the formation of spray can contribute to the formation of drag and lead to the reduction in overall hydrodynamic efficiency. This effect is especially pronounced in surface piercing hydrofoils, where the pressure difference across the foil at the waterline accelerates the water upward and outward, promoting the ejection of droplets into the air. While often secondary, spray-induced drag becomes increasingly relevant at higher speeds and in configurations where portions of the foil operate near or through the free surface, [60].

Finally, another important phenomenon is ventilation. Ventilation occurs when atmospheric air is drawn into low-pressure regions around the hydrofoil or strut, typically on the suction side. This phenomenon leads to substantial loss of lift and a corresponding increase in drag, severely degrading the hydrodynamic performance. Several factors can contribute to the onset and development of ventilation, including cavitation, flow separation and the aeration of tip vortex, particularly at the lower tip of surface piercing struts. These vortex can act as pathways for air entrainment allowing air to be transported along the vortex core deep into the submerged flow field. Ventilation is specially critical in high speed applications, where the interplay between free surface and pressure distribution becomes more intense, and often marks a transition from stable to unsteady, [60].

3.1.6 Cavitation

One of the primary phenomena affecting hydrofoil performance is cavitation. Cavitation occurs when the local pressure in a liquid falls below its saturated vapor pressure, leading to a phase change from liquid to vapor. In hydrofoils, this results in the formation of vapor cavities, which can cause a sudden loss of lift, a significant increase in drag, and potentially erosion or structural damage to the foil surfaces, [60].

A common and particularly damaging form is inertial cavitation, where vapor bubbles rapidly collapse, generating intense shock waves. When this occurs on metallic surfaces, such as foils or propeller blades, it can lead to material fatigue and pitting damage, ultimately compromising structural integrity, [60].

The onset of cavitation can be estimated using Bernoulli's equation which, under inviscid flow assumptions, relates local pressure to flow velocity, fluid depth and other parameters, as shown in Equation 3.5, [60].

$$p = p_a + \rho g h + \frac{\rho}{2} U_\infty^2 \left(1 - \left(\frac{U_L}{U_\infty}\right)^2\right) \tag{3.5}$$

Where:

- p is the local pressure on the hydrofoil surface;
- p_a is the atmospheric pressure;
- ρ is the fluid density;
- g is the gravitational acceleration;
- h is the depth below the free surface;
- U_L is the local velocity on the foil;
- U_∞ is the free stream velocity.

According to this relation, higher local flow velocities, particularly on the suction side of the hydrofoil, reduce local pressure and therefore increase the likelihood of cavitation. For a given foil geometry, the angle of attack is another key factor, by increasing the angle it raises the lift coefficient but also intensifies local flow velocities, thus elevating the cavitation risk, [60].

Additionally, the proximity to the free surface reduces the ambient pressure acting on the foil, further promoting cavitation. Boundary layer separation also contributes by locally distributing the pressure field and potentially triggering cavitation at lower than expected flow values, [60].

3.2 Scaling Laws

In order to design a model-scale boat, is essential to understand the scaling laws that govern the relationship between the model and the full scale vessel. These laws ensure that the model accurately reflects the performance of the full scale vessel under similar conditions.

3.2.1 Froude Similarity

Froude similarity is a fundamental concept in naval architecture, particularly when scaling velocity between full-scale and model-scale displacement vessels. It ensures both geometric and kinematic similarity between the model and the full-scale vessel. This similarity is crucial for achieving dynamic similarity, where the ratio of inertial forces to gravitational forces remains consistent across scales. By equating the Froude numbers of the model and the full-scale vessel, Froude similarity guarantees that the wave resistance coefficients are identical in both cases. The Froude number can be calculated using Equation 3.6, [59].

$$Fr = \frac{V}{\sqrt{g \cdot c}} \tag{3.6}$$

Where:

- V is the characteristic velocity;
- g is the gravitational acceleration;
- c is the characteristic length.

In practical terms, when the Froude numbers of the model and full-scale vessel are matched, the scaling of dynamic effects, such as wave resistance, is preserved. This ensures that the behavior of the model under the same conditions will be representative of the full-scale performance of the vessel, [59].

It is important to note, however, that Froude similarity is primarily applicable in displacement vessels, where the movement of the vessel is primarily influenced by the interaction with the water surface. In contrast, for hydrofoil vessels that operate in foilborne conditions, which is when the hull is elevated above the water surface, the relevance of Froude similarity diminishes, [59].

3.2.2 Reynolds Similarity

Reynolds similarity ensures that the viscous forces acting on a model are properly scaled relative to those on the full-scale vessel. This is particularly important for fully submerged hydrofoil systems, where the flow remains continuously attached to the surface of the foils and viscous effects significantly influence performance. The Reynolds number expresses the ratio between the inertial forces and viscous forces in a fluid flow and is calculated using Equation 3.7, [59].

$$Re = \frac{V \cdot c}{\nu} \tag{3.7}$$

Where:

- V is the characteristic velocity;
- c is the characteristic length;
- ν is the kinematic viscosity of the fluid.

To achieve Reynolds similarity, the relationship shown in Equation 3.8 must be hold between the full-scale and model-scale conditions, [59].

$$V_s \cdot c_s = V_m \cdot c_m \quad \Rightarrow \quad V_m = V_s \cdot \frac{c_s}{c_m} \tag{3.8}$$

However, this requirement often leads to impractically high model speeds, especially for small-scale models. For instance, consider a 1:25 scale hydrofoil vessel with a full-scale cruising speed of 40 m/s. To maintain Reynolds similarity, the model would need to operate at a speed of approximately 200 m/s, a value well beyond the capabilities of most experimental facilities, [59].

One common approach to mitigate this issue is to increase the chord length of the model of the foil. By doing so, the Reynolds number can be adjusted without necessitating extreme velocities. Nevertheless, this introduces a geometric inconsistency, potentially affecting other aspects of the behavior of the model. Additionally, increasing the foil area typically results in greater lift, which must be counterbalanced by increasing the mass of the model to preserve dynamic equilibrium, [59].

Therefore, while Reynolds similarity is critical for capturing viscous effects in submerged hydrofoil systems, it often requires compromises in geometric fidelity or test conditions. These trade-offs must be carefully considered during experimental design to ensure representative results, [59].

3.3 The Finite Element Method

The Finite Element Method (FEM) is a computational strategy used to approximate the solutions of problems governed by differential equations. It is particularly powerful in engineering because it can be applied to a wide range of analyses, from static and dynamic studies to buckling and fracture mechanics. The main strength of FEM is its ability to deal with complex cases, where analytical solutions are impractical due to irregular geometries, non-uniform material properties or complicated loading conditions, [61].

The method works by decomposing the original geometry into smaller, simpler subdomains called finite elements. Each element is easier to model because of its reduced size and straightforward shape. Depending on the formulation, elements can be one-dimensional, two-dimensional and three-dimensional, and may take different forms such as bars, beams, shells, tetrahedra or hexahedra. Collectively, all elements constitute the mesh that represents the structure under study. Connections between neighboring elements occur at specific points known as nodes. For linear elements, these nodes are positioned at the vertices, while quadratic elements also include mid-side nodes and sometimes central ones. Using higher order elements makes it possible to capture more detailed behavior and to represent curved surfaces with greater accuracy, [61].

Each elements response is described mathematically using interpolation, which leads to the definition of shape functions. These functions allow the field variables to be expressed as a combination of nodal values. To obtain the finite element equations, the governing differential equations are reformulated into their weak or variational form, often through the principle of virtual work. For a structural problem, this process yields an element level system seen in Equation 3.9, [61].

$$[M_e]\{\ddot{u}_e\} + [K_e]\{u_e\} = \{F_e\} \tag{3.9}$$

Where $\{u_e\}$ is the nodal displacement vector, which includes translations and rotations, $\{F_e\}$ is the vector of nodal forces, $[K_e]$ is the stiffness matrix containing the geometric and material information and $[M_e]$ is the mass matrix. For linear static problems, the acceleration term vanishes, leading to a simpler relation shown in Equation 3.10, [61].

$$[K_e]\{u_e\} = \{F_e\} \tag{3.10}$$

To assemble the complete model, the local element matrices are combined according to the connectivity of the mesh, producing the global stiffness matrix $[K]$ and the global load vector $\{F\}$. After imposing boundary conditions, such as loads and constraints, the system of equations can be solved for the unknown displacements seen in Equation 3.11, [61].

$$[K]\{u\} = \{F\} \tag{3.11}$$

The solution vector $\{u\}$ provides the displacements and rotations at all nodes. From these, strains and stresses can be derived across the entire structure using the strain displacement relations and Hooke's law. In Equations 3.12 and 3.13, for a linear isotropic elastic material, [61].

$$\varepsilon = \frac{\Delta l}{l_0} = \frac{l - l_0}{l_0} \tag{3.12}$$

$$\sigma = E\,\varepsilon \tag{3.13}$$

Where E is the Young's modulus, which characterizes the stiffness of the material, [61].

Despite their robustness, FEM solutions are not exact. Sources of error include numerical approximations in integration, limitations of polynomial interpolation, singularities and geometric simplifications when discretizing curved domains with straight-edge elements. Refining the mesh reduces some of these errors and improves local accuracy, but at the cost of higher computational effort. A mesh convergence study is therefore essential to balance solution accuracy with computational efficiency, [61].

4

Design and development

The following chapter outlines the methodology adopted for the design and modeling of the hydrofoil system and its main components. It begins by detailing the system design requirements that were imposed and that shaped the geometry of the foils and struts. An *Excel* spreadsheet was utilized to perform and organize all the necessary calculations for the determination of the foil and strut geometry, allowing for quick iteration and validation of design parameters. Following this, it presents the parametric approach used to develop and refine the 3D geometry of the foils and struts, including the integration of the tapering and flaps, through custom-built macros in *SolidWorks*. Next, a description of the of the baseline geometry along with the definition of the study cases is presented. Finally, an in depth functional integration of Case 2 is shown, considering the imposed constraints, actuator selection and the overall workflow adopted.

4.1 Calculation

The calculation stage establishes the foundation for the hydrofoil design by defining the system requirements and translating them into geometric and structural parameters. This includes the evaluation of hull dimensions, foil planform characteristics and strut configuration, all of which are essential to achieve the desired hydrodynamic performance and structural integrity. The results of these calculations serve as the baseline inputs for the subsequent parametric modeling process, ensuring consistency between analytical estimations and the 3D CAD implementation.

4.1.1 System Design Requisites

Before proceeding with the geometric modeling of the hydrofoil system, it is essential to define the key design requirements that drive this configuration. These requisites are based on performance objectives. It is important to highlight that the model being developed is intended as a test platform, specifically for evaluating various components, such as electric actuators, used by the company. As a result, the performance demands for this vessel are lower than those of high-performance hydrofoil catamarans typically designed for competitive use. The requirements outlined in this section provide the foundation for the subsequent modeling and optimization steps.

The design requirements and assumed parameters considered in this work are summarized as follows:

- Maximum mass: 40 kg
- Takeoff velocity: $V_{\text{takeoff}} = 4.626\,\text{m}\,\text{s}^{-1}$ (equivalent to 9 knots)
- Cruise velocity: $V_{\text{cruise}} = 6.168\,\text{m}\,\text{s}^{-1}$ (equivalent to 12 knots)

- Aspect ratio: $AR = 6$
- Lift ratio (rear to front foils): 1:5
- Flap chord ratio: 35% of the total foil chord
- Taper: 50%
- Foil section model: Speer H005
- Strut section model: NACA 0012

The assumed physical constants and aerodynamic parameters used throughout the analysis are:

- Gravitational acceleration: $g = 9.81\,\mathrm{m\,s^{-2}}$
- Water density: $\rho = 1025\,\mathrm{kg\,m^{-3}}$
- Dynamic viscosity: $\mu = 1.14 \times 10^{-3}\,\mathrm{Pa\,s}$
- Oswald efficiency factor: $e = 0.95$
- Sweep angle: $\Lambda = 0°$

4.1.2 Hull Geometry

The hull selected for this design is a catamaran type, based on the geometry of the vessel *Flying Nimbus*. To meet the project constraints, particularly the total length requirement of $2\,m$, the original hull was proportionally scaled down. This choice ensures a stable platform with minimal hydrodynamic resistance, suitable for integration with the hydrofoil system. The final hull geometry can be seen in Figure 4.1.

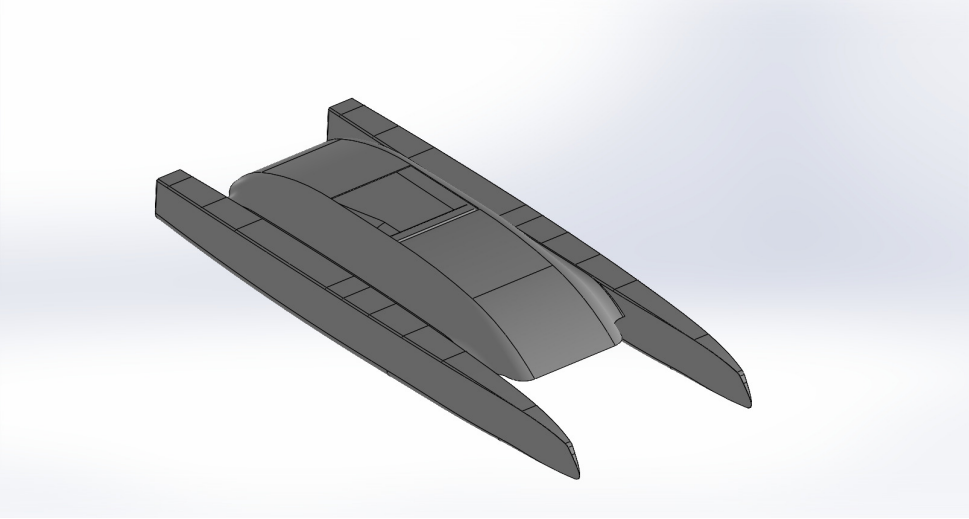

Figure 4.1: Hull.

4.1.3 Foil Geometry

The objective of this section is to determine the foil geometry based on the design requirements. The analysis begins with calculating the necessary lift to meet the performance targets, followed by the definition of the key geometric parameters of the foils. This includes establishing chord lengths, spans and flap dimensions to ensure the hydrofoil achieves the desired hydrodynamic characteristics.

Starting with the lift calculations.

- Total lift required: $L_{\text{total}} = 40 \times 9.81 = 392.4\,\text{N}$
- Front foil lift: $L_{\text{front}} = (\frac{5}{6}) \cdot 392 = 327\,\text{N}$
- Rear foil lift: $L_{\text{rear}} = (\frac{1}{6}) \cdot 392 = 65.4\,\text{N}$
- Lift per front foil: $L_{\text{front, each}} = 163.5\,\text{N}$
- Lift per rear foil: $L_{\text{rear, each}} = 32.7\,\text{N}$

Lift Coefficient

To proceed for the calculation of the geometry from the foils there is one vital component that needs to be calculated, which is the lift coefficient during cruise and take-off. As it was mentioned previously, the foil geometry set as a requirement was the Speer H005, whose specifications can be seen in the Appendix A.1. The most valuable information in the document are the graphics shown in Figures 4.2 and 4.3.

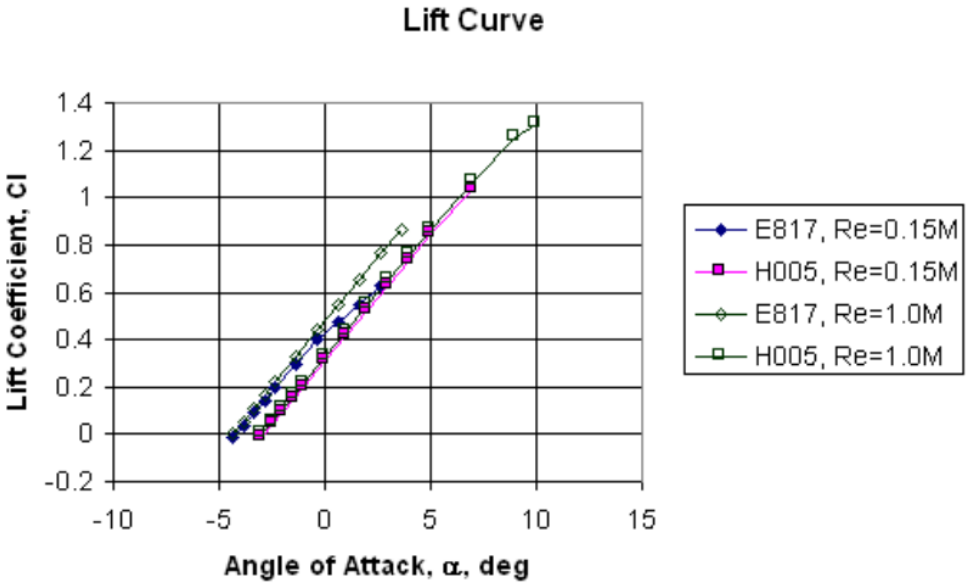

Figure 4.2: Speer H005 angle of attack and lift coefficient relation graphic, [62].

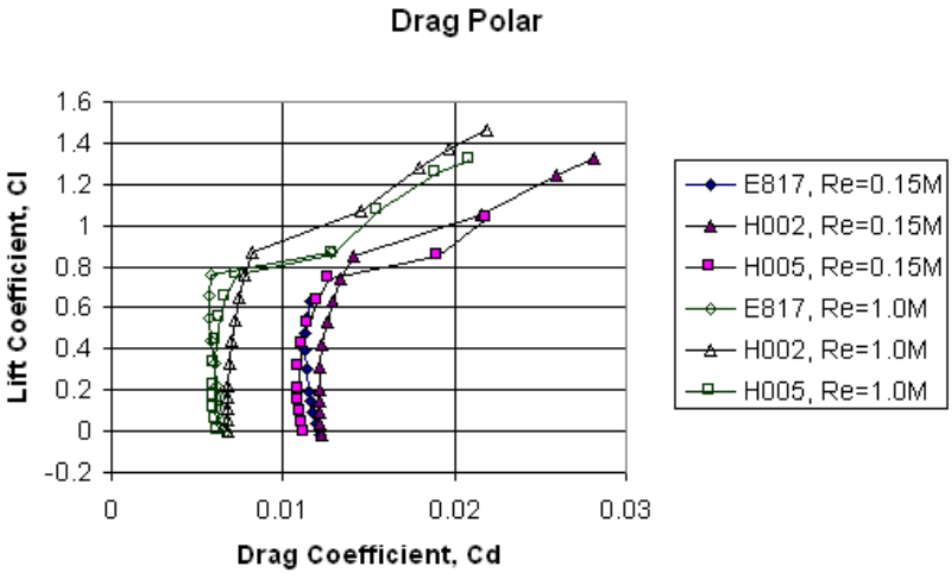

Figure 4.3: Speer H005 drag coefficient and lift coefficient relation graphic, [62].

Due to the lack of available numerical data, both in the referenced document used and online, the values were manually approximated from the published graphics. A graphical analysis tool was then used to estimate the coordinates by visually identifying data points based on their spatial relation with the graphic axes. Consequently, the extracted values for the lift coefficient versus angle of attack, as well as for the lift versus drag coefficient, should be regarded as approximate and subjected to a margin of visual interpretation. Based on the extracted data points, the curves were reconstructed in *Excel*. A linear trendline was applied to the lift coefficient versus angle of attack data, while a polynomial trendline was used to better fit the drag coefficient versus lift coefficient relationship, as illustrated in Figures 4.4 and 4.5.

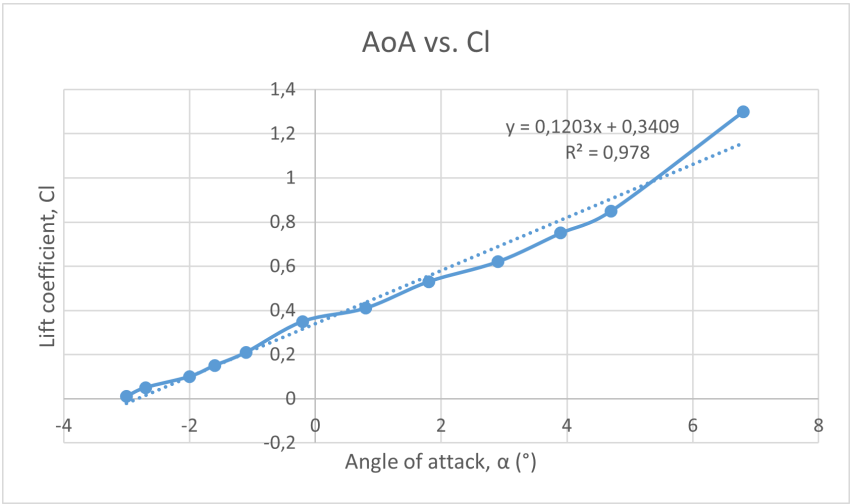

Figure 4.4: Speer H005 angle of attack and lift coefficient excel relation graphic with trendline.

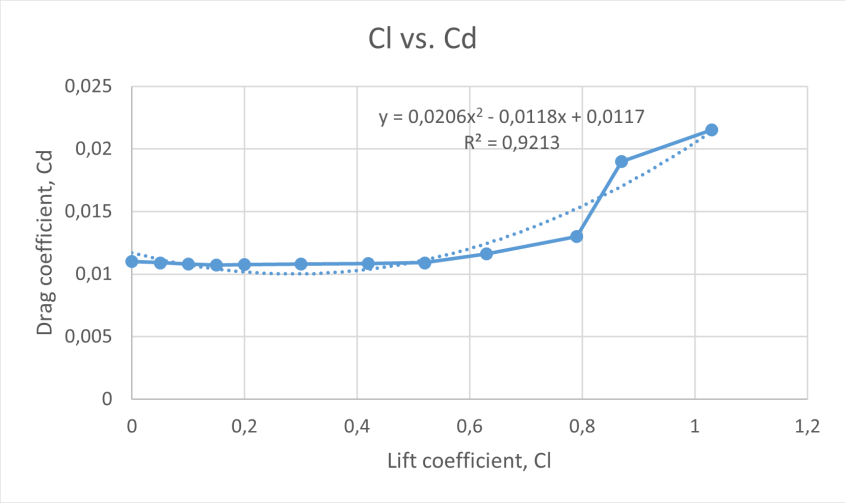

Figure 4.5: Speer H005 drag coefficient and lift coefficient excel relation graphic with trendline.

The fitted trendlines were then used to evaluate the relationships between the relevant aerodynamic parameters over an angle of attack range of $-8°$ to $13°$ and to compute the corresponding values of the lift-to-drag ratio (C_l/C_d) within this interval. However, it is important to note that the extracted data corresponds to a two-dimensional (2D) foil analysis, whereas the foil being designed operates in a three-dimensional (3D) context. To account for this, a correction is required to adapt the 2D to 3D data, based on the lifting-line theory. This is achieved by calculating the 3D lift curve slope a through the following Equation 4.1.

$$a = \frac{a_{2D} \cdot \cos(\Lambda)}{\sqrt{1 + \left(\frac{a_{2D} \cdot \cos(\Lambda)}{\pi \cdot AR}\right)^2} + \left(\frac{a_{2D} \cdot \cos(\Lambda)}{\pi \cdot AR}\right)} \tag{4.1}$$

Where $a_{2D} = 0.1203$ is the slope of the 2D lift curve, $\Lambda = 0°$ is the sweep angle, and $AR = 6$ is the aspect ratio of the foil. Applying this correction yields a 3D lift curve slope of approximately $a = 0.0841$.

Using this corrected value, the 3D lift coefficient can be calculated from the 2D data using Equation 4.2.

$$C_{l_{3D}} = \frac{C_{l_{2D}} \times a}{a_{2D}} \tag{4.2}$$

Similarly, the 3D drag coefficient is computed using Equation 4.3.

$$C_{d_{3D}} = C_{d_{2D}} + \Delta C_{D_0} + \frac{C_{l_{3D}}^2}{\pi \times e \times AR} \tag{4.3}$$

Where $\Delta C_{D,0} = 0.0143$ accounts for additional drag used and $e = 0.95$ is the Oswald efficiency factor.

From these corrected coefficients, the lift-to-drag ratio (Cl/Cd) can be recalculated and its relationship with the angle of attack is shown in Figure 4.6.

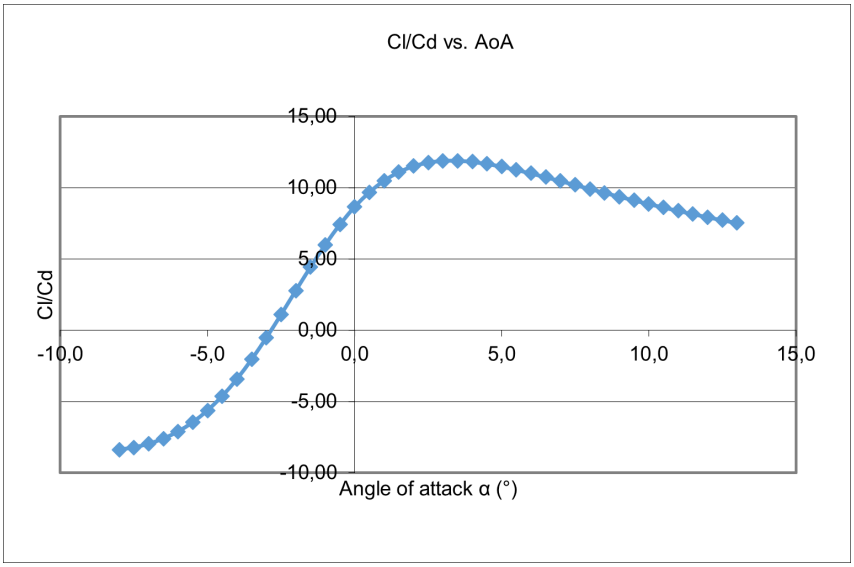

Figure 4.6: Speer H005 lift-to-drag ratio and angle of attack relation graphic.

Furthermore, Table 4.1 shows part of the calculated values including the maximum value for the lift-to-drag ratio, which was found to be approximately 11.886, occurring at an angle of attack $\alpha = 3.5°$ and a corresponding lift coefficient $C_{l_{3D}} = 0.533$.

Table 4.1: Speer H005 Lift, drag, and lift-to-drag ratio over angle of attack.

Alpha (°)	**Cl**	**Cd**	**Cl/Cd**
2.0	0.407	0.0353	11.51
2.5	0.449	0.0381	11.76
3.0	0.491	0.0413	11.88
3.5	**0.533**	**0.0448**	**11.89**
4.0	0.575	0.0487	11.81
4.5	0.617	0.0529	11.67
5.0	0.659	0.0574	11.47

These results indicate that, for optimal performance, the hydrofoils should be designed to operate at a cruise lift coefficient of $C_{l_{cruise}} = 0.533$, which corresponds to a fixed foil angle of attack of approximately 3.5°.

For the following steps, the calculations are performed considering the most critical condition, which is take-off. Therefore, it is necessary to determine the lift coefficient at take-off, $C_{L,\text{takeoff}}$, which can be calculated using Equation 4.4.

$$C_{L,\text{takeoff}} = C_{L,\text{cruise}} \left(\frac{V_{\text{cruise}}}{V_{\text{takeoff}}} \right)^2 \tag{4.4}$$

By substituting the values, we obtain the value of $C_{L,\text{takeoff}}$ as shown in Equation 4.5.

$$C_{L,\text{takeoff}} = 0.533 \left(\frac{6.168}{4.626} \right)^2 = 0.948 \tag{4.5}$$

Front Foils

With the cruise lift coefficient already defined, the geometric characteristics of the front foils can now be determined. The foil dimensions are sized based on the lift required from each of them during the most critical operating condition, the take-off. The first step is to calculate the required planform area of each front foil, based on the lift demand during take-off. This is done using Equation 4.6.

$$S_{front,each} = \frac{2L_{front,each}}{\rho V_{take-off}^2 C_{l_{takeoff}}} = \frac{2 \times 163.7}{1025 \times 4.626^2 \times 0.948} = 0.0157\, m^2 \tag{4.6}$$

With the known area, the span of each front foil can be determined from the aspect ratio, as shown in Equation 4.7.

$$b_{front,each} = \sqrt{AR \times S_{front,each}} = \sqrt{6 \times 0.0157} = 0.3072\, m \tag{4.7}$$

Since the foils are tapered, with a taper ratio defined as $\lambda = c_{tip}/c_{root} = 0.5$, the chord is not constant throughout the span. To determine the root and tip chords, the following relationships are used:

$$c_{front,mideach} = \frac{2 \times S_{front,each}}{b_{front,each} \times (1+\lambda)} = \frac{2 \times 0.0157}{0.3072 \times 1.5} = 0.0683\, m \tag{4.8}$$

$$c_{front,tipeach} = \lambda \times c_{front,mideach} = 0.5 \times 0.0683 = 0.0341\, m \tag{4.9}$$

Finally, the maximum thickness of each front foil is determined by applying the relative thickness of the foil profile. This is based on the H005 profile, which has a maximum thickness equal to 5% of the chord length. For tapered foils, the thickness varies along the span. The maximum thickness at the root can be calculated as indicated in Equation 4.10.

$$t_{front,each} = c_{front,mideach} \times \text{foil type} = 0.0683 \times 0.05 = 0.0034\, m \tag{4.10}$$

This approach ensures an accurate geometric representation of the front foils, consistent with the design assumptions for aspect ratio and tapering.

According to the flap chord ratio, the flap length at the center can be calculated using Equation 4.11.

$$L_{\text{front flap}} = 0.35 \times c_{front,mideach} = 0.35 \times 0.0683 = 0.0239\, m \tag{4.11}$$

Rear Foils

A similar approach is applied to determine the geometry of the rear foils. Since these foils contribute less to overall lift, their dimensions are correspondingly smaller. The same equations detail the computation of the main geometric parameters for each rear foil, starting with Equation 4.12

$$S_{rear,each} = \frac{2L_{rear,each}}{\rho V_{take-off}^2 C_{l_{takeoff}}} = \frac{2 \times 32.7}{1025 \times 4.626^2 \times 0.948} = 0.0031\, m^2 \tag{4.12}$$

The span is then calculated using the same aspect ratio assumption using Equation 4.13.

$$b_{rear,each} = \sqrt{AR \times S_{rear,each}} = \sqrt{6 \times 0.0031} = 0.1374\, m \tag{4.13}$$

Since the rear foils also feature a taper ratio of $\lambda = 0,5$, the chord distribution is not uniform. The root and tip chords are calculated using the following equations 4.14 and 4.15.

$$c_{rear,mideach} = \frac{2 \times S_{rear,each}}{b_{rear,each} \times (1+\lambda)} = \frac{2 \times 0.0031}{0.1374 \times 1.5} = 0.0305\, m \tag{4.14}$$

$$c_{rear,tipeach} = \lambda \times c_{rear,rooteach} = 0.5 \times 0.0305 = 0.0153\, m \tag{4.15}$$

Finally, using the same H005 foil profile as before, the maximum thickness of the rear foil is calculated using Equation 4.16.

$$t_{rear,each} = c_{rear,mideach} \times \text{foil type} = 0.0341 \times 0.05 = 0.0015\, m \tag{4.16}$$

As before, the flap length for the rear foil can be calculated using the flap chord ratio as shown in Equation 4.17.

$$L_{\text{rear flap}} = 0.35 \times c_{front,mideach} = 0.35 \times 0.0305 = 0.0107\, m \tag{4.17}$$

This sizing ensures that the rear foils provide sufficient lift during take-off, while maintaining geometric consistency with the front foil and the design requirements of the H005 profile.

4.1.4 Strut Geometry

The objective of this section is to define the geometry of the hydrofoil struts in accordance with the overall design requirements. The analysis is based on the definition of their main geometric parameters. This includes determining the strut height and chord length to ensure both structural integrity and minimal hydrodynamic drag. As stated previously, the foil profile selected for this project is the NACA 0012, since it was one of the predefined design requirements, whose specifications can be seen in the Appendix A.2.

Front Struts

The front strut height is assumed to be $h = 0.5m$. This value ensures that, under cruise conditions, approximately 10 cm to 20 cm of the strut remain submerged, allowing the vessel to rise up to 30 cm out of the waterline while maintaining adequate foil immersion.

Given the strut height and the assumed aspect ratio, the chord length can be calculated using Equation 4.18.

$$c_{front,strut} = \frac{h}{AR} = \frac{0.5}{6} = 0.08\,m \tag{4.18}$$

As with the foils, the NACA 0012 profile was selected for the struts. This profile has a maximum thickness equal to 12% of the chord length, which results in the thickness calculated using Equation 4.20.

$$t_{front,strut} = c_{front,strut} \times \text{foil type} = 0.08 \times 0.12 = 0.01\,m \tag{4.19}$$

Rear Struts

The rear struts follow the same height assumption, with $h = 0.5\,m$. However, the chord length is scaled relative to the rear foils, maintaining the same proportion observed between the front foils and struts. Based on this ratio, the chord is set to $c_{rear,strut} = 0.05\,m$.

Using the same NACA 0012 profile, the thickness of the strut is calculated as seen in Equation 4.20.

$$t_{rear,strut} = c_{rear,strut} \times \text{foil type} = 0.05 \times 0.12 = 0.006\,m \tag{4.20}$$

This sizing ensures consistency in structural and hydrodynamic performance across all struts, aligned with the design profile and functional requirements.

4.1.5 Geometric Summary of Vessel Components

This subsection provides a consolidate overview of the main geometric parameters defined for the components of the vessel, including the hull, foils and struts. The values presented summarize the results from the previous design calculations, offering a comprehensive reference for the dimensions used in the subsequent parametric modeling and construction phases. Table 4.2 compiles these parameters for ease of interpretation and validation.

Table 4.2: Geometric summary of vessel components.

Component	**Measurement [m]**
Hull	
Total length	2.000
Width	0.900
Hull type	Catamaran
Front foils	
Profile	Speer H005
Span (b)	0.3072
Central chord (c)	0.0683
Thickness (t)	0.0034
Flap size	0.0239
Rear foils	
Profile	Speer H005
Span (b)	0.1374
Central chord (c)	0.0305
Thickness (t)	0.0015
Flap size	0.0107
Front struts	
Profile	NACA 0012
Height (h)	0.5000
Chord (c)	0.0800
Thickness (t)	0.0100
Rear struts	
Profile	NACA 0012
Height (h)	0.5000
Chord (c)	0.0500
Thickness (t)	0.0060

4.2 Parametric Design

This section outlines the parametric modeling approach adopted for the design of the hydrofoil components. The goal is to enable fast, flexible and efficient geometric generation that allows the rapid generation and modification of various foil geometries using a limited set of input parameters. These parameters include chord length, span, thickness, taper ratio, and flap deflection. By integrating these variables and iterative improvements, while also supporting seamless integration into overall 3D model. The development progresses from a simple foil geometry to more complex forms, including tapering and the addition of movable flaps, as detailed in the following subsections.

As established in the previous sections, the foil profile selected for the foils is the Speer H005 and for the struts the NACA 0012. Like all airfoil or hydrofoil profiles, its shape is defined by a set of coordinate points, typically a large number, that describe the profile's upper and lower surfaces with high fidelity. These points are given in relative, non-dimensional coordinates, this means that regardless of the size of the foil, the shape remains geometrically consistent by applying scaling factors.

For this project, all coordinate calculations were performed in an *Excel* spreadsheet. The x positions of the profile were scaled using Equation 4.21 and the y positions using Equation 4.22, where the chord and thickness are outputs from the prior design calculations.

$$x = x_{default} \times c \tag{4.21}$$

$$y = y_{default} \times (t \times \text{foil type}) \tag{4.22}$$

These dimensions, such as chord, thickness and flap size, are directly derived from performance requirements, including lift needs and aspect ratio constraints. As a result, the coordinate data used in the modeling is not arbitrarily scaled, but driven by the design logic established earlier. The *Excel* sheet functions as a parametric engine, when a key parameter changes, the updated geometry is automatically calculated without the need for manual reentry or error prone adjustments.

To fully automate the modeling process, custom macros were developed in *SolidWorks*. All the macros read the geometric parameters and coordinate points directly from the *Excel* sheet and use them to generate 3D sketches and solid features within the CAD environment. This allows for rapid reconstruction of the calculated values and the final 3D model. The macro also supports the inclusion of taper and flaps, enabling the automated generation of increasingly complex foil configurations.

This geometric similarity forms the basis for a parametric modeling approach. Rather than manually recreating the sketches or tables every time a design change is made, a scalable model can also be automatically updated with new values. This automation significantly reduces modeling time and errors, especially considering that some profiles, such as, NACA 0012 can have over 130 defining coordinate points.

Due to this dependency between geometric and calculated parameters, parametric modeling was essential in this project. It ensured design consistency, traceability and

allowed for immediate visualization of changes, enabling a powerful workflow for performance driven hydrofoil development. The next subsections detail the progressive construction of this parametric model, starting from a basic untapered foil, moving on to tapered geometries and finally incorporating flaps and control surfaces.

4.2.1 Foil

As explained previously to streamline the modeling of hydrofoil geometries and support iterative design changes, a parametric modeling approach was implemented using a custom macro developed in VBA for *SolidWorks*. This macro enables automated generation of 3D foil geometries directly from parameterized input data stored in an *Excel* spreadsheet.

The macro performs the following operations:

- Model initialization: The macro begins by launching a new part environment in *SolidWorks* and selecting the *Front Plane* as the base sketch plane to create the foil profile;
- Data acquisition from *Excel*: It establishes a connection to an *Excel* file where the geometric input parameters are stored. Specifically, it reads:
  - The coordinate points (x,y) that define the foil profile;
  - The span value used for the extrusion.

  These coordinates are processed in *Excel* and scale based on the chord length and thickness determined during design calculations. This ensures that any changes in the geometric parameters are automatically reflected in the points used for modeling;
- Profile creation: A spline is generated in the *SolidWorks* sketch using the imported set of points. This forms the 2D cross-section shape of the hydrofoil;
- Solid generation by extrusion: The spline is then extruded along the z-axis by the span value to produce the final 3D foil body. This extrusion is unidirectional and generated as a single, clean solid from the input profile.

This automated process eliminates the need for manual sketching or repetitive input of coordinate data into *SolidWorks*. It allows the user to update the foil design by simply modifying the input parameters in *Excel*. Upon executing the macro, an updated 3D model is generated instantly. This approach significantly enhances design flexibility, minimizes human error and accelerates the modeling workflow, especially when handling foil profiles composed of more than 100 discrete points.

This macro was utilized to generate both the front and rear foils, as well as the front and rear struts, by simply adjusting the input cells referenced from the *Excel* sheet. The full macro code used in this process is provided in the Appendix B.1. An example of the component created through this macro is shown in Figure 4.7.

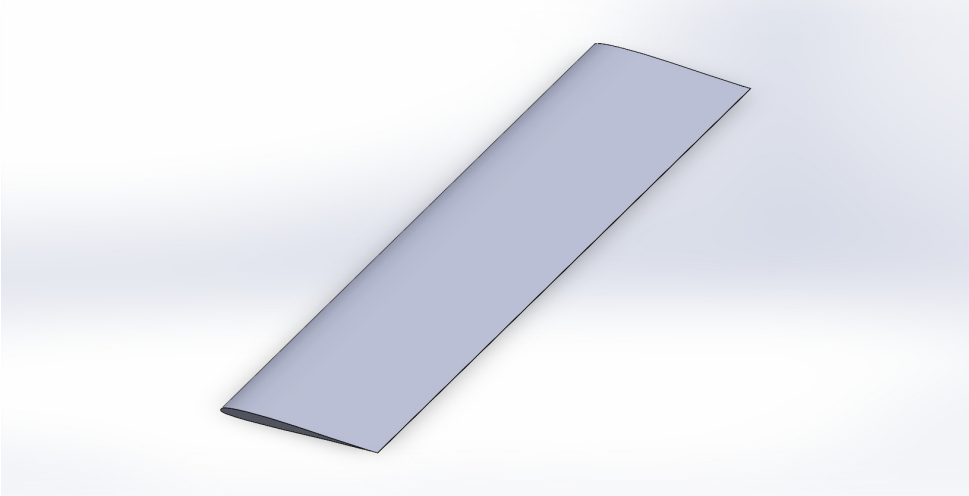

Figure 4.7: Macro foil.

4.2.2 Tapered Foil

As part of the parametric modeling strategy, a second macro was developed to generate tapered hydrofoils using loft ready cross section sketches distributed along the span of the foil. This macro builds on the initial approach by introducing variable chord lengths across the span, controlled via a taper ratio and is intended to more accurately represent realistic foil shapes used in hydrodynamic applications. Like the previous macro, it reads parameterized geometry directly from an *Excel* spreadsheet, allowing for fast design iterations and automatic updates.

The macro performs the following operations:

- Model setup: The macro assumes a part file is already open in *SolidWorks* and uses the *Front Plane* as the baseline reference for positioning the sketches. It generates two additional reference planes at mid-span and tip-span locations by offsetting the *Front Plane*. These planes define the locations where the foil cross sections will be sketched;

- Data acquisition from *Excel*: The macro connects to an external *Excel* spreadsheet and retrieves:

  - The coordinate points (x,y) of the foil profile;
  - The extrusion span;

  The macro also calculates the center of the chord line to ensure proper alignment of the three foil sections. These coordinates are scaled symmetrically at the root and tip according to the specified taper ratio, while the mid-span section retains the original profile scale;

- Sketch generation: Using the retrieved and processed coordinates, the macro creates three-individual sketches, root, mid and tip, each on its respective reference

plane. These sketches reflect the foil geometry at different spanwise locations and are prepared to serve as input profiles for a loft operation.

Although the sketches are successfully created and positioned, it was not possible to implement the loft operation itself in the code. This was due to limitations encountered with automating the loft between complex spline profiles, which requires precise matching of the curve start and end conditions. Nevertheless, the generated sketches can be used directly within the *SolidWorks* interface to perform the loft operation through the standard *FeatureManager* tree, enabling the creation of a fully tapered 3D foil.

This approach enables a more realistic modeling of hydrofoil geometries while preserving the parametric flexibility provided by the *Excel* based workflow. Design updates, such as changes in taper ratio, chord scale or span, can be implemented instantly by modifying the input file. The full code for this macro is provided in the Appendix B.2. Figure 4.8 shows the result produced by this macro, while Figure 4.9 presents an example of a manual loft created using the sketches generated by the macro.

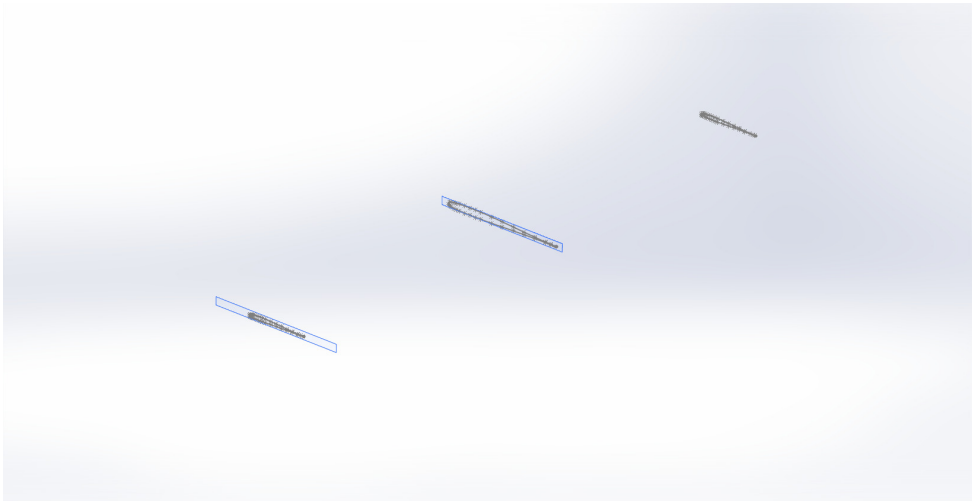

Figure 4.8: Macro tapered foil result.

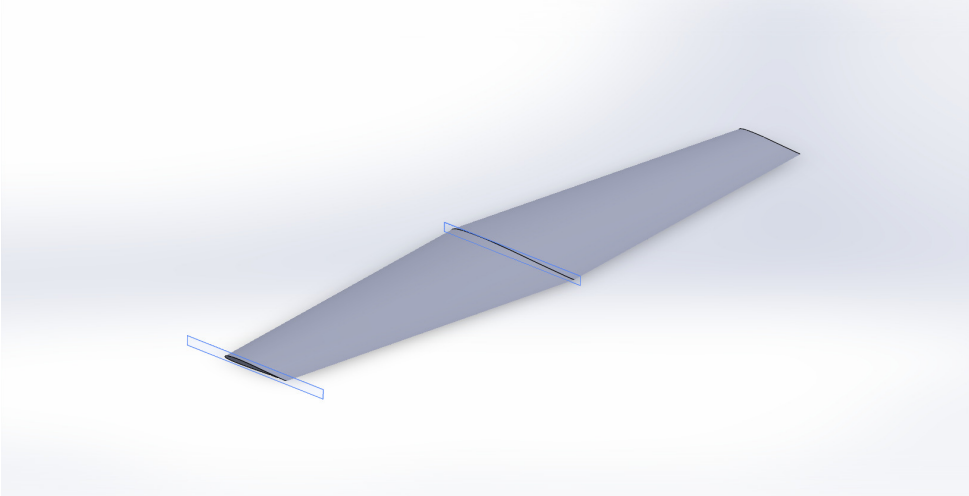

Figure 4.9: Macro tapered foil result with *FeatureManager* tree loft command.

4.2.3 Tapered Foil with Flaps

To support greater control over hydrofoil customization and facilitate the integration of control surfaces such as flaps, an advanced parametric modeling macro was developed. This macro generates a spanwise tapered hydrofoil with an integrated flap segment, using geometric definitions stored in an external *Excel* spreadsheet. The macro produces six individual sketches, enabling subsequent lofting and manipulation directly within CAD environment.

The macro executes the following operations:

- Model and environment preparation: The macro assumes an active part document is open in *SolidWorks*. It begins by creating two reference planes that are offsetted from the *Front Plane*, corresponding to the mid-span and tip sections. These planes are spaced based on the span value retrieved from the input data;
- Data import from *Excel*: A connection is established with an external *Excel* spreadsheet and retrieves:
  - The 2D (x,y) coordinates defining the foil shape;
  - The total span value;

  It then calculates the chord centerline and identifies the bounds of the profile to ensure symmetric scaling about the chord center;
- Main foil geometry definition: Using the imported coordinates, the macro constructs three sets of 3D point arrays representing the root, mid and tip sections of the hydrofoil. Tapering is implemented by applying a fixed scale factor (50%) to the root and tip sections, while the mid remains at full scale. These scaled coordinates are aligned along the same center line to ensure geometric continuity;

- Flap segmentation and transformation: A trailing flap is defined as a partial chord segment occupying the final 35% of the original foil length. The macro identifies this flap region by computing a cutoff point at 65% of the chord. For points ahead of the flap region, coordinates are collapsed onto a single x location to enforce geometric continuity between the foil and the flap. Points within the flap region are scaled to form a miniaturized foil consistent with the original shape, but limited to the flap segment;
- Sketch generation: Once the coordinates are processed, the macro creates six spline sketches;
  - Three for the main foil section;
  - Three for the flap;

  Each spline is drawn on the corresponding reference plane and named systematically for easy identification. These sketches serve as the input profiles for a later loft operation, which is intended to be performed manually in *SolidWorks*.

Similarly to the previous macro, although the sketches were successfully created, it was not possible to implement the loft operation itself. Furthermore, the flap sketches, due to the lack of sufficient points in their creation region, do not fully reproduce the intended foil shape, as illustrated in Figure 4.11. The complete macro code is provided in the Appendix B.3. An example of the result generated by this macro is shown in Figure 4.10, while Figure 4.11 offers a close-up view of the same result.

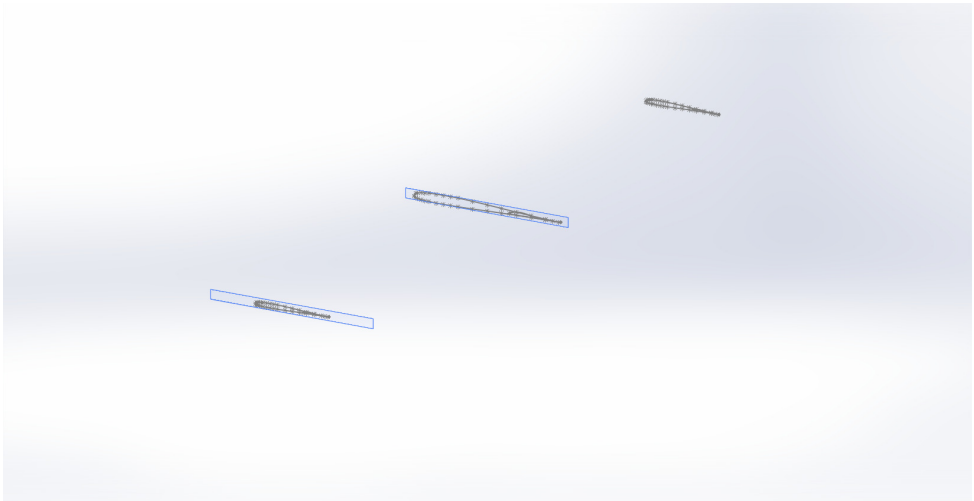

Figure 4.10: Macro tapered foil with flap result.

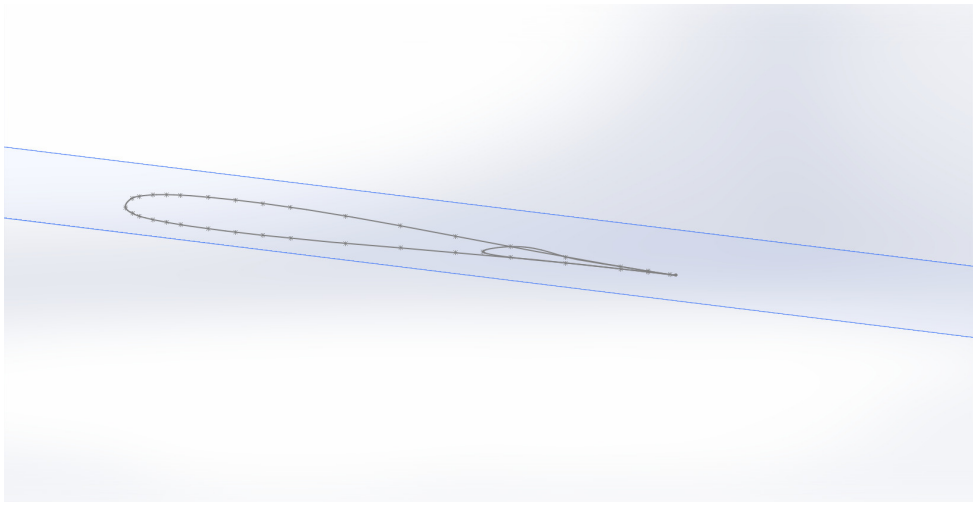

Figure 4.11: Macro tapered foil with flap result up close.

4.2.4 Critical Assessment of the Parametric Workflow

The use of parametric modeling via VBA macros in *SolidWorks* offered clear functional advantages in the development of a complex hydrofoil geometry. Through parameter driven sketches and lofted features, it was possible to automate the creation of a foil with taper and integrated flap mechanism, all governed by numerical inputs extracted from an *Excel* spreadsheet. This automation eliminated the need for repetitive manual tasks, reduced modeling errors and allowed for consistent reproduction of geometry variations, key benefits when dealing with iterative design processes and performance sensitive components such as hydrofoils.

One of the most notable strengths of this method lies in its customization and responsiveness to changes. Adjusting parameters such as chord length, span, taper ratio or flap size in the *Excel* file automatically updates the generated geometry without any additional sketching or modeling effort. In that sense, the macro acts as a dynamic geometry engine, one that is especially well suited for early stage design exploration, rapid prototyping or comparative analysis between variants. For relatively simple components with well defined design rules, this approach can significantly reduce development time.

However, while the concept of parametric macro based modeling is sound, its practical implementation in *SolidWorks* using VBA reveals significant limitations and challenges, so much that the coding process itself could easily be the subject of a separate technical study. The learning curve associated with the *SolidWorks API*, combined with the limitations of the VBA language, often turns what should be a time saving strategy into a time consuming task. Despite the apparent simplicity of the final output, the macro required extensive coding, testing and debugging to function reliably. The ratio between the effort invested in the code development and the complexity of the resulting model is arguably disproportionate.

Part of this inefficiency stems from the rigid nature of the *SolidWorks API*, which demands explicit calls for every minor operation, from plane creation and sketch insertion to spline generation and feature naming. Simple mistakes indexing or feature selection can

cause the macro to fail entirely and because VBA lacks robust error handling, diagnosing these failures is often difficult. Furthermore, the dependence of the macros on specific environment conditions, makes it fragile and non-portable. These characteristics limit its usefulness in broader workflows or collaborative environments.

Another important consideration is scalability. As model complexity increases, for example, when dealing with variable section foils, of parametric assemblies, the VBA macro approach becomes increasingly difficult to maintain and extend. More advanced tools and programming languages, such as *Python*, may offer better solutions in terms of both capability and user experience.

In conclusion, while the VBA macro approach succeeded in automating the generation of a tapered hydrofoil with flap in *SolidWorks*, the process exposed considerable trade-offs between flexibility and complexity. The macro proved the feasibility of parametric modeling within *SolidWorks*, but also highlighted its fragility, steep development cost and limited scalability. Developing the macro took significantly longer than anticipated relative to the complexity of the output, suggesting that while powerful in theory, this method is best suited to controlled and relatively simple use cases. For more advanced applications, further research into alternative modeling paradigms or software environments may be warranted.

4.3 Baseline Geometry

This section presents the workflow and the resulting geometry obtained from the previously defined calculations. It then addresses the constraints identified from the manufacturing of the component, together with the corresponding design objectives. Finally, in order to overcome these constraints, several potential solutions are discussed, leading to the definition of five case studies aimed at identifying the most feasible solution.

4.3.1 Description of the Optimize Hydrofoil Geometry

As mentioned previously, this design was conceived as a test vessel, with the requirement that all components be manufactured by 3D printing using polylactic acid (PLA) as the polymer.

After analyzing the developed macros, it was decided to employ the first macro for the generation of the front and rear struts and the second macro for the creation of the front and rear foils. This approach allowed for straightforward adaptation of the geometry, by modifying the input cells referenced by the macros, the different components could be produced with their respective dimensions, as defined in the earlier calculations.

Front and Rear Struts

The design of the front and rear struts was relatively simple. Once generated through the macro, the main post-processing step consisted of introducing holes along their full height. These holes were designed to allow the insertion of a tube, enabling the connection between the strut and the foil, as well as between the strut and the hull.

Since PLA alone would not provide sufficient mechanical strength in this critical area, the tube is also intended to be manufactured from a more robust material, preferably a metal or a reinforced polymer, to ensure the required structural integrity of the component.

In addition to providing strength, the inclusion of the tube also facilitates the 3D assembly process. By acting as a common interface, it allows the struts to be printed in separate sections, adapted to the limitations of the 3D printer and later aligned and joined together during assembly. This approach improves both the ability to manufacture and the robustness of the final structure.

Since the struts share the same geometry, differing only in overall dimensions, only the rear strut example is shown in Figure 4.12.

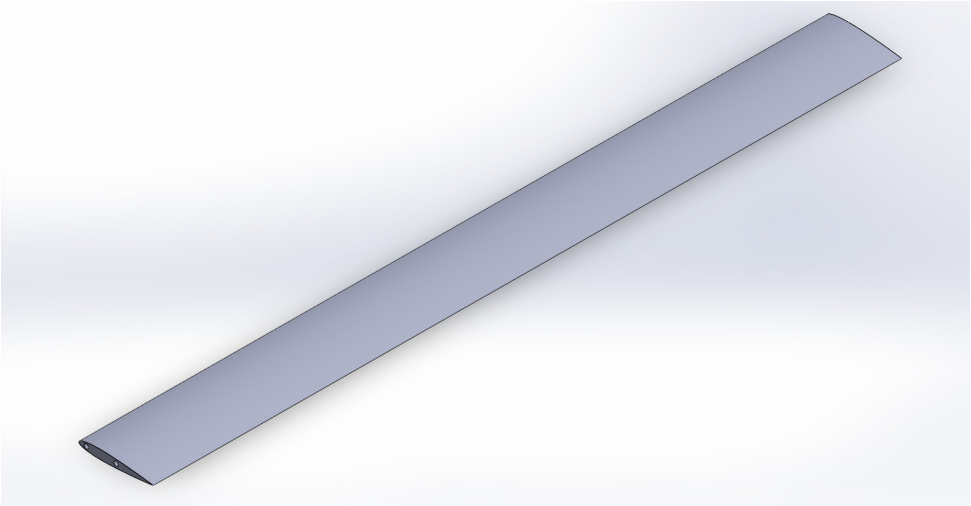

Figure 4.12: Final rear strut optimized model.

Front and Rear Foils

The development of the foils required a slightly different approach. The second macro was employed to generate the necessary foil profiles, while the flap sketches were created manually, as illustrated in Figure 4.13. Once the profiles were defined, each part, the front of the foil and the corresponding flap, were obtained through lofting operations.

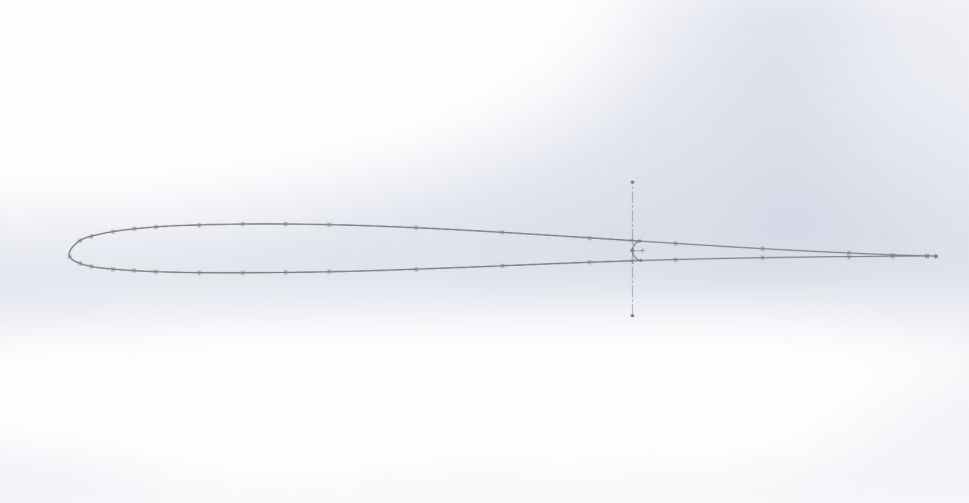

Figure 4.13: Final rear foil front and flap sketches of the optimized model.

To ensure both structural integrity and manufacturability, a hole was introduced through each section of the foil, similar to what was done for the struts. This hole serves a dual purpose, it allows for the insertion of a reinforcement tube to increase strength and it provides the interface needed to subdivide the geometry into smaller components. This subdivision is essential to enable the fabrication by 3D printing and the subsequent assembly of the parts into the complete foil.

As done previously for the struts, because the front and rear foils share the same geometry and differ only in their overall dimensions, so only the rear foil is presented here as an example, as shown in Figure 4.14.

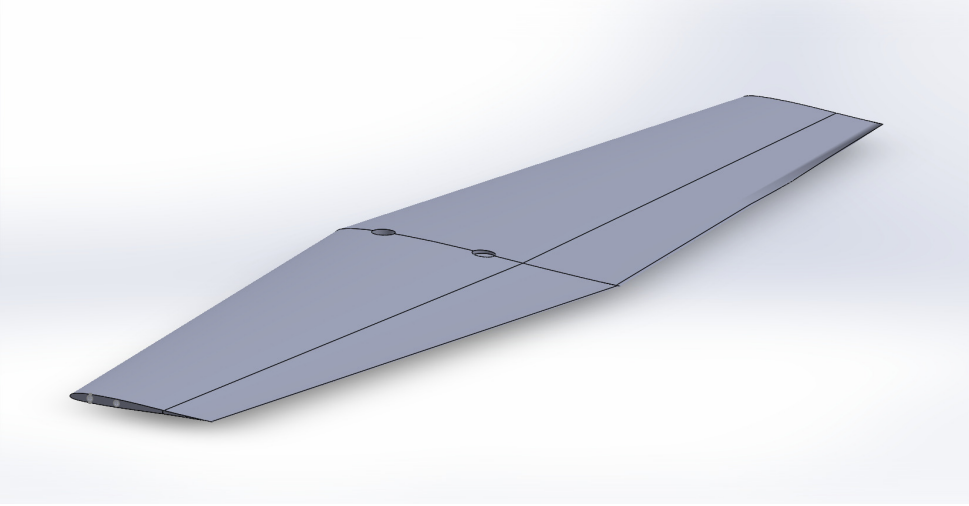

Figure 4.14: Final rear foil optimized model.

Assembly

The assembled configuration of the struts and foils is shown in Figure 4.15. In this assembly, it is important to note the application of one of the previous design calculations, the foil is inclined at an angle of 3.5° to ensure that the flap is aligned at 0° during take-off, as clearly illustrated in the figure.

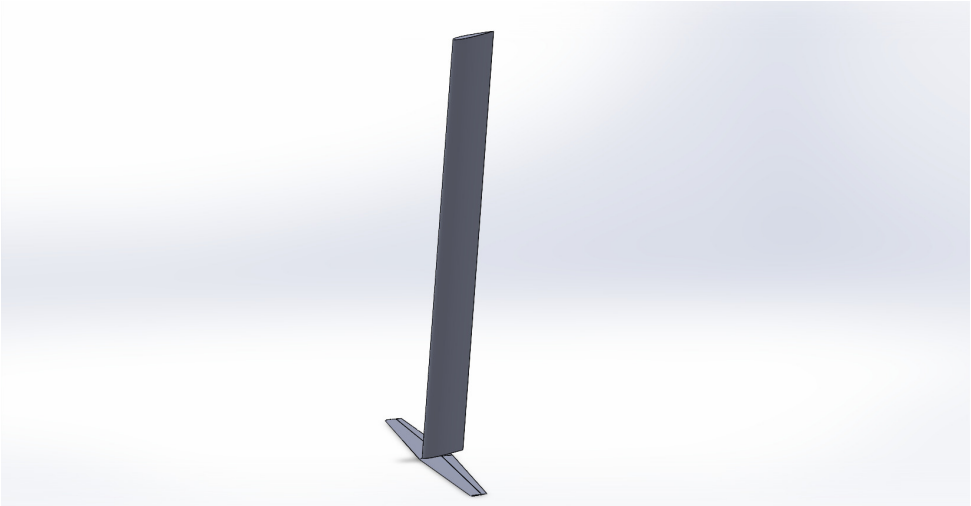

Figure 4.15: Final rear foil and strut assembly optimized model.

4.3.2 Objectives and Design Constraints

As mentioned previously, the primary objective was to manufacture all components using 3D printing. However, both the calculations and the earlier *SolidWorks* models reveal a significant limitation, the components, particularly the rear foil, exhibit an extremely thin maximum thickness, with the rear foil measuring only 2 mm at its thickest point. This very thin geometry poses a major challenge for additive manufacturing, as it falls below the practical limits for reliable 3D printing with standard materials like polylactic acid (PLA).

Furthermore, the original design incorporated holes through the components to accommodate reinforcing tubes, intended to provide structural support and facilitate assembly. Given the extremely thin sections of the foils, implementing these tubes would not be feasible, as the surrounding material is insufficient to maintain integrity around the holes. Attempting to include the tubes in such thin parts would compromise the structural strength, likely resulting in weak or failed prints. Consequently, both the thin geometry and the impracticality of the tube integration make direct 3D printing of the foils unfeasible without further design modifications or alternative manufacturing approaches.

In order to overcome these limitations and identify practical solutions, a series of study cases was developed, which are detailed in the following subsection.

4.3.3 Definition of Study Cases

To explore feasible solutions to the limitations identified in the previous subsection, five study cases were defined. Each case represents a different approach to adapting the hydrofoil components for manufacturability and structural integrity, including variations in geometry, materials and manufacturing processes. The study cases were designed to evaluate how modifications affect both the mechanical performance and the feasibility of using different fabrication techniques.

Case 1

The first case study considers the optimized hydrofoil geometry produced using standard 3D printing. This case serves as a baseline for comparison, particularly in terms of structural integrity and the ability to be manufactured. By analyzing this scenario, it is possible to evaluate how the original design performs when constrained by the limitations of typical 3D printing equipment and to determine wether pursuing specialized printing technologies would provide sufficient benefits to justify the additional complexity and cost. Thus, this baseline case establishes a reference point against which the performance and feasibility of the other study cases can be assessed.

Case 2

The second case study also considers manufacturing via 3D printing, but introduces a redesigned geometry that is not only feasible for additive manufacturing, but also accommodates the actuator system required for flap control. This modification ensures that both structural integrity and functional requirements are addressed simultaneously. The process for creating this redesigned model, including the integration of the actuator mechanism, will be described in detail in the following section.

Case 3

For the third case study, the optimize hydrofoil geometry is considered once again, but with a different manufacturing approach, forged carbon. As previously discussed, forged carbon is an emerging fabrication technique that has gained popularity not only in aerospace applications but also in marine engineering. Its high strength to weight ratio and excellent structural properties makes it a promising option for producing hydrofoil components, allowing the model to achieve both the required performance and durability while potentially overcoming the limitations encountered with 3D printing.

Case 4

For the fourth study case, the optimize hydrofoil geometry is maintained, but the focus shifts to a different manufacturing method, bound metal deposition. This additive manufacturing process enables the production of metal components with high strength and precision while maintaining the advantages of 3D printing, such as geometric flexibility and reduced tooling requirements. By considering BMD, this case aims to evaluate

whether the hydrofoil can achieve the necessary structural performance and durability, while maintaining the flexibility of additive manufacturing.

Case 5

For the fifth and final case, the optimized hydrofoil geometry is once again adopted, however, the fabrication process considered is press molding with carbon fiber. This technique allows the production of lightweight, high strength composite components with excellent structural performance and surface finish. By employing press molded carbon fiber, this case aims to assess wether the hydrofoil can meet both mechanical and dimensional requirements while taking advantage of the superior material properties offered by advanced composites, providing a potential optimal solution in terms of strength to weigh ratio and durability.

In summary, Table 4.3 provides a concise overview of all the study cases that will be analyzed.

Table 4.3: Summary of hydrofoil study cases.

Case	Model	Manufacturing Process
1	Optimized geometry	3D printing
2	Redesigned geometry	3D printing
3	Optimized geometry	Forged carbon
4	Optimized geometry	Bound Metal Deposition
5	Optimized geometry	Press molding with carbon fiber

Overall, these five study cases provide a structured framework for evaluating alternative design and manufacturing strategies for the hydrofoil components. By systematically varying the fabrication method and, when necessary, the geometry, each case addresses specific constraints identified in the previous section. Together, these cases serve as a foundation for comparing the feasibility, performance and practicality of different approaches, guiding the selection of the most suitable solution for both testing and potential future production.

4.4 Functional Integration of Case 2

As previously discussed, the second study case continues to utilize 3D printing as the fabrication method, but with a redesigned hydrofoil geometry. This section provides a detailed examination of the development of this new design, covering the identification of constraints, the rationale behind the design choices and the integration of the actuator system required for the flap control. The workflow and final outcomes of this case are also presented to illustrate how the redesigned geometry addresses both structural and functional requirements.

4.4.1 Constraints and Rationale

The primary constraints for Case 2 arise from the limitations identified in the optimized hydrofoil geometry and the requirements for the functional integration. As discussed earlier, the original design is extremely thin, particularly in the rear foil, which poses significant challenges for 3D printing and for ensuring sufficient thickness in critical regions while remaining compatible with additive manufacturing limitations, such as minimum feature sizes and layer resolution.

In addition, the integration of an actuator system to control the flap introduces both spatial and alignment constraints. Sufficient internal space must be provided to house the actuator without interfering with the foil structure, internal tubes or assembly features, while maintaining precise alignment to ensure correct flap motion along the span. This also affects assembly and maintenance considerations, as the actuator and internal components must remain accessible for installation or potential replacement.

Weight is another important factor, since adding the actuator and any structural reinforcements increases the mass of the hydrofoil. Excess weight could negatively impact the performance of the vessel, stability and takeoff characteristics, so the design must balance strength and functionality with minimal additional mass.

Hydrodynamic performance must also be preserved, any modifications to accommodate the actuator or reinforce the structure should not compromise the lift, drag or overall efficiency of the foil. Finally, the material properties of PLA or other 3D printable polymers must be considered, as their limited mechanical strength necessitates careful design of load bearing sections to prevent failure under operational conditions.

Given the constraints, the redesign follows a clear rationale, the geometry is adjusted to increase local thickness where structural strength is critical, while keeping the overall form close to the optimized foil to preserve hydrodynamic performance. Internal cavities and support features are strategically designed to accommodate the actuator system without interfering with assembly operation. Material usage and weight are optimized to minimize additional mass and 3D printing limitations are considered to ensure manufacturability. Furthermore, the redesign will only focus on the rear foils as it is the critical design for structural analysis due to its smaller size. This train of thought ensures that the new design successfully balances structural all essentials while providing a viable solution for integrating the actuator system into the hydrofoil.

4.4.2 Actuator Selection and Integration

The objective of this section is to select a suitable actuator based on torque and speed requirements and to determine the optimal placement of the actuator within the hydrofoil assembly to ensure precise, reliable and optimal flap control. By combining geometric constraints, hydrodynamic loads and practical considerations, this section outlines the thought behind the choice of actuator and its integration strategy.

For this design, the actuator is integrated directly inside the hydrofoil, close to the flap hinge. This placement minimizes the mechanical linkages, reducing backlash and energy losses and allows for the precise and immediate control of the flap deflection. Embedding the actuator in the foil also reduces overall complexity of assembly, as no external linkages

from the hull are required. An alternative approach, placing the actuator in the hull and connecting it to the flap via rods or levers was considered. While feasible, this solution introduces additional mechanical complexity, potential backlash and increased structural loads along the linkages, which could compromise response accuracy and reliability in the dynamic marine environment. Therefore, internal integration within the foil was chosen as the most efficient robust solution for precise flap actuation. In Figures 4.16 and 4.17 are shown the schematic representations of these two options.

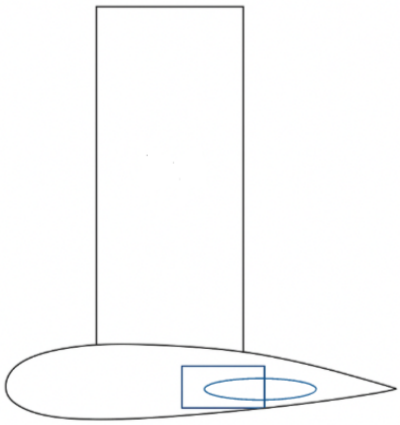

Figure 4.16: Schematic representation of the actuator position foil integrated solution.

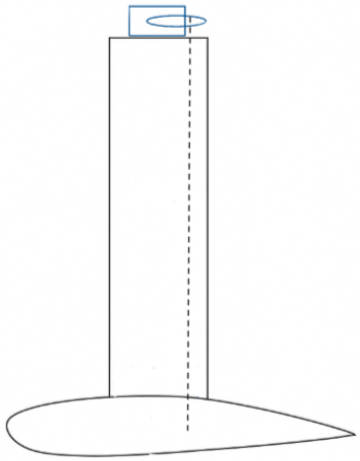

Figure 4.17: Schematic representation of the actuator position hull integrated solution.

To actuate the hydrofoil flaps, the HS-5086WP waterproof servo was selected, where all its technical information is shown in the Appendix C. The primary design requirement was to provide sufficient torque and speed to control the flaps, which represent 35% of the chord of the foil and span the full foil width. Considering the rear foil, with a chord of $0,031\ m$ and a flap length of $0,011\ m$, the resulting flap area can be approximately calculated as shown in Equation 4.23.

$$S_{\text{flap}} = b \cdot c_{\text{flap}} = 0.137 \cdot 0.011 \approx 0.001507 \text{ m}^2 \tag{4.23}$$

Assuming a lift coefficient equal to the foil take-off value, $C_{L,\text{takeoff foil}} = 0.9476$ and a take-off speed $V_{\text{takeoff}} = 4.626$ m/s, the lift generated by the flap is estimated using Equation 4.24.

$$L_{\text{flap}} = \frac{1}{2}\rho V_{\text{takeoff}}^2 S_{\text{flap}} C_{L,\text{foil}} = \frac{1}{2} \cdot 1025 \cdot 4.626^2 \cdot 0.001507 \cdot 0.9476 \approx 14.5 \text{ N}. \tag{4.24}$$

The torque required to rotate the flap about its hinge, assumed at the 35% chord location, is therefore equal to Equation 4.25.

$$\tau_{\text{required}} = L_{\text{flap}} \cdot (c_{\text{flap}} \cdot 0.35) = 14.5 \cdot (0.011 \cdot 0.35) \approx 0.056 \text{ N} \cdot \text{m}. \tag{4.25}$$

Applying a safety factor of 2 to account for uncertainties in lift, unsteady effects and mechanical losses, the design torque becomes as calculated in Equation 4.26.

$$\tau_{\text{design}} = 2 \cdot 0.056 \approx 0.112 \text{ N} \cdot \text{m}. \tag{4.26}$$

The HS-5086WP servo provides a stall torque of 12 $\text{kg} \cdot \text{cm} = 1.18 \text{ N} \cdot \text{m}$, offering a factor of safety of approximately 10.5 relative to the required torque.

Regarding angular speed, the flaps must deflect between $-8°$ and $13°$ and the actuator can achieve $60°$ in $0.14s$, resulting in a rotation time less than $0.05s$ for the full range, well within necessary response time for hydrofoil control.

In Figure 4.18 a representation of the selected servo is presented, while its main dimensional specifications are summarized in Table 4.4. These geometric characteristics are just as important as the performance metrics previously discussed, since the servo must physically fit within the hydrofoil structure compromising its hydrodynamic profile or structural integrity.

Figure 4.18: HS-5086WP servo, [63].

Table 4.4: Physical specifications of the HS-5086WP waterproof servo.

Specification	**Metric**
Length	0.0310 m
Width	0.0152 m
Height	0.0310 m
Weight	0.0285 kg

A direct comparison between the servo dimension and the optimized hydrofoil model reveals that the actuator is considerably larger than the internal volume available in the foil. This apparent incompatibility raises a significant design challenge, how to integrate the actuator without altering the functional requirements or drastically increasing drag.

The strategies adopted to address this issue, together with a re-evaluation of the suitability of this servo for the final geometry, are discussed in the following section.

4.4.3 Design Workflow

The development of the redesigned geometry and its integration with the actuator system required a structured design workflow to ensure feasibility and functionality. This process began with the identification of the key design requirements, namely accommodating the servo dimensions, maintaining the hydrodynamic efficiency and preserving sufficient structural strength despite the limited thickness of the foil. Following this, iterative modeling in *SolidWorks* was carried out to adjust the geometry, with emphases on embedding the actuator inside the foil without compromising its hydrodynamic profile. Each iteration was evaluated against the defined constraints, including manufacturability, actuator integration and assembly considerations, ultimately leading to a refined design that balances performance with practical implementation.

A schematic representation of the design workflow that was followed is shown in Figure 4.19.

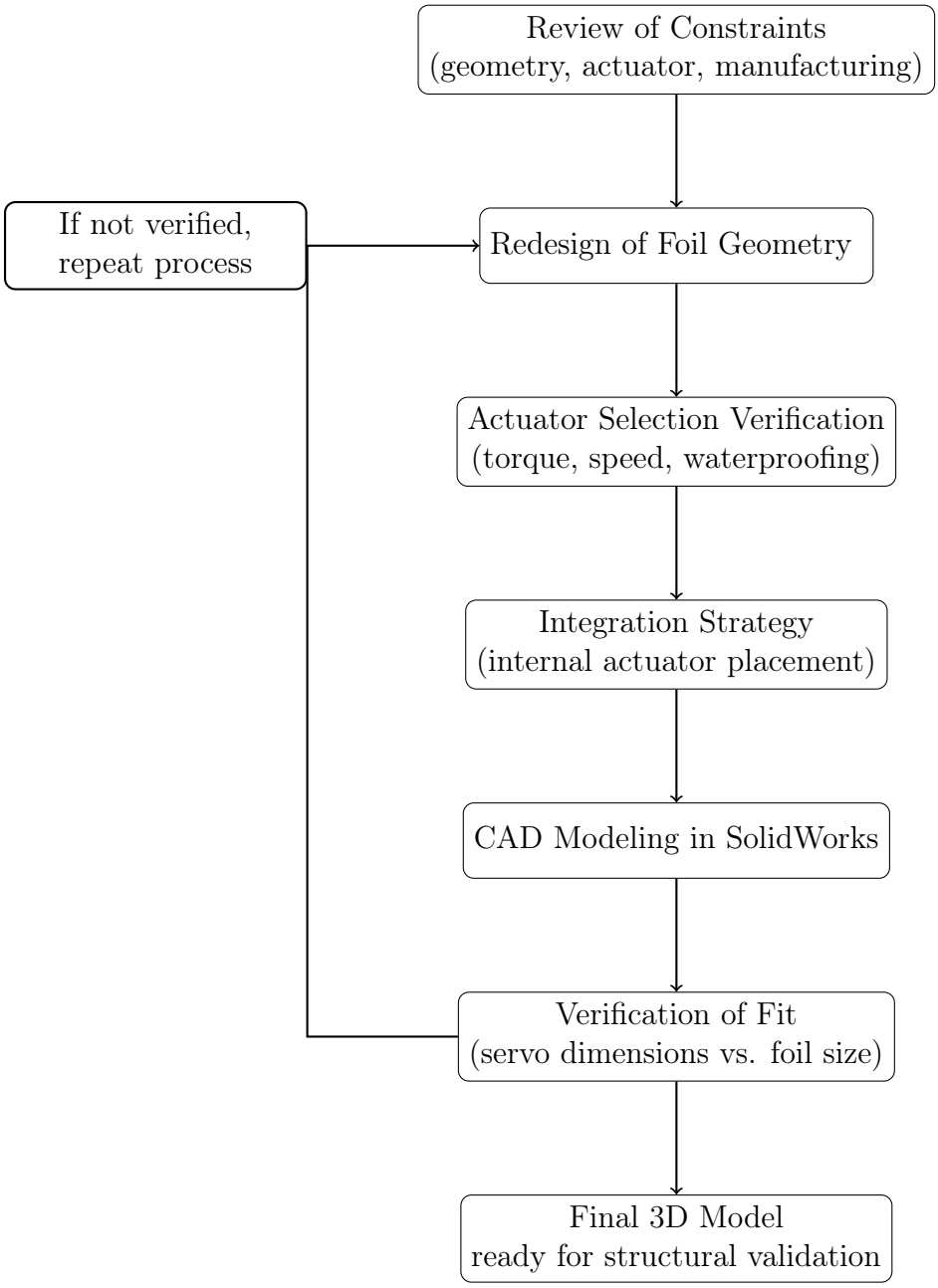

Figure 4.19: Iterative design workflow for Case 2 geometry and actuator integration.

Speer H005

The first strategy for redesigning the foil was based on modifying fundamental geometric and performance parameters, namely the supported weight, aspect ratio (AR) and chord length, with the aim of increasing the thickness of the profile. Since actuator integration requires a minimum internal thickness, the design space was systematically explored through several trial configurations. Some of the explored possibilities and their corresponding parameters are summarized in Table 4.5.

Table 4.5: Geometric parameters for different trial cases.

Try	Weight [N]	AR	Span (b) [m]	Chord (c) [m]	Thickness (t) [m]
1	40	6	0.137 402	0.030 534	0.001 527
2	80	6	0.194 316	0.043 181	0.002 159
3	160	6	0.274 805	0.061 068	0.003 053
4	40	4	0.112 189	0.037 396	0.001 870
5	160	4	0.224 377	0.074 792	0.003 740
6	160	2	0.158 659	0.105 772	0.005 289

The results indicate that varying either the supported weight or the aspect ratio does influence the foil thickness and other geometric parameters. However, the improvement is marginal. For moderate AR values (4-6), thicknesses remain between $1.5 - 3.7\,mm$. This is significantly below the minimum thickness required to accommodate an actuator, based on the actuator dimensions and structural clearance requirements.

Only when adopting extreme geometric configurations, such as reducing the aspect ratio to 2 while maintaining high loading, as it is shown in Try 6, does the thickness reach approximately $5.3\,mm$. While closer to the target, this value is still insufficient for reliable actuator installation and its achieved at the cost of severely disproportionate chord and span values. In such cases, the foil becomes over dimensioned, leading to high drag, reduced hydrodynamic efficiency and poor structural feasibility.

These findings suggest that the strategy of manipulating weight and aspect ratio within the Speer H005 geometry is not effective for achieving the required thickness. The gains in thickness are too limited, while the associated penalties in span and chord dimensions make the designs impractical.

In conclusion, despite extensive trials, this redesign pathway was deemed unsuitable. The inability to reach the target thickness without compromising the overall foil geometry indicates that alternative approaches must be pursued. Therefore, in the following section a different design strategy will be explored to address the integration of actuators in a more feasible manner.

Thickness Scaling About the Camber Line

Since the previous redesign strategy proved ineffective, an alternative approach was explored, thickness scaling about the camber line. This method involves modifying the thickness distribution of the foil while preserving the overall camber shape, with the goal of increasing structural robustness and accommodating internal components without altering the hydrodynamic characteristics of the foil.

To apply thickness scaling about the camber line there are several steps that need to be done.

1. Determine the Camber Line
   The first step was to calculate the camber line $y_c(x)$ of the original foil. Given the upper and lower surface coordinates (x_u, y_u) and (x_l, y_l), the camber line at each

chord wise location x is defined as shown in Equation 4.27.

$$y_c(x) = \frac{y_u(x) + y_l(x)}{2} \tag{4.27}$$

This provides a reference curve along which thickness modifications can be applied.

2. Compute the Original Thickness
Then the original thickness was calculated as shown in Equation 4.28.

$$t_{\text{original}}(x) = y_{\text{upper}}(x) - y_{\text{lower}}(x) \tag{4.28}$$

3. Calculate the Thickness Scaling Factor
Next, the scaling factor was determined based on the desired thickness $t_{\text{desired}}(x)$ as shown in Equation 4.29.

$$k(x) = \frac{t_{\text{desired}}(x)}{t_{\text{original}}(x)} \tag{4.29}$$

4. Compute the New Thickness
The original thickness was scaled by the factor $k(x)$ as presented in Equation 4.30.

$$t_{\text{new}}(x) = t_{\text{original}}(x) \cdot k(x) \tag{4.30}$$

5. Updated Upper and Lower Surface Coordinates
Finally, the new upper and lower surface coordinates were computed relative to the camber line as shown in Equations 4.31 and 4.32.

$$y_{\text{upper}}^{\text{new}}(x) = y_c(x) + \frac{t_{\text{new}}(x)}{2} \tag{4.31}$$

$$y_{\text{lower}}^{\text{new}}(x) = y_c(x) - \frac{t_{\text{new}}(x)}{2} \tag{4.32}$$

After following all the steps, the updated coordinates were used to generate a new foil sketch for evaluation.

Table 4.6 presents the resulting coordinates for the Speer H005 foil after applying the thickness scaling method with a scaling factor of 50%.

Table 4.6: Coordinates of the foil profile with thickness scaling.

x [m]	y + [m]	x [m]	y - [m]
0.030534	0	0	0
0.030229	0.000044	0.000382	-0.003934
0.029007	0.000253	0.000763	-0.005152
0.027480	0.000675	0.001527	-0.006401
0.024427	0.001696	0.002290	-0.007135
0.021374	0.003000	0.003053	-0.007645
0.018320	0.004516	0.004580	-0.008140
0.015267	0.006130	0.006107	-0.008301
0.012214	0.007563	0.007633	-0.008244
0.009160	0.008565	0.009160	-0.008015
0.007633	0.008794	0.012214	-0.007029
0.006107	0.008837	0.015267	-0.005640
0.004580	0.008650	0.018320	-0.004095
0.003053	0.008120	0.021374	-0.002679
0.002290	0.007576	0.024427	-0.001494
0.001527	0.006799	0.027480	-0.000589
0.000763	0.005483	0.029007	-0.000217
0.000382	0.004218	0.030229	-0.000038
0	0	0.030534	0

While Figure 4.20 shows the corresponding sketch generated in *SolidWorks*.

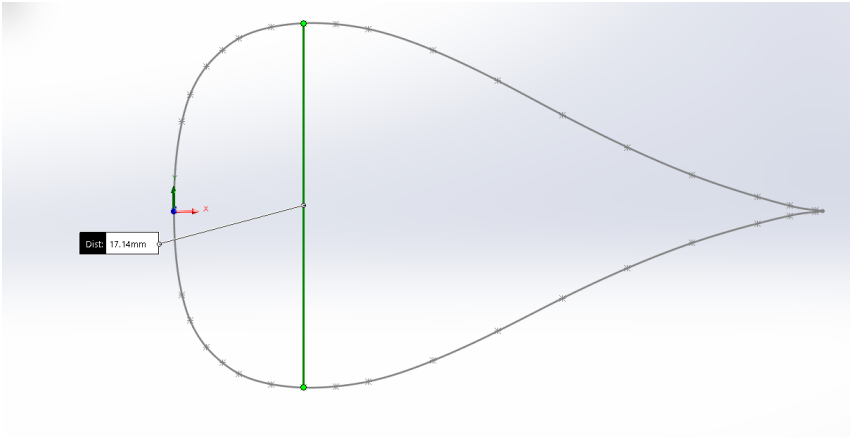

Figure 4.20: Speer H005 foil profile after thickness scaling about the camber line.

As illustrated in Figure 4.20, the resulting foil profile exhibits severe geometric distortions, particularly near the leading and trailing edges. These deformations make the profile poorly suited for hydrodynamic applications, as they compromise flow smoothness and increase the likelihood of undesirable turbulent separation. The extreme distortion arises primarily from the limited number of points defining the original foil, which amplifies errors when scaling thickness about the camber line. It is also necessary to highlight

that even with a scaling factor of 50% the maximum thickness is around 17 mm which is still not enough to house the servo, meaning that the scaling factor should be much higher to achieve the desired thickness. Consequently, the distortion would be even more prominent which makes this approach unsuitable for practical implementation.

Naca 2421

As all previous strategies proved unsuitable for the Speer H005 profile, the only remaining option was to select a foil profile that inherently offered greater thickness. This approach ensures sufficient structural robustness and allows for the integration of internal components without compromising the overall geometry. For this reason, the NACA 2421 profile was chosen, as it provides a naturally thicker section while maintaining favorable hydrodynamic characteristics suitable for the design requirements, its specifications are shown in the Appendix A.3.

In order to design this profile, the same requirements and procedures used previously to calculate the optimized model were applied, including all necessary steps such as the determination of the new lift coefficient C_l. The only modification was the introduction of a safety factor of 2, which effectively doubled the design load. Consequently, all calculations were performed for a vessel weight of $80\,Kg$ instead of the original $40\,Kg$, ensuring that the profile would maintain adequate performance and structural integrity under more demanding conditions.

Table 4.7 presents the final results of the foil design, including the key geometric parameters, calculated lift coefficients and thickness modifications. This summary allows for a clear comparison of the implemented design choices and their impact on performance.

Table 4.7: Dimensional and aerodynamic parameters of the redesigned foil.

Parameter	**Value**	**Unit**
Mass supported (m)	80	kg
Aspect ratio (AR)	6	–
Lift coefficient cruise ($C_{l,\text{cruise}}$)	0.794	–
Lift coefficient take-off ($C_{l,\text{takeoff}}$)	1.412	–
Span (b)	0.160	m
Chord (c)	0.120	m
Maximum thickness (t)	0.025	m

Version 1

After selecting the foil profile, the next step was to design the complete foil assembly. The first decision concerned the method for connecting the front section of the foil to the flap. Two potential approaches were considered. The first was analogous to a door hinge, in which a tube passes through both components to mechanically unite them. However, this solution was ultimately rejected, as it did not provide a sufficiently seamless connection, reducing its suitability for achieving optimal hydrodynamic performance.

The second option which was adopted is illustrated in Figure 4.21. In this design, the root of the flap functions as an outer tube that slides over the end of the front section, creating a smooth and continuous union between the two parts. This configuration not only simplifies assembly but also maintains a hydrodynamical clean profile, minimizing flow disturbances along the foil surface.

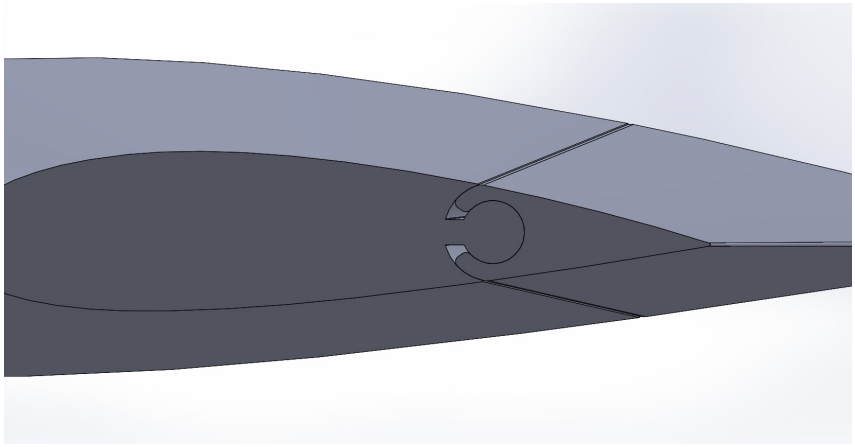

Figure 4.21: Connection between the front of the foil and the flap.

The next major challenge was the integration of the servo mechanism. This stage proved to be one of the most complex and time consuming aspects of the entire design process requiring numerous iterations and repeated attempts before a workable solution could finally be achieved. The main difficulty stemmed from the fact that the servo's axis of rotation had to be perfectly aligned with that of the flap. Furthermore, the servos available for this application were all single output devices, which meant that, in addition to positioning, a mechanical system was needed to connect all the flap sections so that they would rotate together as a single piece.

Another significant constraint was the available thickness of the foil. As mentioned previously, for the servo to function properly, it needed to be positioned along the same plane as the flap's rotational axis, which lies at approximately 35% of the chord length. In practice, this meant that even if there were regions of the foil where the servo could physically fit, the correct alignment with the rotation center could not be achieved.

To address this issue, and inspired by solutions found in other existing models, the first version of the redesigned foil was conceived. Its key characteristic was a modified central section, essentially formed by two overlapping foils placed with a slight offset as illustrated in Figure 4.22. This offset ensured that the maximum thickness region of the secondary foil was located closer to the center of rotation of the flap, thereby providing the necessary internal space for the servo while maintaining the correct alignment. Although this approach inevitably compromised the hydrodynamic profile, producing a bulkier midsection with a geometry that deviated from the ideal hydrofoil shape, it was considered an acceptable trade-off, as similar design choices could be observed in practical applications.

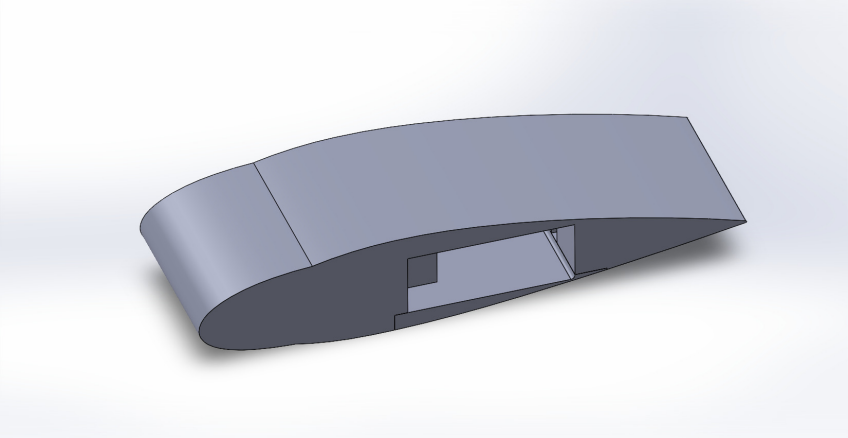

Figure 4.22: Version 1 middle part.

However, solving the alignment problem was only part of the challenge. Another equally demanding issue was the mechanical unification of the flaps across the span. Because the foil was designed with tapering, each flap section varied in size, further complicating the problem. Numerous solutions were explored, such as running a tube through all flap sections, as shown in Figure 4.23 or employing a servo with a larger output arm, but none of these proved feasible in practice. Figure 4.23 shows the most developed version of this model, however, as it can be seen, it is not a feasible model.

u 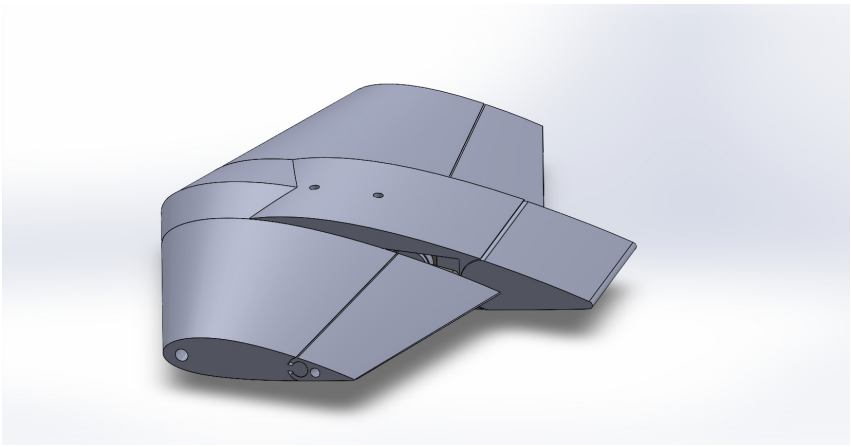

Figure 4.23: Version 1 foil.

Each attempt revealed new limitations, underscoring the complexity of integrating a reliable actuation system within the geometric and hydrodynamic constraints of the foil. Due to these limitations, it was decided to try a different approach which is developed in the next sections.

Version 2

From the many attempts made with the first version, it became evident that that approach was not a viable solution. The limitation in geometry, servo placement and flap unification could not be overcome within the original design framework. At this stage, inspiration was drawn from existing high performance designs, particularly the *Artemis eFoiler*, [64]. This vessel also integrates the servo actuator directly inside the foil, but instead of attempting to align the rotation axis of the servo internally with the flap, the connection is achieved through an external linkage mechanism located outside the foil surface, as shown in Figure 4.24.

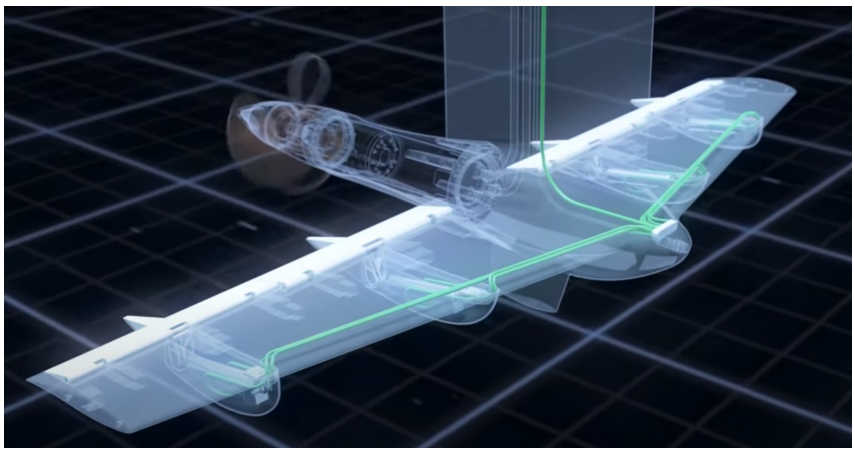

Figure 4.24: Artemis eFoiler, [65].

Adopting a similar concept for this project opened up new possibilities. By using an external linkage, the servo no longer needed to be constrained to the rotational center of the flaps. This freed the actuator to be positioned in regions of the foil where sufficient thickness existed to house it comfortably, without compromising structural integrity. At the same time, the linkage provided a reliable way to transmit motion to the flap, ensuring synchronized rotation while avoiding many of the geometric and spatial conflicts encountered in earlier design. An additional benefit of this approach was that it eliminated the need for a bulkier central region in the foil to accommodate the actuator at the rotation axis of the flap. Without this structural compromise, the overall foil shape could be kept thinner and smoother, resulting in a more hydrodynamical efficient profile.

Although the use of an external linkage introduced some hydrodynamic penalties, since any structure outside the foil inevitably increases drag, the trade-off was considered worthwhile. To mitigate these drawbacks and inspired once again by the Artemis eFoiler, a streamlined protective cover was designed to enclose the linkage. This cover served two key purposes, first, to soften the interaction of the external mechanism with the flow, reducing additional drag, and second, to protect the linkage system itself against water ingress and mechanical wear. With this refinement, the design achieved a more seamless integration of the actuation system, while still retaining the flexibility and practicality offered by external linkage. Overall, the solution struck a balance between hydrodynamic

efficiency and mechanical reliability, reflecting the same compromises often adopted in real world engineering practice.

This marked the transition toward the final design, where the lessons learned from previous iterations were consolidated into a configuration that combined actuation effectiveness, mechanical robustness and hydrodynamic performance.

4.4.4 Final Result

The final design represents the culmination of the iterative development process, integrating both hydrodynamic and mechanical requirements into a single functional geometry. The chosen foil profile, combined with the external linkage solution and streamline protective cover, enabled the servo to be effectively housed while maintaining a clean hydrodynamic shape. This configuration eliminated the need for oversized internal sections and ensured proper flap actuation along the full span. To translate this concept into a physical representation, the complete geometry was modeled in *SolidWorks*, where the foil, flap, actuator placement and linkage cover were systematically defined. This modeling stage was not only essential for visualizing the final solution but also to verify dimensional compatibility, mechanical clearances and overall manufacturability.

Base Geometry Generation

The starting point of the creation of the foil geometry was the second *SolidWorks* macro developed earlier in this project. This macro automated the import of coordinate values directly from the *Excel* file, ensuring that the chosen foil profile was accurately reproduced without manual errors. Using these coordinates, three sketches were generated along the span, one at the mid section, where the geometry matched the original profile data and two at the root and tip sections, which incorporated the taper effect. The taper was achieved by applying a scaling factor to the coordinates in these outer sketches, ensuring that the proportions of the foil were preserved while adapting the geometry to the desired planform. A representation of this base is represented in Figure 4.25.

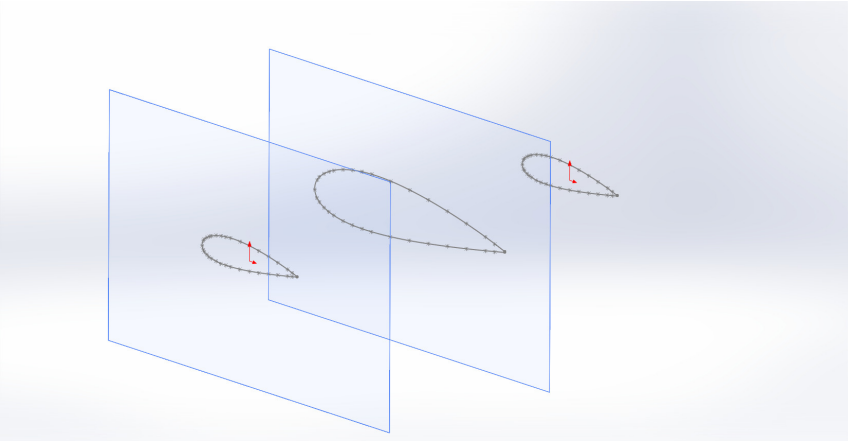

Figure 4.25: 3D rear foil base.

Front and Flap Section Generation

Building on the same geometry, the foil was divided into two distinct parts, the main front section and the flap section. Both were designed in a complementary manner so that, once assembled, the two components could fit seamlessly together while preserving the intended hinge connection. A detailed view of this interface is shown in Figure 4.26, highlighting the way the geometry was tailored to ensure proper alignment and smooth motion between the two sections.

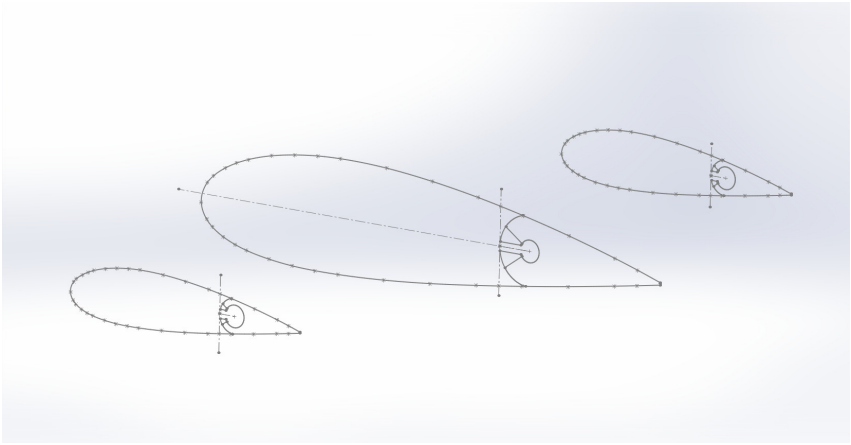

Figure 4.26: 3D rear foil connection sketch.

From the previously generated sketches at the root, mid and tip, separate loft operations were performed to create solid bodies for each part. This process ensured geometric continuity between the two while also enabling independent design considerations. By isolating the foil into these two lofted components, the model gained flexibility for further refinements, particularly assembly approaches. Figure 4.27 represents the assembly between these two lofted parts.

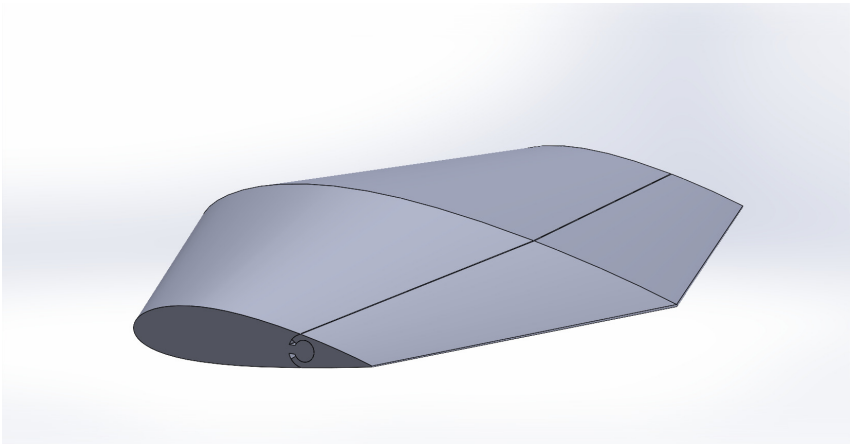

Figure 4.27: 3D rear foil front and flap assembly.

Servo Integration and Flap Horn Design

The next step in the modeling process involved the integration of the servo actuator into the front section of the foil. The servo was first represented as a CAD component, as shown in Figure 4.28, using manufacturer-provided files and then carefully positioned to match the required location within the foil.

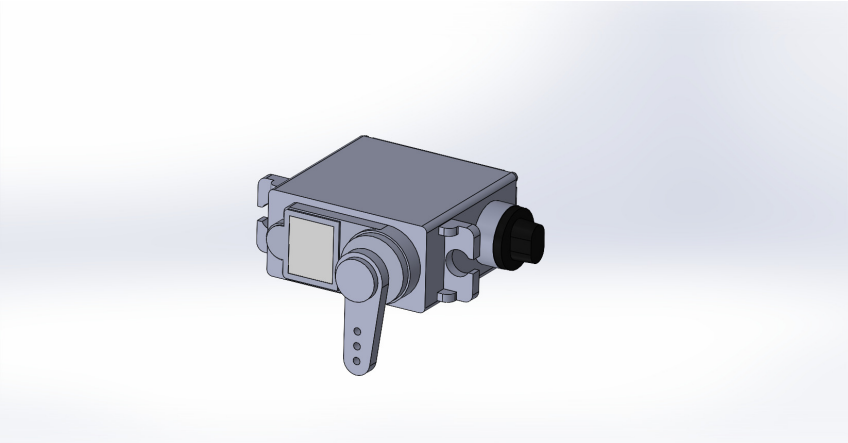

Figure 4.28: HS-5086WP CAD.

Once the servo was correctly placed, a cavity was created in the front section using the cavity command, ensuring sufficient clearance for installation and operation. Additional modifications were made to accommodate the servo, including the removal of certain fillets and the creation of access features to allow the insertion of the actuator into the cavity. The final result of these procedures is shown in Figure 4.29.

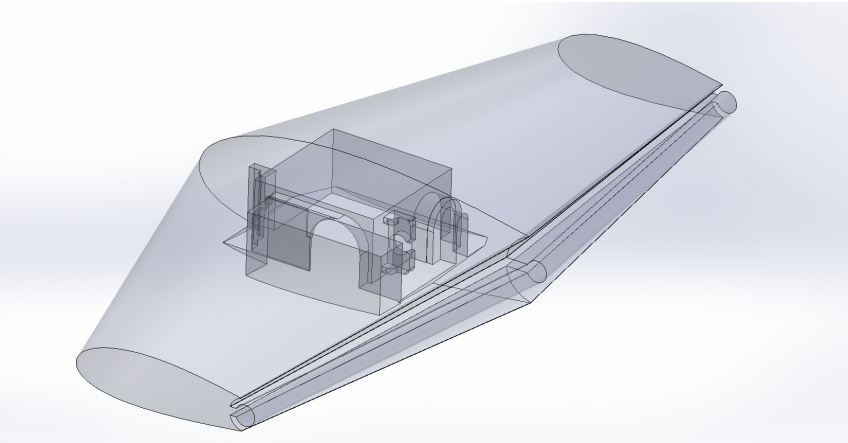

Figure 4.29: 3D rear foil cavity.

Following these, the flap horn was designed on the flap section to serve as the interface for the linkage connecting the servo to the flap. The horn was modeled using standard CAD operations such as extrusions, cuts and holes, providing a robust attachment point for the mechanical linkage and the final result is shown in Figure 4.30.

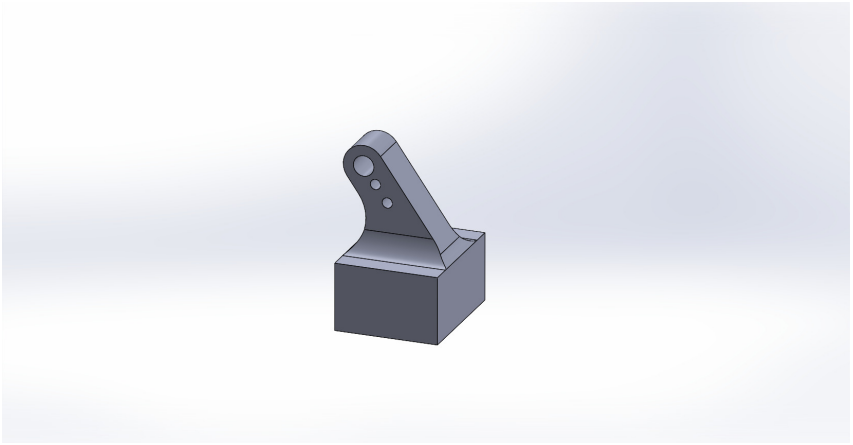

Figure 4.30: 3D horn control.

This step required careful considerations of the hydrodynamic loads and the mechanical advantages provided by the servo horn. To ensure proper flap control, the hinge moment induced by water forces was calculated and the required horn placement for the selected servo was determined, using the previous calculations and requirements.

The hinge moment M_{hinge} is generated by the hydrodynamic force on the flap, applied at the lever arm l from the hinge using Equation 4.33.

$$M_{hinge} = q \cdot A \cdot \Delta C_l \cdot l \tag{4.33}$$

Where $q = \frac{1}{2}\rho V^2$ is the dynamic pressure and ΔC_l represents the lift coefficient change induced by flap deflection, corrected by the flap effectiveness.

So, this way, the dynamic pressure at take-off can be calculated using Equation 4.34.

$$q = 0.5 \cdot 1025 \cdot 4.626^2 \approx 10.970\, Pa \tag{4.34}$$

The hinge moment is therefore given by the calculation in Equation 4.35.

$$M_{hinge} = 10.790 \cdot 0.00192 \cdot 0.9 \cdot 0.006 \approx 0.114\, N \cdot m \tag{4.35}$$

Next, the torque required from the servo is related to the hinge moment by the horn radius and mechanical efficiency, using Equations 4.36 and 4.37.

$$\tau_{servo} \cdot \nu \cdot \frac{d_f}{r_s} = M_{hinge} \tag{4.36}$$

$$d_f = \frac{M_{hinge}}{\tau_{servo} \cdot \nu} \cdot r_s \tag{4.37}$$

Where d is the distance of the horn from the hinge along the flap chord, which is calculated using Equation 4.38.

$$d_f = \frac{0.114}{0.3 \cdot 0.9} \cdot 0.01 \approx 0.0042\, m = 4.2\, mm \tag{4.38}$$

This approach allowed the servo and flap to be accurately aligned and mechanically connected, while preserving the structural and hydrodynamic integrity of the foil. Figure 4.31 illustrates the result, highlighting how the cavity and flap horn were implemented and refined to achieve proper actuation geometry.

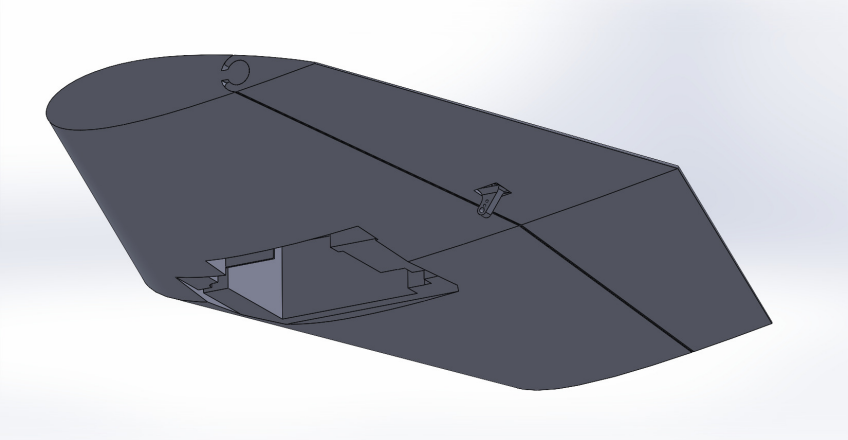

Figure 4.31: 3D rear foil with cavity and horn control.

Linkage Modeling Using 3D Sketch and Sweep

Once the flap horn and servo were properly defined, the mechanical linkage connecting the two components was modeled. Using the 3D sketch tool, key points were defined to create both the path and the cross sectional profile of the linkage. This allowed to precisely control the spatial orientation of the linkage in three dimensions, ensuring alignment with both the servo output and the flap horn.

After establishing the 3D path and profile, a sweep operation was performed to generate the solid geometry of the linkage. This method enabled the creation of a continuous and smoothly curved component that matched the desired mechanical motion while maintaining sufficient structural strength. Figure 4.32 shows the resulting 3D model that accurately represents the linkage geometry and could be incorporated into the entire assembly for further verification.

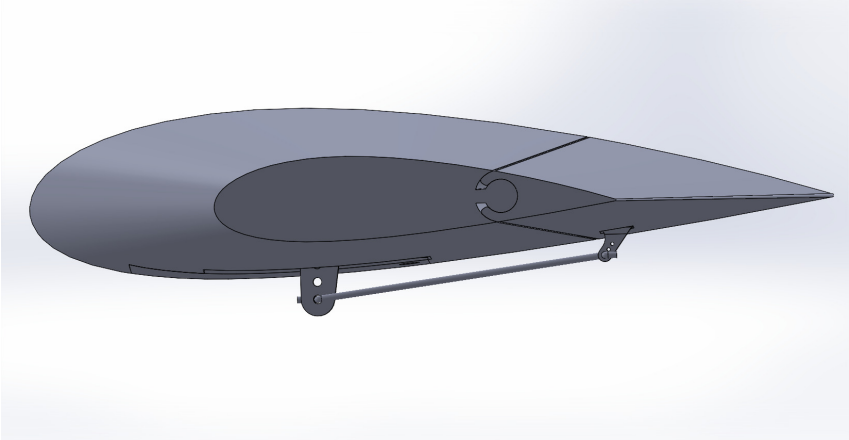

Figure 4.32: 3D rear foil with linkage.

Design of Lid and Protective Covers

The final step in the assembly involved designing the lid and protective covers for both the front section and the flap. In this phase, it was essential to account for the full range of motion of the flap, as well as the reach and clearance requirements of the servo actuator. To achieve this, sketches were first created to define the envelope of the covers, ensuring that they would not interfere with the servo or the flap during operation, as seen in Figure 4.33.

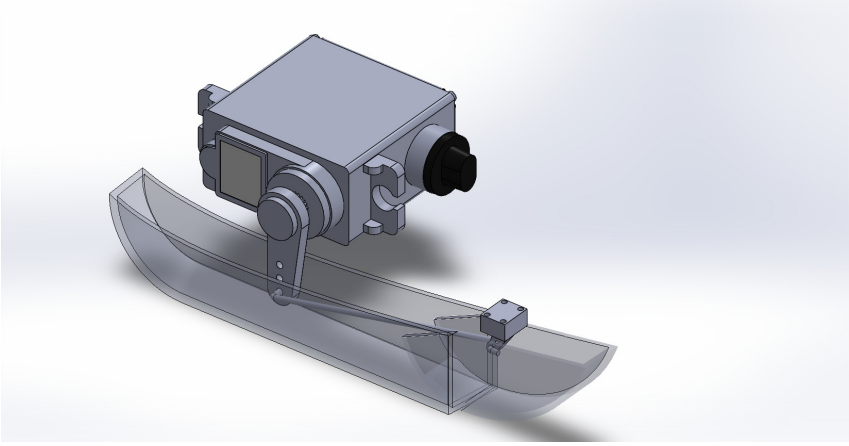

Figure 4.33: 3D rear foil with cover system.

For the front section, the sketch was then extruded and subsequently shelled to create a lightweight, hollow cover that protected the servo while maintaining minimal impact on the hydrodynamic profile. A similar process was applied to the flap section, producing a corresponding protective cover that enclosed the linkage and horn mechanism. These covers provided both structural protection and flow smoothing benefits, completing the mechanical integration of the actuator system while preserving the hydrodynamic performance of the foil and the final result is shown in Figure 4.34.

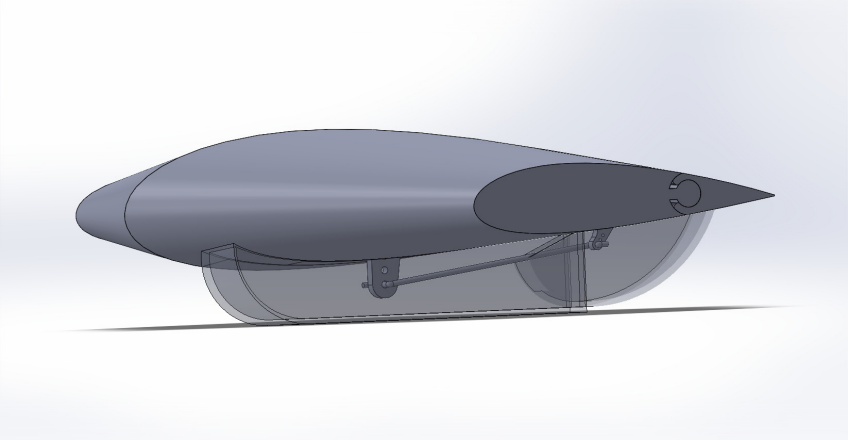

Figure 4.34: 3D rear foil with cover.

Final Result

Lastly, Figures 4.35 and 4.36 show the final redesigned geometry, where the foil and strut were assembled together. The assembly is part of the redesigned geometry and represents the outcome of all design steps carried out.

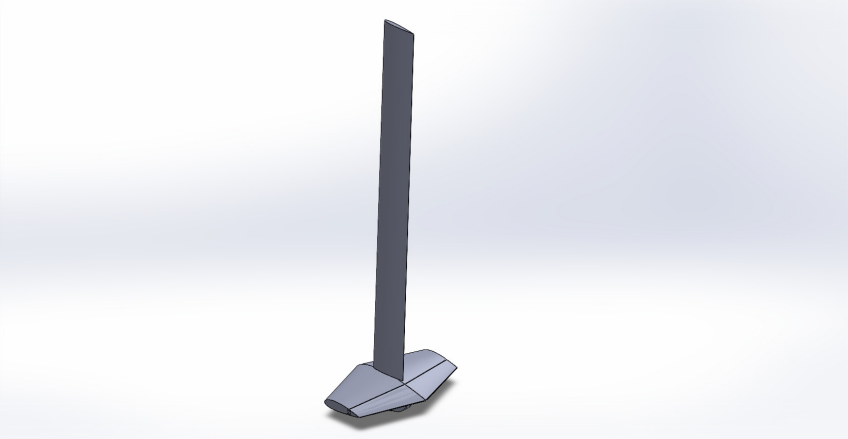

Figure 4.35: 3D rear foil final.

Figure 4.36: 3D rear foil final.

5

Structural Analysis

The structural analysis of the foil is a critical step in ensuring that the final design not only meets hydrodynamic requirements but also withstands the mechanical loads encountered during operation. This chapter presents the methodology and workflow used to evaluate the structural performance of the foil and strut, from the underlying design principles to the detailed finite element analysis (FEA). The analysis begins with a discussion of the general design considerations and the type of structural assessment performed, followed by a step by step presentation of the FEA workflow. Key aspects such as material properties, geometry preparation, element type selection, meshing strategies and the definition of boundary conditions and loading scenarios are addressed. Finally, a mesh refinement study is included to verify that the results are independent of discretization, ensuring the reliability and accuracy of the simulations.

5.1 Design Principles and Type of Analysis Performance

Before performing a structural analysis of a component, it is essential to define the primary design requirements that will guide both the interpretation of the results and the potential improvements. In the context of a foiling boat, one key consideration is the performance of the flight control system. Ideally, the strut should remain vertical to the horizontally positioned foil, which implies that bending and torsion must be minimized. Similarly, the foil must maintain its intended shape under operational loads to provide the desired lift while preserving structural integrity. The stiffness of both the strut and the foil is a critical factor, as higher stiffness generally improves control precision and performance. However, increasing stiffness often leads to higher weight, creating a need to carefully balance these parameters.

Another important aspect is the interaction between structural and hydrodynamic requirements. From a hydrodynamic perspective, a thin profile is desirable to minimize drag, whereas the strut and the foil must maintain a certain thickness to provide sufficient strength. The structural integrity of these components is equally crucial, as it must withstand all operational stresses without yielding or failing, as any structural failure could compromise both the foiling system and the safety of the vessel. Impact resistance is also relevant for safety considerations, although a detailed analysis of this aspect is planned for a later stage once the final configuration is established.

Weight remains a critical design parameter for foiling boats. Reducing the mass of the components is beneficial, provided that stiffness and strength are not compromised. In addition, practical aspects such as manufacturing complexity, production time and cost must be considered when defining the structural design. Collectively, these factors define the main parameters for the strut and foil, stiffness, strength, weight and manufacturability. These parameters often influence one another and their relative importance must be evaluated depending on the specific design objectives. In this study, the focus is compar-

ative, examining different configurations rather than establishing a definite prioritization.

It is important to note that, unlike many studies on foils and struts, computational fluid dynamics (CFD) analyzes are not part of the scope of this project. While CFD is commonly used to optimize hydrodynamic performance, this vessel is intended primarily as a test platform, where structural reliability takes precedence over maximizing lift or minimizing drag. The focus of this work is therefore on the structural behavior of the components, rather than their detailed hydrodynamic performance.

For the structural evaluation, a linear static analysis is employed. This is the most common type of finite element analysis (FEA) for structural components and is often sufficient for initial evaluations. Linear static analysis assumes that loads are applied slowly and remain constant over time and that the component has no motion or acceleration. The materials are considered to behave elastically, remaining within the linear elastic domain, so plastic deformation or failure does not occur under the applied loads. Within this regime, the stress and strain relationship follows Hooke's law, or its generalized form for three-dimensional stress states, providing a reliable approximation for the initial structural assessment.

5.2 Finite Element Analysis Workflow

The structural evaluation using finite element methods involves a series of organized steps to ensure accurate and reliable results. The process begins with preparing the geometry, which includes cleaning the model and removing small or unnecessary details, such as fillets, that do not contribute meaningfully to the analysis but could complicate meshing or increase computational cost. Once the geometry is ready, material properties are defined and assigned to each component, establishing the mechanical behavior of the system under applied loads.

Next, the model is discretized into finite elements, a process known as meshing, which divides the geometry into small, interconnected elements suitable for numerical analysis. When multiple bodies are present, the contacts and interactions between them must be specified, such as bonded surfaces or sliding interfaces, to accurately capture load transfer. Boundary conditions, including external forces, constraints and supports, are then applied to reflect the operational environment of the system. After the setup is complete, the solver computes the response of the structure under the defined loads.

Finally, post processing is conducted to evaluate the results, including stresses, deformations and other relevant quantities, and to verify that the simulation behaves as expected.

In Figure 5.1 is shown a schematic representation of the workflow.

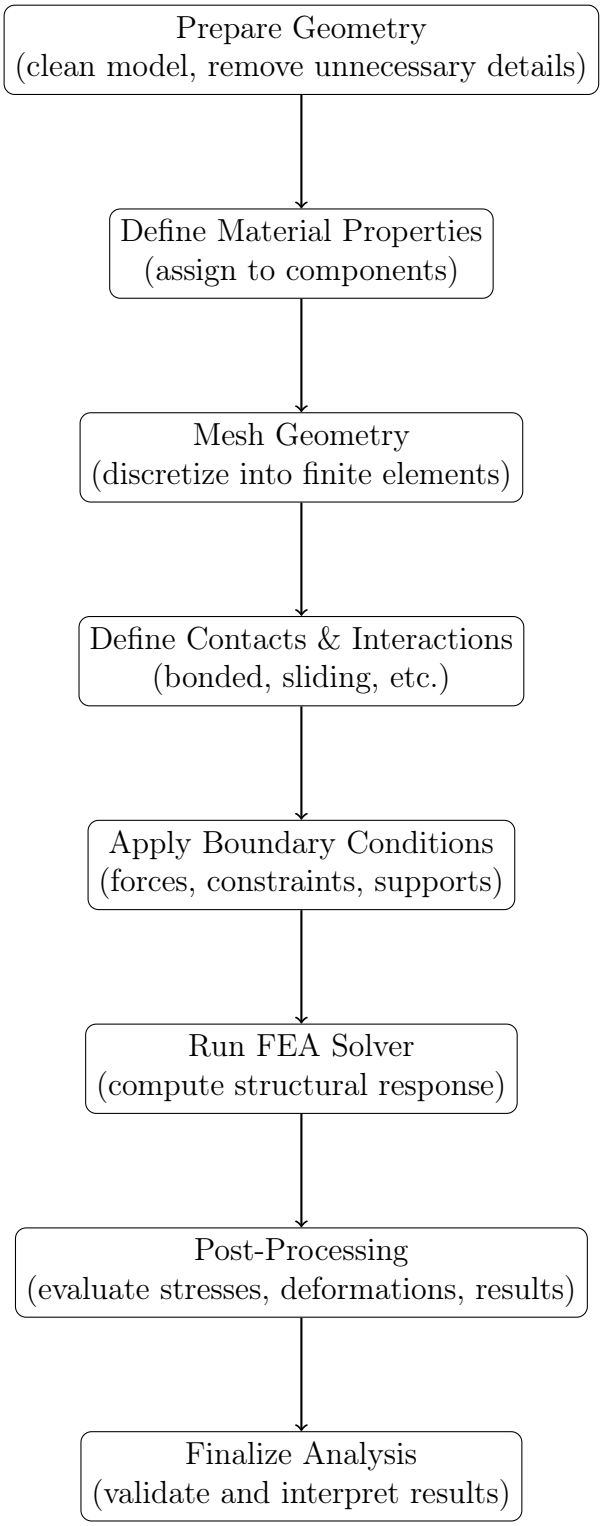

Figure 5.1: Workflow for Finite Element Analysis in Abaqus.

In this project, *Abaqus* was used as the primary FEA software. The tool allows detailed CAD geometries to be imported or created directly within the environment. After defining the materials and mesh, boundary conditions and loads are implemented in the simulation module, and the solver calculates the structural response. *Abaqus* also provides visualization and analysis tools to inspect results and confirm the validity of the model before drawing conclusions.

5.3 Material Properties

In this section, the material properties of the primary materials investigated in this study are presented and discussed. These include FDM printed PLA, forged carbon composite, 3D printed aluminum via bound metal deposition and press molded carbon fiber laminates. Each material exhibits different mechanical behavior depending on its manufacturing process, where each one is going to be discussed in the following sections.

5.3.1 3D printed PLA

Polylactic acid (PLA) is a widely used thermoplastic polymer in Fused Deposition Modeling (FDM) additive manufacturing due to its processability, biodegradability and satisfactory mechanical performance. In the FDM process, PLA is deposited layer by layer along a predefined raster pattern. This layered deposition introduces directionality in the microstructure, resulting in anisotropic mechanical behavior. Specifically, the material exhibits higher stiffness and strength along the filament deposition direction, corresponding to the raster orientation, compared to the transverse and through-thickness directions. The anisotropic response is primarily due to stronger bonding within deposited filaments and weaker inter-layer adhesion, which has been extensively documented in the literature, [66].

Ideally, the characterization of the mechanical response of PLA should involve experimental testing of printed specimens in multiple orientations, including the raster direction, perpendicular to the raster and through the thickness. Such tests would provide reliable values for the elastic modulus, shear modulus and Poisson's ratios in the principle directions. However, in the present study, access to the 3D printed specimens was not available and critical information such as raster orientation, layer thickness and potential void content could not be determined. Consequently, the material properties were estimated from values reported in the literature for fully dense PLA, so 100% infill components. While these estimates are theoretical, they provide a reasonable approximation of the anisotropy behavior for use in finite element modeling.

The elastic properties used in this study reflect directional stiffness variation due to the raster and layering effects. The density of the material was assumed to be $1240\,kg/m^3$. The elastic modulus along the raster direction E_1 was taken as $3.19\,GPa$, while the transverse modulus perpendicular to the raster E_2 and the through thickness modulus E_3 were $2.56\,GPa$ and $2.54\,GPa$, respectively. The Poisson ratios were assigned as 0.429 for ν_{12}, 0.285 for ν_{13} and 0.416 for ν_{23}. The shear moduli were set to $1.12\,GPa$ for G_{12}, $1.04\,GPa$ for G_{13} and $0.90\,GPa$ for G_{23}. These values were adopted directly from

the literature and although the experimental is preferable, they provide a reasonable theoretical representation of the anisotropic behavior of PLA for use in finite element modeling. A summary of the values used is shown in Table 5.1, [67].

Table 5.1: Orthotropic properties of FDM-printed PLA.

Property	**Value**	**Units**
Density (ρ)	1240	kg/m^3
E_1	3.19	GPa
E_2	2.56	GPa
E_3	2.54	GPa
ν_{12}	0.429	–
ν_{31}	0.227	–
ν_{13}	0.285	–
ν_{23}	0.416	–
G_{12}	1.12	GPa
G_{13}	1.04	GPa
G_{23}	0.90	GPa

For finite element implementation, PLA was modeled as an orthotropic material using the above engineering constants, enabling the capture of the directional stiffness effects induced by the FDM process. Although experimental validation would enhance the accuracy of stress distribution predictions and allow for detailed analysis of potential failure mechanisms, the theoretical approach adopted is sufficient for preliminary structural evaluations and comparative studies. The limitations of this approach, primarily due to the absence of detailed manufacturing parameters and experimental data, are acknowledged, but the selected material properties are consistent with the established behavior of FDM printed PLA and are supported by the cited literature.

5.3.2 Forged Carbon

Forged carbon, also known as chopped carbon fiber molding compound is a composite material comprising short, randomly oriented carbon fibers embedded in a thermosetting resin matrix. Unlike traditional continuous fiber composites, forged carbon exhibits a heterogeneous microstructure due to the random distribution of fibers. This randomness introduces complexities in predicting its mechanical behavior, as properties are influenced by factors such as fiber length, volume fraction and resin system, [32] [30].

Experimental studies show that the mechanical properties of forged carbon are sensitive to the manufacturing process and the specific materials used. For instance, variations in fiber tow size and content can significantly affect tensile strength and modulus, with smaller tow sizes generally leading to more homogeneous and higher mechanical properties. Additionally, the molding process, including temperature and pressure conditions, plays a crucial role in determining the final material characteristics, [34].

However, comprehensive and standardized data on the mechanical properties of forged carbon are limited. The heterogeneous nature of the material and the proprietary aspects

of its manufacturing process contribute to this gap in knowledge. As a result, assigning reliable anisotropic or isotropic properties for finite element modeling is challenging without specific experimental data.

In the absence of such data, one conservative approach is to consider the properties of the resin matrix alone. While this ensures that the performance of the material is not overestimated, it under represents the actual stiffness and strength provided by the carbon fiber reinforcement. Therefore, for the purposes of this study and in line with best practices in materials engineering, it is deemed that the available information is insufficient to accurately model the mechanical behavior of forged carbon without experimental validation.

5.3.3 3D Printed Aluminum

Metal deposition manufacturing of aluminum can be achieved through Bound Metal Deposition (BMD), also known as metal fused deposition modeling (metal FDM). In this process, aluminum powder is blended with a polymer binder to create a filament or feedstock, which is then extruded layer by layer in a manner analogous to polymer FDM printing. The result of this stage is a fragile "green part" consisting of both metal particles and binder material, [25] [26].

To obtain a functional metallic component, the green part undergoes a two step post-processing sequence. First, a debinding stage removes most of the polymer binder, leaving behind a porous intermediate structure known as the "brown part". Second, this brown part is subjected to high temperature sintering, where the aluminum particles densify and form metallurgic bonds. During sintering, the original layer structure becomes indistinct as porosity is reduced and inter particle diffusion consolidates the material. Unlike polymer based additive manufacturing, which typically exhibits strong anisotropy due to weak inter layer bonding, sintered metals produced by BMD can be treated as isotropic materials, since the final microstructure does not preserve the anisotropic features of the printed green part, [24] [68] [69].

For the purposes of finite element modeling in this study, the aluminum was therefore assumed to be isotropic, with engineering constants consistent with standard wrought and sintered aluminum alloys such as Al 6061 and Al 7075. The adopted values are shown in Table 5.2, [70].

Table 5.2: Isotropic material properties of 3D printed aluminum, [70].

Property	**Value**	**Units**
Elastic Modulus (E)	70	GPa
Poisson's Ratio (ν)	0.33	–
Density (ρ)	2700	kg/m^3

These parameters provide a reliable baseline for structural simulations and are consistent with values reported in the literature for consolidated aluminum alloys.

By revisiting the manufacturing process and recognizing the homogenizing effect of sintering, it is clear that aluminum produced through BMD can be effectively modeled

as an isotropic material. This approach simplifies finite element implementation without compromising accuracy.

5.3.4 Carbon Fiber Laminate

Press molded carbon fiber laminates are manufactured by stacking multiple layers of unidirectional or woven carbon fiber sheets impregnated with a polymer matrix, typically epoxy, followed by consolidation under heat and pressure. This process yields a high performance composite with strong anisotropy, as stiffness and strength vary significantly depending on the fiber orientation relative to the applied load. In particular, mechanical properties along the fiber direction are an order of magnitude higher than those in the transverse and through thickness directions, due to the dominance of the stiff, continuous carbon fibers over the comparatively weaker polymer matrix, [34] [35].

The degree of anisotropy is determined by fiber type, matrix properties, fiber volume fraction and laminate lay-up sequence. To characterize such composites accurately, experimental tests on molded specimens are required, including tension (ASTM D3039), shear (ASTM D3518) and inter laminar strength tests. These tests allow for precise identification of ply level properties such as elastic moduli, shear moduli and Poisson's ratios, as well as validation of the overall laminate behavior. However, due to the lack of access to experimental specimens and specific lay-up information in this study, the material properties were instead estimated from literature values for epoxy composites, which are widely reported in data sheets and academic studies, [71] [72].

For finite element modeling, the material was represented as an orthotropic lamina with the following properties, an elastic modulus along the fiber direction of $E_1 = 130$ GPa, transverse and through-thickness moduli of $E_2 = E_3 = 10$ GPa, shear moduli of $G_{12} = 4.5$ GPa, $G_{13} = 4.5$ GPa, and $G_{23} = 3.5$ GPa, Poisson's ratios of $\nu_{12} = 0.28$, $\nu_{13} = 0.28$, and $\nu_{23} = 0.50$, and a density of $\rho = 1600$ kg/m^3. These properties are consistent with typical values for carbon fiber reinforced epoxy systems. Table 5.3 summarizes these values.

Table 5.3: Orthotropic material properties of press-molded carbon fiber epoxy laminates.

Property	**Value**	**Units**
Density (ρ)	1600	kg/m^3
Elastic Modulus E_1	130	GPa
Elastic Modulus E_2	10	GPa
Elastic Modulus E_3	10	GPa
Poisson's Ratio ν_{12}	0.28	–
Poisson's Ratio ν_{13}	0.28	–
Poisson's Ratio ν_{23}	0.50	–
Shear Modulus G_{12}	4.5	GPa
Shear Modulus G_{13}	4.5	GPa
Shear Modulus G_{23}	3.5	GPa

Although the use of datasheet and literature values provides a reasonable theoretical estimate of the anisotropy response of carbon fiber laminates, the absence of experimental validation introduces limitations. Experimental testing would not only improve the accuracy of stress and strain predictions, but also enable the assessment of inter laminar properties, defect sensitivity and failure mechanisms. Nonetheless, the selected parameters reflect the established performance range of press molded epoxy laminates and provide an adequate basis for comparative finite element simulations.

5.4 Analysis Preparation

Before running the finite element simulations, a systematic preparation was carried out to ensure that the results would be both reliable and representative of the real structural behavior. This stage involved several key tasks as mentioned previously, beginning with the definition and simplification of the geometry, followed by the assignment of the material properties previously described. Next, appropriate element types and meshing strategies were selected to balance accuracy with computational efficiency. The models were then constrained and loaded to reflect realistic operating conditions and finally, a mesh refinement study was performed to verify that the results were not dependent on mesh size. Together, these steps established a consistent framework for the numerical analysis and laid the foundation for meaningful comparison across for the different case studies.

5.4.1 Geometry Definition and Preparation

Two different foil geometries were considered in this study, the optimized design, which resulted from the initial hydrodynamic and structural optimization process and the redesigned geometry, developed later to address integration requirements. Both models were created in *SolidWorks* and subsequently exported as STEP files for import into *Abaqus*, ensuring compatibility between the CAD environment and the finite element software.

Once imported, the geometries were carefully prepared for analysis. This step involved removing all non essential features, such as fillets, small holes and cavities, that were not expected to contribute significantly to the global structure response. Such details can unnecessarily increase mesh density and computational cost, while introducing potential numerical instabilities. By simplifying the models, the analysis could focus on the key structural characteristics without compromising accuracy at the scale of interest.

A critical modeling decision had to be made at this stage due to extreme slenderness of the foils. Both geometries, and in particular the optimized one, had maximum thickness on the order of $2\,mm$. Performing the analysis using homogeneous solid elements under these conditions was deemed impractical, solid meshes would either require excessively fine elements, leading to prohibitive computational effort, or risk producing distorted elements with unreliable results. To overcome this challenge, the models were converted to shell representations, which are far more suitable for thin walled structures. This was achieved by extracting the mid surfaces of the components and then applying a zero offset definition in *Abaqus*, thereby ensuring that the structural stiffness was correctly captured

without artificially thickening the geometry. The resulting shell model of the front part of the foil is illustrated as an example in Figure 5.2.

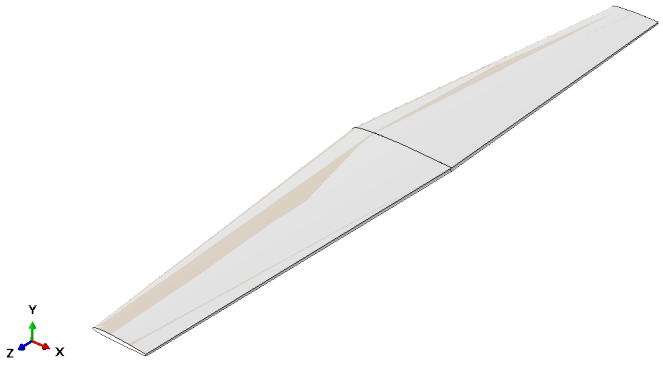

Figure 5.2: Front part shell.

The choice to adopt shell modeling was strongly justified. From a structural mechanics standpoint, shells provide a more accurate and efficient representation for thin geometries where one dimension, in this case the thickness, is much smaller than the other two. They allow stresses and deformations to be captured realistically while avoiding the drawbacks of solid element discretization in such cases. Furthermore, using shell elements significantly reduces the total number of elements required, improving computational efficiency and enabling more detailed mesh refinement where needed.

In summary, the geometry preparation process involved simplifying the CAD models to eliminate unnecessary details, followed by a transformation into shell based representations to address the challenges posed by the very thin foil profiles. This approach ensured that the models remained computationally efficient while still capturing the essential structural behavior required for a meaningful comparison between the optimized and redesigned geometries.

5.4.2 Material Assignment

After the geometry was prepared as mid surface shell models, the next step was the definitions and assignment of the material properties in *Abaqus*. Three materials were considered across the case studies PLA, aluminum and carbon fiber composite. These options were chosen to represent a wide spectrum of manufacturing possibilities, ranging from rapid prototyping to high performance composite construction.

Due to the choice of transforming the components into shell models, this stage also served to assign the components their thickness. In order to accomplish this, the thickness of each component was explicitly defined when assigning the materials to the corresponding shell surfaces. As mentioned previously, the thickness of the foil varies significantly along both the span and the chord, however, for modeling purposes in *Abaqus*, the maximum thickness was assigned uniformly to its shell surfaces, as this was the only practical approach. The same procedure was applied to all components and models, with their

respective maximum thickness used for the shell surfaces, ensuring that the assigned material properties reflected the overall physical dimensions of each part.

For instance, the optimized foil has a maximum thickness of $2\,mm$, which was directly applied as the thickness of its shell surfaces. The same procedure was followed for all other components and models, ensuring that the assigned material properties reflected the physical dimensions of each part.

PLA was modeled as an anisotropic polymer, since its mechanical response is known to depend strongly on the raster orientation and layer deposition in the FDM process. However, because experimental testing of the printed specimens was not possible and no information was available on the specific infill, layer thickness or print orientation, the material was defined using only typical orthotropic elastic properties reported in the literature. This approach allowed directional stiffness differences to be included in the model while acknowledging that exact values would depend on the actual print parameters.

In contrast, the aluminum parts were modeled as isotropic materials. In the metal FDM process, the "green part" undergoes debinding and sintering, during which the powder consolidates and the layer structure effectively disappears. As a result, the mechanical response of the final component can be approximated as uniform in all directions. The aluminum was therefore assigned bulk isotropic properties consistent with sintered aluminum alloys such as AL6061, using the Young's modulus, Poisson's ratio and density as the defining parameters.

Finally, the carbon fiber laminates were modeled as anisotropic composite materials. Here, a more detailed ply-level definition was employed. The laminate was assumed to consist of ten plies, each with a thickness of $0.2\,mm$, stacked in a $[0°, 90°, 0°, 90°, ..]$ lay-up sequence. Unlike quasi isotropic laminates that include $\pm 45°$ orientations, only $0°$ and $90°$ plies were included. This choice was motivated by manufacturing considerations, under the necessary pressure, ± 45 layers could deform or distort the geometry of the component and since experimental validation was not possible, the more conservative $0°/90°$ sequence was adopted. This still allowed the strong anisotropy of the laminate to be captured in the model, while avoiding unrealistic assumptions about the manufacturability of more complex layups.

In all cases, the materials were linked to homogeneous shell sections in *Abaqus*. Since the geometry had been converted to mid surfaces, the assigned shell thicknesses directly represented the real wall thickness of the structural components. This step was crucial for preserving stiffness and mass distribution, as bending rigidity in thin shells scales with the cube of the thickness.

In summary, the material assignment strategy balanced accuracy and practicality, PLA was modeled as orthotropic but based on literature values rather than experimental data, aluminum was treated as isotropic due to the sintering process and carbon fiber laminates were defined with a ply based orthotropic layup of $[0°, 90°]$ plies. This framework captured the essential mechanical behaviors of the materials within the limitations of available data and provided a consistent basis for comparing their structural performance.

5.4.3 Element Type Selection and Meshing Strategy

Once the geometry and materials were prepared, an appropriate element type and meshing strategy were established to accurately capture the structural behavior of the foils and struts while maintaining computational efficiency. The majority of the models were discretized using S4 elements, which are 4-node, quadrilateral, general purpose shell elements suitable for thin walled structures. These elements offer robust performance under bending and membrane loads, making them ideal for the main surfaces of the foils and struts.

In regions where the geometry was too slender or irregular to accommodate quadrilateral elements effectively, such as lateral edges or transitional zones, S3R elements were used. These are 3-node triangular shell elements with reduced integration, which allow the mesh to conform to narrow or complex surfaces without introducing excessive element distortion. The combination of S4 and S3R elements ensured that the mesh could accurately represent both the main structural surfaces and the challenging geometrical features without compromising numerical stability.

To further improve the meshing quality and control, the foil was partitioned into four regions, left and right in the vertical direction and superior and inferior in the horizontal direction. As for the strut it was partitioned into two regions, left and right in the vertical direction. This division facilitated a more uniform element distribution, allowed for local refinement where it was required and supported a structured meshing approach in areas where stress gradients were expected to be higher. It also simplified the assignment of boundary conditions and the management of different material sections, particularly in regions with varying thickness or cross sectional properties.

The mesh density was not uniform across the components but varied according structural and geometric considerations. A biased mesh was applied along the chord of the foil, with finer elements concentrated toward the leading edge and trailing edge, where higher stress concentrations and bending moments were expected. This approach ensured that the solver could resolve critical gradients without unnecessarily increasing the total element count in low stress regions, balancing accuracy with computational efficiency.

In summary, the choice of S4 elements for the main surfaces, supplemented by S3R elements in thin or complex regions, combined with strategic partitioning and a biased mesh density, provided a robust framework for accurately capturing the structural response of the hydrofoil components. This strategy laid the foundation for subsequent analysis steps, including condition application and mesh refinements studies, while maintaining computational tractability across all case studies.

5.4.4 Contacts and Interactions

In the finite element model, the interactions between different components of the hydrofoil assembly were carefully defined to ensure that the overall structural response was captured accurately. The primary interfaces considered were those between the strut and the front section of the foil, as well as between the front section of the foil and the flap.

For both of these interfaces, tie constraints were applied in *Abaqus*. This means that the nodes of one surface were rigidly connected to the corresponding nodes of the adjacent surface, preventing any relative motion between them. The use of tie constraints simplified the interaction modeling while ensuring that load transfer between components was accurately represented. Specifically, the connection between the strut and the foil front allowed bending and torsional loads to propagate naturally into the foil, while the tie between the foil front and the flap maintained structural continuity across the control surface.

It is important to note that the tie constraint between the foil front and flap represents a simplification of reality. In a fully detailed analysis, a more complex contact formulation could allow limited relative motion or local deformation at the hinge or connection region. However, the focus of this study was on the global structural behavior of the foil assembly rather than detailed local contact mechanics. By modeling the front-flap interface as tied, the simulations efficiently captured the stiffness and load bearing behavior of the combined structure without introducing additional nonlinearities or convergence challenges associated with contact interactions.

This approach ensured that the hydrofoil components behaved as a single, cohesive structural system under the applied loads, providing meaningful insight into the overall performance of the assembly while keeping the model computationally tractable.

5.4.5 Boundary Conditions and Loading Scenarios

The finite element model of the hydrofoil assembly was constrained and loaded to represent realistic operational conditions while maintaining simplicity for comparative purposes. The only boundary condition applied in the simulations was a fixed boundary condition at the top of the strut, effectively fixing all translations and rotations at this point. This choice reflects the attachment of the strut to the supporting structure or hull and provides a stable reference for evaluating the structural response of the foils.

Four distinct load cases were considered, each representing different magnitudes and distributions of hydrodynamic forces acting on the hydrofoil. These load cases were derived from the expected operational loads of the boat and the relative weight it supports, as illustrated in the schematic Figure 5.3 provided.

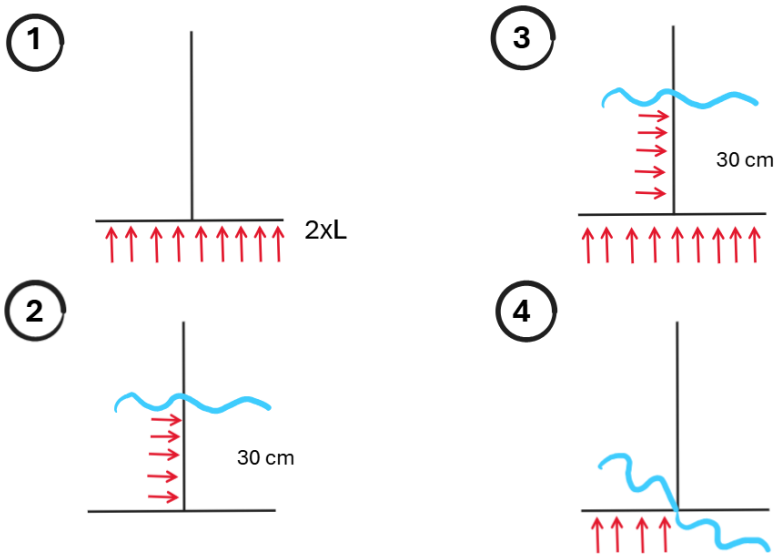

Figure 5.3: Load cases.

1. Load Case 1- Uniform Vertical Load
   In this scenario, the foil is subjected to a uniform vertical load equivalent to two times the total weight of the boat, distributed along the span. This load represents extreme operational conditions, including sudden acceleration or dynamic load amplification during maneuvers. The magnitude of the load per unit length was computed as shown in Equation 5.1.

$$p = \frac{L}{S} = \frac{32.7}{0.0031} = 10392.25534\ Pa \tag{5.1}$$

   Where S is the area of the single foil. Then the load magnitude is doubled, corresponding to Equation 5.2.

$$p = 2 \times 10392.25534 = 20784.51068\ Pa \tag{5.2}$$

   This load represents a conservative scenario for structural safety, capturing the combined effects of high speed operation and potential hydrodynamic load spikes. It helps evaluate the ability of the foil to withstand peak bending moments and ensures that the design maintains sufficient safety margins. It was simply computed in *Abaqus* using the pressure type load and the corresponding amplitude.

2. Load Case 2- Lateral Hydrodynamic Load

   This case represents the side force effects due to yaw maneuvers or cross flow currents. The load acts horizontally on the submerged part of the strut. A uniform horizontal pressure distribution was assumed over the wet area of the strut up to a

depth of 30 cm from the base. To mimic this load it was firstly used the hydrostatic pressure feature from *Abaqus*. Then it was computed the hydrodynamic pressure which the amplitude was calculated through Equation 5.3.

$$p = \frac{1}{2} \times \rho \times v_{takeoff}^2 \times C_l = 3887.956222\ Pa \tag{5.3}$$

For the hydrodynamic pressure similar steps as the ones done in the previous load cases were performed but this time in the strut region.

3. Load Case 3- Vertical Uniform Load and Lateral Hydrodynamic Load

   The third load case represents the most critical operational condition by combining the vertical uniform load of Load Case 1 with the lateral hydrodynamic load of Load Case 2. This superimposed scenario captures simultaneous vertical and lateral stress, which can occur during aggressive maneuvers at high speed or when the foil experiences sudden cross currents while supporting the weight of the vessel.

   In practice, the vertical pressure distribution was applied along the foil span as defined in Load Case 1, while the lateral hydrodynamic pressure was applied on the strut surface as defined in Load Case 2. Both loads were introduced in *Abaqus* and activated in the same step to simulate realistic operating conditions.

   This case was considered the most critical because it leads to maximum combined bending and torsional stresses within the foil strut system. Evaluating this condition provides a conservative assessment of structural performance and ensures that the design can withstand realistic worst case scenarios. The simultaneous action of vertical lift and lateral force generates complex stress states that are more severe than those produced by individual load cases, thus defining the ultimate safety margins for the structure.

4. Load Case 4- Partial Vertical Load
   The final case replicates the situation where part of the foil emerges from the water, as often seen in high performance sailing vessels. This occurs due to foil retraction systems or during maneuvers when the boat rises significantly above the water surface. In this case, the same pressure values as in Load Case 3 were used, but they were applied only to the portion of the foil that remained submerged. This mimics the loss of support area as the foil exits the water, leading to asymmetric loading and potentially higher localized stresses. In *Abaqus*, this was implemented by selecting only the submerged surfaces of the foil and applying the pressure condition there. The diagonal waterline condition shown in the schematic representation was approximated by restricting the loaded surface region. This load case provides insight into the performance of the foil and strength when subjected to uneven immersion, ensuring the design remains robust under dynamic sailing conditions.

These four load cases together provide a comprehensive evaluation of the structural response of the hydrofoil under both nominal and extreme operational conditions. By

combining a fixed boundary condition at the strut top with vertical and distributed hydrodynamic forces, the model captures the key bending and torsional effects, ensuring that stress concentrations, deflections and overall structural behavior can be accurately compared across the different materials and geometries.

5.4.6 Mesh Refinement Study

As discussed previously, carrying out a mesh refinement study is essential to verify wether the results converge as the characteristic element size decreases, while also finding a balance between accuracy and computational cost. Since the finite element models used for the different configurations are different, the optimize and the redesigned model, the refinement study was performed in both designs.

To evaluate mesh convergence, a refinement study was carried out by varying the number of seeds assigned to each component of the model, rather than prescribing a single characteristic element size. This approach resulted in different node and element counts for each refinement level.

The optimized version was analyzed with meshes ranging from 3184 to 17499 nodes. Computational times increased accordingly, from only $0.6\,s$ for the coarsest mesh to $3.9\,s$ for the finest. The maximum displacement magnitude decreased slightly with refinement, starting at $13.75\,mm$ and converging toward $13.09\,mm$. On the other hand, the maximum compressive stress rose from $10.29\,MPa$ to $12.31\,MPa$, with progressively smaller changes between successive refinements, indicating convergence. All the results are shown in Table 5.4.

Table 5.4: Mesh refinement results for the optimized model.

Number of Nodes	**Number of Elements**	**Computational Time [s]**	**Maximum Displacement [mm]**	**Maximum Compression [MPa]**
3184	3259	0.6	13.7525	10.2878
10194	10300	2.2	13.5889	11.5497
17499	17619	3.9	13.5728	12.3127

For the redesigned model, three refinements were studied, producing models with 8.348 to 25.468 nodes. Computational effort ranged from 1.7 to 8.2 seconds. The displacement magnitude remained practically constant across all refinements, around $0.258mm$, suggesting that further refinement negligible impact on this result. The maximum compressive stress increased modestly from $0.479\,MPa$ to $0.546\,MPa$, again showing stabilization as the mesh became finer. All the results are shown in Table 5.5.

Table 5.5: Mesh refinement results for the redesigned model.

Number of Nodes	Number of Elements	Computational Time [s]	Maximum Displacement [mm]	Maximum Compression [MPa]
8348	8618	1.7	0.258113	0.478747
18503	19190	5.2	0.257866	0.530393
25468	26414	8.2	0.258416	0.545859

In both models, displacements showed very limited sensitivity to refinement, confirming their reliability across different mesh densities. The compressive stresses increased moderately with refinement, but the variations diminished progressively, which demonstrates convergence. However, the computational demand grew significantly for the densest meshes, particularly in the optimized configuration. Consequently, intermediate refinement levels represent the best compromise, providing accurate results within acceptable computational times.

5.4.7 Organization of the Study Cases

To comprehensively assess the mechanical behavior and performance of different manufacturing approaches and design optimizations, all cases were systematically organized based on model type and load condition. This structured approach enabled a thorough comparative analysis, ensuring that each variable, both manufacturing methods and applied loads could be evaluated consistently.

As mentioned previously, each of the four models was subjected to the four loading cases. For clarity and traceability, each case was assigned a unique identifier combining the model type and the load case as seen in Table 5.6.

Table 5.6: Organization of cases by model and load.

Model	Load Case 1	Load Case 2	Load Case 3	Load Case 4
3D printing – optimized model	1.1	1.2	1.3	1.4
3D printing – redesigned model	2.1	2.2	2.3	2.4
BMD – optimized model	3.1	3.2	3.3	3.4
Pess Molding – optimized model	4.1	4.2	4.3	4.4

This organization, models as the primary variable and load cases as the second variable, enable systematic comparison across both dimensions. Each case was analyzed using consistent criteria, including stress distribution and deformation, allowing for a direct comparison of the mechanical performance between manufacturing techniques and design options.

In summary, this approach ensured that the evaluation was rigorous, reproducible and directly comparable, providing a clear framework for understanding how different materials, manufacturing methods and optimization influence the mechanical behavior of the components under realistic loading scenarios.

6

Results

This chapter presents the outcomes of the finite element analyses carried out in *Abaqus* for the five models under investigation. Each model was subjected to four distinct load cases, designed to simulate different operational conditions and assess structural performance. The results are organized by model to provide a comprehensive view of how each design responds to the applied loads. For every model, the analysis includes the evaluation of deformation patterns, stress distribution and performance metrics such as stiffness, strength and weight. The structure allows for a deeper understanding of the individual behavior of each model, while setting the foundation for the comparative discussion that follows in the next chapter.

6.1 Model 1

For the optimized foil manufactured through 3D printing in PLA, the numerical analysis was updated to account for the anisotropic behavior of the material. The anisotropic definition allows the model to capture direction dependent stiffness and strength, reflecting the influence of the printing process and the internal structure of the polymer. The simulation was carried out using a shell representation of the geometry, which ensures computational efficiency while providing accurate insight into the global structural response. The results obtained include reaction forces, displacement fields, stresses and strains under four distinct loading scenarios. These outputs form the basis for assessing the stiffness, strength and overall structural reliability of the optimized design.

Reaction Forces

The reaction forces recorded at the encastre provide critical insight into how the applied loads are transmitted through the structure into its supports, reflecting the overall equilibrium of the system. Across all four load cases, the reactions were concentrated at the fully fixed support, confirming that the boundary conditions were correctly implemented.

In Load Case 1, the uniform vertical loads, the structure resisted mainly through a vertical reaction of approximately 12.27 N acting upward at the support, balancing the applied pressure. Small lateral reaction components were also observed, arising from minor geometric effects and anisotropy in the PLA material.

For Load Case 2, lateral hydrodynamic load, the horizontal component dominated the response, with a reaction force of about 186.5 N laterally. The vertical reaction was comparatively small, confirming that the load was primarily absorbed as a side force on the strut.

The most demanding condition was Load Case 3, where the vertical and lateral loads were combined. Here, the support resisted 194.3 N vertically and 198.8 N laterally, with

an additional 82.39 N along the 33 direction. These values identify this case as structurally critical, since the anchorage simultaneously carries substantial forces in multiple directions.

Finally, Load Case 4, representing a less intense load condition, produced smaller reactions, around 3.73 N vertically, confirming the reduced structural demand under lighter loading.

Table 6.1 summarizes the results of the reaction forces.

Table 6.1: Reaction forces for each load case of Model 1 [N].

Load Case	**Total [N]**	**11 [N]**	**22 [N]**	**33 [N]**
1	12.27	-4.20	-11.45	2.77
2	186.54	55.82	-184.30	79.61
3	194.28	-57.75	191.76	82.39
4	3.37	-0.99	3.33	-1.37

From a design perspective, these reaction forces represent the demands that would be transferred from the foil to the hull in a real configuration. While the absolute magnitudes in Load Cases 2 and 3 are significant, they remain within the safe range for the anisotropic PLA material when compared against its stress based capacity. However, it must be emphasized that the connection at the encastre becomes the critical element, even if the foil material itself can withstand the applied stresses, failure at the joint would compromise the entire system. For this reason, the reaction forces highlight the need for robust fastening or embedding strategies, particularly under combined load cases where forces approach 200 N in multiple directions.

Overall, the reaction forces demonstrate that the anisotropic PLA foil behaves consistently with the applied loads, vertical loads induce primarily vertical reactions, lateral hydrodynamic loads generate dominant horizontal reactions and combined loading cases yield proportionally higher multi directional reactions. The scaling of these values with load intensity validates the model and underscores the necessity of considering simultaneous loading scenarios in the structural design process, as they define the governing demands for both the component and its connections.

Displacements and Stiffness

The displacement field of the optimized 3D printed model demonstrates that the largest deflections occur at the lateral ends of the foil, which is consistent with the cantilever like encastre applied at the top of the strut. Across the four load cases, the maximum displacement magnitudes vary considerably, reflecting the different nature and intensity of the applied loads as seen in Table 6.2.

Table 6.2: Maximum displacement for each load case of Model 1 [mm].

Load Case	**Max Displacement [mm]**	**Max Displacement 11 [mm]**	**Max Displacement 22 [mm]**	**Max Displacement 33 [mm]**
1	31.48	2.70	21.24	23.25
2	535.97	-11.85	133.03	520.31
3	563.79	13.47	154.26	543.45
4	20.16	0.31	9.68	-17.73

The largest deflection, observed in Load Case 3, which confirms that the combined vertical and lateral loading produces the most severe challenge to global stiffness. Load Case 2 also induces very large displacements, while Load 1 and 4 produce substantially smaller deformations. This spread in magnitudes reflects the different loading character, single direction or light loads give modest deflections, whereas lateral and combined loadings excite large bending and off axis deformations of the thin, printed geometry.

The observed deformation pattern is predominantly bending dominated and aligned with the principal load directions, the tip of the foil being the farthest point from the encastre shows the largest displacements as expected for a cantilevered member. Small but measurable components in the other principal directions indicate mild torsional and coupling effects under multi directional loading, the nonzero displacement components 11, 22 and 33 reveal that the response is not purely planar but includes out of plane and coupled motion. This mixed bending torsion behavior is consistent with the orthotropic elastic response of the printed PLA, where direction dependent stiffness and geometry together control the deformation mode.

From a stiffness and serviceability standpoint, the absolute values of the displacements in Load Case 2 and 3 are critical. Deflections on the order of half a meter are large for a foil component and will almost certainly violate practical serviceability limits for most structural applications. Even if material strength were adequate in principal stress, such large deformations would impair performance and may lead to secondary damage at attachments or induce unacceptable dynamic behavior. In contrast, the smaller deflections in Load Cases 1 and 4 are likely tolerable provided application specific deflection criteria are respected.

The displacement results thus provide a quantitative measure of the global stiffness of the system and identify the combined lateral vertical scenarios as the dominant drivers of excessive flexibility. For design development, these findings imply that stiffness, not only strength, must be addressed. Practical mitigation strategies include increasing local or global section stiffness, modifying the foil geometry to move neutral axes and reduce bending moments, changing print orientation and lay-up to align the stiffer material direction with primary loading, increasing infill or employing denser print settings in critical regions, or introducing a metallic insert or bonded reinforcements.

Finally, because the displacement and stress results are coupled, the next steps should be an integrated approach, verify the predicted deformations experimentally on a printed

prototype, establish application specific allowable deflection limits and iterate the geometry or print strategy to achieve acceptable serviceability and strength simultaneously.

Stress Distribution

The stress analysis of the optimized 3D printed model was carried out using the maximum principle stress criterion, which is appropriate for anisotropic and brittle polymer materials such as PLA produced by fused filament fabrication. The maximum principal stresses obtained for each load case are summarized in Table 6.3.

Table 6.3: Maximum principal stress for each load case of Model 1 [MPa].

Load Case	Max Stress	Max Stress 11	Max Stress 22	Max Stress 33
1	-24.19	-16.19	25.64	0
2	92.59	34.21	91.62	0
3	96.24	35.45	95.16	0
4	6.97	-6.06	6.68	0

To assess safety, these maximum principal stresses are compared against a conservative allowable tensile strength of $35\,MPa$ for 3D printed PLA. While PLA can reach ultimate tensile strengths in the range of $45 - 60\,MPa$ under favorable conditions, lower values around $33MPa$ have also been reported for prints with unfavorable orientations or reduced inter layer adhesion. Adopting $35MPa$ as the allowable strength is therefore a conservative design basis that reflects this variability, [73] [74] [75]. Using the standard scalar safety factor definition as shown in Equation 6.1.

$$SF = \frac{Allowable\ strength}{Maximum\ principle\ stress} \tag{6.1}$$

The resulting safety factors are shown in Table 6.4.

Table 6.4: Safety factors for Model 1.

Load Case	Max Principal Stress (MPa)	SF (35 MPa)
1	24.19	1.45
2	92.59	0.38
3	96.24	0.36
4	6.97	5.02

These results show that Load Case 1 and Load Case 4 have safety factors greater than 1 under the conservative assumption, indicating acceptable strength in those scenarios. By contrast, Load Case 2 and 3 produce safety factors well below unity, meaning the computed maximum principal stresses exceed the conservative allowable strength and the part is predicted to fail in principal tension under these lateral and combined loading conditions.

Spatially, the principal stresses concentrate near the encastre at the top of the structure where boundary constraints generate the largest bending moments, stresses then decay

toward the free end of the foil. The distribution is predominantly bending dominated, with higher stresses at the outer edges of the strut and small asymmetries that reflect minor torsional effects under combined loading. The strength check therefore identifies the encastre region and adjacent outer edges as the primary locations of concern of material failure and suggests that either local stiffening, redesign of the geometry or a change in print strategy, such as orientation, infill and layer bonding, is required to mitigate failure in Load Cases 2 and 3.

Finally, it is important to note that safety factor addresses strength only. Overall, the maximum principal stress analysis demonstrates that the 3D printed anisotropic PLA foil responds predictably to the applied loads, with the highest stresses occurring near the encastre and along bending paths and no regions of overstress. These results provide a clear quantitative basis for evaluating structural safety and serve as a reference for comparison across different material configurations or designs.

Strain Distribution

The strain response of Model 1 mirrors the behavior seen in stress and displacement fields, highlighting the structural weaknesses of the optimized PLA configuration. Table 6.5 presents the maximum principal strain values recorded for each load case.

Table 6.5: Maximum principal strain for each load case of Model 1.

Load Case	**Max Principal Strain**
1	-8.1×10^{-3}
2	3.2×10^{-2}
3	3.3×10^{-2}
4	2.9×10^{-3}

The results show that the most critical strain levels occur in Load Cases 2 and 3, reaching values on the order of 3×10^{-2}. These magnitudes are considerably higher than those of Load Case 1 and 4, which remain below 10^{-2}. The difference reflects the severe deformation imposed by lateral and combined loading conditions, compared to the more moderate structural demand from axial and torsional loads.

The strain distribution is strongly localized near the fixed support, coinciding with regions of high bending stresses. Compressive strains dominate in Load Case 1, whereas Load Cases 2 and 3 exhibit tensile strains approaching the failure threshold of the material, indicating overstretching in critical regions. Load Case 4, with maximum strain values of 2.9×10^{-3}, produces relatively minor deformations in comparison.

In summary, the strain analysis confirms insufficient stiffness of Model 1, with critical demand concentrated in lateral and combined loading cases. These values suggest that the optimized PLA foil is highly vulnerable to premature failure due to excessive localized deformation.

Structural Performance Conclusion

The combined analysis of reaction forces, displacements and stresses for Model 1 indicates that the anisotropic 3D printed PLA foil responds consistently and predictably to the four load cases. Among these, Load Case 3, which applies combined vertical and lateral loads, emerges as the most critical scenario, it produces the highest maximum principal stresses, the largest global displacement and the greatest reaction forces at the encastre. The corresponding strain distribution reinforces these findings, showing that tensile strains in Load Cases 2 and 3 approach the deformation limits of the material, particularly near the fixes support, highlighting regions of potential overstretching.

While the maximum principal stresses remain below the conservative allowable for anisotropic PLA in single direction load cases, the combined scenario clearly represents the limiting structural condition. The deformation field shows predominantly bending dominated behavior, with minor torsion effects under multi directional loading. Displacements in Load Cases 2 and 3, although physically reasonable in the simulation, highlight that stiffness could be a limiting factor for serviceability, particularly at the tip of the foil and near the encastre.

Reaction forces confirm that the boundary receives the full transmitted load and the encastre region is subjected to the highest structural demand, reinforcing the importance of robust attachment design in real world applications. Overall, the foil demonstrates expected behavior for a cantilevered, anisotropic polymer structure, vertical loads produce vertical reactions, lateral loads produce lateral reactions and combined loads scale appropriately across both stresses, displacements and strains.

In conclusion, Model 1 meets strength requirements under conservative assumptions for single direction loads, but the combined loading scenario identifies both stress and stiffness, as well as critical strain concentrations, as the governing factors for structural performance. This integrated assessment provides a clear quantitative basis for evaluating structural performance, guides attention to critical regions for design optimization and establishes a reference for comparison with alternative materials or configurations in subsequent studies.

6.2 Model 2

For the redesigned foil manufactured via 3D printing, the numerical study was conducted using an anisotropic material definition to account for the direction dependent mechanical properties granted by the printing process. By representing the foil geometry with shell elements, the simulations achieve both computational efficiency and an accurate description of the global structural behavior. The analysis provides detailed outputs including reaction forces, displacement fields, principal stresses and strains for four distinct loading scenarios. These results serve as the basis for assessing the overall structural performance, stiffness and strength of the redesigned foil, highlighting the impact of the geometric modifications on its load carrying capacity and reliability.

Reaction Forces

Again, the reaction forces calculated at the encastre provide essential information on how the applied loads are transmitted through the redesigned foil into its support, reflecting the overall equilibrium of the system. For all four load cases, the reactions are concentrated at the fully fixed boundary, confirming that the support conditions were correctly implemented in the numerical model.

In Load Case 1, corresponding to a uniform vertical load, the structure resisted primarily through a vertical reaction of approximately $14.43\,N$ at the support, balancing the applied pressure. Minor reaction components were also observed in the lateral directions, arising from slight geometric effects and the anisotropy response of the PLA material.

For Load Case 2, dominated by lateral hydrodynamic loading, the reaction was primarily in the horizontal plane, with a 22 direction component of about $82.16\,N$ and additional contributions of $22.70\,N$ in the 11 axis and $75.64\,N$ in the 33 axis. The vertical reaction in this case remained relatively small, indicating that the lateral load was absorbed predominantly as a side force on the strut.

The most critical scenario was Load Case 3, where vertical and lateral loads were applied simultaneously. Here, the support carried a total reaction of $90.70\,N$, with components of $75.93\,N$ along the 11 axis, $89.69\,N$ along the 22 axis and $75.93\,N$ along the 33 axis. Although this represents the governing condition for the redesigned model, the magnitudes are considerably lower than in Model 1, demonstrating the effectiveness of the geometric modifications in reducing peak loads at the support.

Finally, Load Case 4 corresponding to a lighter load scenario, produced minimal reactions with a total of $1.31\,N$, confirming the reduced structural demand under less severe loading conditions.

Table 6.6 summarizes the reaction force components for the redesigned PLA foil.

Table 6.6: Reaction forces for each load case of Model 2 [N].

Load Case	Total [N]	11 [N]	22 [N]	33 [N]
1	14.43	9.01	-11.27	3.60
2	83.20	22.70	82.16	75.64
3	90.70	24.18	-89.69	75.93
4	1.31	-1.01	-0.48	0.81

From a design perspective, these reactions reflect forces that would be transmitted from the foil to the hull in a real system. While Load Cases 2 and 3 involve the highest forces, they remain moderate compared to Model 1, suggesting that the redesign successfully reduced the structural demand at the encastre. Nevertheless, the support region remains a critical element, as any failure there could compromise the entire foil, even if the PLA material itself is capable of resisting the applied stresses.

Overall, the reaction forces that the redesigned foil behaves predictably with respect to the loading conditions, vertical loads produce primarily vertical reactions, lateral loads dominate the horizontal components and combined loads generate moderate multi directional reactions. The reduced magnitude of these reactions relative to the original model demonstrates the effectiveness of the geometric modifications in improving structural performance and lowering the demands on the connection, highlighting the importance of considering the encastre in the design evaluation.

Displacements and Stiffness

The displacement field of the redesigned 3D printed PLA foil demonstrates a significant improvement in structural stiffness compared to the original configuration. As with Model 1, the largest deflections occur at the tip of the foil, farthest from the encastre, which is consistent with the cantilever like boundary condition applied at the top of the strut. Across the four load cases, maximum displacement magnitudes vary according to the load intensity and direction, as summarized in Table 6.7.

Table 6.7: Maximum displacement for each load case of Model 2 [mm].

Load Case	Max Displacement [mm]	Max Displacement 11 [mm]	Max Displacement 22 [mm]	Max Displacement 33 [mm]
1	0.60	-0.15	0.30	0.54
2	44.96	0.01	10.00	44.89
3	45.51	-0.14	10.29	45.43
4	1.79	-0.02	0.80	-1.74

In Load Case 1, under a uniform vertical load, the maximum displacement is only 0.60 mm, with minor contributions in the lateral directions. This indicates that the

redesign has significantly increased vertical bending stiffness, limiting deflections even at the foil tip.

For Load Cases 2 and 3, which involve lateral and combined vertical lateral loads, the displacements increase to approximately 45 mm. Despite being the largest in the redesigned model, these values are dramatically lower than the corresponding deflections in Model 1, illustrating the effectiveness of the geometric modifications in improving stiffness and redistributing loads along the structure. The displacement patterns remain largely bending dominated, with minor torsional effects visible in the asymmetries along the 22 and 33 directions, particularly in the combined loading scenario of Load Case 3.

Load Case 4, representing a lighter load combination, produces very small deformations, demonstrating that the redesigned foil maintains high stiffness under less demanding conditions.

The overall displacement behavior highlights several important structural improvements. First, the tip deflections are significantly reduced compared to Model 1, reducing the risk of interference with surrounding components and improving serviceability. Second, the more uniform distribution of displacements along the foil length indicates that stresses are more evenly shared, which helps to prevent localized overstress and potential material failure. Finally, the reduced torsional response under multi directional loads suggests that the redesigned geometry improves resistance to twisting, a critical factor for maintaining alignment and stability during operation.

In summary, the displacement analysis confirms that the redesigned PLA foil achieves enhanced stiffness across all load cases. It is particularly effective under combined lateral and vertical loads, where deflections are minimized without introducing new stress concentrations. These results provide a clear quantitative demonstration that the geometric modifications have successfully improved the structural performance of the foil, ensuring both reliability and durability under realistic loading conditions.

Stress Distribution

The stress response of the 3D printed redesigned model was evaluated using maximum principal stress criterion, which is particularly suitable for anisotropic and brittle polymer materials produced via fused filament fabrication. The maximum principal stresses calculated for each load case are summarized in Table 6.8.

Table 6.8: Maximum principal stress for each load case of Model 2 [MPa].

Load Case	**Max Stress**	**Max Stress 11**	**Max Stress 22**	**Max Stress 33**
1	0.94	0.87	1.08	0.00
2	7.35	2.46	7.29	0.00
3	7.16	-2.57	-7.55	0.00
4	-0.46	-0.13	-0.46	0.00

To evaluate structural safety, these stresses are compared against a conservative allowable tensile strength 35 MPa for 3D printed PLA as done for the previous model.

This conservative limit accounts for potential weak inter layer adhesion and non optimal orientations. The scalar factor is calculated using Equation 6.1 as previously mentioned.

The resulting safety factors for each load care are presented in Table 6.9.

Table 6.9: Safety factors for Model 2.

Load Case	**Max Principal Stress (MPa)**	**SF (35 MPa)**
1	0.94	37.20
2	7.35	4.76
3	7.16	4.89
4	0.46	76.10

These safety factors indicate that the redesigned foil exhibits excellent strength under all considered load cases. Even in the most demanding scenarios, Load Case 2 and 3, the maximum principal stresses are well below the conservative allowable, resulting in safety factors above 4. This demonstrates substantial improvement over the original design, where combined lateral and vertical loads generated critical stress levels.

Spatially, the stresses are highest near the encastre at the top of the strut, where boundary constraints induce bending moments. From this region, stress decays progressively toward the free tip of the foil. The stress distribution remains largely bending dominated, with slightly higher stresses along the outer edges of the strut and minor asymmetries that reflect limited torsional effects under combined loading. The redesign effectively distributes stresses more evenly along the strut, reducing localized peaks and mitigating the risk of material failure near the encastre.

It is important to note that the safety factor addresses material strength only. The stress analysis confirms that the redesigned PLA foil responds predictably to the applied loads, with the highest stresses concentrated along bending paths near the encastre and no regions approach the material limit. These results provide a robust quantitative basis for assessing structural reliability and offer a clear reference for comparing future design modifications or alternative material choices.

Strain Distribution

The strain distribution of Model 2 follows the same general trends observed in the displacement and stress fields. Table 6.10 summarizes the maximum principal strains obtained for each load case.

Table 6.10: Maximum principal strain for each load case of Model 2.

Load Case	**Max Principal Strain**
1	3.7×10^{-4}
2	2.9×10^{-3}
3	-3.0×10^{-3}
4	-1.8×10^{-4}

As expected, the largest strains occur under Load Cases 2 and 3, which correspond to lateral and combined loading conditions. Their maximum values are approximately an order of magnitude higher than those of Load Cases 1 and 4, reflecting the more severe deformation imposed by these loading. The relatively small strain magnitudes in Load Case 1 and 4 confirm that these scenarios are less demanding for the structure.

Spatially, the strain distribution is concentrated near the encastre, coinciding with the regions of maximum bending stresses. Small tensile and compressive strain components in the secondary directions also indicate the presence of mild torsional and anisotropic effects, consistent with the direction dependent stiffness of 3D printed PLA.

Overall, the strain results provide additional validation of the displacement and stress analyses, showing that the anisotropic foil undergoes predictable deformation patterns , with critical demand concentrated in lateral and combined loads.

Structural Performance Conclusion

The numerical analysis of the redesigned 3D printed PLA foil demonstrates clear improvements in overall structural performance compared to the original Model 1. The evaluation of reaction forces, displacements and maximum principal stresses provides a comprehensive understanding of how the redesign influences load transfer, stiffness and material safety.

From the reaction forces perspective, the redesigned foil exhibits lower total and directional reactions across all load cases. For instance, in the most critical combined loading scenario, Load Case 3, the total reaction magnitude is approximately 90.7 N, with component forces of 24.2 N (11-axis), -89.7 N (22-axis) and 75.9 N (33-axis). These values are significantly lower than the peak reactions observed in Model 1, indicating that the geometric modifications have successfully reduced the loads transmitted to the encastre. This reduction not only decreases the risk of joint failure but also highlights the efficiency of the structural redesigning in distributing forces more uniformly.

The displacement analysis reinforces these findings. Across all load cases, maximum tip deflections are considerably reduced compared to Model 1. Even under lateral and combined loading, maximum displacements remain around $45mm$, whereas Model 1 experienced deflections exceeding $560mm$. The deformation patterns remain primarily bending dominated, with minor torsional effects, but the more uniform displacement field indicates improved stiffness and better load sharing along the strut. The redesigned geometry thus mitigates excessive deflections, enhancing serviceability and reducing the likelihood of interference or misalignment during operation.

The stress distribution further confirms the success of the redesign. Maximum principal stresses under all load cases remain well below the conservative allowable of 35 MPa, with safely factors ranging from approximately 4.8 to 76.2. Even in the most critical scenarios, the stress peaks are localized near the encastre but are substantially lower than in Model 1, showing that the redesign effectively reduces bending and torsional stress concentrations. The combination of lower peak stresses and higher safety factors demonstrates that the redesigned foil achieves a robust margin of strength while maintaining predictable structural behavior.

Finally, the strain results are consistent with the observed improvements in displacement and stress response. Maximum strains in the redesigned foil are an order of magnitude lower than those in Model 1, particularly in Load Cases 2 and 3, which were previously critical. This reduction in strain confirms not only the enhanced stiffness but also the improved material utilization of the new geometry, with deformations kept within levels compatible with the anisotropic properties of printed PLA.

Overall, the integrated assessment of reaction forces, displacements and stresses illustrates the redesigned PLA foil offers superior structural performance. The reduction in peak reactions and displacements, along with enhanced safety factors, confirms that the redesign improves both stiffness and strength, ensuring reliable load transfer and minimizing the risk of failure. These results provide a solid foundation for final design validation and establish a quantitative benchmark for future iterations, highlighting that the geometric modifications effectively optimize the foil for the expected operational load scenarios.

6.3 Model 3

For the optimized aluminum foil produced via 3D printing, the numerical analysis was carried out assuming an isotropic material definition, appropriate for metals where mechanical properties are uniform in all directions. The foil geometry was modeled using shell elements, providing a balance between computational efficiency and accurate representation of the global structural response. The simulations deliver comprehensive results, including reaction forces, displacement fields and von Mises stresses under four distinct loading conditions. These outputs form the foundation for evaluating the structural performance, stiffness and strength of the aluminum foil, allowing comparison with previous PLA designs and highlighting how the material substitution influences load bearing capacity, deformation and overall reliability.

Reaction Forces

The reaction forces at the fully fixed encastre provide crucial insight how the applied loads are transmitted through the aluminum foil to its supports and reflect the overall equilibrium of the system. Across all four load cases, the reactions remain concentrated at the encastre, confirming that the boundary conditions were correctly applied and that the isotropic material efficiently distributes the applied loads.

In Load Case 1, under a uniform vertical load, the structure primarily resisted through a vertical reaction of approximately 12.28 N at the support. Minor lateral reaction components were observed, arising from geometric effects, but their magnitudes are negligible compared to the vertical reaction, reflecting the high stiffness of the aluminum foil.

For Load Case 2, dominated by a lateral hydrodynamic load, the horizontal reaction component is significant, reaching 187.12 N laterally, while the vertical reaction remains small, indicating that the load is primarily absorbed as a side force. This highlights the ability of the aluminum foil to efficiently transmit lateral loads to the support without excessive bending.

The most critical scenario, Load Case 3, combines vertical and lateral loads. Here, the total reactions are the highest, with approximately 194.97 N vertically and 193.08 N laterally, along with 51.69 N in the 33 direction. This confirms that the combined loading case imposes the greatest demand on the support, as it must simultaneously resist forces in multiple directions.

Finally, Load Case 4, representing a lighter load condition, generates minimal reaction forces, with vertical reactions around 3.37N demonstrating the reduced structural demand under less intense loading.

Table 6.11 summarizes the reaction force components for all four load cases.

Table 6.11: Reaction forces for each load case of Model 3 [N].

Load Case	**Total [N]**	**11 [N]**	**22 [N]**	**33 [N]**
1	12.28	-2.54	-11.97	1.72
2	187.12	43.82	-185.66	49.95
3	194.97	-45.61	193.08	51.69
4	3.37	-0.80	3.35	-0.85

From a design standpoint, these reaction forces indicate the loads that would be transferred to the foil to hull connection in a real system. While the absolute values in the combined and lateral load cases are substantial, the high stiffness and strength of aluminum ensure that both the foil and the encastre remain well within safe limits. The most critical forces occur in Load Case 3, yet the isotropic aluminum material provides sufficient capacity to withstand these loads without risk of structural failure.

Overall, the reaction forces confirm that the aluminum foil behaves predictably under all load scenarios. Vertical loads primarily induce vertical reactions, lateral loads produce dominant horizontal reactions and combined load cases generate multi directional reactions. The consistent scaling of these values with the applied load validates the isotropic model and emphasizes the importance of considering combined loading scenarios in the structural design process, ensuring both component and connection safety.

Displacements and Stiffness

The displacement field of the optimized 3D printed aluminum foil demonstrates a significant increase in structural stiffness compared to both PLA configurations. As expected for a cantilever like boundary condition at the encastre, the largest deflections occur at the tip of the foil, farthest from the fixed support. Across the four load cases, the maximum displacement magnitudes vary according to load intensity and direction, as summarized in Table 6.12.

Table 6.12: Maximum displacement for each load case of Model 3 [mm].

Load Case	**Max Displacement [mm]**	**Max Displacement 11 [mm]**	**Max Displacement 22 [mm]**	**Max Displacement 33 [mm]**
1	1.16	0.10	0.79	0.86
2	19.79	-0.52	4.90	19.22
3	20.81	0.59	5.68	20.07
4	0.74	0.01	0.36	-0.65

In Load Case 1, the vertical load generates a maximum displacement of just $1.16\,mm$ at the tip, with negligible lateral contributions. This reflects the high bending stiffness of the aluminum foil under vertical loads, confirming that the material and geometry can effectively resist deformation in this direction.

For Load Cases 2 and 3, which involve lateral and combined vertical loads, the maximum displacements increase to approximately $19.8 - 20.8\,mm$. While these represent the largest deflections in the aluminum foil, they are still considerably smaller than those observed in the PLA foils under the same loading conditions. The displacement patterns are predominantly bending dominated, with minor torsional contributions caused from asymmetries in the 22 and 33 directions, especially under the combined Load Case 3. This indicates that the aluminum foil effectively resists twisting while allowing controlled bending, ensuring predictable deformation under multi directional forces.

Load Case 4, representing a lighter scenario, produces very small deflections, demonstrating that the aluminum foil remains nearly rigid under low demand conditions.

Overall, the displacement behavior highlights several key structural advantages. First, the tip deflections are drastically reduced compared to the PLA foils, lowering the risk of interference with surrounding components and improving operational reliability. Second, the displacement field is more uniform along the foil length, which implies a more even stress distribution and reduces the likelihood of localized overstress. Finally, the limited torsional response under combined loading confirms that the foil geometry and isotropic material properties maintain stability and alignment even under complex force combinations.

In summary, the displacement analysis shows the 3D printed aluminum foil provides markedly improved stiffness across all load cases. It performs particularly well under lateral and combined loading, minimizing deflections while maintaining structural integrity. These results quantitatively demonstrate the benefits of the aluminum material in enhancing the performance of the foil, ensuring both durability and reliable behavior under realistic operational loads.

Stress Distribution

The stress response of the optimized 3D printed aluminum foil was evaluated using von Mises, which is suitable for isotropic, ductile materials and provides a reliable measure of yielding under multi axial loading conditions. The isotropic assumption is appropriate

here because, unlike the PLA foils, the aluminum foil does not exhibit direction dependent stiffness from the printing process, allowing the material to be treated as uniform in all directions. Maximum von Mises for the four load cases are presented in Table 6.13.

Table 6.13: Maximum von Mises stress for each load case of Model 3 [MPa].

Load Case	**Max Stress**	**Stress 11**	**Stress 22**	**Stress 33**
1	22.06	-13.95	24.55	0
2	80.85	25.81	89.66	0
3	84.06	26.73	93.13	0
4	8.24	-5.52	6.99	0

For safety evaluation, the maximum von Mises stresses are compared against a conservative yield strength of 250 MPa for aluminum produced via Bound Metal Deposition (BMD). While fully dense aluminum alloys can achieve yield strengths between $270-500MPa$, BMD parts typically exhibit reduced mechanical properties due to residual porosity and incomplete sintering introduced during the printing and debinding processes. Adopting $250MPa$ as the allowable yield strength therefore provides a conservative design basis, accounting for these process related variations, [76] [77]. The scalar safety factor is calculated as shown previously in Equation 6.1. The resulting safety factors, shown in Table 6.14, indicate that all load cases remain well within the elastic limit of the material.

Table 6.14: Safety factors for Model 3.

Load Case	**Max von Mises Stress [MPa]**	**Safety Factor**
1	22.06	11.34
2	80.85	3.09
3	84.06	2.97
4	8.24	30.31

Load Case 1, corresponding to uniform vertical loading, produces minimal stress concentrated near the encastre, reflecting primarily bending induced stresses. The stress decays along the foil toward the tip, with the outer edges experiencing slightly higher stress due to the bending moment distribution. Minor asymmetries in the 11 and 22 directions indicate limited torsional contributions, but these remain negligible compared to the primary bending stresses.

Load Case 2, representing a lateral hydrodynamic load, exhibits elevated von Mises stresses with the highest stresses again located near the fixed support. The lateral component induces significant bending in the 22 direction, while the 11 direction stress remains moderate. This confirms that the aluminum foil efficiently resists lateral bending with minimal deflection, reflecting its superior stiffness compared to PLA foils.

Load Case 3, which combines vertical and lateral loading, produces the highest stresses in the system, highlighting the structural demand for the foil to resist multi directional bending simultaneously. Despite this, the resulting safety factor of approximately 2.97 demonstrates a robust margin, ensuring that the foil remains well within elastic limits

and no yielding is expected. Stress patterns indicate that the encastre and the adjacent outer edges are the critical regions, where the bending moments and shear combine to produce the peak stresses.

Load Case 4, a less intense load scenario, produces minimal von Mises stress confirming that the aluminum foil behaves nearly rigidly under low load conditions, with stresses almost uniformly distributed along the length.

Overall, the stress distribution demonstrates that the aluminum foil responds predictably under all loading scenarios. The isotropic nature of the material ensures stress transmission without significant localized overstress and the high stiffness of aluminum limits deformation even under combined loads. The analysis identifies the encastre and outer edges of the foil as the primary regions of structural demand, providing a clear target for inspection or potential local reinforcement if necessary. Compared to PLA foils, the aluminum configuration achieves substantially higher safety factors, reduced deflections and more uniform stress distribution, confirming that the material choice and optimized geometry yield a reliable and durable structural component.

Strain Distribution

The strain response of Model 3 reflects the results observed in its stress and displacement fields. Table 6.15 presents the maximum principal strains recorded for each load case.

Table 6.15: Maximum principal strain for each load case of Model 3.

Load Case	**Max Principal Strain**
1	-3.11×10^{-4}
2	1.17×10^{-3}
3	1.22×10^{-3}
4	1.15×10^{-4}

The highest strains occur in Load Cases 2 and 3, which correspond to the lateral and combined loading scenarios. Their magnitude exceed those of Load Cases 1 and 4 by roughly an order of magnitude, highlighting the additional structural demand under these conditions. Load Cases 1 and 4, with significantly smaller strains, represent comparatively mild loading.

The strain is concentrated primarily near the fixed support, aligning with regions of peak bending stresses. While compressive and tensile strains dominate the principal direction, minor contributions in the secondary direction indicate slight torsional effects.

In summary, the strain analysis confirms that Model 3 behaves predictably under the imposed loads, with critical stress and deformation localized near the encastre. The lateral and combined load cases are the governing conditions, providing key insight for identifying potential regions of overstretching and guiding design optimization.

Structural Performance Conclusion

The structural assessment of the optimized aluminum foil demonstrates a clear improvement in both stiffness and strength compared to the PLA configurations. Reaction improvement in both stiffness and strength compared to the PLA configurations. Reaction forces at the encastre confirm that the foil effectively transmits the applied loads to its support, with the largest multi directional forces occurring under the combined vertical lateral loading of Load Case 3. Despite the magnitude of these forces, approaching $195\,N$ in vertical and lateral directions, the aluminum foil maintains a high margin of safety, owing to the isotropic material properties and the optimized geometry. Strain analysis further confirms this behavior, showing that maximum principal strains remain low, on the order of 10^{-3} even in the most critical regions near the encastre, indicating limited local deformation and minimal risk of overstretching.

Displacement analysis further highlights the structural benefits of aluminum. Maximum tip deflections remain below $21\,mm$ even under the most demanding combined loads, a substantial reduction relative to the PLA foils. The bending dominated deformation pattern, with minor torsional effects, ensures predictable behavior under complex loading and minimizes the risk of misalignment or interference with neighboring components. The uniform distribution of displacements along the foil indicates efficient load sharing, which reduces localized stress concentrations and potential sites of failure.

Von Mises stress evaluation confirms that the aluminum foil remains well within the elastic limit for all loading scenarios. Even under the combined loading of Load Case 3, the peak stress reaches only $84\,MPa$, yielding a conservative safety factor of nearly 3. The highest stresses are concentrated at the encastre and along the outer edges, consistent with bending response, while the free tip remains largely unstressed. Compared to the PLA foils, the aluminum configuration achieves both higher stiffness and lower relatives stress, reflecting the superior elastic modulus and strength of the material.

Taken together, these results provide a comprehensive understanding of the structural performance of the foil. The optimized aluminum design exhibits enhanced load carrying capacity, reduced deflections and substantial safety margins, ensuring reliable operation under realistic load scenarios. Furthermore, the analysis highlights critical regions near the encastre for monitoring or reinforcement, while confirming that the overall geometry and material selection effectively mitigate the risk of yielding or excessive deformation. These findings underscore the suitability of the aluminum foil for high demand applications combining stiffness, strength and predictable multi directional performance in a single optimized structural component.

6.4 Model 4

For the optimized foil manufactured from carbon fiber laminates through press molding the numerical analysis was performed using an anisotropic layered material definition to represent the directional stiffness and strength of the composite. The laminate was modeled with ten plies of $0.2mm$ thickness in a $[0°, 90°, 0°, 90°]$ stacking sequence, capturing the effects of fiber orientation on the global response. Shell elements were used for the geome-

try, ensuring computational efficiency while accurately representing the through thickness layup behavior. The simulations provide results including reaction forces, displacement fields and stresses under four distinct loading scenarios. These outputs serve as the basis for assessing the stiffness, strength and overall structural reliability of the composite foil, while also enabling direct comparison with the PLA and aluminum counterparts to evaluate the impact of material substitution and laminate design on performance.

Reaction Forces

The reaction forces recorded at the encastre of the carbon fiber laminated foil provide insight into how the applied loads are transferred through the structure into its fixed boundary, reflecting both the anisotropic stiffness of the laminates and the global equilibrium of the system. As expected, all reaction are concentrated at the fully fixed support, confirming the proper definition of the boundary conditions and highlighting the dominant role of the anchorage in carrying the applied load.

In Load Case 1, representing uniform vertical loading, the support resists a total reaction of approximately 32.56 N, dominated by a vertical component of 32.46 N along the 22 direction. Small contributions in the 11 and 33 directions indicate that, despite the strong bending character of this case, minor lateral and torsional effects are present due to the anisotropic stiffness distribution of the laminate.

For Load Case 2, which applies a lateral hydrodynamic load, the reactions are much larger, with a total magnitude of 189.94 N. The lateral component of 189.49 N dominates the response, while smaller but non negligible reactions appear in the 11 and 33 directions. This confirms that the load is primarily absorbed as a side force on the strut, with the laminates efficiently channeling forces along the fiber orientations.

The combined loading of Load Case 3 produces the most critical condition, with a total load reaction of 221.44 N. In this case, the vertical and lateral components act together, with an additional contribution of 4.36 N along the 33 direction. This case highlights the structural demand for the simultaneous resistance in multiple directions and emphasizes the importance of the layup sequence in distributing loads between the longitudinal and transverse fiber orientations.

Finally, Load Case 4, representing a lighter loading scenario, generates only 0.99 N in total reactions. This very small demand demonstrates the negligible structural impact of this condition, confirming that the foil maintains stability with minimal force transfer at the support.

Table 6.16 summarizes the reaction forces for each load case.

Table 6.16: Reaction forces for each load case of Model 4 [N].

Load Case	**Total [N]**	**11 [N]**	**22 [N]**	**33 [N]**
1	32.56	3.01	32.46	1.03
2	189.94	12.56	189.49	-3.80
3	221.44	15.51	220.89	-4.36
4	0.99	0.10	0.99	0.04

From a structural perspective, these results demonstrate that the laminate composite efficiently transmits applied loads into the support, scaling proportionally with the load intensity and direction. The combined loading case clearly emerges as the most critical, requiring the anchorage to withstand reactions above 220 N in multiple directions simultaneously. While the material itself possesses significantly higher strength and stiffness compared to PLA and aluminum, the connection remains the governing factor for structural safety. Thus, in practical applications, ensuring a robust integration of the foil into the hull as important as the inherent mechanical capacity of the material.

Overall, the reaction force analysis confirms that the carbon fiber laminate behaves predictably under different loading conditions, with reactions scaling appropriately and reflecting the directional stiffness imposed by the laminate lay-up. These results provide a strong basis for evaluating the performance of the foil relative to the earlier designs and highlight the advantages of carbon fiber in handling multi directional loads with reduced mass.

Displacements and Stiffness

The displacement behavior of the carbon fiber laminated foil reveals the strong influence of the anisotropic material properties and the layered architecture on the global stiffness of the structure. The maximum displacements under each load case are summarized in Table 6.17, showing that while the structure is considerably stiffer than PLA foils, it still experiences significant deflections under high load conditions due to the relatively low transverse stiffness of the laminate.

Table 6.17: Maximum displacement for each load case of Model 4 [mm].

Load Case	**Max Displacement [mm]**	**Max Displacement 11 [mm]**	**Max Displacement 22 [mm]**	**Max Displacement 33 [mm]**
1	7.14	0.59	4.26	5.87
2	21.00	-1.55	4.94	20.52
3	27.40	1.03	9.15	25.92
4	0.26	0.02	-0.16	0.20

In Load Case 1, under a uniform vertical load, the foil reaches a maximum displacement of 7.14 mm. The response is primarily bending dominated, with the largest component occurring along the vertical axis, while moderate lateral displacement appears in the 22 direction. The relatively small displacement along 11 indicates limited torsional distortion. Compared to PLA and aluminum foils, this demonstrates an intermediate stiffness, with the laminate resisting vertical bending effectively allowing some redistribution of deflections due to its anisotropy.

Load Case 2, driven by lateral loading, produces larger deflections of approximately 21.0 mm. The displacement field is dominated by motion along the 33 axis, consistent with the side bending of the cantilevered strut. Smaller contributions in the 22 direction

reflect bending coupling from the 0°/90° lay-up, while the negative displacement along 11 points to slight torsional twisting induced by off axis shear.

In Load Case 3, which combines the vertical and lateral loads, the structure undergoes its largest deformation, reaching $27.40\,mm$. The majority of the displacement occurs along the vertical axis, with significant contributions along the 22 direction. This case highlights the directional stiffness imbalance, while the laminate is extremely stiff along the fiber dominated axis. The comparatively lower stiffness in transverse directions permits substantial bending and shear coupling. The observed asymmetry in displacement components reflects how the laminate redistributes loads through its layered structure, with fibers oriented at 0° carrying axial forces while 90° plies engage under transverse loading.

Load Case 4, the least demanding scenario produces negligible displacements, with a maximum displacement of only $0.26mm$. This confirms that under low loading conditions, the foil retains near rigid behavior with minimal bending or twisting.

Overall, the displacement analysis highlights several key features of the laminated carbon fiber design. First, the structure achieves favorable compromise between stiffness and weight, while displacements under combined loading remain significant, they are reduced when compared to PLA foils of similar geometry, despite the much lower density of the material. Second, the anisotropic response emphasizes the critical role of ply orientation, while 0°/90° lay-up provides balance in plane stiffness, it still leaves the structure vulnerable to bending and shear along the weak transverse directions. Third, the relatively low torsional response across all load cases demonstrates the effectiveness of the symmetric lay-up in reducing distortion.

In summary, the laminated carbon fiber foil achieves improved stiffness to weight efficiency compared to polymer based designs, with displacements that remain within manageable limits under the most demanding load cases. The results confirm the importance of the fiber architecture in governing structural behavior, suggesting that further optimization of ply sequences or thickness distribution could yield additional gains in stiffness and stability while maintaining the lightweight advantages of composite materials.

Stress Distribution

The stress analysis of the laminated carbon fiber foil was performed using the maximum principal stress criterion, which is appropriate for anisotropic materials where load resistance is strongly dependent on fiber orientation. Table 6.18 summarizes the maximum stresses for each load case, resolved along the principal material directions of the laminate.

Table 6.18: Maximum principal stress for each load case of Model 4 [MPa].

Load Case	**Max Stress**	**Max Stress 11**	**Max Stress 22**	**Max Stress 33**
1	181.32	181.30	8.42	0
2	153.35	153.34	3.23	0
3	180.65	180.63	8.43	0
4	-8.92	-8.92	0.31	0

The highest stresses occur under Load Case 1 and Load Case 3, both reaching values around 180 MPa aligned almost entirely with the fiber direction. By contrast, the transverse stresses remain below 10 MPa, confirming that the laminate behavior is fiber dominated. In Load Case 2, with lateral load only, the maximum stress drops slightly to 135 MPa, while the least demanding scenario, Load Case 4, produced negligible compressive stresses of about -9 MPa.

To evaluate safety, these stresses were compared against conservative strength values for unidirectional carbon fiber composites. Typical ultimate tensile strength along the fiber axis ranges from 600 to 1000 MPa depending on the fiber quality and lay-up, here a conservative allowable of 900 MPa was adopted for the 0° direction. In the transverse direction, matrix dominated strength is significantly lower, typically between 40 and 60 MPa a conservative 50 MPa was used for the 90° plies, [78] [79]. The safety factor was then calculated following Equation 6.1 as mentioned previously. The resulting safety factors are reported in Table 6.19.

Table 6.19: Safety factors for Model 4.

Load Case	**Max Stress 11 [MPa]**	**Safety Factor (0^o)**	**Max Stress 22 [MPa]**	**Safety Factor (90^o)**
1	181.30	4.96	8.42	5.94
2	153.34	5.87	3.23	15.48
3	180.63	4.98	8.43	5.93
4	-8.92	100.89	0.31	161.2

The results demonstrate that the foil maintains a safety factor of approximately 5 along the fiber direction in the most demanding load cases. In the transverse direction, where stresses are far lower than the conservative 50 MPa limit, the safety factors exceed 5 and in some cases 15, confirming that matrix dominated failure is not a critical concern under the current loading scenarios. Load Case 4 produces compressive stresses of negligible magnitude, providing effectively infinite tensile safety factors.

Spatially, stress concentrations are observed near the encastre, consistent with cantilever bending and diminish toward the free end of the foil. The symmetric 0°/90° layup ensures that stresses remain balanced through the laminate thickness, reducing the likelihood of warping or delamination. Importantly, the fiber alignment allows the material to carry vertical and combined loads efficiently, with stresses almost exclusively aligned along the stiffer 0° plies.

In summary, the stress distribution analysis confirms that the laminated carbon fiber foil is highly efficient at resisting loads along the fiber axis, with safety factors consistently well above unity across all scenarios. The results highlight the superior strength to weight performance of the laminate when compared to PLA and aluminum, while emphasizing that reliability ultimately depends on maintaining fiber alignment and preventing defects such as poor inter laminar bonding.

Strain Distribution

The strain behavior of Model 4 aligns closely with the trends observed in its stress and displacement responses. Table 6.20 summarizes the maximum principal strains for each load case.

Table 6.20: Maximum principal strain for each load case of Model 4.

Load Case	Max Principal Strain
1	1.47×10^{-3}
2	1.17×10^{-3}
3	1.47×10^{-3}
4	-6.71×10^{-5}

Load Cases 1 and 3, corresponding to vertical and combined loading, produce the largest strains, exceeding those in Load Case 2. Load Case 4 exhibits negligible strain, reflecting the minimal structural demand under that scenario.

Strain concentrations are primarily located near the fixed support, coinciding with the regions experiencing peak bending stresses. The principal strain components dominate the response, while secondary directions contribute to minor torsional effects, consistent with the anisotropic characteristics of the carbon fiber laminate.

Overall, the strain results indicate that Model 4 responds predictably to all applied loads, with the highest deformations localized near the encastre. Lateral and combined loadings define the critical conditions, providing guidance for potential reinforcement and highlighting areas of structural significance in the design.

Structural Performance Conclusion

The results for the carbon fiber laminate demonstrate a substantial improvement in structural performance compared to the polymer and metallic counterparts analyzed previously. The high stiffness of the laminate in the fiber direction ensures minimal displacements under all load cases, with maximum deflections of only about 27 mm even under the combined vertical lateral loading scenario.

Correspondingly, the maximum principal strains remain low, on the order of 10^{-3}, indicating that the laminate undergoes limited local deformation and that overstretching is unlikely.T his represents an order of magnitude reduction relative to the PLA designs and a significant improvement over the aluminum configuration, highlighting the effectiveness of the laminate lay-up in distributing loads and limiting deformations.

From a strength perspective, the stress analysis shows that the maximum fiber direction stresses remain around $180\,MPa$, far below the conservative $900\,MPa$ tensile strength of unidirectional carbon fiber plies. Corresponding safety factors are consistently near 5, indicating a comfortable margin against failure even in the most demanding cases. In the transverse and matrix dominated directions, stresses remain below $10\,MPa$, yielding safety factors greater than 15 and confirming that matrix cracking is not a governing failure mode for the studied scenarios.

The overall reaction forces confirm proper load transfer into the encastre, with values scaling predictably with load case intensity. Since the structural demand is primarily carried in the fiber direction, the anchoring region must be carefully designed to ensure adequate load transfer between plies and to the hull. Nevertheless, the results indicate that the laminate system maintains equilibrium without excessive local concentrations that could initiate delamination.

In summary, the structural assessment validates the carbon fiber laminate, as a high performance solution, combining low strain, high stiffness, minimal displacement and large safety factors into a lightweight solution. The press molded laminate not only outperforms the PLA and aluminum versions in terms of serviceability and strength, but also demonstrates excellent reliability under combined loading conditions.

7

Discussion

This chapter interprets and compares the results obtained from the numerical analyses of the four different configurations. While the previous chapter focused on presenting displacement, stress and reaction data for each model, this chapter places these findings in contact, highlighting the relative performance of each manufacturing approach. The comparison addresses four main aspects, structural stiffness, material, strength, overall weight and practical considerations related to production time and complexity. By evaluating these factors together, it is possible to identify trade-offs and advantages inherent to each design and manufacturing method, providing a comprehensive understanding of which solution best meets the design requirements for the components.

7.1 Stiffness

Stiffness is a governing criterion for the operational reliability of hydrofoil, as excessive deflections compromise both hydrodynamic efficiency and structural safety. In this study, stiffness was quantified through the maximum displacements observed at the foil tip under four distinct load cases, providing a direct measure of each ability that the model has to resist deformation. The comparative values are presented in Table 7.1.

Table 7.1: Comparison of maximum displacements across all models [mm].

Load Case	**Model 1**	**Model 2**	**Model 3**	**Model 4**
1	31.48	0.60	1.16	7.14
2	535.97	44.96	19.79	21.00
3	563.79	45.51	20.81	27.40
4	20.16	1.79	0.74	0.26

The results reveal a clear hierarchy in stiffness across the models. Model 1, optimized PLA, displays extremely poor stiffness, with displacements above half a meter in the critical load cases, Load Case 2 and 3. Such values are incompatible with practical operation, as the foil would undergo severe geometric distortions, altering its hydrodynamic profile and likely leading to premature failure. The low stiffness of PLA and the original inefficiency of the geometry in bending resistance combine to produce this unfavorable performance.

Model 2, redesigned PLA, demonstrates the decisive role of geometry. Despite relying on the same material with identical elastic properties, displacements are reduced by more than 90% compared to Model 1. Under combined loading, Load Case 3, the maximum tip deflections fall to approximately 45 mm, an order of magnitude improvement over Model 1. This confirms that geometric optimization can, in certain cases, compensate for limitation in material stiffness by redistributing stresses and aligning load paths more effectively. Nevertheless, displacements remain significant compared to the metallic and

composite alternatives, suggesting that PLA, even in the redesigned form, would struggle to meet stiffness requirements for high performance hydrofoils.

Model 3, 3D printed aluminum, achieves further improvements, with maximum deflections around $20\,mm$ under the most demanding conditions. This behavior aligns with the much higher Young's modulus $70\,GPa$ of aluminum, approximately 25 times greater than PLA. The results also confirm the advantage of isotropy, aluminum responds uniformly to loading regardless of direction, producing predictable displacement patterns with limited torsional distortions. Importantly, while aluminum clearly outperforms PLA in stiffness, the difference between Models 2 and 3 is less dramatic than raw modulus might suggest. This highlights that geometry remains a governing factor in stiffness and that material improvements alone cannot fully eliminate large displacements without concurrent design optimization.

Model 4, carbon fiber laminate, exhibits the most complex but also the most efficient stiffness response. With a lay-up sequence of $[0°, 90°]$, the laminate shows highly directional stiffness, loads aligned with the fiber direction $0°$ benefit from an elastic modulus of $130\,GPa$, while transverse loads experience a much lower modulus of $10\,GPa$. This anisotropy explains the mixed performance observed. In lighter vertical loading, Load Case 4, the foil displays exceptional stiffness with displacements as low as $0.26\,mm$, far superior to aluminum. However, in combined or transverse load cases, Load Case 2 and 3, displacements increase to around $20 - 27\,mm$, similar to or slightly worse than aluminum. Thus, carbon fiber provides unmatched stiffness to weight ratio performance but requires precise fiber orientation and lay-up tailoring to fully exploit this potential.

From a comparative perspective, three conclusions emerge. First, PLA in its initial form, Model 1, is structurally inadequate due to excessive displacements, but the redesigned version, Model 2, drastically improves stiffness, highlighting geometry as a first order design parameter. Second, aluminum, Model 3, provides reliable and isotropic stiffness, ensuring predictable deformation under all load cases, though at a significant weight penalty compared to composites, as it is going to be developed in the following sections. Third, carbon fiber laminates, Model 4, deliver the best stiffness to weight ratio, with extremely low deflections when fiber are aligned with the load, but their anisotropy requires careful laminate design to avoid under performance in off axis loading scenarios.

In summary, stiffness considerations show that while geometry can partially mitigate the limitations of PLA, metallic and composite solutions remain more suitable for demanding structural applications. Aluminum offers isotropic reliability, while carbon fiber achieves superior stiffness efficiency provided that manufacturing processes ensure accurate lay-up and orientation. This establishes stiffness as both a material and design driven property, where optimization requires a balance between geometry, material modulus and anisotropy.

7.2 Strength

Strength represents the ultimate capacity of the foil to resist loads without material failure. Unlike stiffness, which governs deformation and serviceability, strength evaluation is tied directly to the intrinsic mechanical limits of each material. To allow meaningful

comparison, the maximum stresses obtained in each model were evaluated against conservative allowable strengths, 35 MPa along the fiber for 3D printed PLA, 250 MPa for aluminum alloys and 900 MPa along the fiber direction for carbon fiber laminates. These values reflect realistic lower bound properties considering 3D printing imperfections and laminate anisotropy. Table 7.2 summarizes the results obtained.

Table 7.2: Maximum principal stress and safety factors for all models.

Load Case	**Model 1**	**Model 2**	**Model 3**	**Model 4**
Allowable Strength [MPa]	35	35	250	900
1	Stress = 24.19 SF = 1.45	Stress = 0.94 SF = 37.20	Stress = 22.06 SF = 11.34	Stress = 181.30 SF = 4.96
2	Stress = 92.56 SF = 0.38	Stress = 7.35 SF = 4.76	Stress = 80.85 SF = 3.09	Stress = 153.34 SF = 5.87
3	Stress = 96.24 SF = 0.36	Stress = 7.16 SF = 4.89	Stress = 84.06 SF = 2.97	Stress = 180.63 SF = 4.98
4	Stress = 6.97 SF = 5.02	Stress = 0.46 SF = 76.10	Stress = 8.24 SF = 30.31	Stress = 8.92 SF = 100.89

For Model 1, optimized PLA, stresses under Load Cases 2 and 3 are nearly three times higher than the conservative strength of 35 MPa. This results in safety factors below 0.4, which clearly predict failure under hydrodynamic and combined loading. Load Case 1 is borderline acceptable with SF ≈ 1.45, but the model provides no reliable margin under realistic conditions. Stress distributions show concentration near the encastre, where bending and shear effects dominate, reflecting the vulnerability of PLA to brittle failure at constrained regions.

Model 2, redesigned PLA, performs significantly better. Geometric changes redistribute stresses, bringing peak values down to the $7 - 8\,MPa$ range in the critical lateral and combined load cases. This corresponds to safety factors of around 4.8 to 4.9, compared with less than 0.4 for the original PLA configuration. Load Case 1 shows an extremely conservative margin, with stresses below 1 MPa and safety factors exceeding 30, while the lighter load combination in Load Case 4 remains well within safe limits. These results demonstrate that while PLA remains a weak material overall, the redesigned is highly effective at mitigating stress concentrations and preventing premature failure, making it a more viable option for moderate loading scenarios.

Model 3, 3D printed aluminum, performs far more favorably. Peak stresses range from 22 MPa in Load Case 1 to 84 MPa in Load Case 3, all of which are comfortably below 250 MPa yield strength threshold. Therefore, safety factors remain between 2.9 and 30 across all cases, ensuring that failure is not expected even under the most demanding scenario. The stress patterns are smoother and more uniformly distributed due to the isotropic nature of the material, which eliminates weak orientations. The critical zones remain at the encastre region and outer surfaces of the strut, but with the aluminum ductility and margin, localized yielding would not compromise overall structural integrity.

Model 4, carbon fiber laminate, presents the highest stress magnitudes, with peaks of $181\,MPa$ under axial or combined loading. While these values appear critical in absolute terms, they remain well below the fiber direction strength of the carbon fiber. This yields safety factors above 4.5 in the critical load cases. However, the analysis also shows transverse stresses of $3-9\,MPa$, which must be compared against the much weaker matrix and inter laminar shear capacity. In practice, this means that while the laminate is strong in fiber aligned directions, it may be vulnerable to delamination or transverse cracking under multi axial states. Proper layer sequencing mitigates some of the risk, but joints and edges remain potential failure sites.

In comparing the four designs, several trends emerge. First, PLA in its original optimized form, Model 1, is unequivocally strength limited, despite design optimization, it cannot survive realistic loading due to low allowable stress and brittle failure modes. Second, the redesigned PLA, Model 2, demonstrates that geometry can play a decisive role in overcoming material weaknesses. By redistributing stresses and reducing concentrations, the redesign achieves safety factors well above unity in all cases, showing that PLA can remain a viable option when loads are moderate and designs are carefully optimized. Third, aluminum, Model 3, provides robust and isotropic strength, offering generous safety factors across all load cases and ensuring ductile, predictable failure modes. Fourth, carbon fiber laminates combine very high strength along fiber directions with anisotropic weaknesses, achieving excellent global safety factors but requiring careful design to avoid inter laminar or transverse failures.

In summary, while PLA as a material is inherently limited in strength, Model 2 proves that intelligent geometric redesign can ensure structural adequacy. Both aluminum and carbon fiber remain stronger overall, with aluminum offering isotropic reliability and carbon fiber achieving the best strength to weight ratios. However, PLA with redesigned geometry provides a surprisingly effective, lightweight and low cost solution, particularly when high loads are not the primary design driver.

7.3 Weight

The weight of the foil is a key factor in assessing its overall performance, particularly in applications where mass directly affects handling, dynamic response and energy consumption. Table 7.3 summarizes the mass of each model, allowing a direct comparison between material choices and design configurations.

Table 7.3: Comparison of model weights [kg].

Model	**Material**	**Weight [kg]**
1	PLA (optimized)	0.161
2	PLA (redesigned)	1.792
3	Aluminum	0.341
4	Carbon Fiber	0.200

Model 1, the original optimized PLA foil, has a mass of $0.161 kg$. Its low weight reflects the inherently low density of PLA and the minimal material use in the original topology optimization. While this provides excellent mass efficiency, the structural performance under realistic loading is limited, as previously discussed in the strength and displacement analyses.

Model 2, the redesigned PLA foil, has a substantially higher mass of $1.792\,kg$, compared to $0.161\,kg$ for the optimized PLA Model 1. The increase arises from additional material incorporated to improve stiffness and redistribute stresses throughout the structure. While the redesign successfully reduces displacements and brings safety factors comfortably above unity across all load cases, the mass increase is significant, more than ten times higher. This illustrates that geometric modifications can dramatically improve structural performance, but they can also drastically affect the lightweight advantage of PLA. It should be carefully evaluated wether the stiffness and strength gains justify the added weight and explore alternative strategies such as local reinforcement, topology optimization or variable infill to achieve a better balance.

Model 3, the aluminum foil, weights $0.341\,kg$, more than twice the redesigned PLA. The higher mass is a direct consequence of the higher density of aluminum compared to PLA. While this adds a weight penalty, aluminum provides isotropic strength and stiffness that are unattainable with PLA. The extra mass may be acceptable in applications where reliability, durability and predictable isotropic behavior are prioritized over minimal weight. The weight increase is also accompanied by substantial improvements in safety factors, which highlight the trade-off between mass and structural robustness.

Model 4, the carbon fiber laminate, weights $0.200\,kg$, positing it between the PLA and the aluminum foil. The stiffness to weight ratio of carbon fiber allows it to carry very high loads with safety factors above 2.5 while keeping the mass significantly lower than aluminum. The layered design of the composite provides excellent strength in the fiber directions, although it requires careful attention to transverse and inter laminar stresses to prevent delamination. From a mass perspective, carbon fiber offers a near optimal balance, low weight and very high directional strength, making it the preferred material when both weight and performance are critical.

In summary, the weight comparison highlights key trade-offs. The original PLA foil is extremely lightweight at $0.161\,kg$ but its strength is limited under realistic loading. The redesigned PLA achieves significantly improved stiffness and strength, providing safe margins across all load cases, but its mass increases substantially. This demonstrates that geometric modifications can compensate for material limitations, but at the cost of major weight increase, which may affect handling or integration in practical applications. Aluminum provides isotropic reliability and excellent structural performance, though with a higher mass than the original PLA. Lastly, carbon fiber laminates achieve high directional strength with minimal mass increase, achieving an exceptional strength to weight ratio and efficient load distribution. Overall, the results demonstrate that weight alone is not the sole criterion, it should exist a balance between material properties, structural performance and application specific demands to select the optimal solution.

7.4 Time and Complexity of Production

The production method and associated complexity play a decisive role in selecting the optimal material and geometry of the foil. While mechanical performance and weight are crucial, the feasibility of fabrication often constraints the design space, especially when transitioning from prototyping to functional parts. Table 7.4 summarizes all the production methods.

Table 7.4: Comparison of production time and complexity for the four foil models

Model	**Production Time**	**Complexity**
Model 1	Short	Low
Model 2	Moderate	Low-Moderate
Model 3	Long	High
Model 4	Long	Very High

For Model 1, optimized PLA, the production process is straightforward, standard Fused Filament Fabrication allows rapid prototyping of complex geometries with minimal setup. Print and post processing requirements are low, making this approach highly accessible and cost effective. The main advantages are speed, availability of materials and minimal equipment requirements. However, the relatively low strength of PLA limits the potential applications and the simplicity of the process does not compensate for this intrinsic material limitation.

Model 2, demonstrates that geometric optimization can substantially improve stiffness and safety margins without dramatically complicating manufacturing. The more complex geometry slightly increases printing time and demands careful attention to print orientation, infill strategy and layer adhesion to preserve the anisotropic properties. Despite the increase in complexity, the fabrication remains feasible on standard printers. This illustrates a critical trade-off, modest increases in production effort and material usage can yield disproportionate improvements in structural performance. The redesign therefore exemplifies how process aware optimization can enhance performance while maintaining low production costs.

In contrast, Model 3 requires additive manufacturing processes capable of handling metals, which inherently involve higher temperature, specialized equipment and post processing steps such as support removal, surface finishing and heat treatment. These additional stages significantly extend production time and complexity, but they can be justified by the superior isotropic strength, ductility and reliability of aluminum. The process enables complex geometries similar to PLA, but with mechanical performance suitable for demanding load cases, highlighting the trade-off between manufacturing complexity and structural capability.

Model 4 introduces yet another dimension of complexity. The press molding of 10 layers in a $0°/90°$ lay-up requires precise fiber placement, curing cycles and strict quality control to ensure alignment and avoid defects. Even small deviations in layer orientation or bonding can drastically affect strength and stiffness, making the process sensitive and

labor intensive. Post processing, trimming and finishing steps further add to production time and cost. However, the material achieves an exceptional strength to weight ratio, providing performance that neither PLA nor aluminum can match. The manufacturing complexity is therefore justified when maximum performance and minimal mass are critical, particularly in aerospace or high performance marine applications.

Overall, comparing the four models reveals clear trade-offs. PLA models are fast, low cost and simple to produce, but inherently limited in strength and stiffness. Redesigned PLA demonstrates that modest increases in production effort can yield significant structural gains, illustrating the value of process aware design. Aluminum offers reliable mechanical performance with isotropic behavior but at the expense of more complex production. Carbon fiber laminates maximize strength to weight ratio efficiency but require careful manufacturing and quality assurance, making them the most complex to produce.

This analysis underscores that, time, manufacturing complexity and material behavior are deeply interconnected and optimal design decisions require balancing these factors against mechanical requirements, production constraints and cost considerations. Production feasibility is therefore not merely a secondary concern, it fundamentally shapes which material and geometry combinations are practical and sustainable for real world applications.

7.5 Cost

Beyond stiffness, strength, weight and production complexity, economic considerations are a fundamental factor in material selection and manufacturing strategy. The cost analysis of the four foil models considers three primary components, material price, process duration and production complexity. Where available, market data and literature estimates for 3D printing, metal additive manufacturing and composite press molding are incorporated to provide realistic comparisons.

Polylactic acid (PLA) filament is widely recognized for its affordability, typically ranging from $20 € - 30 €$ per kilogram. The optimized PLA foil weights only $0.161\,kg$, resulting in negligible material cost of roughly $3 € - 5 €$ per part. Fused Deposition Modeling 3D printing requires moderate build times, 4-13 hours depending on layer resolution and infill density, but minimal post-processing. Labor demands are low due to high levels of automation and equipment requirements are comparatively modest. Collectively, these factors make PLA highly cost effective, particularly for rapid prototyping, educational applications or load functional components. Its low material and processing costs are corroborated by multiple sources highlighting the economic advantage that PLA presents for small scale production, [80] [81].

The redesigned PLA foil weights more at $1.792\,kg$, raising the material cost to approximately $35 € - 55 €$ per part. Print times increase marginally due to additional material and potentially denser infill or modified layer strategies aimed at enhancing stiffness. Despite the slight increase in printing time and filament usage, production complexity remains similar to the original model. Post-processing requirements are minimal and automate operation minimizes labor costs. The modest cost increase is justified by

the improved mechanical performance, reduced tip deflections, better load redistribution and safety factors exceeding unity across all load cases. This demonstrates that careful geometric optimization can provide meaningful structural gains at an economic expense, a conclusion supported by recent studies, [82].

The aluminum foil requires metal additive manufacturing, specifically bound metal deposition, a metal FDM process where a metal filled thermoplastic filament is extruded layer by layer to form a "green" part. This is followed by debinding to remove the polymer binder and sintering to densify the metal, producing a fully metallic component. Aluminum powders for BMD are considerably more expensive than PLA, typically $93 € - 140 €$ per kilogram and with a part mass of $0.350\ Kg$, the material cost per foil is approximately $32 € - 49 €$. Total production time is substantial, often taking multiple days due to printing, debinding and sintering steps. The process also requires specialized equipment, controlled atmospheres during sintering and skilled operators, all of which contribute to higher costs. Despite this, the elevated expense can be justified by the isotropic mechanical properties of the foil, as well as ductility and structural reliability, which cannot be achieved with PLA. Literature confirms that the metal FDM processes are costlier than polymer printing but enable complex geometries and high performance metallic components suitable for demanding structural applications, [69].

The carbon fiber laminate foil, consisting of 10 layers of 0°/90° prepreg carbon fiber, weights $0.199\ kg$. Prepreg materials are relatively expensive, typically $50 € - 100 €$ per kilogram, resulting in material costs of approximately $10 € - 20 €$ per part. Press molding requires dedicated tooling, temperature and pressure controlled curing and skilled labor, increasing both direct and indirect costs. However, the resulting part achieves an exceptional strength to weight ratio, high directional stiffness and minimal mass. The combination of high performance material and precise manufacturing can justify the elevated cost in applications where mechanical efficiency and performance are essential, [83].

Table 7.5 summarizes the values for each manufacturing process.

Table 7.5: Estimated cost per foil model [€].

Model	**Material**	**Weight [kg]**	**Component Cost [€]**
Model 1	PLA	0.161	3–5
Model 2	PLA	1.796	35–55
Model 3	Aluminum	0.350	33–47
Model 4	CF	0.199	10–20

The economic comparison reveals clear trade-offs. PLA based foils are extremely low cost and highly automated but limited by their intrinsic mechanical properties, constraining their use in high load scenarios. Aluminum foils provide robust isotropic strength and reliability but require more extensive materials, specialized equipment and longer production times, reflecting a moderate cost performance trade-off. Carbon fiber laminates achieve the highest strength to weight ratio, but the cost is elevated due to both material price and labor intensive press molding. These findings underscore that while cost is a critical factor, it must be balanced with structural performance, stiffness, strength and

application, specific requirements to inform optimal material selection and manufacturing strategy.

8

Conclusions and Future Work

The final chapter summarized the key findings of this study and highlights the implications of the different manufacturing methods on structural performance, weight and production efficiency. It reflects on the comparative evaluation of the five analyzed models, integrating insights from the numerical simulations and the discussions on stiffness, strength and manufacturability. This chapter also outlines potential directions for further research and development, emphasizing opportunities to improve design optimization, material selection and production techniques for future iterations of the model.

8.1 Conclusions

This study encompassed multiple stages of the design, analysis and evaluation of the foil and strut assembly, highlighting both the challenges and opportunities while developing a functional and experimentally flexible test vessel. The initial phase focused on the calculations and later the development of *SolidWorks* macros, which facilitated rapid generation of various foil and strut geometries. This automation significantly accelerated the design process and allowed the exploration of a wide range of hydrodynamic profiles, demonstrating the utility of computational tools in the early stages of structural design.

The geometric design of the redesigned foil presented a significant challenge due to the need to balance structural performance, actuator placement and manufacturability. Throughout this work, multiple configurations were evaluated to identify a practical and mechanical sound design. The implemented design successfully integrated the servo actuator system, providing reliable actuation while maintaining structural integrity. The arrangement of the actuator and the overall geometry allowed for the intended load transfer and motion control, demonstrating that the chosen configuration meets the objectives of the test vessel while ensuring sufficient mechanical performance and experimental functionality.

The numerical analysis considered four distinct manufacturing cases, two based on PLA, the optimized and redesigned model, one in aluminum and one in carbon fiber laminates. Each model was analyzed under four representative load cases, providing detailed outputs on displacement fields, stress distributions and reaction forces. Material definitions were chosen to reflect the nature of each process, anisotropic properties for PLA to account for 3D printing directionality, isotropic behavior for aluminum and an orthotropic laminate representation for carbon fiber with a $0°/90°$ lay-up. While simplifications were necessary, particularly in neglecting certain inter laminar effects, the modeling framework provided consistent and comparable insight into stiffness, strength and safety margins across the four candidates.

The comparative results highlighted clear trends. The optimized PLA, Model 1, proved insufficient in strength, with stresses exceeding the conservative tensile strength of the polymer under hydrodynamic and combined loading. The redesigned PLA, Model 2, by

contrast, successfully controlled displacements and achieved safety factors above unity in all cases, but its weight increased significantly. Nevertheless, is still considered well suited for experimental prototyping, especially due to its low production costs and rapid manufacture. The aluminum model, Model 3, demonstrated excellent isotropic strength and ductility, maintaining safety factors well above 2 across all cases, but at the expense of higher mass and significantly longer production time due to the complexities of metal additive manufacturing. The carbon fiber laminate, Model 4, provided the highest stiffness to weight ratio and excellent strength in the fiber directions, but its anisotropy introduced potential risks of delamination or matrix cracking under complex multi axial stresses, requiring careful attention to lay-up and manufacturing quality.

Taken together, these findings indicate that Model 2, the redesigned PLA foil, is the most appropriate choice for the current stage of the project. Its balance between mechanical adequacy, low mass and rapid low cost manufacturability makes it ideal for iterative design and repeated experimental testing. Once the design has been validated and operational performance requirements become more demanding, more advanced materials such as carbon fiber laminates or forged composited could be employed to achieve superior long term performance.

In summary, this work demonstrates that the integration of automated design tools, careful geometric optimization and systematic numerical evaluation can effectively guide decision making in the development of experimental and functional structures. Beyond the specific findings for this foil and strut assembly, the methodology presented here provides a robust framework for future projects that require rapid iteration, experimental flexibility and informed trade-offs between material choice, manufacturability and mechanical performance.

8.2 Future Work

Although this study successfully evaluated multiple designs and manufacturing approaches for the strut and foil assembly, there are still several avenues for further development and refinement. One important direction is the continued development of the *SolidWorks* macros used to generate the foils and strut geometries. Enhancing these tools could allow for an even faster iteration, integration of more complex geometries and automated checks for manufacturability or structural constraints, further streamlining the design process.

Exploration of alternative actuator systems and placements also represent a key area for future work. While the current servo configuration met the basic functional requirements, other types of actuators, control strategies or placement options could improve response time, reduce energy consumption or minimize weight. Additionally, the development of a retractable system for the strut would also add functional versatility, particularly for experimental setups or testing in constrained environments.

From a structural analysis perspective, the present study relied on simplified material models to enable comparison across the four models, treating PLA as anisotropic, aluminum as isotropic and carbon fiber as anisotropic. While this provided useful insights, it does not fully capture the process dependent behavior of additively manufactured parts

or the inter layer effects in composites. Future work should therefore include more refined anisotropic analyses, complemented by experimental testing of manufactured prototypes to validate numerical predictions. In particular, systematic evaluation of manufacturing parameters, such as printing settings in PLA, process conditions for bound metal deposition and curing quality for carbon fiber, will be essential to establish reliable design data and ensure that structural performance performance translates from simulation to practice.

Further investigations could also incorporate fluid-structure interaction through computational fluid dynamic (CFD). Evaluating the hydrodynamic loads and resulting structural responses in a coupled CFD-FEA framework would provide a more realistic assessment of performance, particularly for applications where lift, drag and torsional effects are significant.

Other potential future studies include exploring alternative manufacturing methods, such as hybrid approaches that combine additive manufacturing with traditional composites or experimenting with lightweight infill structures for 3D printing to further optimize stiffness to weight ratios. Finally, long term durability testing, including fatigue and environmental exposure, would be essential for validating the designs under realistic operating conditions, ensuring that the test vessel and future operational versions maintain performance over time.

Collectively, these directions offer a road map for refining both the design methodology and the physical implementation of the hydrofoil assembly, providing opportunities to enhance performance, manufacturability and experimental versatility.

Bibliography

[1] John R. Meyer Jr. *Ships That Fly: A Story of the Modern Hydrofoil.* Accessed: 2025-02-27. Hydrofoil Technology, Inc., 1990.

[2] America's Cup. *The Boats: AC75, AC40 & LEQ12.* https://www.americascup.com/the-boats.
Accessed: 2025-02-27.

[3] SurferToday. *The Foil Windsurfing Experience in the 1970s-1980s.* https://www.surfertoday.com/windsurfing/the-foil-windsurfing-experience-in-the-1970s-1980s.
Accessed: 2025-02-27. 2020.

[4] Lift Foils. *A complete history and guide to Hydrofoil Surfing.* https://liftfoils.com/stories/hydrofoil-surfing-the-complete-history-and-guide.
Accessed: 2025-02-27. 2020.

[5] America's Cup. *Full-On Flying: Foiling Machines.* https://www.americascup.com/news/2489_FULL-ON-FLYING-FOILING-MACHINES.
Accessed: 2025-02-27. 2020.

[6] Rodriquez Consulting. *Hydrofoil Superyacht.* https://rodriquezconsulting.com/hydrofoil-superyacht/.
Accessed: 2025-02-27. 2020.

[7] Cal-Tek. *Proceedings of the i3M 2021 EMSS Conference.* https://www.cal-tek.eu/proceedings/i3m/2021/emss/038/pdf.pdf.
Accessed: 2025-02-27. 2021.

[8] Mobyfly. *Mobyfly.* https://mobyfly.com/.
Accessed: 2025-02-27. 2020.

[9] Associated Press. *Stockholm launches electric hydrofoil ferry in archipelago.*
Accessed: 2025-03-01. 2024.
https://apnews.com/article/stockholm-electric-ferry-archipelago-sweden-clean-energy-e2b39de682f97e657538c61999c8291a.

[10] SNAME. *The Hydrofoil: A Historical Review of Development and Application.*
Accessed: 2025-03-01. 1953.
https://www.foils.org/wp-content/uploads/2018/01/SNAMEtransactionsVol61-1953.pdf.

[11] SNAME. *Hydrofoil Handbook Volume I.*
Accessed: 2025-03-02. 1954.
https://www.foils.org/wp-content/uploads/2018/01/HFhdbkVol_I_1954.pdf.

[12] INEOSTEAM. *Carbon Fibre.*
Accessed: 2025-03-02. 2025.
https://ineosteamuk.americascup.com/en/articles/400_Carbon-Fibre.html.

[13] Michael F. Ashby. *Materials Selection in Mechanical Design (2nd Edition).* Accessed: 2025-03-02. 1999. https://www.utc.fr/~hagegebe/UV/MQ12/CORRECTIONS_TD/%5BASHBY99%5D%20-%20Materials%20Selection%20In%20Mechanical%20Design%202Ed.pdf.

[14] Gurit. *Guide to Composites.* Accessed: 2025-03-02. 2022. https://www.gurit.com/wp-content/uploads/2022/12/guide-to-composites-1.pdf.

[15] University of Wisconsin-Madison. *Additive Manufacturing.* Accessed: 2025-03-02. 2025. https://additive-mfg.me.wisc.edu/?p=2717.

[16] Nils Lundqvist and Elias L. Favrum. *Hydrodynamic Design, System Design, and Control System for a Model-Scale Foiling Boat.* Available at https://www.chalmers.se.
Master's thesis, Chalmers University of Technology, Gothenburg, Sweden. Accessed: 2025-03-02. 2022.

[17] Hugh R.R. Dougherty. *The Design, Verification, and Validation of a Personal Hydrofoil Craft.* Available at https://vtechworks.lib.vt.edu/.
Master's thesis, Virginia Polytechnic Institute and State University, Blacksburg, Virginia, USA. Accessed: 2025-03-02. 2023.

[18] Pol Bernad Serra. *Hydrofoil Design and Construction.*
Bachelor's thesis, UPC ESEIAAT, Spain. Accessed: 2025-03-02. 2019.

[19] F. L. Bento. "A Functional Analysis of an Additively Manufactured Bellcrank with Long Fibre Reinforcement".
Accessed: 2025-03-02. MA thesis. Instituto Superior Técnico, Universidade de Lisboa, 2019.

[20] X. Wang et al. "3D Printing of Polymer Matrix Composites: A Review and Prospective". In: *Composites Part B: Engineering* 110 (2017).
Accessed: 2025-03-02, pp. 442–458. DOI: 10.1016/j.compositesb.2016.11.034.

[21] B. Jackson. *Northrop Grumman Granted Patent for Composite Fiber 3D Printing.* Accessed: 2025-03-02. 2019. https://3dprintingindustry.com/news/northrop-grumman-granted-patent-for-composite-fiber-3d-printing-149306/.

[22] J. Frketic, T. Dickens, and S. Ramakrishnan. "Automated Manufacturing and Processing of Fiber-Reinforced Polymer (FRP) Composites: An Additive Review of Contemporary and Modern Techniques for Advanced Materials Manufacturing". In: *Additive Manufacturing* 14 (2017).
Accessed: 2025-03-02, pp. 69–86. DOI: 10.1016/j.addma.2017.01.003.

[23] Andrea Zocca et al. "Challenges in the Technology Development for Additive Manufacturing in Space". In: *Chinese Journal of Mechanical Engineering: Additive Manufacturing Frontiers* 1.2022 (2022).
Accessed: 2025-05-20, p. 100018. DOI: 10.1016/j.cjmeam.2022.100018.

[24] Chanun Suwunpreecha and Anchalee Manonukul. "A Review on Material Extrusion Additive Manufacturing of Metal and How It Compares with Metal Injection Moulding". In: *Metals* 12.3 (2022).
Accessed: 2025-03-02, p. 429. DOI: 10.3390/met12030429.
https://www.mdpi.com/2075-4701/12/3/429.

[25] Desktop Metal. *Deep Dive: Bound Metal Deposition (BMD).*
Accessed: 2025-03-02. 2022.
https://www.desktopmetal.com/resources/deep-dive-bmd.

[26] Proto3000. *Metal 3D Printing: Bound Metal Deposition vs Single Pass Jetting.*
Accessed: 2025-03-02. 2021.
https://proto3000.com/3d-printing/metal-3d-printing-bound-metal-deposition-vs-single-pass-jetting/.

[27] Tommaso Mancia et al. "Effect of build-up orientation angle and printing speed on mechanical properties and micro- and macro-defect formation in 17-4 PH stainless steel components manufactured by Bound Metal Deposition". In: *The International Journal of Advanced Manufacturing Technology* 132.9-10 (2024).
Accessed: 2025-05-20, pp. 4285–4295. DOI: 10.1007/s00170-024-13628-2.

[28] Sakine Kiratli. "An Overview of the Mechanical Characterizations and Applications of Chopped Fiber Reinforced Composites". In: *International Journal of Advanced Natural Sciences and Engineering Researches* 7.4 (2023).
Accessed: 2025-03-02, pp. 186–190. DOI: 10.59287/ijanser.2023.7.4.648.
https://www.researchgate.net/publication/370674418_An_overview_of_the_mechanical_characterizations_and_applications_of_chopped_fiber_reinforced_composites.

[29] Abdullah Sayam et al. "A Review on Carbon Fiber-Reinforced Hierarchical Composites: Mechanical Performance, Manufacturing Process, Structural Applications and Allied Challenges". In: *Carbon Letters* 32 (2022).
Accessed: 2025-03-02, pp. 1173–1205. DOI: 10.1007/s42823-022-00358-2.
https://link.springer.com/article/10.1007/s42823-022-00358-2.

[30] Easy Composites. *Comparing the Mechanical Properties of Forged Carbon Fibre.*
Accessed: 2025-03-02. 2025.
https://www.easycomposites.co.uk/learning/mechanical-properties-of-forged-carbon-fibre.

[31] Paolo Feraboli et al. *Lamborghini "Forged Composite®" Technology for the Suspension Arms of the Sesto Elemento.*
Accessed: 2025-03-02. 2010.
https://www.swcompositeworks.com/wp-content/uploads/2021/03/08a1d5_7154fa58ce5c4bfcbf0506723c8d0c4b.pdf.

[32] Covalo Motion. *Exploring Forged Carbon Fiber: Versatile, Cost-Effective, and Lightweight.* Accessed: 2025-03-02. 2025.
https://covalomotion.com/exploring-forged-carbon-fiber-versatile-cost-effective-and-lightweight/.

[33] Easy Composites. *Forged Carbon Fibre Mould Design and Strength Optimisation.* https://www.easycomposites.eu/learning/forged-carbon-mould-design-and-optimisation.
Accessed: 2025-05-20. 2024.
https://www.easycomposites.eu/learning/forged-carbon-mould-design-and-optimisation.

[34] Nikhil Gupta and Manjusri Misra. "Lightweight composite materials processing". In: *Lightweight Ballistic Composites*. 2nd ed.
Accessed: 2025-03-02. Elsevier, 2016, pp. 133–161. ISBN: 978-0-08-100406-7. DOI: 10.1016/B978-0-08-100406-7.00006-4.
https://www.sciencedirect.com/science/article/pii/B9780081004067000064.

[35] Leonhard K. Doppelbauer et al. "A macroscopic model of the compaction process during compression molding of carbon fiber sheet molding compounds". In: *Composites Part A: Applied Science and Manufacturing* 169 (2023).
Accessed: 2025-03-02, p. 107535. DOI: 10.1016/j.compositesa.2023.107535.
https://www.sciencedirect.com/science/article/pii/S1359835X23001112.

[36] Ltd. Cowin Extrusion Machinery Co. *8 Carbon Fibre Composite Moulding Techniques.* https://www.cowinextrusion.com/8-carbon-fibre-composite-moulding-techniques/.
Accessed: 2025-05-20. 2025.
https://www.cowinextrusion.com/8-carbon-fibre-composite-moulding-techniques/.

[37] United States Patent and Trademark Office. *Autonomous Hydrofoil Control System.*
Accessed: 2025-03-03. 2023.
https://patentimages.storage.googleapis.com/a8/e1/0c/9e4b5184b907ae/US20230382496A1.pdf.

[38] Chinese Patent Office. *Hydrofoil System.*
Accessed: 2025-03-03. 2018.
https://patents.google.com/patent/CN105905232B/en?oq=+CN105905232B.

[39] United States Patent and Trademark Office. *Hydrofoil System for Outboard Boats.*
Accessed: 2025-03-03. 2019.
https://patentimages.storage.googleapis.com/25/e3/1c/f1cd73f170d09d/US10179628.pdf.

[40] Dutch Patent Office. *Hydrofoil System Integrated into Hull Units.*
Accessed: 2025-03-03. 2020.
https://patents.google.com/patent/NL2026134B1/en?oq=Patent+NL2026134B1.

[41] Navier Electric Hydrofoiling Boats. *Navier N30 Pioneer Edition*. https://www.navierboat.com/product.
Accessed: 2025-03-04. 2024.

[42] Candela. *Technology - Candela*.
Accessed: 2025-03-04. 2024.
https://candela.com/technology/.

[43] SeaBubbles. *Our Boats - SeaBubbles*.
Accessed: 2025-03-04. 2024.
https://www.seabubbles.com/our-boats/.

[44] FOILER Official Website. *FOILER Specifications*.
Accessed: 2025-03-04. 2025.
https://foiler.com/page/specifications.

[45] Greater Geneva Bern area (GGBA). *MobyFly to Launch its First Zero-Emission Hydrofoil Boats in 2025*.
Accessed: 2025-03-04. 2023.
https://ggba.swiss/en/mobyfly-to-launch-its-first-zero-emission-hydrofoil-boats-in-2025/.

[46] R. H. Meyer and H. Dugoff. *Development of Automatic Control Systems for Hydrofoil Craft*.
Accessed: 2025-03-04. 1971.
https://foils.org/wp-content/uploads/2017/12/Development-of-Automatic-Control-Systems-For-Hydrofoil-Craf-71234.pdf.

[47] Viktor Åkerblom and Axel Eriksson. *Object Detection and Avoidance Using LiDAR on a Hydrofoil Boat*.
Accessed: 2025-03-04. 2018.
https://lup.lub.lu.se/luur/download?func=downloadFile&recordOId=8969793&fileOId=8969794.

[48] Mohanraj Thangamuthu et al. *Fluid Power Actuators*.
Accessed: 2025-03-04. 2020. DOI: 10.1002/9781119662693.ch8.

[49] Eltra Trade. *Rodless Pneumatic Cylinder Working Principle*.
Accessed: 2025-03-04. 2024.
https://eltra-trade.com/blog/rodless-pneumatic-cylinder-working-principle.

[50] Power & Motion Staff. *Fundamentals of Hydraulic Motors*.
Accessed: 2025-03-04. 2014.
https://www.powermotiontech.com/hydraulics/hydraulic-pumps-motors/article/21884401/fundamentals-of-hydraulic-motors.

[51] Bojan Polajžer, Boštjan Zagrajšek, and Matevž Hriberšek. *A Practical Approach to Hydrofoil Vessel Control in Various Operating Conditions*.
Accessed: 2025-03-04. 2019. DOI: 10.3390/en12122423.
https://www.mdpi.com/1996-1073/12/12/2423.

[52] Electrical Technology. *Types of Electric Motors – AC, DC, and Special Motors*. Accessed: 2025-03-13. 2021. https://www.electricaltechnology.org/2021/01/types-of-electric-motors.html#dc-motor.

[53] Monolithic Power Systems. *Types of AC Motors*. Accessed: 2025-03-13. 2025. https://www.monolithicpower.com/en/learning/mpscholar/electric-motors/ac-motors/types-of-ac-motors.

[54] Hermitage Automation. *Difference Between Induction and Synchronous Motor*. Accessed: 2025-03-13. 2025. https://hermitageautomation.com/difference-induction-and-synchronous-motor/.

[55] Monolithic Power Systems. *An Introduction to Stepper Motors, DC Motors, and Motor Drivers*. Accessed: 2025-03-15. 2023. https://www.monolithicpower.com/learning/resources/an-introduction-to-stepper-motors-dc-motors-and-motor-drivers.

[56] Haredata Electronics. *Brushed DC Motors vs Brushless DC Motors*. Accessed: 2025-03-13. 2025. https://www.haredataelectronics.co.uk/brushed-dc-motors-vs-brushless-dc-motors.

[57] Frank M. White. *Fluid Mechanics*. McGraw-Hill Education, 9th Edition. Accessed: 2025-03-07. 2016.

[58] Jr. John D. Anderson. *Fundamentals of Aerodynamics*. Accessed: 2025-03-07. New York, NY, 2017.

[59] Philip M. Gerhart et al. *Munson, Young and Okiishi's Fundamentals of Fluid Mechanics*. Accessed: 2025-03-07. 2016.

[60] Odd M. Faltinsen. *Hydrodynamics of High-Speed Marine Vehicles*. https://www.cambridge.org/9780521845687. Cambridge University Press, ISBN: 978-0-521-84568-7. Accessed: 2025-03-07. 2005.

[61] J. N. Reddy. *An Introduction to the Finite Element Method*. 2nd ed. Accessed: 2025-03-02. New York: McGraw-Hill, 1993. ISBN: 9780070513554.

[62] T. Speer. *Hydrofoil Design (H105)*. http://www.tspeer.com/Hydrofoils/h105/h105.htm. Accessed: 2025-03-20. n.d.

[63] Hitec RCD. *HS-5086WP Metal Gear Micro Digital Waterproof Servo*. https://hitecrcd.com/hs-5086wp-metal-gear-micro-digital-waterproof-servo/. Accessed: 2025-04-20.

[64] Artemis Technologies. *Artemis eFoiler®*. https://www.artemistechnologies.co.uk/efoiler/.
Accessed: 2025-04-20. 2025.

[65] Artemis Technologies. *Artemis eFoiler® – How it works*. https://www.youtube.com/watch?v=KQV7bcrcmsk.
Accessed: 2025-04-20. 2025.

[66] M. Khosravani et al. "Characterization of 3D-printed PLA parts with different printing parameters". In: *Scientific Reports* 12.1 (2022).
Accessed: 2025-07-20, pp. 1–10. DOI: 10.1038/s41598-022-05005-4.

[67] Y.-H. Huang and C.-Y. Lin. "Measurement of Orthotropic Material Constants and Discussion on 3D Printing Parameters in Additive Manufacturing". In: *Applied Sciences* 12.13 (2022).
Accessed: 2025-07-20, p. 6812. DOI: 10.3390/app12136812.

[68] Jean-Pierre Kruth, Ming C Leu, and T. Nakagawa. "Progress in additive manufacturing and rapid prototyping". In: *CIRP Annals* 47.2 (2005).
Accessed: 2025-07-20, pp. 525–540.

[69] William E. Frazier. "Metal additive manufacturing: A review". In: *Journal of Materials Engineering and Performance* 23.6 (2014).
Accessed: 2025-07-20, pp. 1917–1928.

[70] MIT 6.777 Course. *Material Property Database – Aluminum (including alloys with Si or Si+Cu)*.
Accessed: 2025-07-20. 2025.
https://www.mit.edu/~6.777/matprops/aluminum.htm.

[71] ASTM International. *ASTM D3039/D3039M-17: Standard Test Method for Tensile Properties of Polymer Matrix Composite Materials*.
Accessed: 2025-07-20. 2017.

[72] ASTM International. *ASTM D3518/D3518M-18: Standard Test Method for In-Plane Shear Response of Polymer Matrix Composite Materials by Tensile Test of a ±45° Laminate*.
Accessed: 2025-07-20. 2018.

[73] Partsnap. *PLA Material Properties for FFF 3D Printing*. https://www.partsnap.com/3d-printing/fff/material-properties/.
Accessed: 2025-07-20. 2023.

[74] Creallo. *PLA FDM Material Capability Datasheet*. https://creallo.com/en/capability/material/FF/
Accessed: 2025-07-20. 2023.

[75] S. R. Subramaniam et al. "Preliminary Investigations of Polylactic Acid (PLA) Properties". In: *AIP Conference Proceedings* 2059.1 (2019).
Accessed: 2025-07-20, p. 020038. DOI: 10.1063/1.5085981.
https://pubs.aip.org/aip/acp/article-abstract/2059/1/020038/790230/Preliminary-investigations-of-polylactic-acid-PLA?redirectedFrom=fulltext.

[76] ASM International. *Aluminum 6061-T6; 6061-T651*. https://asm.matweb.com/search/specificma
Accessed: 2025-07-20.

[77] ASM International. *Aluminum 7075-T6; 7075-T651*. https://asm.matweb.com/search/specificma
Accessed: 2025-07-20.

[78] Kimiyoshi Naito, Yuto Seki, and Ryo Inoue. "Static and Fatigue Tensile Properties of Cross-Ply Carbon-Fiber-Reinforced Epoxy-Matrix-Composite Laminates with Thin Plies". In: *Journal of Composites Science* 7.4 (2023).
Accessed: 2025-07-20, p. 146. DOI: 10.3390/jcs7040146.
https://doi.org/10.3390/jcs7040146.

[79] Qing Liu et al. "Micromechanics Modeling of Transverse Tensile Strength for Unidirectional CFRP Composite". In: *Materials* 15.21 (2022).
Accessed: 2025-07-20, p. 8577. DOI: 10.3390/ma15218577.
https://pmc.ncbi.nlm.nih.gov/articles/PMC9738460/pdf/materials-15-08577.pdf.

[80] Ian Gibson, David Rosen, and Brent Stucker. *Additive Manufacturing Technologies*. 3rd.
Accessed: 2025-07-20. Springer, 2021.

[81] T. D. Ngo et al. "Additive manufacturing (3D printing): A review of materials, methods, applications and challenges". In: *Composites Part B: Engineering* 143 (2018).
Accessed: 2025-07-20, pp. 172–196. DOI: 10.1016/j.compositesb.2018.02.012.

[82] S. Yang, X. Zhang, and H. Chen. "Design-for-additive-manufacturing: Methods and applications". In: *Journal of Manufacturing Systems* 62 (2022).
Accessed: 2025-07-20, pp. 376–392. DOI: 10.1016/j.jmsy.2021.12.010.

[83] P. K. Mallick. *Fiber-Reinforced Composites: Materials, Manufacturing, and Design*. 3rd.
Accessed: 2025-07-20. CRC Press, 2007.

A

Hydrofoil Profile Data

A.1 H005 profile data

The following appendix includes the original hydrofoil profile document of the Speer H005.

Low Reynolds Number Hydrofoils

Most hydrofoil sections, like the Eppler E817, are designed for small ships traveling at high speeds, typically 40 knots or more. Sailing hydrofoil boats have different requirements. Their hydrofoils are physically smaller, and they operate at slower speeds, say, 20 to 30 knots, so their Reynolds number range is much lower. This calls for a different design philosophy. The H105 hydrofoil section was designed to avoid laminar separation and ventilation when operating at low speeds and moderate angles of attack, while still having low velocities at small angles of attack to avoid caviatation at high speeds.

Eppler used a rooftop philosophy in the design of the E817, which has a constant maximum velocity at the design angle of attack. This results in a pressure recovery zone aft of the rooftop which is too short for low Reynolds numbers, and the flat rooftop makes for a tendency toward leading edge stall.

The H105 section has convex velocity profiles, which use the entire surface to control the position of the laminar separation bubble. The location of the maximum velocity also changes with angle of attack. The H105 is restrained in its use of aft loading to avoid possible trailing edge separation problems. The result is a hydrofoil which sacrifices some of the upper range of the cavitation envelope for a significantly higher maximum lift, while still maintaining low drag and a high incipient cavitation speed.

The H002 section shown for comparison is an earlier design. This hydrofoil was designed for a higher range of angles of attack than the H005. It had a similar upper surface design approch to the H005, but he lower surface used a rooftop distribution similar to the Eppler hydrofoils. This section had a higher minimum drag, and slightly lower incipient cavitation speed. Its biggest drawback was its excessive aft loading, which may not have worked well in practice. Its chief advantage, higher maximum lift, was more than required since hdyrofoil craft tend to operate within a narrow range of pitch attitudes.

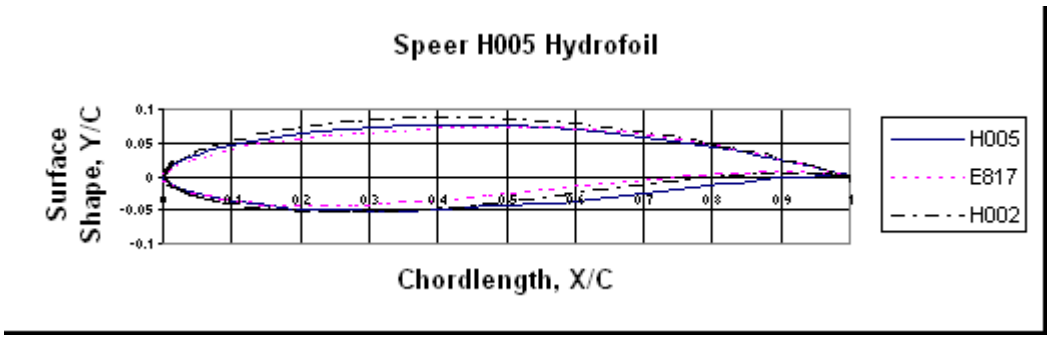

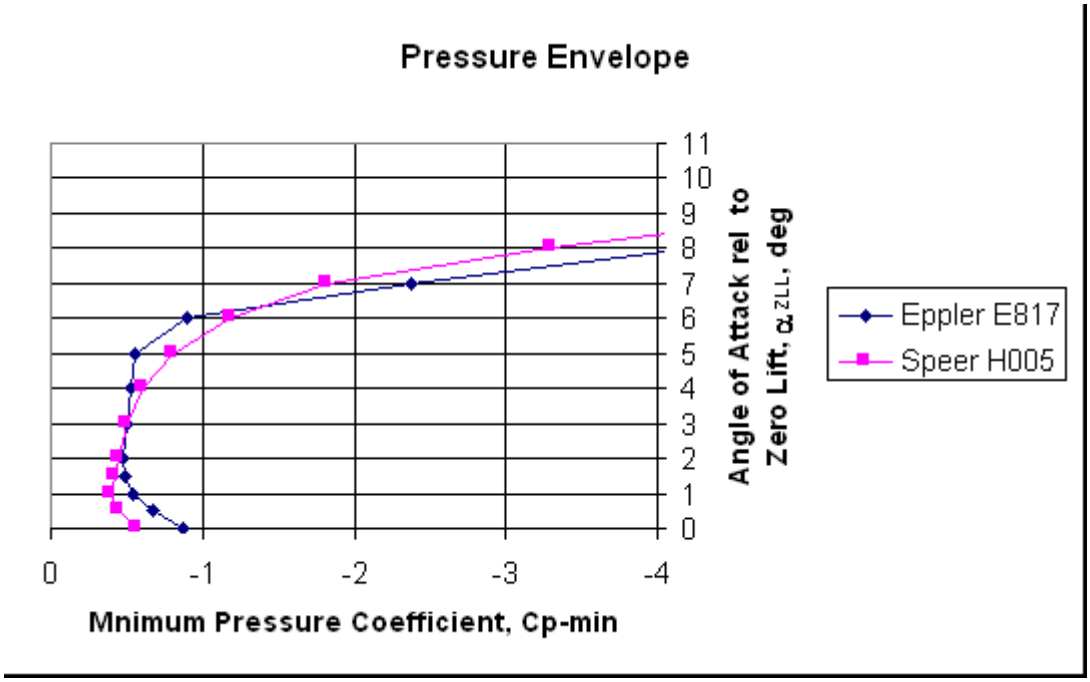
Pressure Envelope
Angle of Attack rel to Zero Lift, α ZLL, deg
Mnimum Pressure Coefficient, Cp-min
Eppler E817
Speer H005

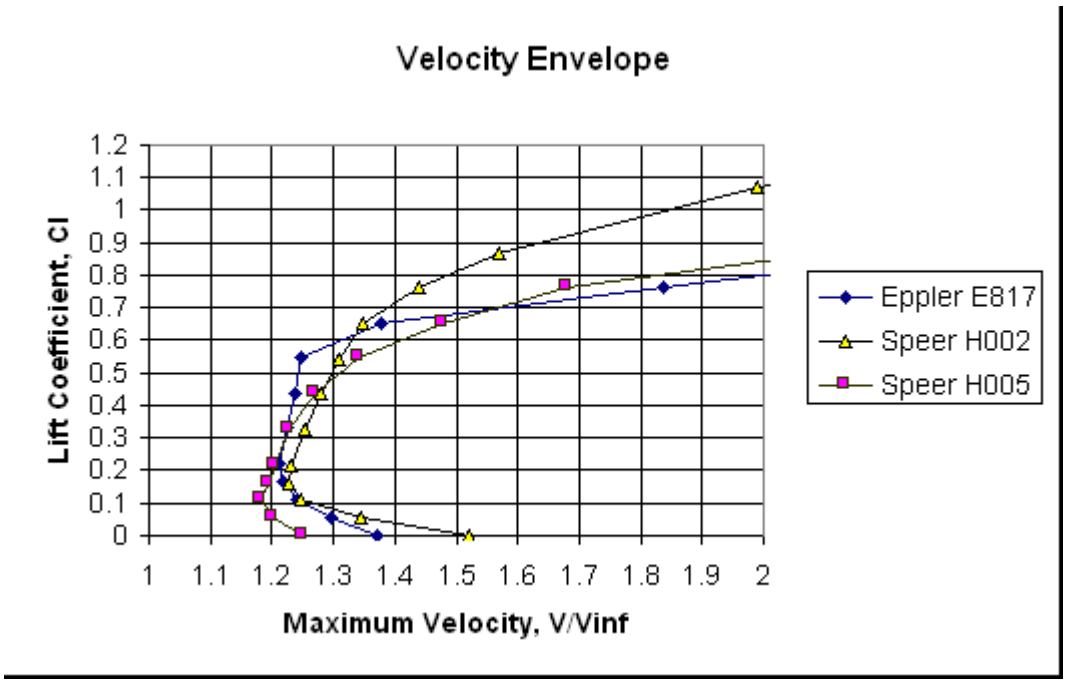
Velocity Envelope
Lift Coefficient, Cl
Maximum Velocity, V/Vinf
Eppler E817
Speer H002
Speer H005

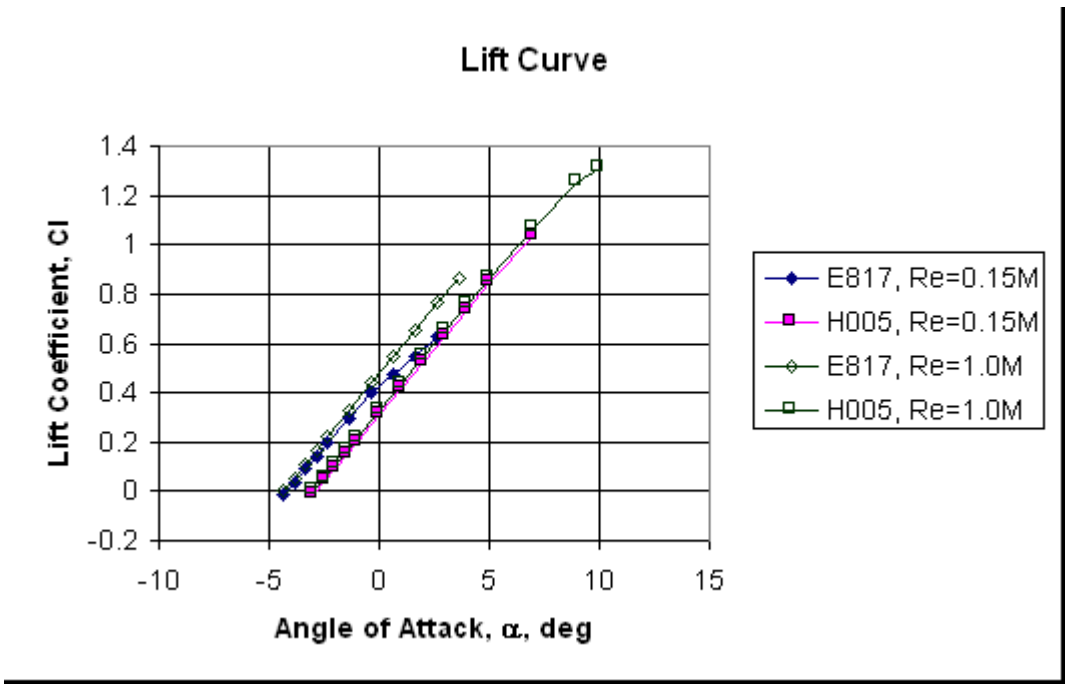
Lift Curve
Lift Coefficient, Cl
Angle of Attack, α, deg
E817, Re=0.15M
H005, Re=0.15M
E817, Re=1.0M
H005, Re=1.0M

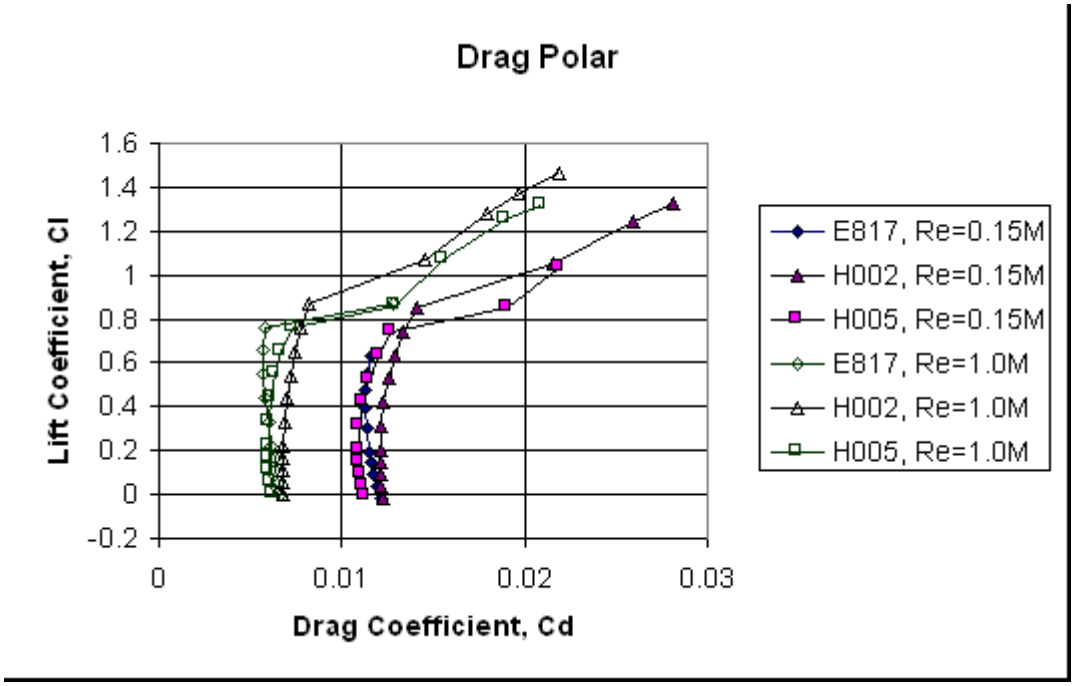
Drag Polar
Lift Coefficient, Cl
1.6
1.4
1.2
1
0.8
0.6
0.4
0.2
0
-0.2
0
0.01
0.02
0.03
Drag Coefficient, Cd
E817, Re=0.15M
H002, Re=0.15M
H005, Re=0.15M
E817, Re=1.0M
H002, Re=1.0M
H005, Re=1.0M

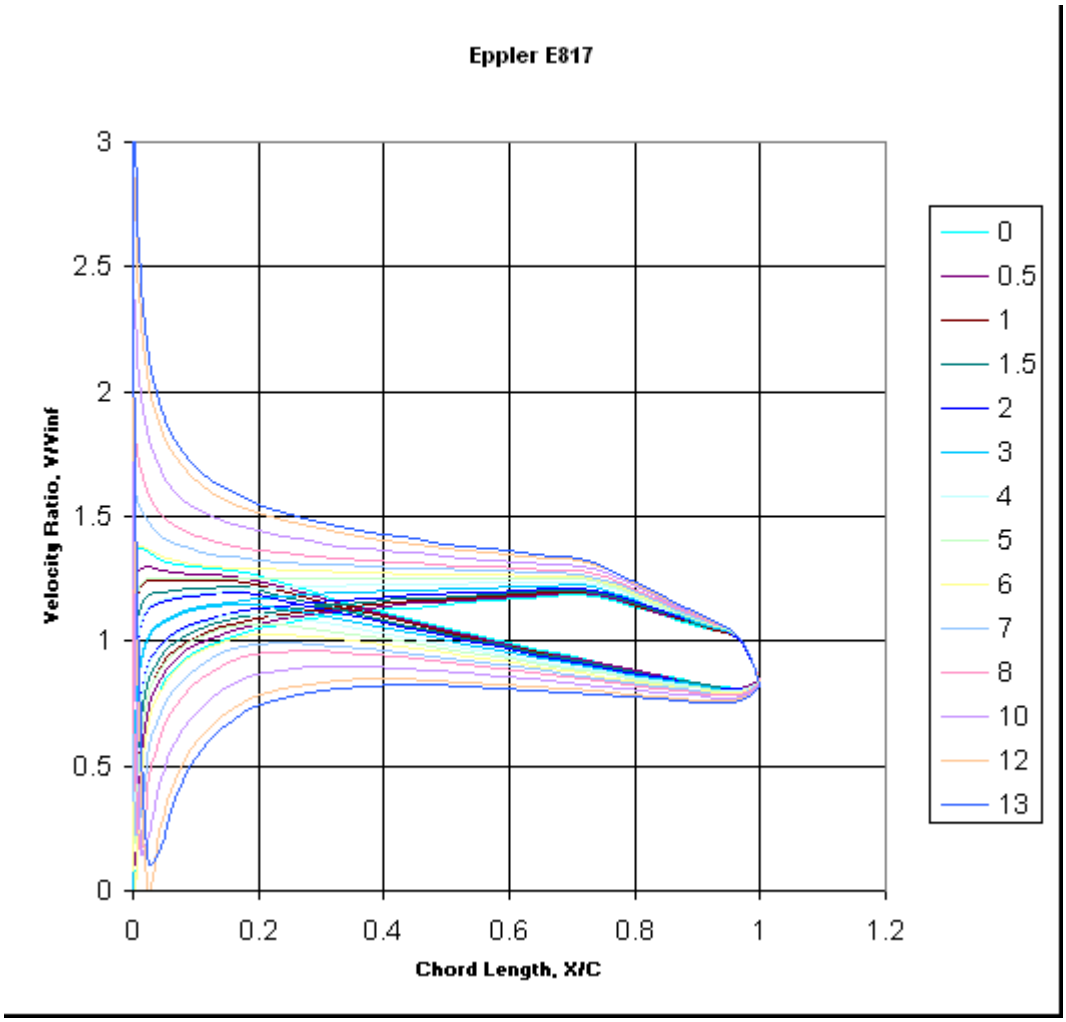
Eppler E817
Velocity Ratio, V/Vinf
3
2.5
2
1.5
1
0.5
0
0
0.2
0.4
0.6
0.8
1
1.2
Chord Length, X/C
0
0.5
1
1.5
2
3
4
5
6
7
8
10
12
13

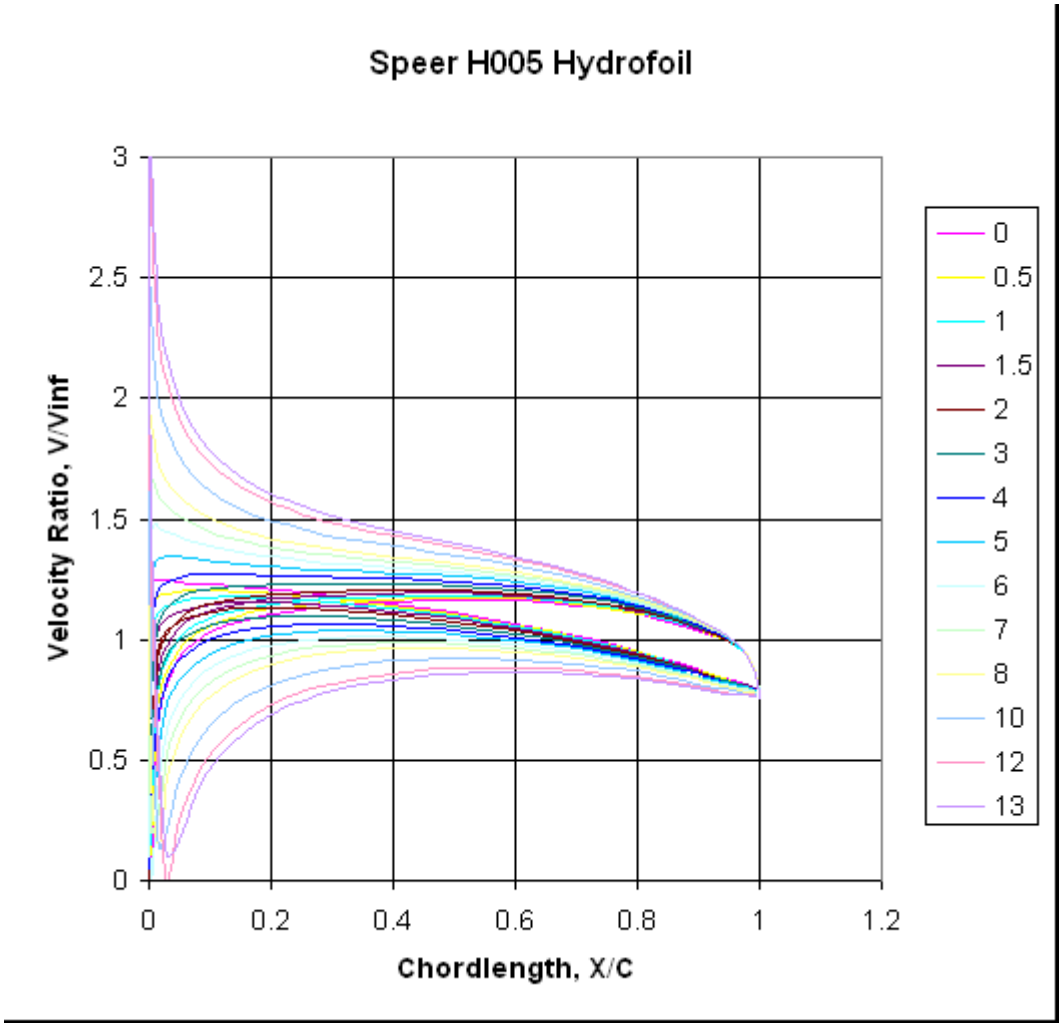
Speer H005 Hydrofoil
Velocity Ratio, V/Vinf
Chordlength, X/C
0
0.5
1
1.5
2
3
4
5
6
7
8
10
12
13

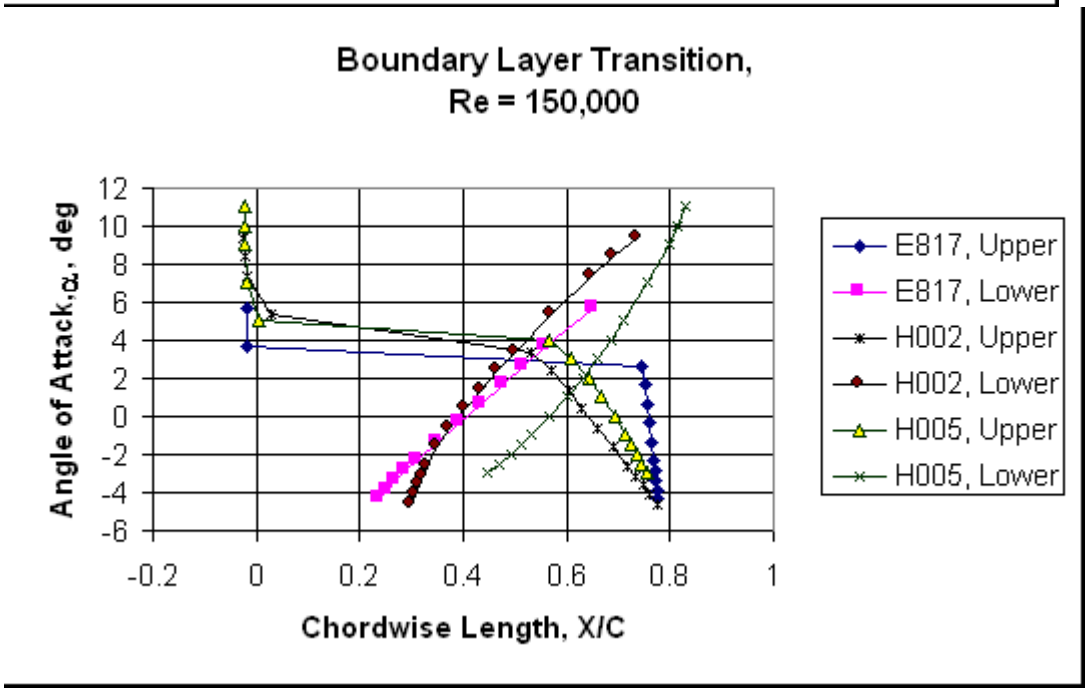
Boundary Layer Transition,
Re = 150,000
Angle of Attack,α, deg
Chordwise Length, X/C
E817, Upper
E817, Lower
H002, Upper
H002, Lower
H005, Upper
H005, Lower

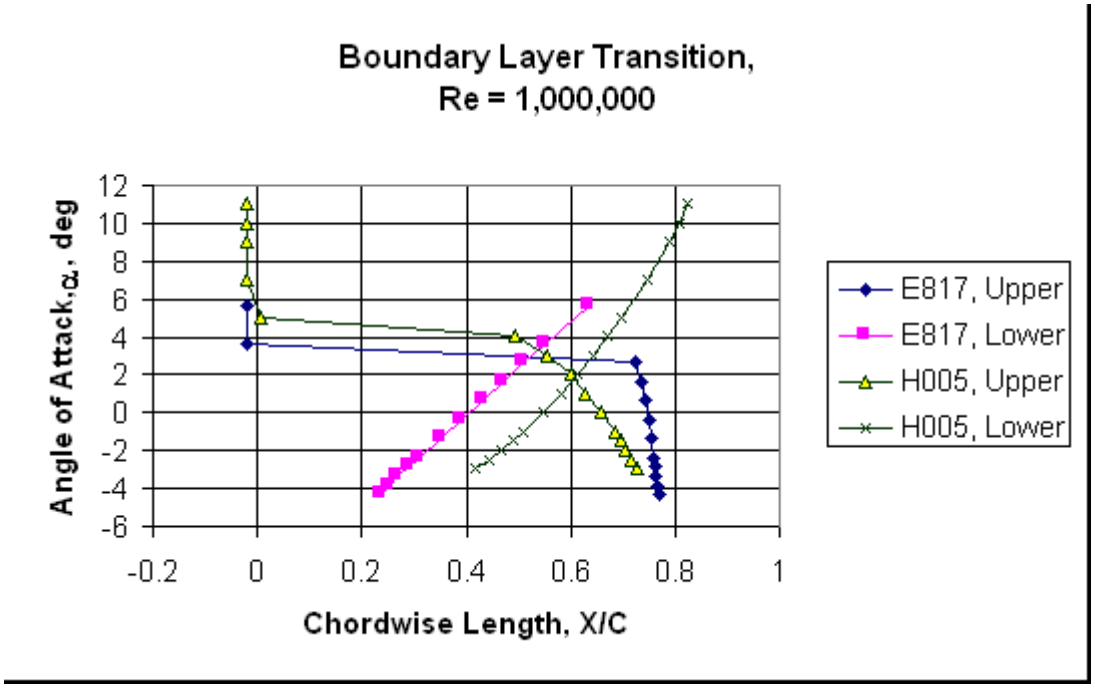
Boundary Layer Transition,
Re = 1,000,000
Angle of Attack,α, deg
12
10
8
6
4
2
0
-2
-4
-6
-0.2
0
0.2
0.4
0.6
0.8
1
Chordwise Length, X/C
E817, Upper
E817, Lower
H005, Upper
H005, Lower

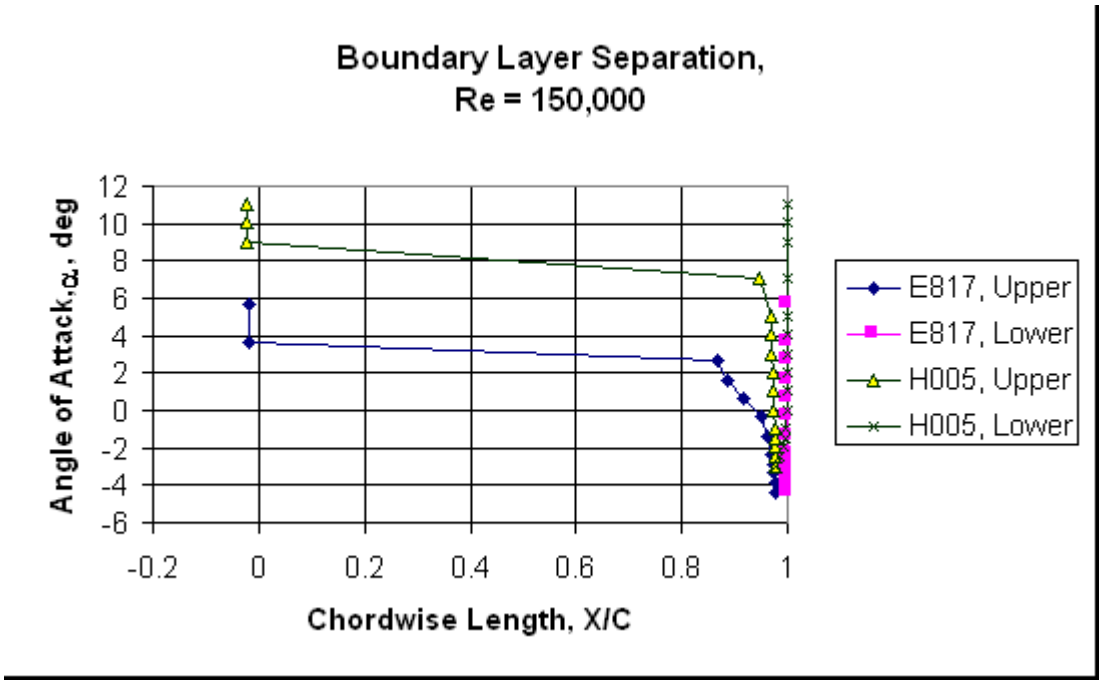
Boundary Layer Separation,
Re = 150,000
Angle of Attack,α, deg
12
10
8
6
4
2
0
-2
-4
-6
-0.2
0
0.2
0.4
0.6
0.8
1
Chordwise Length, X/C
E817, Upper
E817, Lower
H005, Upper
H005, Lower

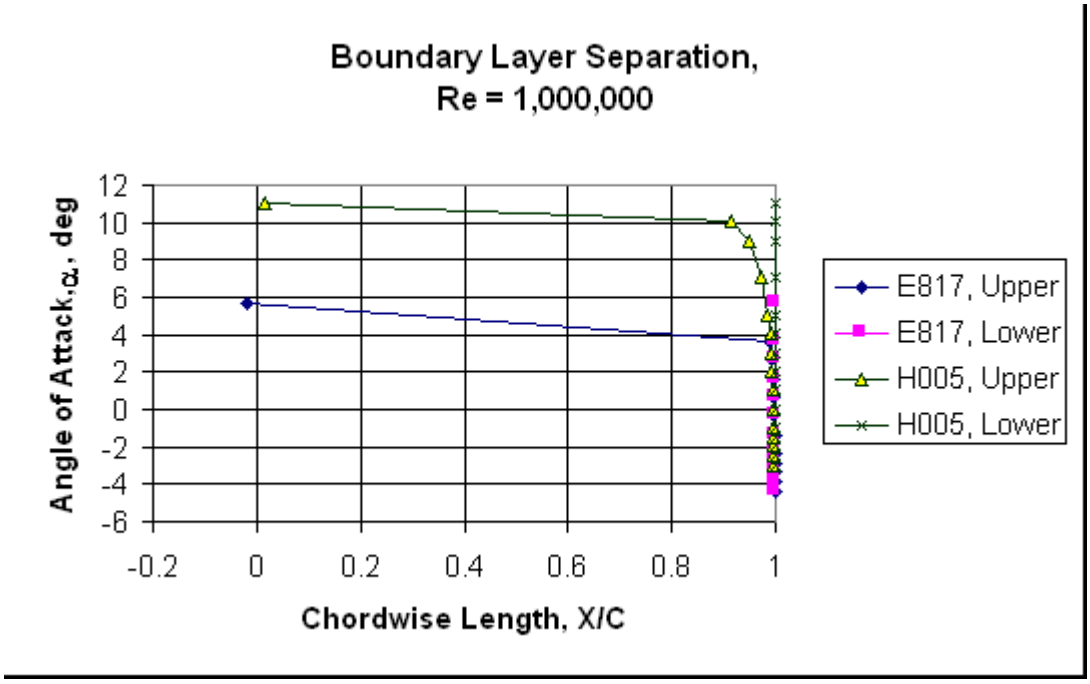
Boundary Layer Separation,
Re = 1,000,000
Angle of Attack,α, deg
12
10
8
6
4
2
0
-2
-4
-6
-0.2
0
0.2
0.4
0.6
0.8
1
Chordwise Length, X/C
E817, Upper
E817, Lower
H005, Upper
H005, Lower

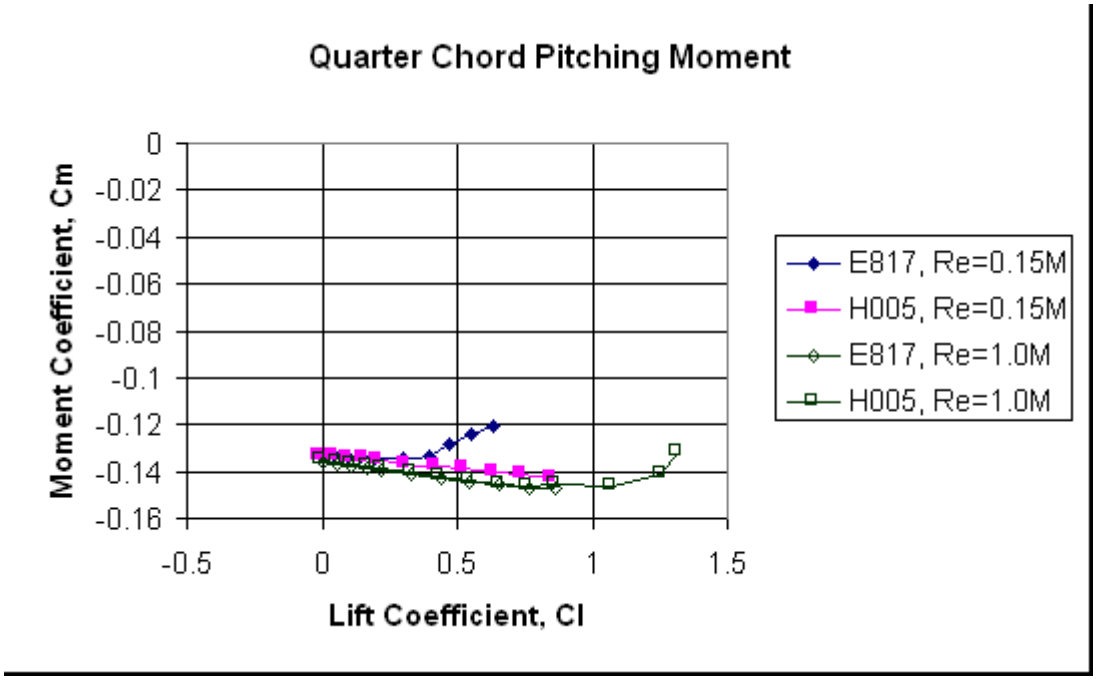

Last Updated on 1/16/99
By Thomas E. Speer
Email: tspeer@gte.net

Home

A.2 NACA 0012 profile data

The following appendix includes the original hydrofoil profile document of the NACA 0012.

NACA 0012 AIRFOILS (n0012-il)

NACA 0012 AIRFOILS - NACA 0012 airfoil

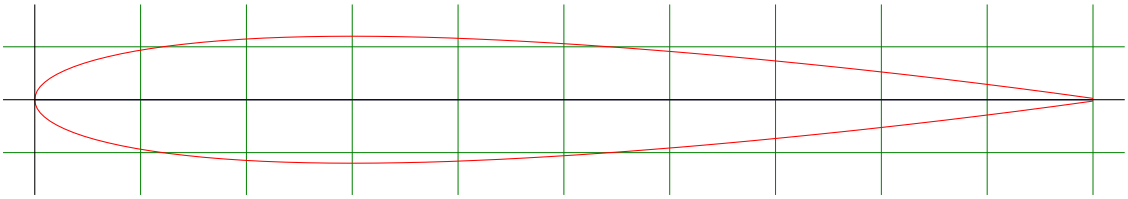

Details

(n0012-il) NACA 0012 AIRFOILS
NACA 0012 airfoil
Max thickness 12% at 30% chord.
Max camber 0% at 0% chord
Source **UIUC Airfoil Coordinates Database**
Source dat file
The dat file is in Lednicer format

Dat file

```
NACA 0012 AIRFOILS
     66.       66.

0.0000000 0.0000000
0.0005839 0.0042603
0.0023342 0.0084289
0.0052468 0.0125011
0.0093149 0.0164706
```

Parser

No parser warnings

Send to airfoil plotter
Add to comparison
Lednicer format dat file
Selig format dat file

Similar airfoils

EPPLER EA 6(-1)-012 AIRFOIL	Preview	Details
NACA M3 AIRFOIL	Preview	Details
NACA M3	Preview	Details
WORTMANN FX 76-120	Preview	Details
(Dicke 12.28%)	Preview	Details
FX 79-L-120	Preview	Details
RAF 30 AIRFOIL	Preview	Details
E168 (12.45%)	Preview	Details
GOE 409 AIRFOIL	Preview	Details
GOE 459 AIRFOIL	Preview	Details

Polars for NACA 0012 AIRFOILS (n0012-il)

Plot	Airfoil	Reynolds #	Ncrit	Max Cl/Cd	Description	Source	
☑	n0012-il	50,000	9	25.7 at α=5°	Mach=0 Ncrit=9	Xfoil prediction	Details
☐	n0012-il	50,000	5	26.5 at α=5.5°	Mach=0 Ncrit=5	Xfoil prediction	Details
☑	n0012-il	100,000	9	36.7 at α=5°	Mach=0 Ncrit=9	Xfoil prediction	Details
☐	n0012-il	100,000	5	36.1 at α=5.5°	Mach=0 Ncrit=5	Xfoil prediction	Details
☑	n0012-il	200,000	9	47.4 at α=5°	Mach=0 Ncrit=9	Xfoil prediction	Details
☐	n0012-il	200,000	5	45.9 at α=6.5°	Mach=0 Ncrit=5	Xfoil prediction	Details
☑	n0012-il	500,000	9	61.7 at α=6.5°	Mach=0 Ncrit=9	Xfoil prediction	Details
☐	n0012-il	500,000	5	61.7 at α=7.5°	Mach=0 Ncrit=5	Xfoil prediction	Details
☑	n0012-il	1,000,000	9	75.6 at α=7.5°	Mach=0 Ncrit=9	Xfoil prediction	Details
☐	n0012-il	1,000,000	5	75.4 at α=8.5°	Mach=0 Ncrit=5	Xfoil prediction	Details

Update plots

Reynolds number calculator

Set Reynolds number and Ncrit range

Update Range

	Low	High
Reynolds Number	50,000	1,000,000
NCrit	7	9

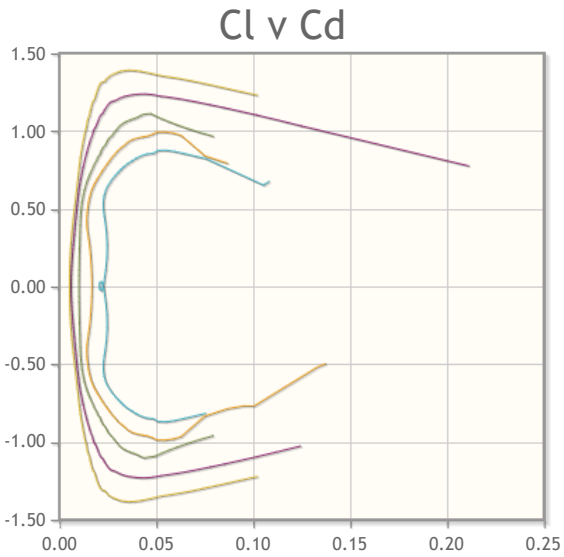

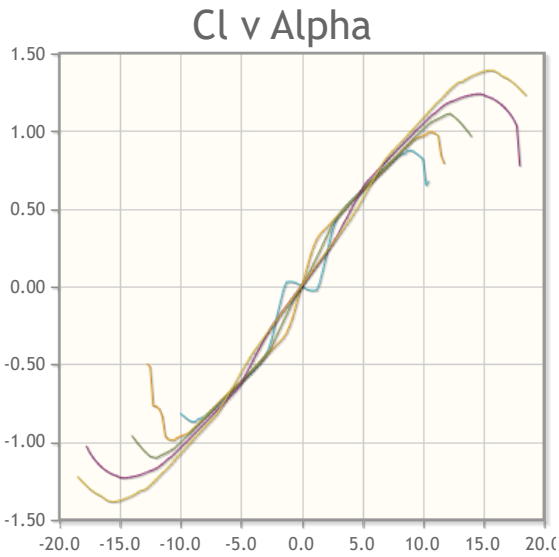

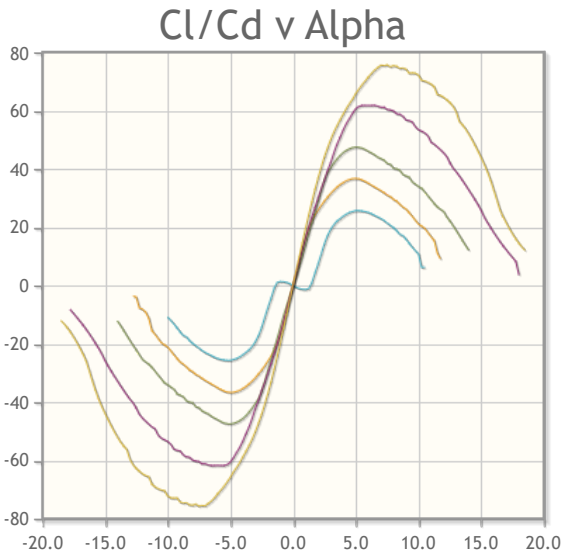

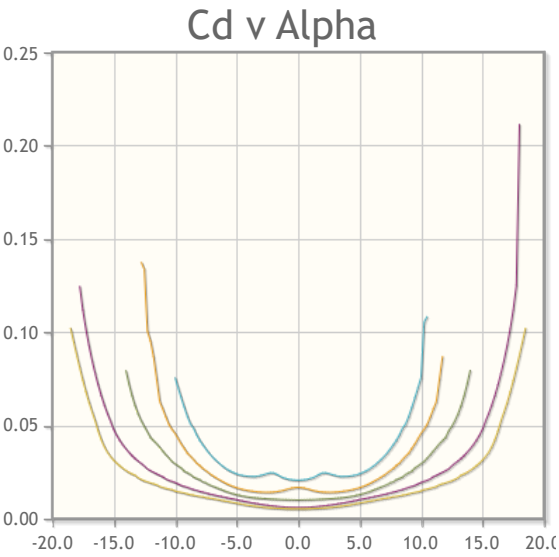

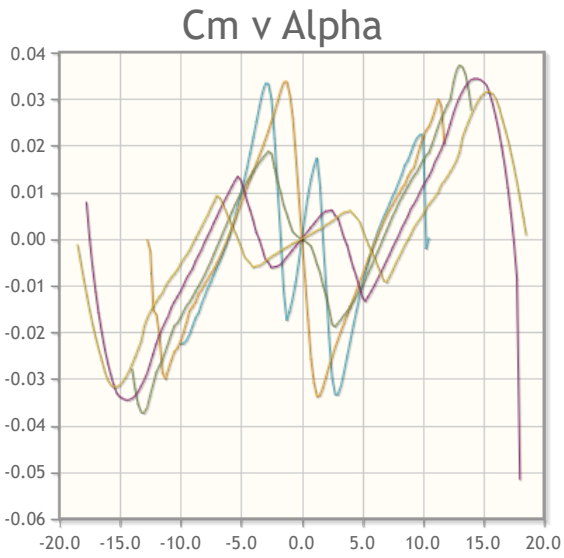

A.3 NACA 2421 profile data

The following appendix includes the original hydrofoil profile document of the NACA 2421.

NACA 2421 (naca2421-il)

NACA 2421 - NACA 2421 airfoil

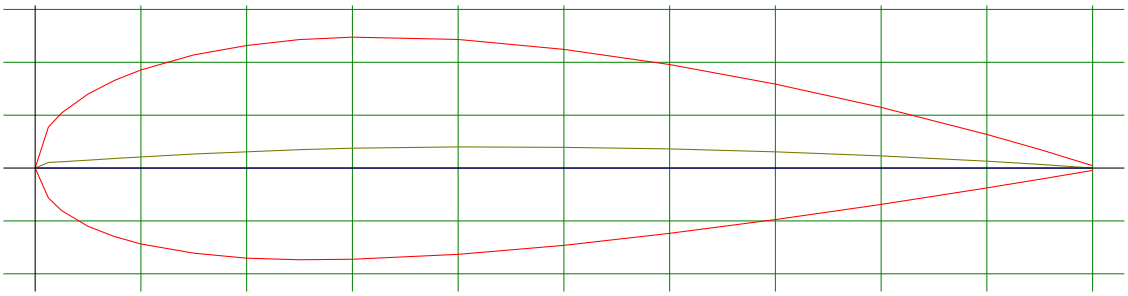

Details

(naca2421-il) NACA 2421
NACA 2421 airfoil
Max thickness 21% at 30% chord.
Max camber 2% at 40% chord
Source UIUC Airfoil Coordinates Database
Source dat file
The dat file is in Selig format

Dat file

```
NACA 2421
1.0000     0.0022
0.9500     0.0176
0.9000     0.0318
0.8000     0.0574
0.7000     0.0794
0.6000     0.0979
0.5000     0.1122
```

Parser

No parser warnings

Send to airfoil plotter
Add to comparison
Lednicer format dat file
Selig format dat file

Similar airfoils

NASA/LANGLEY LS(1)-0421MOD AIRFOIL	Preview	Details
RAF 69 AIRFOIL	Preview	Details
NACA 63(4)-421	Preview	Details
NACA 64(4)-421	Preview	Details
AH 93-W-215	Preview	Details
B-29 ROOT AIRFOIL	Preview	Details
NACA 63(4)-221	Preview	Details
NACA 64(4)-221	Preview	Details
EPPLER 1214 AIRFOIL	Preview	Details
FX 84-W-218	Preview	Details

Polars for NACA 2421 (naca2421-il)

Plot	Airfoil	Reynolds #	Ncrit	Max Cl/Cd	Description	Source	
☑	naca2421-il	50,000	9	6.9 at α=2°	Mach=0 Ncrit=9	Xfoil prediction	Details
☐	naca2421-il	50,000	5	23.8 at α=5°	Mach=0 Ncrit=5	Xfoil prediction	Details
☑	naca2421-il	100,000	9	39.5 at α=8.5°	Mach=0 Ncrit=9	Xfoil prediction	Details
☐	naca2421-il	100,000	5	41.1 at α=6.25°	Mach=0 Ncrit=5	Xfoil prediction	Details
☑	naca2421-il	200,000	9	57.5 at α=6.5°	Mach=0 Ncrit=9	Xfoil prediction	Details
☐	naca2421-il	200,000	5	53.3 at α=7.25°	Mach=0 Ncrit=5	Xfoil prediction	Details
☑	naca2421-il	500,000	9	75.5 at α=7.75°	Mach=0 Ncrit=9	Xfoil prediction	Details
☐	naca2421-il	500,000	5	67.6 at α=7.5°	Mach=0 Ncrit=5	Xfoil prediction	Details
☑	naca2421-il	1,000,000	9	89.5 at α=7.5°	Mach=0 Ncrit=9	Xfoil prediction	Details
☐	naca2421-il	1,000,000	5	81.1 at α=6.5°	Mach=0 Ncrit=5	Xfoil prediction	Details

Update plots Reynolds number calculator

Set Reynolds number and Ncrit range

Update Range

	Low	High
Reynolds Number	50,000	1,000,000
NCrit	7	9

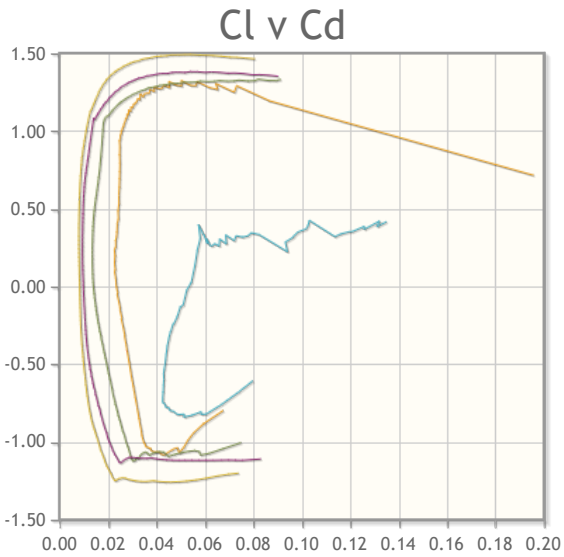

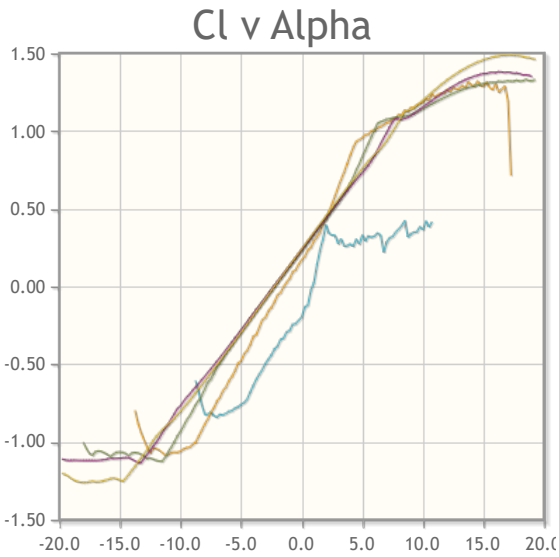

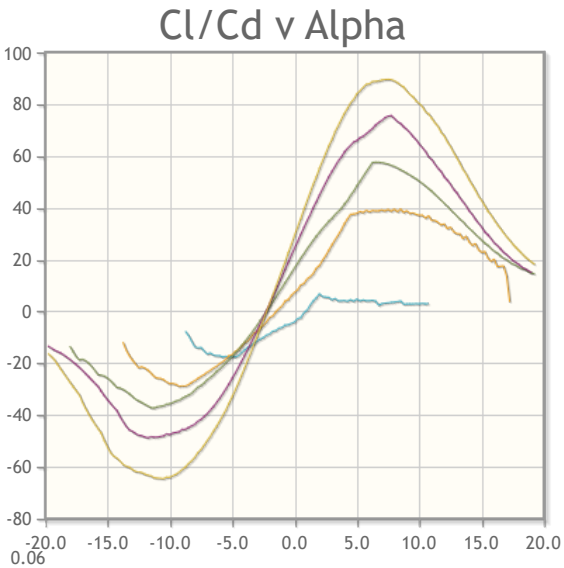

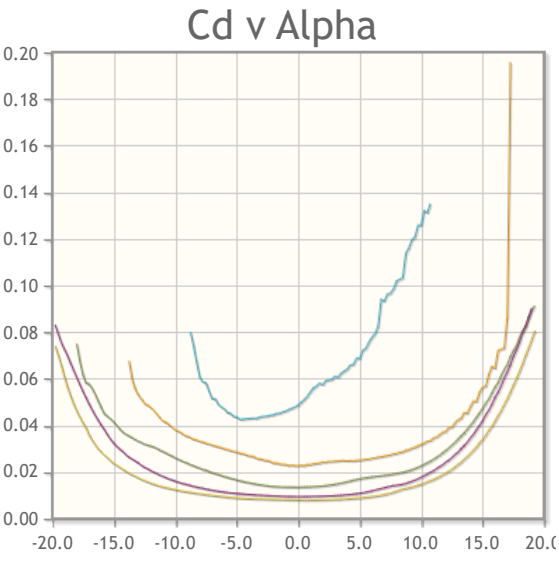

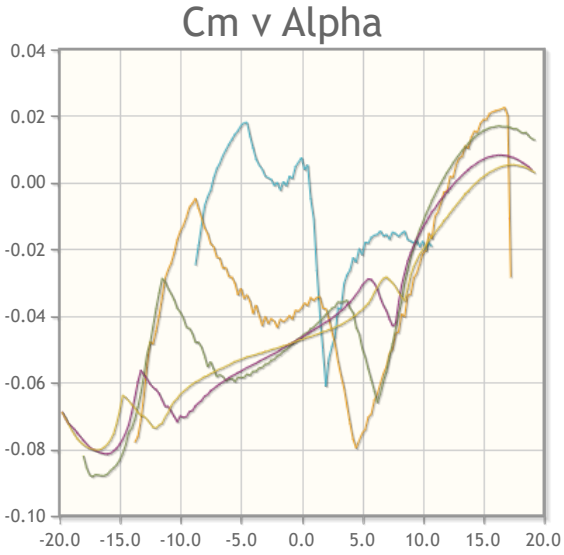

B

SolidWorks Macros

B.1 Foil Macro

Listing B.1: Create Foil Spline and Extrude Macro

```
1
2  Sub CriarSplineEExtrudirDoExcel()
3      Dim swApp As SldWorks.SldWorks
4      Dim swModel As SldWorks.ModelDoc2
5      Dim swSketchMgr As SldWorks.SketchManager
6      Dim swFeatMgr As SldWorks.FeatureManager
7      Dim swFeat As SldWorks.Feature
8      Dim swFrontPlane As Object
9
10     ' Launch SolidWorks
11     Set swApp = Application.SldWorks
12     If swApp Is Nothing Then
13         MsgBox "Warning: SolidWorks is not open!", vbCritical
14         Exit Sub
15     End If
16
17     ' Creation of the new model
18     Set swModel = swApp.NewPart
19     Set swSketchMgr = swModel.SketchManager
20     Set swFeatMgr = swModel.FeatureManager
21
22     ' Front Plane selection
23     Set swFrontPlane = swModel.FeatureByName("Front Plane")
24     If swFrontPlane Is Nothing Then
25         MsgBox "Did not find Front Plane.", vbCritical
26         Exit Sub
27     End If
28     If Not swFrontPlane.Select2(False, -1) Then
29         MsgBox "Error when selecting front plane.", vbCritical
30         Exit Sub
31     End If
32
33     swSketchMgr.InsertSketch True
34
35     ' Connect with Excel
36     Dim excelApp As Object
37     Dim wb As Object, wsFoil As Object, wsGeom As Object
38     Dim path As String
39     path = "C:\Users\ritam\Desktop\Uni\5\2\Excel\Hydrofoil_novo.xlsx"
40
41     If Dir(path) = "" Then
42         MsgBox "Excel file not found!", vbCritical
43         Exit Sub
```

```
44      End If
45
46      Set excelApp = CreateObject("Excel.Application")
47      Set wb = excelApp.Workbooks.Open(path)
48      Set wsFoil = wb.Sheets("Speer H005 geom")      ' Folha dos pontos
49      Set wsGeom = wb.Sheets("Geometria")            ' Folha da extrusao/
            span
50
51      ' Obtain the extrusion value (span) (in this case its cell D12 of
            the Geometria sheet of Excel because its where the value of the
            span for the front foil is)
52      Dim extrusionDepth As Double
53      extrusionDepth = wsGeom.Range("D12").Value
54
55      If Not IsNumeric(extrusionDepth) Or extrusionDepth <= 0 Then
56          MsgBox "Invalid span value in 'Geometria'! Cell D12", vbCritical
57          wb.Close False
58          excelApp.Quit
59          Exit Sub
60      End If
61
62      ' Read the coordinates of the points in sheet "Speer H005 geom"
63      Dim i As Integer, count As Integer
64      Dim x As Double, y As Double
65      Dim temp() As Double
66      ReDim temp(0 To 0)
67      count = 0
68
69      For i = 26 To 63
70          If IsNumeric(wsFoil.Cells(i, 1).Value) And IsNumeric(wsFoil.
                Cells(i, 2).Value) Then
71              x = CDbl(wsFoil.Cells(i, 1).Value)
72              y = CDbl(wsFoil.Cells(i, 2).Value)
73              ReDim Preserve temp(0 To (count + 1) * 3 - 1)
74              temp(count * 3) = x
75              temp(count * 3 + 1) = y
76              temp(count * 3 + 2) = 0
77              count = count + 1
78          End If
79      Next i
80
81      wb.Close False
82      excelApp.Quit
83      Set excelApp = Nothing
84
85      If count < 2 Then
86          MsgBox "Not enough points from the foil read!", vbCritical
87          Exit Sub
88      End If
89
90      ' Create the spline
91      Dim skSpline As Object
92      Set skSpline = swSketchMgr.CreateSpline(temp)
```

```
93
94      If skSpline Is Nothing Then
95          MsgBox "Error when creating the spline!", vbCritical
96          Exit Sub
97      End If
98
99      swSketchMgr.InsertSketch True
100
101     ' Extrude the profile with the span from the cell chosen before
102     Set swFeat = swFeatMgr.FeatureExtrusion2( _
103         True, False, False, 0, 0, _
104         extrusionDepth, 0, _
105         False, False, False, False, _
106         0, 0, False, False, _
107         False, False, True, True, _
108         False, 0, 0, False)
109
110     If swFeat Is Nothing Then
111         MsgBox "Error when extruding the profile!", vbCritical
112     Else
113         MsgBox "Profile extruded successfully! Span: " & extrusionDepth
                & " m"
114     End If
115
116     swModel.ViewZoomtofit2
117 End Sub
```

B.2 Tapered Foil Macro

Listing B.2: Create Foil Spline with Taper Macro

```
1
2   Sub CriarFoilComTaper()
3
4       Dim swApp As SldWorks.SldWorks
5       Dim swModel As SldWorks.ModelDoc2
6       Dim swSketchMgr As SldWorks.SketchManager
7       Dim swFeatMgr As SldWorks.FeatureManager
8       Dim swPlaneRoot As Object, swPlaneMid As Object, swPlaneTip As
            Object
9       Dim boolStatus As Boolean
10
11      Dim excelApp As Object
12      Dim wb As Object, wsFoil As Object, wsGeom As Object
13      Dim path As String
14      Dim i As Integer, count As Integer
15
16      Dim extrusionDepth As Double
17      Dim scaleFactor As Double: scaleFactor = 0.5
18
19      Dim tempRoot() As Double
```

```
20      Dim tempMid() As Double
21      Dim tempTip() As Double
22      Dim tempCenter() As Double
23
24      path = "C:\Users\ritam\Desktop\Uni\5\2\Excel\Hydrofoil_novo.xlsx"
25
26      Set swApp = Application.SldWorks
27      Set swModel = swApp.ActiveDoc
28      If swModel Is Nothing Then
29          MsgBox "Open␣a␣document␣of␣a␣part␣before␣running␣the␣macro!",
               vbCritical
30          Exit Sub
31      End If
32
33      Set swSketchMgr = swModel.SketchManager
34      Set swFeatMgr = swModel.FeatureManager
35
36      Set excelApp = CreateObject("Excel.Application")
37      excelApp.Visible = False
38      If Dir(path) = "" Then
39          MsgBox "Excel␣file␣not␣found!", vbCritical
40          Exit Sub
41      End If
42
43      Set wb = excelApp.Workbooks.Open(path)
44      Set wsFoil = wb.Sheets("Speer␣H005␣geom")
45      Set wsGeom = wb.Sheets("Geometria")
46
47      extrusionDepth = wsGeom.Range("D12").Value
48      If extrusionDepth > 10 Then extrusionDepth = extrusionDepth / 100
49
50      If Not IsNumeric(extrusionDepth) Or extrusionDepth <= 0 Then
51          MsgBox "Invalid␣value␣for␣the␣span␣in␣D12", vbCritical
52          wb.Close False: excelApp.Quit: Exit Sub
53      End If
54
55      ' Read the Excel coordinates
56      count = 0
57      ReDim tempCenter(0 To 0)
58      For i = 26 To 63
59          If IsNumeric(wsFoil.Cells(i, 1).Value) And IsNumeric(wsFoil.
               Cells(i, 2).Value) Then
60              ReDim Preserve tempCenter(0 To (count + 1) * 3 - 1)
61              tempCenter(count * 3) = wsFoil.Cells(i, 1).Value
62              tempCenter(count * 3 + 1) = wsFoil.Cells(i, 2).Value
63              tempCenter(count * 3 + 2) = 0
64              count = count + 1
65          End If
66      Next i
67
68      ' Find the center of the chord
69      Dim minX As Double, maxX As Double, centerX As Double
70      minX = tempCenter(0)
```

```
71      maxX = tempCenter(0)
72      For i = 0 To count - 1
73          If tempCenter(i * 3) < minX Then minX = tempCenter(i * 3)
74          If tempCenter(i * 3) > maxX Then maxX = tempCenter(i * 3)
75      Next i
76      centerX = (minX + maxX) / 2
77
78      ' Create the profiles with the chord aligned
79      ReDim tempRoot(0 To (count * 3) - 1)
80      ReDim tempMid(0 To (count * 3) - 1)
81      ReDim tempTip(0 To (count * 3) - 1)
82
83      For i = 0 To count - 1
84          Dim Xc As Double: Xc = tempCenter(i * 3) - centerX
85          Dim Yc As Double: Yc = tempCenter(i * 3 + 1)
86
87          ' Root (taper)
88          tempRoot(i * 3) = Xc * scaleFactor
89          tempRoot(i * 3 + 1) = Yc * scaleFactor
90          tempRoot(i * 3 + 2) = 0
91
92          ' Mid (original profile)
93          tempMid(i * 3) = Xc
94          tempMid(i * 3 + 1) = Yc
95          tempMid(i * 3 + 2) = 0
96
97          ' Tip (taper)
98          tempTip(i * 3) = Xc * scaleFactor
99          tempTip(i * 3 + 1) = Yc * scaleFactor
100         tempTip(i * 3 + 2) = 0
101     Next i
102
103     wb.Close False
104     excelApp.Quit
105     Set excelApp = Nothing
106
107     swModel.ClearSelection2 True
108
109     ' Create the offset planes
110     boolStatus = swModel.Extension.SelectByID2("Front␣Plane", "PLANE",
            0, 0, 0, False, 0, Nothing, 0)
111     If boolStatus = False Then
112         MsgBox "Selection␣of␣the␣Front␣Plane␣failed␣when␣trying␣to␣
                create␣Middle␣Plane", vbCritical
113         Exit Sub
114     End If
115     Set swPlaneMid = swFeatMgr.InsertRefPlane(8, extrusionDepth / 2, 0,
            0, 0, 0)
116     If swPlaneMid Is Nothing Then
117         MsgBox "Error␣when␣creating␣Middle␣Plane", vbCritical
118         Exit Sub
119     End If
120
```

```
121     swModel.ClearSelection2 True
122     boolStatus = swModel.Extension.SelectByID2("Front␣Plane", "PLANE",
            0, 0, 0, False, 0, Nothing, 0)
123     If boolStatus = False Then
124         MsgBox "Selection␣of␣the␣Front␣Plane␣failed␣when␣trying␣to␣
                create␣Tip␣Plane", vbCritical
125         Exit Sub
126     End If
127     Set swPlaneTip = swFeatMgr.InsertRefPlane(8, extrusionDepth, 0, 0,
            0, 0)
128     If swPlaneTip Is Nothing Then
129         MsgBox "Error␣when␣creating␣Tip␣Plane", vbCritical
130         Exit Sub
131     End If
132
133     ' Sketch Root
134     boolStatus = swModel.Extension.SelectByID2("Front␣Plane", "PLANE",
            0, 0, 0, False, 0, Nothing, 0)
135     If boolStatus = False Then
136         MsgBox "Selection␣of␣the␣Front␣Plane␣failed␣when␣trying␣to␣
                create␣the␣sketch␣root", vbCritical
137         Exit Sub
138     End If
139     swSketchMgr.InsertSketch True
140     swSketchMgr.CreateSpline tempRoot
141     swSketchMgr.InsertSketch False
142     swModel.ClearSelection2 True
143
144     Set swFeat = swModel.FeatureByName("Sketch1")
145     If Not swFeat Is Nothing Then swFeat.Name = "Sketch_Root"
146
147     ' Sketch Middle
148     boolStatus = swPlaneMid.Select2(False, -1)
149     If boolStatus = False Then
150         MsgBox "Selection␣of␣the␣Middle␣Plane␣failed␣when␣trying␣to␣
                create␣the␣sketch␣mid", vbCritical
151         Exit Sub
152     End If
153     swSketchMgr.InsertSketch True
154     swSketchMgr.CreateSpline tempMid
155     swSketchMgr.InsertSketch False
156     swModel.ClearSelection2 True
157
158     Set swFeat = swModel.FeatureByName("Sketch2")
159     If Not swFeat Is Nothing Then swFeat.Name = "Sketch_Mid"
160
161     ' Sketch Tip
162     boolStatus = swPlaneTip.Select2(False, -1)
163     If boolStatus = False Then
164         MsgBox "Selection␣of␣the␣Tip␣Plane␣failed␣when␣trying␣to␣create␣
                the␣sketch␣tip", vbCritical
165         Exit Sub
166     End If
```

```
167     swSketchMgr.InsertSketch True
168     swSketchMgr.CreateSpline tempTip
169     swSketchMgr.InsertSketch False
170     swModel.ClearSelection2 True
171 
172     Set swFeat = swModel.FeatureByName("Sketch3")
173     If Not swFeat Is Nothing Then swFeat.Name = "Sketch_Tip"
174 
175     MsgBox "Sketches␣created␣with␣symmetric␣taper␣and␣centered␣chord:␣
            Root,␣Mid␣and␣Tip.", vbInformation
176 
177 End Sub
```

B.3 Tapered Foil with Flaps Macro

Listing B.3: Create Foil Spline With Taper and Flap Splines Macro

```
1 
2 Sub CriarFoilComTaperEFlap()
3 
4     Dim swApp As SldWorks.SldWorks
5     Dim swModel As SldWorks.ModelDoc2
6     Dim swSketchMgr As SldWorks.SketchManager
7     Dim swFeatMgr As SldWorks.FeatureManager
8     Dim swPlaneMid As Object, swPlaneTip As Object
9     Dim boolStatus As Boolean
10    Dim swFeat As Object
11 
12    Dim excelApp As Object
13    Dim wb As Object, wsFoil As Object, wsGeom As Object
14    Dim path As String
15    Dim i As Integer, count As Integer
16 
17    Dim extrusionDepth As Double
18    Dim scaleFactor As Double: scaleFactor = 0.5
19    Dim flapRatio As Double: flapRatio = 0.35 ' 35% of the chord for the
          flap
20 
21    Dim tempRoot() As Double
22    Dim tempMid() As Double
23    Dim tempTip() As Double
24 
25    Dim tempRootFlap() As Double
26    Dim tempMidFlap() As Double
27    Dim tempTipFlap() As Double
28 
29    path = "C:\Users\ritam\Desktop\Uni\5\2\Excel\Hydrofoil_novo.xlsx"
30 
31    Set swApp = Application.SldWorks
32    Set swModel = swApp.ActiveDoc
33    If swModel Is Nothing Then
```

```
34          MsgBox "Open␣a␣document␣of␣a␣part␣before␣running␣the␣macro!",
               vbCritical
35          Exit Sub
36      End If
37
38      Set swSketchMgr = swModel.SketchManager
39      Set swFeatMgr = swModel.FeatureManager
40
41      Set excelApp = CreateObject("Excel.Application")
42      excelApp.Visible = False
43      If Dir(path) = "" Then
44          MsgBox "Excel␣file␣not␣found!", vbCritical
45          Exit Sub
46      End If
47
48      Set wb = excelApp.Workbooks.Open(path)
49      Set wsFoil = wb.Sheets("Speer␣H005␣geom")
50      Set wsGeom = wb.Sheets("Geometria")
51
52      extrusionDepth = wsGeom.Range("D12").Value
53      If extrusionDepth > 10 Then extrusionDepth = extrusionDepth / 100
54
55      If Not IsNumeric(extrusionDepth) Or extrusionDepth <= 0 Then
56          MsgBox "Invalid␣value␣for␣the␣span␣in␣D12", vbCritical
57          wb.Close False: excelApp.Quit: Exit Sub
58      End If
59
60      ' Read the Excel coordinates
61      count = 0
62      For i = 26 To 63
63          If IsNumeric(wsFoil.Cells(i, 1).Value) And IsNumeric(wsFoil.
               Cells(i, 2).Value) Then
64              count = count + 1
65          End If
66      Next i
67
68      ' Resize of the arrays for foil and flap
69      ReDim tempRoot((count * 3) - 1)
70      ReDim tempMid((count * 3) - 1)
71      ReDim tempTip((count * 3) - 1)
72
73      ReDim tempRootFlap((count * 3) - 1)
74      ReDim tempMidFlap((count * 3) - 1)
75      ReDim tempTipFlap((count * 3) - 1)
76
77      Dim Xc As Double, Yc As Double
78      Dim minX As Double, maxX As Double, centerX As Double
79      minX = 9999
80      maxX = -9999
81
82      ' Read points to find minX and maxX
83      For i = 0 To count - 1
84          Xc = wsFoil.Cells(i + 26, 1).Value
```

```
85          Yc = wsFoil.Cells(i + 26, 2).Value
86
87          If Xc < minX Then minX = Xc
88          If Xc > maxX Then maxX = Xc
89      Next i
90
91      centerX = (minX + maxX) / 2
92      Dim chordLength As Double
93      chordLength = maxX - minX
94
95      ' Create the profiles with the chord aligned
96      For i = 0 To count - 1
97          Xc = wsFoil.Cells(i + 26, 1).Value - centerX
98          Yc = wsFoil.Cells(i + 26, 2).Value
99
100         tempRoot(i * 3) = Xc * scaleFactor
101         tempRoot(i * 3 + 1) = Yc * scaleFactor
102         tempRoot(i * 3 + 2) = 0
103
104         tempMid(i * 3) = Xc
105         tempMid(i * 3 + 1) = Yc
106         tempMid(i * 3 + 2) = 0
107
108         tempTip(i * 3) = Xc * scaleFactor
109         tempTip(i * 3 + 1) = Yc * scaleFactor
110         tempTip(i * 3 + 2) = 0
111     Next i
112
113     ' --- FLAPS ---
114
115     ' Define a beginning point for the flap at 65 % of the chord
116     Dim flapStartX As Double
117     flapStartX = minX + chordLength * (1 - flapRatio) ' 65% of the chord
118
119     ' Loop to create the flap points
120     For i = 0 To count - 1
121         Dim Xorig As Double, Yorig As Double
122         Xorig = wsFoil.Cells(i + 26, 1).Value
123         Yorig = wsFoil.Cells(i + 26, 2).Value
124
125         If Xorig < flapStartX Then
126             ' Create the beginning of the flap by putting all the points
                    for continuity
127             tempRootFlap(i * 3) = (flapStartX - centerX) * scaleFactor
128             tempRootFlap(i * 3 + 1) = 0
129             tempRootFlap(i * 3 + 2) = 0
130
131             tempMidFlap(i * 3) = (flapStartX - centerX)
132             tempMidFlap(i * 3 + 1) = 0
133             tempMidFlap(i * 3 + 2) = 0
134
135             tempTipFlap(i * 3) = (flapStartX - centerX) * scaleFactor
136             tempTipFlap(i * 3 + 1) = 0
```

```
137             tempTipFlap(i * 3 + 2) = 0
138
139         Else
140             ' Point inside the flap: scale for X and Y for the mini foil
141             Dim XflapLocal As Double, YflapLocal As Double
142             ' Localize the relative position inside the flap
143             Dim relX As Double
144             relX = (Xorig - flapStartX) / (maxX - flapStartX) ' 0 a 1
145
146             ' Scale the flap chord for 35% of the original chord
147             XflapLocal = relX * chordLength * flapRatio
148
149             ' Y scaled the same to the original
150             YflapLocal = Yorig
151
152             ' Adjust the right position
153             Dim Xfinal As Double
154             Xfinal = (flapStartX - centerX) + XflapLocal
155
156             ' Apply the scale and taper in Root, Mid and Tip
157             tempRootFlap(i * 3) = Xfinal * scaleFactor
158             tempRootFlap(i * 3 + 1) = YflapLocal * scaleFactor
159             tempRootFlap(i * 3 + 2) = 0
160
161             tempMidFlap(i * 3) = Xfinal
162             tempMidFlap(i * 3 + 1) = YflapLocal
163             tempMidFlap(i * 3 + 2) = 0
164
165             tempTipFlap(i * 3) = Xfinal * scaleFactor
166             tempTipFlap(i * 3 + 1) = YflapLocal * scaleFactor
167             tempTipFlap(i * 3 + 2) = 0
168
169         End If
170     Next i
171
172     wb.Close False
173     excelApp.Quit
174     Set excelApp = Nothing
175
176     swModel.ClearSelection2 True
177
178     ' Create the offset planes Middle and Tip
179     boolStatus = swModel.Extension.SelectByID2("Front␣Plane", "PLANE",
            0, 0, 0, False, 0, Nothing, 0)
180     If boolStatus = False Then
181         MsgBox "Selection␣of␣the␣Front␣Plane␣failed␣when␣trying␣to␣
                create␣Middle␣Plane", vbCritical
182         Exit Sub
183     End If
184     Set swPlaneMid = swFeatMgr.InsertRefPlane(8, extrusionDepth / 2, 0,
            0, 0, 0)
185     If swPlaneMid Is Nothing Then
186         MsgBox "Error␣when␣creating␣Middle␣Plane", vbCritical
```

```
187         Exit Sub
188     End If
189     swModel.ClearSelection2 True
190 
191     boolStatus = swModel.Extension.SelectByID2("Front␣Plane", "PLANE",
            0, 0, 0, False, 0, Nothing, 0)
192     If boolStatus = False Then
193         MsgBox "Selection␣of␣the␣Front␣Plane␣failed␣when␣trying␣to␣
                create␣Tip␣Plane", vbCritical
194         Exit Sub
195     End If
196     Set swPlaneTip = swFeatMgr.InsertRefPlane(8, extrusionDepth, 0, 0,
            0, 0)
197     If swPlaneTip Is Nothing Then
198         MsgBox "Error␣when␣creating␣Tip␣Plane", vbCritical
199         Exit Sub
200     End If
201     swModel.ClearSelection2 True
202 
203 
204     ' Sketch Root (Front Plane)
205     boolStatus = swModel.Extension.SelectByID2("Front␣Plane", "PLANE",
            0, 0, 0, False, 0, Nothing, 0)
206     If boolStatus = False Then MsgBox "Selection␣of␣the␣Front␣Plane␣
            failed␣when␣trying␣to␣create␣the␣sketch␣root", vbCritical: Exit
            Sub
207     swSketchMgr.InsertSketch True
208     swSketchMgr.CreateSpline tempRoot
209     swSketchMgr.InsertSketch False
210     swModel.ClearSelection2 True
211     Set swFeat = swModel.FeatureByName("Sketch1")
212     If Not swFeat Is Nothing Then swFeat.Name = "Sketch_Root"
213 
214     ' Sketch Middle (Middle Plane)
215     boolStatus = swPlaneMid.Select2(False, -1)
216     If boolStatus = False Then MsgBox "Selection␣of␣the␣Middle␣Plane␣
            failed␣when␣trying␣to␣create␣the␣sketch␣mid", vbCritical: Exit
            Sub
217     swSketchMgr.InsertSketch True
218     swSketchMgr.CreateSpline tempMid
219     swSketchMgr.InsertSketch False
220     swModel.ClearSelection2 True
221     Set swFeat = swModel.FeatureByName("Sketch2")
222     If Not swFeat Is Nothing Then swFeat.Name = "Sketch_Mid"
223 
224     ' Sketch Tip (Tip Plane)
225     boolStatus = swPlaneTip.Select2(False, -1)
226     If boolStatus = False Then MsgBox "Selection␣of␣the␣Tip␣Plane␣failed
            ␣when␣trying␣to␣create␣the␣sketch␣tip", vbCritical: Exit Sub
227     swSketchMgr.InsertSketch True
228     swSketchMgr.CreateSpline tempTip
229     swSketchMgr.InsertSketch False
230     swModel.ClearSelection2 True
```

```
231     Set swFeat = swModel.FeatureByName("Sketch3")
232     If Not swFeat Is Nothing Then swFeat.Name = "Sketch_Tip"
233 
234     ' Create flap sketches
235 
236     ' Root Flap (Front Plane)
237     boolStatus = swModel.Extension.SelectByID2("Front Plane", "PLANE",
            0, 0, 0, False, 0, Nothing, 0)
238     If boolStatus = False Then MsgBox "Selection of the Front Plane
            failed when trying to create the sketch root flap", vbCritical:
            Exit Sub
239     swSketchMgr.InsertSketch True
240     swSketchMgr.CreateSpline tempRootFlap
241     swSketchMgr.InsertSketch False
242     swModel.ClearSelection2 True
243     Set swFeat = swModel.FeatureByName("Sketch4")
244     If Not swFeat Is Nothing Then swFeat.Name = "Sketch_Root_Flap"
245 
246     ' Middle Flap (Middle Plane)
247     boolStatus = swPlaneMid.Select2(False, -1)
248     If boolStatus = False Then MsgBox "Selection of the Middle Plane
            failed when trying to create a sketch mid flap", vbCritical: Exit
             Sub
249     swSketchMgr.InsertSketch True
250     swSketchMgr.CreateSpline tempMidFlap
251     swSketchMgr.InsertSketch False
252     swModel.ClearSelection2 True
253     Set swFeat = swModel.FeatureByName("Sketch5")
254     If Not swFeat Is Nothing Then swFeat.Name = "Sketch_Mid_Flap"
255 
256     ' Tip Flap (Tip Plane)
257     boolStatus = swPlaneTip.Select2(False, -1)
258     If boolStatus = False Then MsgBox "Selection of the Tip Plane failed
            when trying to create the sketch tip flap", vbCritical: Exit Sub
259     swSketchMgr.InsertSketch True
260     swSketchMgr.CreateSpline tempTipFlap
261     swSketchMgr.InsertSketch False
262     swModel.ClearSelection2 True
263     Set swFeat = swModel.FeatureByName("Sketch6")
264     If Not swFeat Is Nothing Then swFeat.Name = "Sketch_Tip_Flap"
265 
266 End Sub
```

C

HS-5086WP technical information

The following appendix includes the technical information of the servo HS-5086WP.

(0)

SEARCH...

HS-5086WP 28.5g Waterproof Metal Gear Digital Micro Servo

Part #: 35086W

$55.99

1 ADD TO CART ADD TO WISH LIST

NON-HOBBY CUSTOMERS ORDER HERE

PRODUCT DESCRIPTION

The HS-5086WP is the smallest in Hitec's class of waterproof servos. With heavy-duty metal gears and a ball bearing supported output shaft, the HS-5086WP is among the most durable and reliable micro servo for wet conditions. Possessing the same size as our popular HS-85MG and the industry's first IP67*rating, this spunky mini will keep your RC vehicle, boat, aircraft or robot watertight, no matter what the weather or surroundings.

Features

- Programmable Circuit

Programmable Functions

- End Point Adjustments
- Direction
- Fail Safe
- Dead Band
- Speed (Slower)
- Data Save / Load
- Program Reset

HS-5086WP Servo Specifications

Performance Specifications	
Operating Voltage Range (Volts DC)	4.8V ~ 6.0V
Speed (Second @ 60°)	0.18 ~ 0.15
Maximum Torque Range oz. / in.	42 ~ 50
Maximum Torque Range kg. / cm.	3.0 ~ 3.6
Current Draw at Idle	3 mA
No Load Operating Current Draw	280 mA
Stall Current Draw	1,800 mA
Dead Band Width	2 µs
Physical Specifications	
Dimensions (Inches)	1.22 x 0.60 x 1.22
Dimensions (Metric)	31.0 x 15.2 x 31.0
Weight (Ounces)	1.00
Weight (Gram)	28.5
Circuit Type	G1 Programable Digital
Motor Type	3 Pole Metal Brush Ferrite
Gear Material	Metal
Bearing Type	Top Ball Bearing

(0)

Dust / Water Resistance	IP 67
Connector Gauge (AWG) / Strand Count	25 / 40
Radio Control Applications	
Parkflyer	< 50 oz.
Sport Plane	42 - 50 oz.
Sailplane	<2 meter/DLG
3D Performance	N / A
Scale	N / A
Electric Helicopter	N / A
Gas Helicopter	N / A
On Road	1/6th
Monster Truck	N / A
Buggies	1/6th
Truggies	N / A
Short Course / Truck	1/6th
Crawlers	N / A
Sail Boat	N / A
Power Boat	1/6th

WARRANTY INFO

RELATED PRODUCTS